

HARVARD UNIVERSITY
Graduate School of Arts and Sciences



DISSERTATION ACCEPTANCE CERTIFICATE

The undersigned, appointed by the
Department of Physics
have examined a dissertation entitled

Dissipation of Magnetic Energy in Collisionless Accretion Flows

presented by Michael Edward Rowan

candidate for the degree of Doctor of Philosophy and hereby
certify that it is worthy of acceptance.

Signature

A handwritten signature in black ink, appearing to read "Masahiro Morii".

Typed name: Professor Masahiro Morii, Chair

Signature

A handwritten signature in black ink, appearing to read "R. Narayan".

Typed name: Professor Ramesh Narayan, Co-Chair

Signature

A handwritten signature in black ink, appearing to read "Douglas Finkbeiner".

Typed name: Professor Douglas Finkbeiner

Date: August 26, 2019

Dissipation of Magnetic Energy in Collisionless Accretion Flows

A DISSERTATION PRESENTED
BY
MICHAEL ROWAN
TO
THE DEPARTMENT OF PHYSICS

IN PARTIAL FULFILLMENT OF THE REQUIREMENTS
FOR THE DEGREE OF
DOCTOR OF PHILOSOPHY
IN THE SUBJECT OF
PHYSICS

HARVARD UNIVERSITY
CAMBRIDGE, MASSACHUSETTS
AUGUST 2019

©2019 – MICHAEL ROWAN
ALL RIGHTS RESERVED.

Dissipation of Magnetic Energy in Collisionless Accretion Flows

ABSTRACT

In a series of investigations, we explore magnetic dissipation in collisionless accretion flows of black hole (BH) coronae. We study energy partition between electrons and protons via magnetic reconnection for the idealized geometry of antiparallel reconnection, and develop an electron heating prescription, motivated by the results of fully-kinetic particle-in-cell (PIC) simulations, which depends on plasma β_i (the ratio of proton thermal pressure to magnetic pressure) and magnetization σ_w (the ratio of magnetic energy density to enthalpy density). We extend the study of antiparallel reconnection to the more general case of ‘guide field’ reconnection, in which an out-of-plane component of magnetic field B_g is superposed on antiparallel reconnecting field lines (with magnitude B_0); we study the dependence of energy partition between electrons and ions on plasma parameters β_i , σ_w , the guide field strength $b_g \equiv B_g/B_0$, the initial electron-to-ion temperature ratio T_{e0}/T_{i0} , and the ion-to-electron mass ratio, m_i/m_e ; we consider mass ratios up to the realistic value, $m_i/m_e = 1836$. We develop a general prescription for electron irreversible heating efficiency via magnetic reconnection as a function of β_i , σ_w , b_g , T_{e0}/T_{i0} , and m_i/m_e , and we explore with guiding center formalism the mechanism of electron heating in guide field reconnection. We study the Kelvin-Helmholtz (KH) instability with linear stability analysis, magnetohydrodynamic simulations, and PIC simulations; for a test case, we explore magnetic dissipation and heating in KH-induced reconnection. We implement the [Esirkepov \(2001\)](#) method of current deposition, as a way of reducing numerical heating in our PIC experiments. This work addresses the crucial question of dissipation of magnetic energy in collisionless accretion flows of BH coronae, and shows

that KH-induced magnetic reconnection may both heat particles and accelerate particles into a power-law energy tail.

Contents

1	INTRODUCTION	1
1.1	Sweet-Parker magnetic reconnection: a simplified analytic model	4
1.2	Particle-in-cell simulation	8
1.2.1	Particle-in-cell simulation with TRISTAN-MP	11
1.3	Outline	12
2	ELECTRON AND PROTON HEATING IN TRANS-RELATIVISTIC MAGNETIC RECONNECTION	14
2.1	Abstract	14
2.2	Introduction	15
2.3	Simulation setup	18
2.4	Technique for extracting the heating efficiency	24
2.4.1	Time evolution of the reconnection layer	25
2.4.2	Upstream and downstream identification	28
2.4.3	Characterization of heating	30
2.5	Results	36
2.5.1	Reconnection physics as a function of β_i	40
2.5.2	Dependence of inflow and outflow velocity on β_i and T_e/T_i	44
2.5.3	Dependence of particle heating on β_i and T_e/T_i	45
2.5.4	Dependence of particle heating on m_i/m_e	54
2.5.5	Dependence of particle heating on magnetization	56
2.5.6	Dependence of particle heating on T_e/T_i for $m_i/m_e = 1836$	63
2.6	Summary and discussion	65
2.A	Convergence with respect to domain size	68
2.B	Outflow versus periodic boundary conditions	69
2.C	Convergence with respect to spatial resolution	71
2.D	Control of numerical heating	73
2.E	Anisotropy in the downstream	75
2.F	Convergence of the layer width when varying the initial sheet thickness	76
2.G	Heating efficiencies in terms of internal energy per particle	77
3	ELECTRON AND PROTON HEATING IN TRANSRELATIVISTIC GUIDE FIELD MAGNETIC RECONNECTION	81
3.1	Abstract	81
3.2	Introduction	82
3.3	Simulation setup	85
3.4	Measurement of late-time heating	92
3.4.1	Time evolution of the reconnection layer	92
3.4.2	Measurement of particle heating in the primary island	95
3.5	Results	100
3.5.1	Electron and proton heating: weak vs. strong guide field	100
3.5.2	Reconnection rate	105
3.5.3	Electron and proton heating: b_g and β_i dependence	105
3.5.4	Electron irreversible heating efficiency: T_{e0}/T_{i0} and σ_w dependence	111

3.5.5	Fitting function	114
3.5.6	Temperature anisotropy	115
3.5.7	Mechanisms of electron heating in guide field reconnection	116
3.6	Summary and discussion	122
3.A	Convergence of irreversible heating fractions with respect to domain size L_x	126
3.B	Guiding center formalism	126
4	KELVIN-HELMHOLTZ I	140
4.1	Introduction	140
4.2	Problem descriptions and linear analysis	141
4.2.1	Shearing flow problem descriptions	141
4.2.2	Relativistic MHD equations	144
4.2.3	Linear analysis of instability	145
4.2.4	Astrophysical jet: numerical results	159
4.3	Relativistic MHD simulation	169
4.3.1	Simulation setup	170
4.3.2	Simulation results: astrophysical jet	171
4.3.3	Simulation results: symmetric shear flow	178
4.4	Summary	181
4.A	Astrophysical jet: dispersion relation equations	181
4.B	Convergence of measured growth rate with respect to α	184
5	KELVIN-HELMHOLTZ II	186
5.1	Introduction	186
5.2	Simulation setup	186
5.2.1	Description of setup	186
5.2.2	Fiducial parameters and numerical choices	195
5.3	Results	197
5.3.1	Time evolution	197
5.3.2	Instability growth rates	197
5.3.3	Magnetic dissipation	204
5.4	Summary	211
5.A	Convergence of measured growth rate with respect to box size	212
5.B	Estimate of uncertainty using different random initial conditions	212
6	ESIRKEPOV CURRENT DEPOSITION SCHEME	215
6.1	Introduction	215
6.2	Esirkepov scheme	215
6.3	Tests	221
6.3.1	Numerical heating in a uniform plasma	222
6.3.2	Filamentation instability	226
6.3.3	Numerical Cherenkov instability	230
6.4	Performance	233
6.5	Summary	236
6.A	Esirkepov coefficients	236
6.B	Numerical heating in 2D	240

APPENDIX A PERFORMANCE AND PARALLEL SCALING OF TRISTAN-MP	242
A.1 Code performance	242
A.2 Parallel scaling	243
APPENDIX B WidPy: TOOL FOR VISUALIZATION AND ANALYSIS OF TRISTAN-MP DATA	245
APPENDIX C IMPLEMENTATION OF ESIRKEPOV DENSITY DECOMPOSITION	247
REFERENCES	262

IN MEMORY OF AUNT MARE.

Acknowledgments

It is with extreme gratitude that I thank the following people.

I am enormously thankful to my adviser, Ramesh Narayan, who agreed to work with me in the beginning, and who helped me on the path to becoming a researcher. I thank Ramesh especially for his patience in working with me, for always being accessible to discuss research, for providing me with the best computing resources, workspace, and any other opportunities I could ask for, and for his pure dedication to physics, which is genuinely inspiring. Ramesh has an uncanny ability to piece together a problem as I try to explain it (oftentimes haphazardly), then recast it lucidly, and provide key feedback that helps to circumvent research roadblocks; this has been crucial in navigating all of the research projects explored in this dissertation. There are too many episodes for me to list here, wherein I was convinced that a problem was severe, and Ramesh got us ‘unstuck’ within a mere hour or two. This work would not have been possible without Ramesh’s scientific contributions and larger vision, and moreover it would not have been possible without Ramesh taking the time to cultivate my learning and research ability, and my thinking on collisionless accretion flows/MHD/plasma physics. Ramesh’s habit of clear thinking about research problems has inspired me to strive for the same clear thinking.

Any graduate student would be fortunate to have one excellent adviser; I was unusually lucky to have a second, in Lorenzo Sironi. Lorenzo’s boundless optimism and energy have been contagious, and chatting with Lorenzo on research has always been a morale booster. I am especially thankful to Lorenzo for teaching me anything I know about plasma physics, the particle-in-cell method, and the code `TRISTAN-MP`, which is the cornerstone of the work presented in this dissertation. I think the first time I sat down with Lorenzo to discuss the first project on simulations of magnetic reconnection, I barely knew how to open `Terminal` on my computer; Lorenzo took me from this

stage, to becoming a somewhat experienced user of the **TRISTAN-MP** code, and eventually to making nontrivial contributions to our version of the code; I am enormously grateful for all of the time and energy Lorenzo invested in me throughout this process. I am also thankful to Lorenzo for teaching me how to effectively read research papers, and also for his thorough feedback on my work; Lorenzo's diligence and attention to detail have inspired in me an effort to produce work that is as complete and high quality as I can manage.

I am extremely grateful to my committee member and academic adviser Masahiro Morii, who has provided me with excellent advice since my first year, and whose intervention helped me to avert what was sure to be a non-ideal outcome. Apart from the excellent advice Masahiro provided during advising meetings, I appreciated the unpredictable and amusing discussions that would somehow sprout up, which always helped to brighten my perspective by the end of our meetings.

I am thankful to my committee member Doug Finkbeiner, who helped direct me into a research area/group that would ultimately be a good fit for me, and for all of the useful advice on research, regarding graduate school and also looking to the future. I remember we had one of our advising meetings over food at the physics department picnic, and we were discussing the dangers of using codes as 'black boxes,' a habit that I was sure I was guilty of at the time, but wasn't quite sure how to break out of. I remember Doug suggesting that typically you need to take the initiative so that code does not remain a black box, and it is sometimes easiest to do that by finding a small project that involves modifications to the code; I wholeheartedly believe that this advice implanted in my subconscious to try some of the coding projects that helped me to overcome the barrier of using my main code as a black box.

I thank the administrators at the Physics Department, the Black Hole Initiative (BHI), and the Center for Astrophysics (CfA), for keeping everything running like clockwork, and for their kindness and welcoming. I am especially thankful to Barbara Elfman at the BHI; Nina Zonnevylle, Mark

Palmer, and Robb Scholten at the CfA; and Lisa Cacciabuado and Carol Davis in the Physics Department. All of these people went above and beyond to help me, whether it was help with moving my stuff from the CfA to the BHI, helping me to navigate Byzantine reimbursement forms, or providing suggestions of places to visit in and around Boston.

I thank FAS research computing, and especially Paul Edmon, for all of the technical help in using the Odyssey computing cluster, and for responding to my frequent help tickets. Paul's expertise and speedy response have been crucial in helping me to use effectively the local computing resources needed for the work in this dissertation.

I thank current and previous research group members, for sharing their expertise, for their inspiring dedication to research, and even just their company in the office (oftentimes late into the night). I am especially thankful to Andrew Chael, for his always useful input on various computing and physics questions, and with whom I was fortunate to work with on the magnetic reconnection heating prescription project; Brandon Curd, for never-dull afternoon conversations, for his overall positivity, and for his willingness to discuss research questions in detail; and Xinyi Guo, whose work ethic and quick processing speed have been truly inspiring. I am thankful also to more senior group members and BHI (and other) postdocs, including Atish Kamble, Xuening Bai, Nick Murphy, Paul Chesler, Feraz Azhar, Maciek Wielgus, and Dom Pesce. Interacting with such high-caliber researchers, teachers, and overall amazing people over the past several years has been a profound learning experience, and has inspired me to put forth my best effort in research; I am extremely thankful for their kindness and advice on various topics.

I thank my friends for contributing to my overall quality of life, and helping me to balance research with other sorts of activities. I am especially thankful to my good friend and kindred spirit Jae Hyeon Lee, whose similar sense of humor has helped me to keep things in perspective; Dom Wild, for thoughtfulness, incredible generosity, and forcing me to have fun against my better

judgment; Matt Rispoli, for always being willing to lend a helping hand, for injecting a hefty dose of humor into my graduate school experience, and for his upbeatness; Ron Alexander, for his kindness, humor, and fun times over our shared interests in SNES, ‘The Room,’ and other respectable hobbies; Chris Frye, for the many fun hikes, camping, and backpacking trips (and whom I cannot recall ever making an incorrect physics statement). I am thankful also to my good friend and fellow graduate student Michael Grome, whom I have known since elementary school, and who has always been a wonderful sounding board for creative science questions, and is responsible for expanding my science horizons with fantastic discussions on molecular biology and genetic engineering.

I am indebted to my undergraduate physics and math advisers Jason Stalnaker and Bob Bosch, without whose support and guidance, I could not have attended graduate school. Jason’s selflessness, highest-quality teaching, optimism, and patience have made a lasting impact, and originally inspired me to further pursue physics; Bob’s support, kindness, and creativity helped to engender in me a genuine feeling of self-efficacy in my research, and working with him was a highlight of my undergraduate years.

Finally, I thank my family: Mom, Dad, and my brother Ren; even if you don’t understand exactly why I wanted to attend graduate school, you’ve always been supportive, and without your sacrifices, support, and unconditional caring, none of this would have been possible; I owe everything to you.

1. Introduction

Magnetic reconnection is believed to play a central role in some of the most violent plasma phenomena observed, including solar flares, coronal mass ejections, magnetic storms in the Earth’s magnetosphere, and sawtooth crashes in tokamaks. (Le et al., 2009)

Magnetic reconnection often leads to explosive release of energy and is thought to be operative in space, laboratory, and astrophysical plasmas. (Liu et al., 2014)

Magnetic reconnection is an important fundamental plasma process involving a rapid change of magnetic topology and often leading to a violent release of magnetic energy. (Uzdensky, 2011)

Magnetic reconnection drives the release of magnetic energy in explosive events such as disruptions in laboratory experiments, magnetic substorms in the Earth’s magnetosphere and flares in the solar corona. (Shay et al., 2007)

These are the opening lines from a few journal articles about magnetic reconnection (Dungey, 1953), and numerous others begin similarly. The ‘violent’ and ‘explosive’ capacity of reconnection is quoted so often that repeating it borders on platitude. By briefly reviewing the details of a particularly severe instance of a reconnection-induced solar storm, we may redouble our convictions about the explosive power of reconnection.

The [Halloween solar storms of 2003](#) were some of the most energetic solar storms ever recorded. Two to three years after solar max (i.e. the timeframe in which solar activity such as coronal mass ejections, sunspots, solar irradiance, etc., reaches the local maximum of its \sim 11 year solar cycle; see Fig. 1.1), which is typically a period of declining magnetic activity on the Sun, it was surprising that 17 intense sunspots were observed in the span of just a few weeks from mid-October to early November (NASA, 2008). A large fraction of these flared on October 28th, releasing $\sim 6.2 \times 10^{34}$ GeV of electromagnetic energy (Mozer & Pritchett, 2010); this is the energy equivalent of more than 20 mass-extinction-sized meteors, or around 400 \times the cumulative world energy consumption

from 1830 to 2019. Astonishingly, up to 50% of the magnetic energy that is dissipated during a solar flare can manifest as accelerated electrons (Mozer & Pritchett, 2010).¹

The day after these flares erupted, the corresponding coronal mass ejection reached the Earth, battering its magnetic field and inducing currents in the Earth’s northern latitudes (Mozer & Pritchett, 2010). This led to power outages in Sweden, and forced air-traffic controllers to reroute flights, so as to avoid communication deadzones and reduce exposure to the geomagnetically induced radiation (NASA, 2008; Mozer & Pritchett, 2010). NASA would later report that more than half of its near-Earth and space science missions were damaged or affected by the solar storm (NASA, 2008).

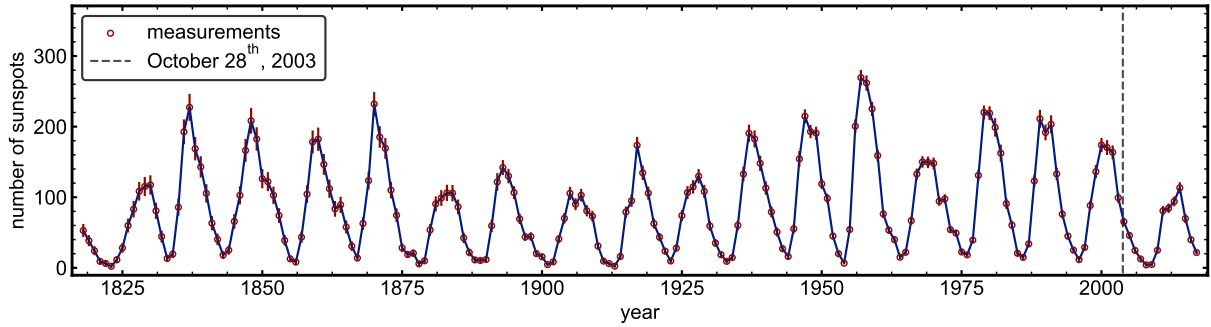


Figure 1.1: Number of sunspots vs. time (in years) from 1818–2017. Measurements denote the yearly average of daily measurements, and error bars denote the standard deviation computed from daily measurements over the corresponding year. Sunspot data are publicly available from the [World Data Center SILSO, Royal Observatory of Belgium, Brussels](#).

The average magnetic field in the Sun’s corona is around 1 G, and within sunspots is measured to be many times larger, of order 4000 G (Livingston et al., 2006). While known with less certainty, average magnetic fields in the extreme environment of supermassive black hole (BH) coronae (i.e., the gas far above and below the midplane of the BH accretion disk) and relativistic jets are expected to be of order 100 G (Yuan & Narayan, 2014; Johnson et al., 2015; Dallilar et al., 2017);² one can

¹The efficiency with which magnetic reconnection can heat and accelerate particles will prove to be crucial in our later discussion of collisionless accretion flows around black holes.

²The field is even stronger around stellar mass BH.

imagine that, in analogy with the Sun, there are regions of intense magnetic field, thousands of times stronger than the average, ~ 100 G. Given the efficiency with which magnetic reconnection, in the context of solar physics, is known to convert magnetic energy into kinetic energy (heating and acceleration of particles, and bulk motion of plasma), it is natural to ask what may be the role of magnetic reconnection in dissipating magnetic energy in BH coronae; this is one of the main questions explored in this thesis.

A realistic description of magnetic dissipation via reconnection, and electron heating in particular, is vitally important in generating models that may be reliably compared with observations of black holes ([The EHT Collaboration et al., 2019](#)). Two of the primary targets of the Event Horizon Telescope (EHT) are Messier 87 (M87), with its distinctive jet, and Sagittarius A* (Sgr A*), the supermassive BH at the center of the Milky Way. These active galactic nuclei (AGN) differ from other distant AGN in that they radiate at only a small fraction of the Eddington limit. This puzzling property can be explained within the framework of advection-dominated accretion flows (ADAFs, [Narayan & Yi \(1995a\)](#); also known as radiatively inefficient accretion flows, RIAFs ([Stone et al., 1999](#); [Igumenshchev et al., 2003](#); [Beckwith et al., 2008](#))).³

In the ADAF model, the accreting plasma (i.e., ionized gas) onto the BH is unable to cool efficiently, so the plasma heats up to very high temperatures and puffs up into a geometrically thick, optically thin disk. Because of the low gas density, the plasma is accurately modeled as a ‘collisionless’ gas, meaning that the mean free path in the plasma is much larger than the dynamical timescale, i.e. Coulomb collisions may be neglected. Despite the absence of Coulomb collisions, energy transfer amongst particle constituents (and also between particles and the electromagnetic field) of the plasma may proceed through various plasma processes, e.g. reconnection.

Dissipation of magnetic energy, and the associated particle heating, in collisionless, magnetized

³An ‘accretion flow’ refers to the material orbiting a massive central body; in our case, the material is plasma, and the central body we consider is a black hole.

gas is controlled by fundamental plasma physics, which is absent in scale-free theories such as magnetohydrodynamics (MHD), and variants thereof. This limitation of traditional MHD simulations is potentially severe. Without first-principles, fully-kinetic modeling of magnetic dissipation in plasma, and the corresponding energy partition between electrons and protons, conventional MHD simulations have no way of resolving the plasma microphysics that is crucially important to controlling the heating of electrons, the particles in BH accretion flows which produce the radiation that is ultimately compared with simulated radiation based on general relativistic MHD models of accretion flows (see Fig. 1.2 for an illustration). The situation may be improved by providing a sub-grid prescription for electron heating, motivated by fully-kinetic modeling of magnetic reconnection. Developing such a prescription is a main goal of this thesis (See Chs. 2 and 3).

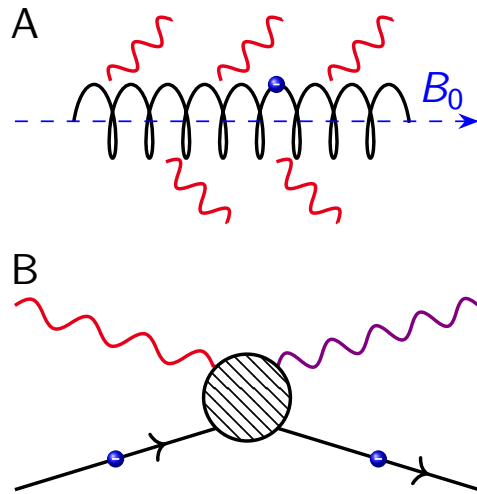


Figure 1.2: Electrons (blue circles) can produce radiation (wavy lines) through (A) synchrotron radiation, where the electron gyrates about a magnetic field line (indicated by the dashed blue arrow; the magnitude is B_0) and (B) inverse Compton scattering, wherein a low-energy photon gains energy via scattering off a higher-energy electron; because electrons produce the radiation that is ultimately observable on Earth, a detailed understanding of the microphysics of electron heating in collisionless accretion flows is critical when comparing models of BH accretion flows with observations.

1.1 Sweet-Parker magnetic reconnection: a simplified analytic model

For the moment, let us abstract away the (important and complicated) contextual details of reconnection in BH coronae, and focus on a simplified analytical description of reconnection, the

Sweet-Parker model (Sweet, 1958; Parker, 1957). While the Sweet-Parker model is imperfect (e.g., it predicts a ‘slow’ reconnection rate which is incompatible with experimentally observed reconnection rates in the solar atmosphere, Earth’s magnetosphere, and laboratory plasmas), a good deal of physical intuition may be gleaned from the Sweet-Parker model.

We consider a reconnection layer with half-length L and half-thickness δ (see Fig. 1.3). Plasma in the ‘inflow’ (equivalently, ‘upstream’) regions, corresponding roughly to the blue and red areas, flow along $\pm y$ with speed v_{in} into the current sheet (green region), and then is ejected along $\pm x$ (along the ‘outflows’ or ‘downstream’) with speed v_{out} . The magnetic field points along $-x$ in the upper part of the domain, and along $+x$ in the lower half. The mass density in the upstream is ρ_{in} ; as a simplification, we assume equal inflow and outflow densities. The configuration shown in Fig. 1.3 is assumed to be time-independent, as well as symmetric and isotropic along the inflows and outflows. With this intuitive picture of magnetic reconnection, we will derive the scaling of the outflow speed v_{out} with the strength of the magnetic field B_{in} and mass density ρ_{in} in the upstream. We can start by noting that mass-flux is conserved from the inflow boundary to the outflow boundary. The mass (per unit length in z per time) advected into the current sheet is $2L \times 2\rho_{\text{in}}v_{\text{in}}$, and the mass advected out of the current sheet is $2\delta \times 2\rho_{\text{in}}v_{\text{out}}$, so by mass-flux conservation, the aspect ratio of the reconnection layer governs the ratio of inflow to outflow speeds,

$$\frac{\delta}{L} = \frac{v_{\text{in}}}{v_{\text{out}}}. \quad (1.1)$$

We get a second equation by balancing the magnetic energy advected across the inflow with the kinetic energy advected across the outflow,

$$\frac{\delta}{L} = \frac{v_{\text{in}}B_{\text{in}}^2/(8\pi)}{\frac{1}{2}\rho_{\text{in}}v_{\text{out}}^3}. \quad (1.2)$$

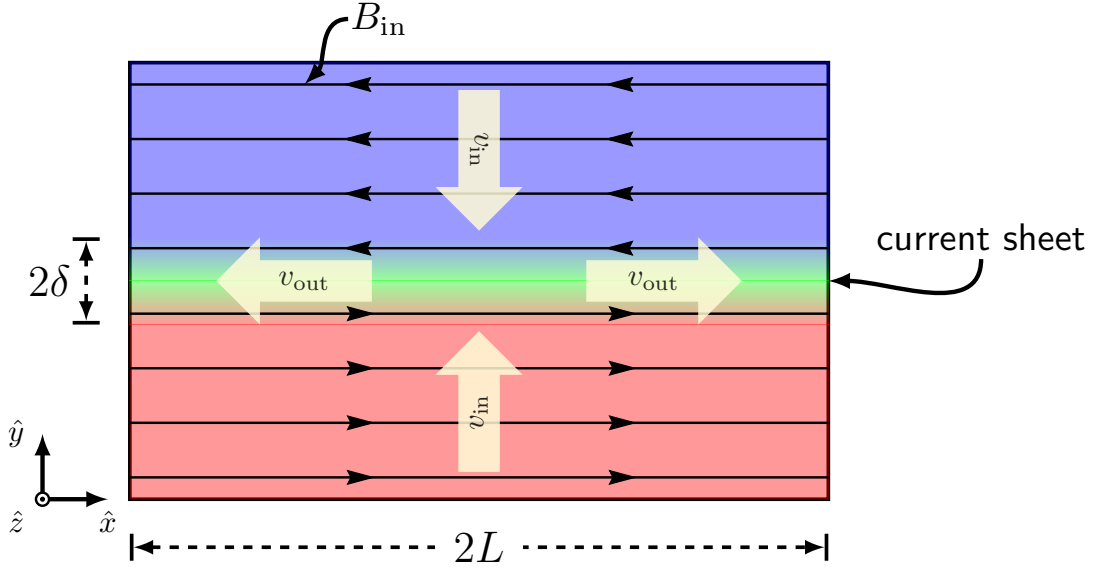


Figure 1.3: Setup for the Sweet-Parker model of magnetic reconnection. Magnetic fields of opposite polarity (shown by blue and red; the magnitude is B_{in}) permeate plasma in the inflow regions. In the transition region between the magnetic fields, current flows in the out-of-plane direction (z), consistent with Ampère’s law. Dissipation of magnetic energy occurs in the ‘current sheet’ (green region), modeled as a box of dimension 2δ by $2L$. Inflowing plasma along the $\pm y$ directions is ejected along the outflow directions $\pm x$, as magnetic energy in the upstream is converted to kinetic energy.

Using Eqs. 1.1 and 1.2, we get a scaling law for the outflow speed with inflow magnetic field and mass density:

$$v_{\text{out}} \sim \sqrt{\frac{B_{\text{in}}^2}{4\pi\rho_{\text{in}}}}, \quad (1.3)$$

which we identify as the (nonrelativistic) definition of Alfvén speed. We can introduce the magnetization in the upstream, $\sigma_{\text{in}} \equiv B_{\text{in}}^2/(4\pi\rho_{\text{in}}c^2)$, then the scaling law Eq. 1.3 says that the outflow velocity scales with magnetization as

$$\frac{v_{\text{out}}}{c} \sim \sqrt{\sigma_{\text{in}}}. \quad (1.4)$$

The Sweet-Parker model yields the physically intuitive result that as the reconnection upstream

becomes more magnetized, the outflow velocity increases, which is intuitive because as the magnetization increases in the upstream, more free magnetic energy is available to be dissipated as kinetic energy in the outflows. Using an argument that is similar to the above, and assuming also that the plasma is force free in the upstream (i.e. $E_{\text{in}} \sim (v_{\text{in}}/c)B_{\text{in}}$), the Sweet-Parker model provides a scaling for the reconnection electric field⁴ E_{rec} in the current sheet (Parker, 1957),

$$E_{\text{rec}} \sim \frac{\delta}{L} \sigma_{\text{in}} \sqrt{4\pi\rho_{\text{in}}c^2}. \quad (1.5)$$

While simple and elegant, the Sweet-Parker model of magnetic reconnection is not realistic. Parker originally proposed that the scaling laws could explain the fast magnetic dissipation observed in solar flares, but soon realized that they predict a reconnection rate that is too low (Parker, 1963). The physical limitation of the model is that the reconnection rate (Eq. 1.5) depends on the aspect ratio of the current sheet, δ/L ; as the aspect ratio decreases, the inflow speed decreases, because conservation of mass-flux advected across the inflow and across the outflow demands $v_{\text{in}}/v_{\text{out}} \sim \delta/L$, and the outflow speed is fixed according to Eq. 1.3 (Cassak et al., 2017).

Searching for a physical, quantitative, and precise understanding of the scaling laws Eqs. 1.3 and 1.5 has consumed decades worth of research in magnetic reconnection. A battery of evidence from observational, theoretical, and computational studies suggests that the reconnection rate is ‘universally’ (Parker, 1973; Borovsky et al., 2008; Comisso & Bhattacharjee, 2016; Cassak et al., 2017)

$$\frac{v_{\text{in}}}{v_{\text{out}}} \sim 0.1. \quad (1.6)$$

This scaling is especially relevant when considering reconnection in an environment that is not

⁴The value E_{rec} is often referred to in the literature as the ‘reconnection rate’.

directly accessible via observation, e.g. BH coronae, and implies that reconnection efficiently dissipates magnetic energy, even in the collisionless accretion flows surrounding black holes.

1.2 Particle-in-cell simulation

In Sec. 1.1, we reviewed the details of a simplified, time-independent model of reconnection; while it provides physically reasonable scalings, it is known to be, at a quantitative level, incompatible with the fast energy conversion rates observed in actual reconnection events (e.g., solar flares or the Earth’s magnetosphere). For the full time-dependent, nonlinear problem of reconnection, computer simulations, and in particular particle-in-cell (PIC) simulations (Hockney & Eastwood, 1988; Birdsall & Langdon, 1991), have proven enormously useful in providing quantitatively accurate models of reconnection (Birn et al., 1957; Shay et al., 2014; Liu et al., 2017), thereby providing also a framework in which to address the reason for puzzling aspects of reconnection, such as the apparently universal value of the reconnection rate, and the fraction of dissipated magnetic energy partitioned to electrons vs. protons (Eastwood et al., 2013; Yamada et al., 2015; Hoshino, 2018).

There are several comprehensive texts (Hockney & Eastwood, 1988; Birdsall & Langdon, 1991) and review papers (Dawson, 1983; Buneman et al., 1993; Cai et al., 2003; Pritchett, 2003; Lapenta, 2015) which cover the PIC method. Here, we review briefly the fundamentals of PIC, but refer the reader to the previously mentioned sources for a more complete description.

Formally, the PIC method is a numerical approach to solving the full seven-dimensional (three spatial dimensions \mathbf{x} ; three momentum dimensions \mathbf{p} ; one time dimension t) collisionless Vlasov-

Maxwell system, i.e.

$$\frac{df(\mathbf{x}, \mathbf{p}, t)}{dt} = 0, \quad (1.7)$$

$$\nabla \cdot \mathbf{E} = 4\pi\rho, \quad (1.8)$$

$$\nabla \cdot \mathbf{B} = 0, \quad (1.9)$$

$$\nabla \times \mathbf{E} = -\frac{1}{c} \frac{\partial \mathbf{B}}{\partial t}, \quad (1.10)$$

$$\nabla \times \mathbf{B} = \frac{4\pi}{c} \mathbf{j} + \frac{1}{c} \frac{\partial \mathbf{E}}{\partial t}. \quad (1.11)$$

The first equation Eq. 1.7 is the collisionless Boltzmann equation, and Eqs. 1.8–1.11 are the Maxwell equations; the charge density ρ and current density \mathbf{j} here are computed as moments of the distribution function f . Expanding the total derivative in Eq. 1.7, and employing the Lorentz force law, the collisionless Boltzmann equation is

$$\frac{\partial f_s}{\partial t} + \mathbf{v}_s \cdot \nabla f_s + q_s \left(\mathbf{E} + \frac{\mathbf{v}_s}{c} \times \mathbf{B} \right) \cdot \frac{\partial \mathbf{f}_s}{\partial \mathbf{p}} = 0, \quad (1.12)$$

where the subscript s refers to the particle species (in BH coronae, this can be electrons or protons), and q_s is the charge of the particle; for each particle species in the plasma, there is a Boltzmann equation of the form of Eq. 1.12.

To solve the Vlasov-Maxwell system Eqs. 1.7–1.11, PIC simulations time evolve discretized chunks of the phase space of $f(\mathbf{x}, \mathbf{p}, t)$, each of which corresponds to many physical particles (these are often referred to as ‘macro’ or ‘super’ particles). Time evolution of macroparticles proceeds in a series of steps:

1. Particle positions and momenta are stepped forward in time $\mathbf{x}(t) \rightarrow \mathbf{x}(t + \Delta t)$, $\mathbf{p}(t) \rightarrow \mathbf{p}(t + \Delta t)$, according to the Lorentz force law;
2. According to the distance moved and the charge of the particle, current is deposited on the

grid;

3. Deposited current is treated as a source term in the Maxwell equations, and used to update the (discretized) electromagnetic field;
4. Electric and magnetic fields, defined at discrete points on the computational grid, are used to interpolate the value of the electric and magnetic fields at (continuous) particle locations.

The procedure described in steps 1–4 above is known as the ‘PIC loop’ (Buneman, 1959; Dawson, 1962), and in principle may be repeated for as long as computational resources allow. In practice, one must also consider effects such as ‘numerical heating’ (Birdsall & Maron, 1980; Birdsall & Langdon, 1991; Melzani et al., 2013), which corresponds to a nonphysical increase in the plasma temperature, and may occur for different reasons, including violation of energy conservation that is inherent in certain standard PIC algorithms (including the Boris (1970) pusher⁵), and also instabilities associated with coupling between plasma modes and the discretized grid (e.g. ‘Finite Grid Instability,’ see Birdsall & Langdon (1991)). Adequate control of numerical heating and related numerical instabilities is crucial to obtaining reliable results with PIC simulations, and is an omnipresent consideration for all of the simulation work presented in this thesis; Ch. 6 is devoted to the exploration of numerical heating, and a current deposition scheme that can reduce its impact.

In the last few years, crucial advances in numerical methods and high-performance computing hardware have enabled PIC simulations to model collisionless plasmas up to the long time durations and large length scales required of astrophysical problems. PIC simulation is one of the main tools we use to study BH coronae in Chs. 2–5.

As a prelude to later detailed discussions, we show in Fig. 1.4 a representative PIC simulation of magnetic reconnection. The setup here is similar to that shown in Fig. 1.3, with magnetic fields

⁵Despite violating energy conservation, the Boris pusher is a stable algorithm, in the sense that with sufficient spatio-temporal resolution, the associated numerical heating, which occurs in a predictable manner, may be adequately controlled.

of opposite polarity threading plasma in the top and bottom parts of the domain (see panel A); however, since Fig. 1.4 corresponds to a PIC simulation, the full time-dependent reconnection problem is solved, and the electromagnetic field and particles evolve according to the Vlasov-Maxwell system (Eqns. 1.7–1.11). Panel B shows how the magnetic field (black lines) have rearranged at a later time in the simulation, capturing details of reconnection that are absent in the simplified description of Sec. 1.1.

1.2.1 Particle-in-cell simulation with **TRISTAN-MP**

To simulate collisionless plasma, we use the electromagnetic PIC code **TRISTAN-MP** (Spitkovsky, 2005), a massively parallel descendant of the PIC code **TRISTAN** originally developed by Buneman (1993). **TRISTAN-MP** uses a finite-difference scheme to solve the Maxwell equations. Electric and magnetic fields are staggered on a Yee (1966) mesh. Standard particle position and momentum integrators, i.e. the Boris (1970) and Vay (2008) pushers are implemented (for the vast majority of simulations presented in Chs. 2–5, we use the Vay algorithm, which we find is more accurate in our setups than the Boris pusher). A three-point digital filter is used to smooth currents deposited by particles onto the computational grid, which we find significantly improves control over numerical heating in our simulations. Two versions of the code exist, one in which the computational domain is decomposed along x , and another along both x and y . Message Passing Interface (MPI) Standard is used for parallel communication on the decomposed domain. Output data from **TRISTAN-MP** are saved at user-selected intervals via Hierarchical Data Format 5 (HDF5) libraries.

In Appendix A, we present measurements and data on the parallel scalability of **TRISTAN-MP**. In these tests, we find that our code shows excellent parallel scalability as the number of compute nodes increases.

To buttress the simulational capabilities of **TRISTAN-MP**, we developed a graphical user interface for visualization and analysis of **TRISTAN-MP** data; this tool is described in Appendix B.

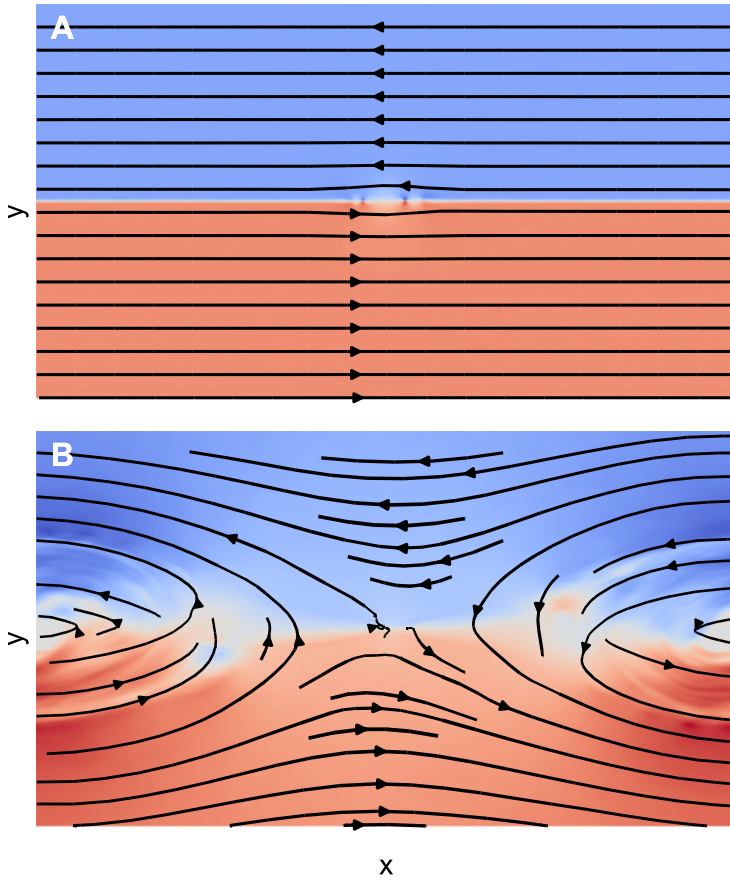


Figure 1.4: Illustration of reconnecting magnetic field lines (shown by black). (A) Initially anti-parallel configuration of magnetic field; the red region indicates magnetic field pointing in the $+x$ direction, and the blue region indicates magnetic field pointing in the $-x$ direction. (B) After reconnection is triggered, magnetic field lines ‘break apart’ and ‘reconnect,’ which leads to particle heating, acceleration of particles, and bulk motion of plasma along the outflows ($\pm x$ directions). The central region of the domain corresponds to an ‘X-point,’ called so because the shape of the magnetic field there resembles an ‘X.’

1.3 Outline

In this chapter, we introduced the fundamental plasma process of magnetic reconnection, provided motivation as to the importance of magnetic dissipation via reconnection in collisionless accretion flows of black holes, and discussed how such extreme environments may be studied using particle-in-cell simulations of collisionless plasma. In the following chapters, we explore several important

questions at the intersection of pure plasma physics, and black hole astrophysics.

In Ch. 2, investigate energy partition in the idealized case of antiparallel reconnection, and develop a prescription for electron heating which depends on only a few plasma parameters. Next, in Ch. 3, we study a more general configuration called ‘guide field’ reconnection; we study the scaling of energy partition with different plasma parameters, and develop a general prescription for electron heating via magnetic reconnection; we explore also the mechanisms responsible for electron heating in guide field reconnection. In Ch. 4, we investigate the Kelvin-Helmholtz (KH) instability via linear stability analysis and magnetohydrodynamic simulation, with an eye towards the possibility of KH-induced magnetic reconnection. Next, in Ch. 5, a companion to Ch. 4, we continue our exploration of the KH instability with PIC simulations; for a test case, we study magnetic dissipation induced by the KH instability. Finally, in Ch. 6, we study the [Esirkepov \(2001\)](#) algorithm of current deposition, as a method of increasing numerical control in our PIC experiments. The work in this thesis addresses the important question of how magnetic energy is dissipated in the collisionless plasma of BH accretion flows, and suggests further lines of inquiry regarding the connection between the KH instability and magnetic reconnection.

2. Electron and proton heating in trans-relativistic magnetic reconnection

*Text in this chapter was originally published in:
ApJ, 850, 29, (2017; Rowan, M., Sironi, L., & Narayan, R.).*

2.1 Abstract

The coronae of collisionless accretion flows, such as Sgr A* at our Galactic center, provide a unique setting for the investigation of magnetic reconnection. Here, protons are generally non-relativistic while electrons can be ultra-relativistic, a regime that is largely unexplored. By means of two-dimensional particle-in-cell simulations, we investigate electron and proton heating in the outflows of trans-relativistic (i.e., $\sigma_w \sim 0.1$, where the magnetization σ_w is the ratio of magnetic energy density to enthalpy density) anti-parallel reconnection. We explore the dependence of the heating efficiency on mass ratio (up to the realistic value), magnetization σ_w , proton plasma β_i (i.e., the ratio of proton thermal pressure to magnetic pressure), and electron-to-proton temperature ratio T_e/T_i . For both electrons and protons, heating at high β_i tends to be dominated by adiabatic compression (“adiabatic heating”), while at low β_i it is accompanied by a genuine increase in entropy (“irreversible heating”). For our fiducial $\sigma_w = 0.1$, we find that at $\beta_i \lesssim 1$ the irreversible heating efficiency is nearly independent of T_e/T_i (which we vary from 0.1 up to 1). If $T_e/T_i = 1$, the fraction of inflowing magnetic energy converted to electron irreversible heating decreases from $\sim 1.6\%$ down to $\sim 0.2\%$ as β_i ranges from $\beta_i \sim 10^{-2}$ up to $\beta_i \sim 0.5$, but then it increases up to $\sim 3\%$ as β_i approaches ~ 2 . Protons are heated much more efficiently than electrons at low and moderate β_i (by a factor of ~ 7), whereas the electron and proton heating efficiencies become comparable at $\beta_i \sim 2$ if $T_e/T_i = 1$, when both species start already relativistically hot. We find comparable heating efficiencies between the two species also in the limit of relativistic reconnection, when the magnetization exceeds unity. Our results have important implications for the two-temperature

nature of collisionless accretion flows, and may provide the sub-grid physics needed in general relativistic MHD simulations.

2.2 Introduction

The ultra-low-luminosity source at the center of the Milky Way, Sagittarius A* (Sgr A*), is thought to be powered by accretion onto a supermassive black hole. Sgr A* radiates well below the Eddington limit and there is strong evidence that the accreting gas can be described as an advection-dominated accretion flow (ADAF, also referred to as a radiatively inefficient accretion flow, RIAF) (Narayan & Yi, 1994, 1995b,a; Abramowicz et al., 1995; Narayan & McClintock, 2008; Yuan & Narayan, 2014). In ADAFs, the disk is geometrically thick and optically thin. Additionally, the plasma is predicted to be two-temperature for several reasons: first, in the ADAF configuration, the density of accreting gas is low enough that Coulomb collisions between electrons and protons are extremely rare on accretion timescales, so that the species become thermally decoupled. Second, electrons radiate more efficiently than protons. Lastly, relativistic electrons are heated less than non-relativistic protons when subjected to the same adiabatic compression. For all these reasons, the plasma is expected to be two-temperature, with protons significantly hotter than electrons (Narayan & Yi, 1995b; Yuan et al., 2003).

Despite the above arguments, the two-temperature gas may be driven to a single-temperature state by kinetic processes, such as reconnection and instabilities (Quataert et al., 2002; Riquelme et al., 2012, 2015; Sironi & Narayan, 2015; Sironi, 2015; Werner et al., 2016). To capture the effects of these plasma processes, one requires a fully-kinetic description, which can be achieved via numerical techniques such as particle-in-cell (PIC) simulations. In principle, such *ab initio* simulations can be used to provide the necessary sub-grid physics that, to date, cannot be captured in magnetohydrodynamic (MHD) simulations (e.g., Ressler et al., 2015, 2017b; Ball et al., 2016, 2017; Chael et al., 2017; Sadowski et al., 2017).

In supermassive black hole accretion flows, the ratio of ion thermal pressure to magnetic pressure,

$$\beta_i = \frac{8\pi n_0 k_B T_i}{B_0^2}, \quad (2.1)$$

(where n_0 is the ion number density, k_B is Boltzmann's constant, T_i is the ion temperature, and B_0 is the magnitude of the magnetic field) is expected to vary in the disk midplane in the range $\beta_i \sim 10 - 30$ (See Fig. 1 of [Sadowski et al., 2013](#)). However, in plasma far above and below the midplane, the “corona,” the system is expected to be magnetically dominated, such that $\beta_i \lesssim 1$. Here, the dissipation of magnetic energy via reconnection can result in particle heating, acceleration, and bulk motion.

Even in the magnetized corona, the magnetization,

$$\sigma_i = \frac{B_0^2}{4\pi n_0 m_i c^2}, \quad (2.2)$$

is generally small, i.e., $\sigma_i \lesssim 1$. Electron heating by reconnection in the non-relativistic limit ($\sigma_i \ll 1$) has been studied extensively, both theoretically and by means of PIC simulations, in the context of the solar wind, Earth's magnetotail, and laboratory plasmas ([Hoshino et al., 2001](#); [Jaroschek et al., 2004](#); [Loureiro et al., 2013](#); [Schöffler et al., 2011, 2013](#); [Shay et al., 2014](#); [Dahlin et al., 2014](#); [Daughton et al., 2014](#); [Li et al., 2015](#); [Haggerty et al., 2015](#); [Numata & Loureiro, 2015](#); [Le et al., 2016](#); [Li et al., 2017a](#)). Though less commonly studied, relativistic reconnection (i.e., $\sigma_i \gg 1$) in electron-proton plasmas has also received some attention in recent years ([Sironi et al., 2015](#); [Guo et al., 2016](#)).

The collisionless plasma in hot accretion flows around black holes provides a peculiar environment for reconnection, since $\sigma_i \lesssim 1$, a regime that falls between the well-studied non-relativistic and ultra-relativistic regimes. For $\beta_i \sim 1$ and $\sigma_i \lesssim 1$, protons are generally non-relativistic, yet electrons

can be ultra-relativistic. This territory remains largely unexplored, in terms of both simulation and theory, and studies have only recently begun to probe reconnection in this parameter regime (Melzani et al., 2014; Werner et al., 2016).

The aim of this work is to explore particle heating via magnetic reconnection in the trans-relativistic regime $\sigma_i \lesssim 1$. We study heating in the outflows of anti-parallel reconnection (i.e., in the absence of a guide field perpendicular to the alternating fields) by means of fully-kinetic PIC simulations, choosing inflow parameters appropriate for the coronae of collisionless accretion flows. We present the electron and proton heating as a function of mass ratio (up to the physical value), inflow magnetization, ion plasma β_i and temperature ratio T_e/T_i .

We show that heating in the high- β_i regime is primarily dominated by adiabatic compression (we shall call this contribution “adiabatic heating”), while for low β_i the heating is genuine, in the sense that it is associated with an increase in entropy (“irreversible heating”). At our fiducial $\sigma_i \sim 0.1$, we find that for $\beta_i \lesssim 1$ the irreversible heating efficiency is independent of T_e/T_i (which we vary from 0.1 up to 1). For equal electron and proton temperatures, the fraction of inflowing magnetic energy converted to electron irreversible heating at realistic mass ratios decreases from $\sim 1.6\%$ down to $\sim 0.2\%$ as β_i ranges from $\beta_i \sim 10^{-2}$ up to $\beta_i \sim 0.5$, but then it increases up to $\sim 3\%$ as β_i approaches ~ 2 . Protons are heated much more efficiently than electrons at low and moderate β_i (by a factor of ~ 7), whereas the electron and proton heating efficiencies become comparable at $\beta_i \sim 2$ if $T_e/T_i = 1$, when both species start already relativistically hot. We find comparable heating efficiencies between the two species also in the limit of relativistic reconnection, when the magnetization exceeds unity. The unifying feature of these two cases (i.e., high magnetization, and high β_i at low magnetization) is that the scale separation between electrons and protons in the reconnection outflows approaches unity, so the two species behave nearly the same. Motivated by our findings, we propose an empirical formula (Eq. 2.34) that captures the magnetization and

plasma- β_i dependence of the electron heating efficiency (normalized to the overall electron + proton heating efficiency) over the whole range of magnetization and β_i that we explore.

We also measure the inflow speed (i.e., the reconnection rate) as a function of the flow conditions, finding that for our fiducial magnetization $\sigma_w = 0.1$ it decreases from $v_{\text{in}}/v_A \approx 0.08$ down to 0.04 as β_i ranges from $\beta_i \sim 10^{-2}$ up to $\beta_i \sim 2$ (here, v_A is the Alfvén speed). Similarly, the outflow speed saturates at the Alfvén velocity for low β_i , but it decreases with increasing β_i down to $v_{\text{out}}/v_A \approx 0.7$ at $\beta_i \sim 2$. The inflow (outflow, respectively) speed is independent of T_e/T_i at low β_i , with only a minor tendency for lower (higher, respectively) speeds at larger T_e/T_i in the high- β_i regime.

The organization of the paper is as follows. In Section 2.3, we provide details about the simulation setup and parameters. In Section 2.4, we discuss our technique for extracting from PIC simulations the heating efficiencies. In Section 2.5, we discuss the dependence of the reconnection rate, the outflow speed and the electron and proton heating efficiencies on the flow conditions. We conclude in Section 2.6, with a summary and discussion.

2.3 Simulation setup

We use the electromagnetic PIC code **TRISTAN-MP** to perform fully-kinetic simulations of reconnection (Buneman, 1993; Spitkovsky, 2005). We employ two-dimensional (2D) simulations, but all three components of velocity and electromagnetic fields are tracked. Our setup is similar to that described in Sironi & Spitkovsky (2014). The initial field configuration is illustrated in Fig. 2.1. From the red to the blue region, the polarity of the inflow magnetic field reverses, as shown by the white arrows. An out-of-plane current, in the green region, satisfies Ampere's law for the curl of the magnetic field. The reconnection layer is initialized in Harris equilibrium, with a magnetic field profile $\mathbf{B} = B_0 \tanh(2\pi y/\Delta) \hat{\mathbf{x}}$. We focus on anti-parallel reconnection, postponing the study

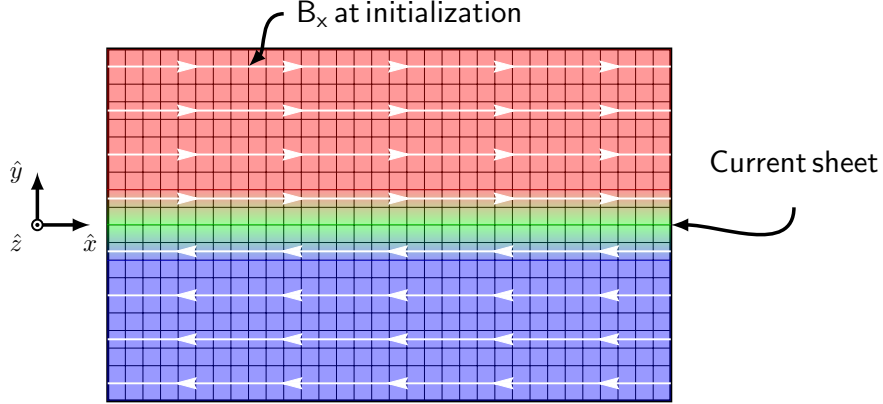


Figure 2.1: Schematic depiction of the reconnection layer initial configuration. Red and blue regions show magnetic field lines of opposite polarity. A hot, over-dense component of plasma (green region) balances the magnetic pressure outside the current sheet.

of guide field effects to a future work. The field strength is parameterized via the magnetization,

$$\sigma_w = \frac{B_0^2}{4\pi w}, \quad (2.3)$$

where B_0 is the magnitude of the magnetic field in the inflow region, $w = (\rho_e + \rho_i)c^2 + \hat{\gamma}_e u_e + \hat{\gamma}_i u_i$ is the enthalpy density per unit volume, and $\rho_e = m_e n_0$, $\rho_i = m_i n_0$, $\hat{\gamma}_e$, $\hat{\gamma}_i$, and u_e , u_i are the rest mass densities, adiabatic indices, and internal energy densities, respectively, of electrons and protons. Here, n_0 is the electron number density in the inflow region, m_e and m_i are the electron and proton masses. The definition of magnetization in Eq. 2.3 reduces to Eq. 2.2 in the limit of non-relativistic temperatures, but for relativistic particles the enthalpy in σ_w properly accounts for the relativistic inertia.

In all runs, we set the current sheet thickness to be $\Delta = 40 c/\omega_{pe}$, where c/ω_{pe} is the electron skin depth,

$$\omega_{pe} = \sqrt{\frac{4\pi n_0 e^2}{m_e}} \left(1 + \frac{\theta_e}{\hat{\gamma}_e - 1}\right)^{-1/2} \quad (2.4)$$

is the electron plasma frequency. Here, $\theta_e = k_B T_e / m_e c^2$ is the dimensionless electron temperature,

whereas e is the electric charge. The size of the computational domain in the x direction is $L_x = 4318 c/\omega_{pe}$, which is large enough to resolve both electron and proton heating physics (see Appendix 2.A, where we study the convergence of our results with respect to the domain size). While L_x in units of c/ω_{pe} remains fixed across our simulations, the domain size in units of the proton skin depth

$$\frac{c}{\omega_{pi}} \approx \frac{c}{\omega_{pe}} \sqrt{\frac{m_i}{m_e}} \left(1 + \frac{\theta_e}{\hat{\gamma}_e - 1}\right)^{-1/2} \left(1 + \frac{\theta_i}{\hat{\gamma}_i - 1}\right)^{1/2}, \quad (2.5)$$

increases as electrons become more relativistic (see Tab. 2.1). Here, $\theta_i = k_B T_i / m_i c^2$ is the dimensionless proton temperature.

We typically employ periodic boundary conditions along the x direction, but we have tested that our main results do not change when using outflow boundary conditions, similar to those described in Sironi et al. (2016). With the latter, it is possible to study the dynamical evolution of the reconnection system over multiple Alfvénic crossing times, whereas the evolution of a periodic simulation is limited to a few Alfvénic crossing times, before the periodic boundaries start affecting the reconnection physics. We compare the results of simulations with outflow and periodic boundaries in Appendix 2.B.

Fresh plasma, described by a Maxwell-Jüttner distribution, is introduced at two moving injectors. Each injector recedes from $y = 0$ at the speed of light, and the simulation domain is enlarged when the injectors reach the boundaries, so that the injectors may continue receding in the $\pm \hat{\mathbf{y}}$ directions. This strategy — described in more detail in Sironi & Spitkovsky (2011) — ensures that the domain includes all causally connected regions throughout the evolution of the system, while making efficient use of the available memory and computing time. Additional computational optimization is achieved by allowing the injectors to periodically “jump” backwards (toward $y = 0$),

removing all particles beyond the injectors and resetting the electromagnetic fields to their initial values (Sironi & Spitkovsky, 2011).

A hot, over-dense population of particles is initialized in the current sheet to balance the magnetic pressure from outside. These particles have temperature $k_B T_{cs}/m_i c^2 = \sigma_i/2\eta$, where η is the over-density relative to the inflowing plasma; we use $\eta = 3$. Reconnection is triggered at the initial time by cooling by hand the over-dense population in the middle of the current sheet $(x, y) \approx (0, 0)$. This causes a local collapse of the layer, leading to the formation of an X-point, after which the system evolves self-consistently (Sironi et al., 2016).

Adequate resolution of the electron skin depth c/ω_{pe} is required for accuracy and stability of PIC codes. We use 4 cells per electron skin depth, and fix $c = 0.45$ cells/timestep, which is less than required by the Courant-Friedrichs-Lowy condition in 2D. The time resolution of our simulations is then $\Delta t \approx 0.1 \omega_{pe}^{-1}$, which properly captures the physics at electron scales. For two cases ($\beta_i = 0.0078$ and $\beta_i = 2$, with the same $\sigma_w = 0.1$ and $T_e/T_i = 1$), we have tested for convergence by varying the spatial resolution (we have tested with $c/\omega_{pe} = 2$ or 8 cells), which has the effect of changing also the temporal resolution (we still fix $c = 0.45$ cells/timestep). For both choices of β_i , our results are essentially the same (see Appendix 2.C, where we study the convergence of our results with respect to the spatial resolution of the electron skin depth).

For simulations with $\beta_i = 2$, we use 64 particles per cell (N_{ppc}), whereas $N_{ppc} = 16$ at lower β_i . We have found that these values of N_{ppc} are sufficient to keep numerical heating under control, even for $T_e/T_i \ll 1$. We have extensively tested the impact of numerical heating in simulations with $\beta_i = 2$ for several values of N_{ppc} , in some cases up to $N_{ppc} = 256$; see Appendix 2.D for some discussion.

In our parameter scan (Tab. 2.1), we fix σ_w and study the reconnection physics as a function of β_i and T_e/T_i . We choose to fix σ_w rather than σ_i , given that the parameter space we probe involves

ID	A[0]	A[1]	A[2]	A[3]	A[4]
β_i	0.0078	0.031	0.13	0.50	2.0
β_e	0.00078	0.0031	0.013	0.050	0.20
θ_i	0.00041	0.0016	0.0066	0.028	0.16
θ_e	0.0010	0.0041	0.017	0.070	0.39
v_i	0.00061	0.0024	0.010	0.043	0.27
v_e	0.0015	0.0062	0.025	0.11	0.78
σ_i	0.10	0.10	0.10	0.11	0.15
T_e/T_i	0.10	0.10	0.10	0.10	0.10
N_{ppc}	16	16	16	16	64
c/ω_{pi}	20	20	20	19	16
$L_x[c/\omega_{pi}]$	860	870	870	890	1100
ID	B[0]	B[1]	B[2]	B[3]	B[4]
β_i	0.0078	0.031	0.13	0.50	2.0
β_e	0.0023	0.0094	0.038	0.15	0.60
θ_i	0.00041	0.0016	0.0066	0.029	0.18
θ_e	0.0031	0.012	0.050	0.21	1.3
v_i	0.00061	0.0025	0.010	0.044	0.32
v_e	0.0046	0.019	0.079	0.39	3.3
σ_i	0.10	0.10	0.10	0.11	0.17
T_e/T_i	0.30	0.30	0.30	0.30	0.30
N_{ppc}	16	16	16	16	64
c/ω_{pi}	20	20	19	17	11
$L_x[c/\omega_{pi}]$	870	870	890	1000	1600
ID	C[0]	C[1]	C[2]	C[3]	C[4]
β_i	0.0078	0.031	0.13	0.50	2.0
β_i	0.0078	0.031	0.13	0.50	2.0
θ_i	0.00041	0.0016	0.0067	0.031	0.39
θ_e	0.010	0.041	0.17	0.77	9.9
v_i	0.00061	0.0024	0.010	0.048	0.79
v_e	0.015	0.064	0.30	1.8	29
σ_i	0.10	0.10	0.10	0.12	0.38
T_e/T_i	1.0	1.0	1.0	1.0	1.0
N_{ppc}	16	16	16	16	64
c/ω_{pi}	20	19	17	12	5.0
$L_x[c/\omega_{pi}]$	870	890	990	1500	3400

Table 2.1: Initial parameters for the $m_i/m_e = 25$ simulations with our fiducial $\sigma_w = 0.1$. The proton skin depth c/ω_{pi} , calculated according to Eq. 2.5, is expressed in number of cells. The definition of the various quantities is in Section 2.3. Simulation sets **A**, **B**, and **C** differ by the initial temperature ratio, with $T_e/T_i = 0.1, 0.3$, and 1 , respectively. From left to right, β_i increases. We fix the mass ratio $m_i/m_e = 25$, magnetization $\sigma_w = 0.1$, electron skin depth $c/\omega_{pe} = 4$ cells, and domain size $L_x = 4318 c/\omega_{pe}$. We also perform a number of additional simulations, up to the realistic mass ratio $m_i/m_e = 1836$ and with higher magnetizations ($\sigma_w = 0.3, 1, 3, 10$), as described in Section 2.3.

relativistic particles whose thermal contribution to the inertia is non-negligible (see Eq. 2.3). For a constant σ_w , the Alfvén velocity

$$\frac{v_A}{c} = \sqrt{\frac{\sigma_w}{1 + \sigma_w}}, \quad (2.6)$$

remains fixed across our simulations. The reconnection layer is evolved for ~ 1 Alfvénic crossing time ($t_A = L_x/v_A$), which for our reference magnetization of $\sigma_w = 0.1$ and $L_x = 4318 c/\omega_{pe}$ corresponds to $t \approx 14000 \omega_{pe}^{-1}$.

The focus of our investigation is the so-called *trans-relativistic* regime of reconnection, hence we select $\sigma_w = 0.1$ as our fiducial magnetization, and we vary β_i from 0.0078 to 2. Additionally, we study the effect of the initial electron-to-proton temperature ratio T_e/T_i on the reconnection physics. For each value of β_i , we run three simulations with $T_e/T_i = 0.1, 0.3$, and 1. Our choice of initial parameters, both physical (σ_w, β_i , and T_e/T_i) and computational ($N_{ppc}, c/\omega_{pe}$), is summarized in Tab. 2.1. Other derived physical parameters in the inflow region, namely the electron plasma $\beta_e = \beta_i T_e/T_i$, the dimensionless proton and electron temperatures $\theta_i = k_B T_i/m_i c^2$ and $\theta_e = k_B T_e/m_e c^2$, the dimensionless internal energy per particle for protons and electrons $v_i \equiv u_i/n_0 m_i c^2$ and $v_e \equiv u_e/n_0 m_e c^2$, and the ratio σ_i of magnetic pressure to rest mass energy density, are also included. In addition to the simulations listed in the table, which employ mass ratio $m_i/m_e = 25$, we also investigate mass ratios $m_i/m_e = 10, 50$, and 1836 for β_i in the range $5 \times 10^{-4} - 2$ (with fixed $\sigma_w = 0.1$ and a fixed electron-to-proton temperature ratio $T_e/T_i = 1$). With realistic mass ratios and $T_e/T_i = 1$, we also explore the β_i -dependence of the heating efficiency at higher values of the magnetization: $\sigma_w = 0.3, 1, 3$ and 10.

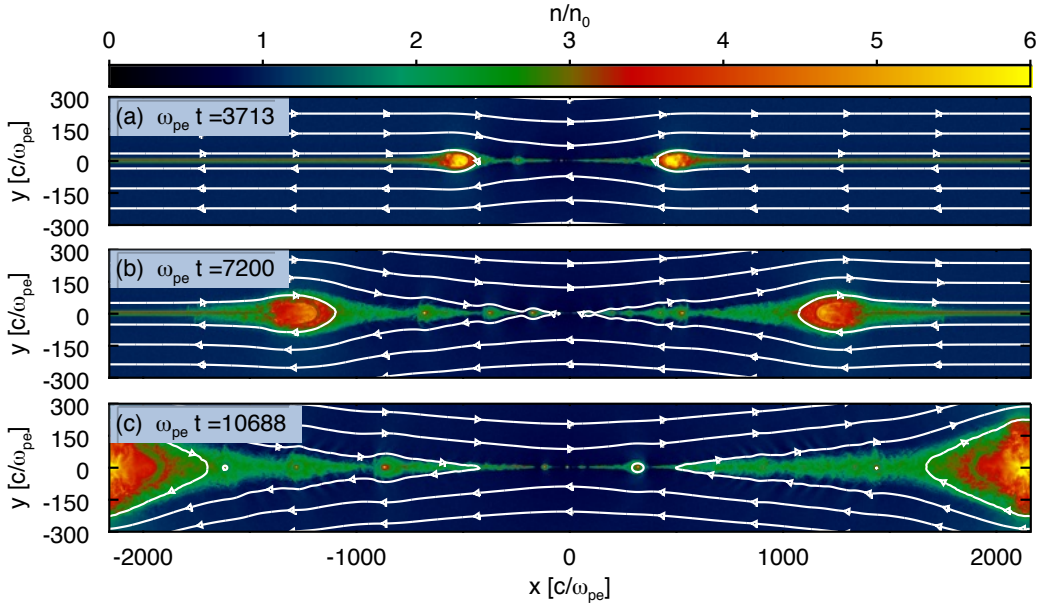


Figure 2.2: Time evolution of a representative low- β_i simulation (**A[0]** in Tab. 2.1), with $\beta_i = 0.0078$ and $T_e/T_i = 0.1$. The snapshots show number density of electrons in units of the initial density at (a): $t = 3713 \omega_{pe}^{-1} \approx 0.25 t_A$; (b): $t = 7200 \omega_{pe}^{-1} \approx 0.50 t_A$; (c): $t = 10688 \omega_{pe}^{-1} \approx 0.75 t_A$. We show the whole dimension of the box in x , and only a small portion close to the center in y . A characteristic feature of this and other low- β_i simulations is the presence of *secondary* magnetic islands, i.e., structures like those at $x \approx 300 c/\omega_{pe}$ and $x \approx -900 c/\omega_{pe}$ (panel (c)). These are to be distinguished from the large *primary* island at $x \approx \pm 2200 c/\omega_{pe}$, whose properties depend on choices at initialization. As the primary island grows, it will eventually inhibit further accretion of magnetic flux and the reconnection process will terminate.

2.4 Technique for extracting the heating efficiency

In this section, we discuss our method of extracting the heating efficiency from PIC simulations. First, in Section 2.4.1, we discuss the time evolution of the reconnection layer for two representative cases at low and high β_i . Then, in Section 2.4.2, we describe the identification of inflow (upstream) and outflow (downstream) regions. Lastly, in Section 2.4.3, we isolate the irreversible heating, i.e., the part associated with a genuine increase in entropy, from the reversible heating induced by adiabatic compression.

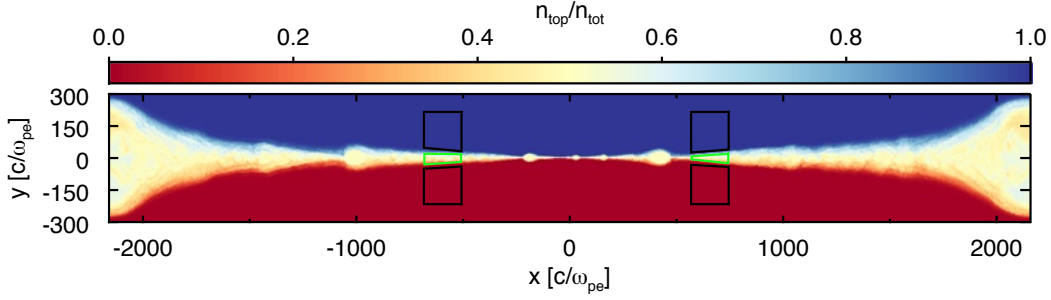


Figure 2.3: 2D plot of the ratio of top-to-total particle density, $n_{\text{top}}/n_{\text{tot}}$, for a representative simulation with $\beta_i = 0.0078$ and $T_e/T_i = 0.1$ (**A[0]** in Tab. 2.1) at time $t \approx 11000 \omega_{\text{pe}}^{-1} \approx 0.8 t_A$. The green and black contours show the boundaries of the regions we use to calculate the downstream and upstream temperatures, respectively. The box edges at the interface between upstream and downstream change as the system evolves, and are calculated according to Eqs. 2.7 and 2.8. Particle mixing serves as a tracer for the downstream region. Particles from the top ($y > 0$) of the domain are tagged; as they enter the reconnection layer, they mix with particles from the bottom ($y < 0$) of the domain. The reconnection downstream is identified via the mixing fraction $n_{\text{top}}/n_{\text{tot}}$, and a choice of the threshold r_{down} , as in Eq. 2.7.

2.4.1 Time evolution of the reconnection layer

To illustrate the time evolution of the reconnection layer, we show in Fig. 2.2 a few snapshots of density from a representative simulation (**A[0]** in Tab. 2.1) with $\beta_i = 0.0078$ and $T_e/T_i = 0.1$. We plot the 2D profile of the number density in units of the initial value, n/n_0 . In each panel, we show only a small fraction of the domain in the y direction (we present only the region closest to the current sheet), and the full extent of the domain in x . White lines with arrows show magnetic field lines.

Panels (a)–(c) show the time evolution of the system over ~ 1 Alfvénic crossing time. By removing by hand the plasma pressure at the center of the current sheet ($x \sim 0$), we trigger a local collapse of the layer, forming an X-point. After the formation of the central X-point, two reconnection “wavefronts” are pulled outwards in the $\pm \hat{x}$ directions by the magnetic tension of the field lines, and the fronts recede from the center at close to the Alfvén speed. In panels (a), (b), and (c), the wavefronts are located at $x \approx \pm 400, 1100$, and $1800 c/\omega_{\text{pe}}$, respectively, corresponding to the innermost (i.e., closest to $x = 0$) locations of the large semi-circular red/yellow density blobs.

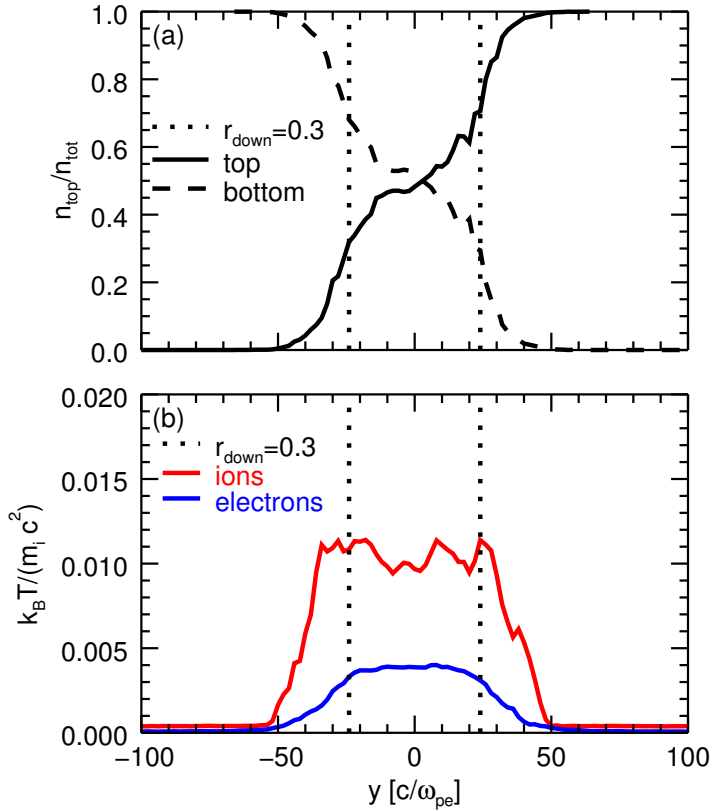


Figure 2.4: (a): 1D profile along the y direction of top-to-total particle density ratio (solid line) and bottom-to-total ratio (dashed line) in a slice at $x \approx 1000 c/\omega_{pe}$, at time $t \approx 8400 \omega_{pe}^{-1} \approx 0.60 t_A$. The profiles are from the same simulation we show in Fig. 2.3 (with $\beta_i = 0.0078$ and $T_e/T_i = 0.1$). Vertical dotted lines indicate the locations in x where the top-to-total density ratio is between 0.3 and 0.7 (at $y \approx -25$ and $25 c/\omega_{pe}$, respectively). Between the vertical dotted lines (i.e., in the region we define as the reconnection downstream), mixing has efficiently occurred. (b): Proton and electron temperature profiles in the same region. In between the vertical dotted lines, the temperature profiles are nearly flat.

The fronts carry away the hot particles initialized in the current sheet. With periodic boundary conditions, this leads to the formation of a *primary* island at the boundary of the simulation domain (in Fig. 2.2(c), located at $x \approx \pm 2200 c/\omega_{pe}$). The primary island continues to accrete plasma as the system evolves, but eventually it grows so large that further accretion of magnetic flux into the layer is inhibited, and reconnection stops.

The primary island shows the hottest electron temperatures. Here, electron heating might be due in part to reconnection, but also in part to weak shocks at the interface between the reconnection outflow and the island. In addition, the plasma conditions in the island are sensitive to our arbitrary choice for the current sheet initialization. For these reasons, we choose not to focus on the heating physics in the primary island.

In this paper, we focus exclusively on the outflow (i.e., before the the plasma reaches the primary island; see also [Shay et al. \(2014\)](#), in the context of non-relativistic reconnection), shown by the green region between the two wavefronts in Fig. 2.2. In Section 2.4.2, we detail the steps we take to avoid contamination of our temperature measurements by the primary island.

As the two reconnection fronts recede from the center, plasma flows into the reconnection layer and particles are heated and accelerated as a bulk, flowing along $\pm \hat{x}$ toward the domain boundaries. The dense (green) region in between the two wavefronts is the reconnection outflow. A key feature of low- β_i simulations is the formation in the reconnection exhausts of *secondary* islands due to the secondary tearing instability, e.g., Fig. 2.2(c) at $x \approx 300 c/\omega_{pe}$ and $x \approx -900 c/\omega_{pe}$ ([Daughton & Karimabadi, 2007](#); [Uzdensky et al., 2010](#)). Between each pair of secondary islands, there is a secondary X-point, e.g., at $x \approx -1000 c/\omega_{pe}$. We discuss the structure of the reconnection layer as a function of β_i in Section 2.5.1.

2.4.2 Upstream and downstream identification

We now describe how we determine which computational cells in the simulation domain belong to the upstream (or, inflow) and downstream (or, outflow) regions. We identify downstream cells by using a particle mixing criterion between the two sides of the current sheet. Particles that originate above $y = 0$ (top of the domain) are tagged, to distinguish them from particles originating below $y = 0$ (bottom of the domain).

In Fig. 2.3, we show the ratio of top-to-total number density. Away from the current sheet, i.e., in the blue and red regions, there is no mixing between the two populations. Particles from the two sides of the current sheet get mixed as they enter the reconnection layer; the region with the greatest amount of mixing is shown in white/light-yellow. We compute the ratio of top-particle density n_{top} to total-particle density $n_{\text{tot}} = n$ (including particles from both top and bottom) in each cell. If this ratio in a given cell exceeds a chosen threshold r_{down} and is below the complementary threshold, i.e.,

$$r_{\text{down}} < \frac{n_{\text{top}}}{n_{\text{tot}}} < 1 - r_{\text{down}}, \quad (2.7)$$

then the cell is counted as one where plasma has reconnected (i.e., the cell belongs to the reconnection downstream). This technique is similar to that used in [Daughton et al. \(2014\)](#). In our analysis, we choose $r_{\text{down}} = 0.3$, but we have verified that the identification of the reconnection region, and therefore the heating efficiencies that we extract, do not significantly depend on this choice. For r_{down} in the range $0.1 - 0.3$, the heating efficiencies typically differ only by $\sim 15\%$. The choice $r_{\text{down}} = 0.3$ is restrictive enough to exclude contamination by the upstream region. This is especially important for high β_i , where, even if the electron gyrocenter is located in a cell that is safely part of the downstream, if the cell is close to the interface between downstream and upstream,

the particle gyro-motion may temporarily lead this “downstream” electron to the upstream side. If r_{down} were to be too small, the region where the electron motion extends into the upstream might be incorrectly counted as part of the downstream, biasing our temperature estimates toward lower values. Our choice of r_{down} is to some extent arbitrary, but we have found that a relatively large value like $r_{\text{down}} = 0.3$ is suitable for identifying the genuine reconnection downstream.

In Fig. 2.4, we show 1D plots of the density fraction of tagged particles and the temperature profiles along the y direction, in a slice located at $x \approx 1000 c/\omega_{\text{pe}}$. In panel (a), we show the profiles of the ratio of top- and bottom-density to total density, denoted by solid and dashed lines, respectively, at time $t \approx 8400 \omega_{\text{pe}}^{-1} \approx 0.60 t_{\text{A}}$. Between the two vertical dotted lines, the ratio of top-to-total density ranges between 0.3 and 0.7, as required to satisfy our mixing criterion. As shown in panel (b), both the electron (blue) and the proton (red) temperature in the region between the vertical lines are remarkably uniform, proving that our mixing criterion can confidently capture the reconnection downstream.

The upstream region is identified via

$$\left(\frac{n_{\text{top}}}{n_{\text{tot}}} < r_{\text{up}} \right) \text{ or } \left(\frac{n_{\text{top}}}{n_{\text{tot}}} > 1 - r_{\text{up}} \right), \quad (2.8)$$

and we choose $r_{\text{up}} = 3 \times 10^{-5}$. As before, this definition avoids contamination of the upstream region by any “downstream” particles that leak out of the current sheet. In practice, a buffer zone with a width on the order of a few tens of c/ω_{pe} is established between the regions we identify as upstream and downstream.

While Eq. 2.7 (Eq. 2.8, respectively) identifies the whole reconnection outflow (inflow, respectively), we enforce an additional constraint on the downstream and upstream regions that we employ to extract our heating efficiencies. We select downstream regions far enough from the central X-

point that the electron and proton outflow bulk velocities have saturated, and also that the electron and proton temperatures have reached their asymptotic values. At the same time, we select these regions to be far enough from the boundaries to avoid contamination from the material inside the primary island, and only capture the genuine reconnection outflow. The downstream region that satisfies these constraints (identified by the green contours in Fig. 2.3) varies for different simulations: for $\beta_i < 2$ it is located at a distance of $\sim 630 c/\omega_{pe}$ from the center, whereas for $\beta_i = 2$ it is at $\sim 350 c/\omega_{pe}$ from the center (as we show below, the primary island tends to be larger at higher β_i). The extent of the downstream region across the layer (i.e., along y) is determined by the mixing criterion in Eq. 2.7, while the length along the layer is fixed at $\sim 170 c/\omega_{pe}$ (see the green contours in Fig. 2.3). The corresponding upstream values are measured at the same distance from the center of the layer, within the black contours in Fig. 2.3. Their extent along the y direction does not significantly affect our results.

2.4.3 Characterization of heating

In this section, we describe our assessment of particle heating. First, in Section 2.4.3.1, we describe our calculation of rest-frame internal energy and temperature. Next, in Section 2.4.3.2, we define ratios that characterize the total amount of heating. Finally, in Section 2.4.3.3, we provide a more detailed analysis of the heating physics by isolating the effect of a genuine entropy increase (which we call “irreversible heating”) from the contribution of adiabatic compression (giving “adiabatic heating”).

2.4.3.1 Temperature calculation

We measure the total particle energy density in the simulation frame, then extract the corresponding fluid-frame internal energy and temperature, by employing the perfect, isotropic fluid

approximation, i.e.

$$T^{\mu\nu} = (e + p) U^\mu U^\nu - p g^{\mu\nu}, \quad (2.9)$$

where $T^{\mu\nu}$ is the stress-energy tensor of the fluid, e is the rest-frame energy density, p is the pressure, U^μ is the fluid dimensionless four-velocity, and $g^{\mu\nu}$ is the flat-space Minkowski metric. The rest-frame energy density is the sum of rest-mass and internal energy densities, i.e.

$$e = \bar{n}mc^2 + u \quad (2.10)$$

$$= \bar{n}mc^2 + \frac{p}{\hat{\gamma} - 1}, \quad (2.11)$$

where \bar{n} is the rest-frame particle number density, u is the internal energy density, and $\hat{\gamma}$ is the adiabatic index. The dimensionless internal energy per particle in the fluid rest frame v_s may be expressed as

$$v_s = \frac{(T_s^{00}/n_s m_s c^2 - \Gamma_s)\Gamma_s}{1 + \hat{\gamma}_s(\Gamma_s^2 - 1)}, \quad (2.12)$$

where T_s^{00} is the total energy density in the simulation frame, n_s is the lab-frame particle number density, Γ_s is the Lorentz factor corresponding to the local fluid velocity, $\hat{\gamma}_s$ is the adiabatic index, and the subscript $s = e, i$ refers to the particle species.

To make use of Eq. 2.12, we need to express the adiabatic index $\hat{\gamma}_s$ as a function of the internal energy per particle, so that the equation may be solved iteratively. For a plasma described by a Maxwell-Jüttner distribution with dimensionless temperature θ_s ,

$$f_{MJ}(\gamma, \theta_s) \propto \gamma \sqrt{\gamma^2 - 1} \exp(-\gamma/\theta_s), \quad (2.13)$$

where γ denotes the particle Lorentz factor, the dimensionless internal energy is given by

$$v_s = \frac{\int_1^\infty \gamma f_{\text{MJ}}(\gamma, \theta_s) d\gamma}{\int_1^\infty f_{\text{MJ}}(\gamma, \theta_s) d\gamma} - 1. \quad (2.14)$$

We have numerically evaluated the integral on the right hand side for a range of temperatures and thereby produced interpolating tables for $\hat{\gamma}_s(v_s)$ and $\theta_s(v_s)$, to be used for finding v_s in Eq. 2.12.

Eqs. 2.9 and 2.12 assume that the stress-energy tensor is diagonal and isotropic in the fluid frame. We have explicitly tested this assumption by measuring all the components of the stress-energy tensor in our computational domain. By boosting into the local fluid frame, we can calculate all the components of the pressure tensor. We find that the off-diagonal components are generally negligible. As regard to the diagonal components, we quantify the degree of anisotropy with the temperature ratios T_{xx}/T_{tot} , T_{yy}/T_{tot} , and T_{zz}/T_{tot} , where $T_{\text{tot}} = (T_{xx} + T_{yy} + T_{zz})/3$. For an isotropic fluid, $T_{xx}/T_{\text{tot}} = T_{yy}/T_{\text{tot}} = T_{zz}/T_{\text{tot}} = 1$. For electrons in the reconnection downstream, we find that these ratios typically lie in the range $T_{yy}/T_{\text{tot}} \approx T_{zz}/T_{\text{tot}} \approx 0.9 - 0.95$ and $T_{xx}/T_{\text{tot}} \approx 1.2 - 1.1$ (see Appendix 2.E for further discussion, including the dependence of the anisotropy on β_i and T_e/T_i). We find greater anisotropy along the outflow direction \hat{x} than either \hat{y} or \hat{z} . This is in qualitative agreement with the findings of [Shay et al. \(2014\)](#), who demonstrated that the electron pressure tensor in the immediate reconnection exhausts is anisotropic, with the component parallel to the local magnetic field larger than the perpendicular component.

As an additional test, we have also measured the temperature and internal energy via an explicit boost of the stress-energy tensor into the fluid rest frame, and compared the results to those computed by employing the perfect-fluid approximation as described above. We find that the disagreement between the two methods is only of order $\sim 1\%$, providing *a posteriori* a justification for the perfect-fluid assumption.

2.4.3.2 Total heating

The main focus of our investigation is particle heating by reconnection, and how the heating efficiency depends on the upstream parameters. From each simulation, we extract a dimensionless ratio $M_{ue,tot}$, which we define as

$$M_{ue,tot} \equiv \frac{v_{e,down} - v_{e,up}}{\sigma_i m_i / m_e}. \quad (2.15)$$

The numerator is the difference in dimensionless internal energy per electron between downstream and upstream, while the denominator represents (apart from a factor of two) the available magnetic energy per electron in the upstream, in units of the electron rest mass energy ($= B_0^2 / 4\pi n_0 m_e c^2$). The ratio $M_{ue,tot}$ is then a measure of the efficiency of reconnection in converting available magnetic energy to electron heating. Alternatively, the efficiency parameter may be phrased in terms of the dimensionless temperature,

$$M_{Te,tot} \equiv \frac{\theta_{e,down} - \theta_{e,up}}{\sigma_i m_i / m_e}, \quad (2.16)$$

as in [Shay et al. \(2014\)](#). We define analogous ratios for protons as

$$M_{ui,tot} \equiv \frac{v_{i,down} - v_{i,up}}{\sigma_i}, \quad (2.17)$$

and

$$M_{Ti,tot} \equiv \frac{\theta_{i,down} - \theta_{i,up}}{\sigma_i}. \quad (2.18)$$

For the results presented below, we average the dimensionless internal energy and temperature appearing in the above equations over time, starting at ~ 0.3 Alfvénic crossing times (or equivalently,

$\sim 4500 \omega_{\text{pe}}^{-1}$), when the two reconnection wavefronts — and with them, the particles initialized in the current sheet — have moved beyond the region that we use for our computations (green and black boxes in Fig. 2.3). We typically time-average our results over an interval of ~ 0.3 Alfvénic crossing times.

2.4.3.3 Adiabatic and irreversible heating

When gas is adiabatically compressed, its internal energy increases while its entropy remains constant. The reconnecting plasma may experience such adiabatic heating, since the downstream region is denser than the upstream (see Fig. 2.2). However, adiabatic heating is not a genuine signature of the conversion of field energy into particle energy. We isolate the irreversible heating generated by magnetic field dissipation by subtracting out the adiabatic heating from the total particle heating.

The predicted internal energy per particle in the downstream resulting from adiabatic compression alone (which we shall call $v_{s,\text{down}}^{\text{ad}}$ for species s) is calculated from the upstream internal energy per particle $v_{s,\text{up}}$, the upstream rest-frame number density $\bar{n}_{s,\text{up}}$ and the downstream rest-frame number density $\bar{n}_{s,\text{down}}$ using the second law of thermodynamics for constant entropy,

$$dU_s = -p_s dV \quad (2.19)$$

From the ideal gas equation of state, the pressure is $p_s = \bar{n}_s k_B T_s = (\hat{\gamma}_s - 1) u_s$. Using the relation $U_s/V = u_s = v_s \bar{n}_s m_s c^2$, we can integrate Eq. 2.19 to obtain

$$\int_{v_{s,\text{up}}}^{v_{s,\text{down}}^{\text{ad}}} \frac{1}{(\hat{\gamma}(v_s) - 1)v_s} dv_s - \log \left(\frac{\bar{n}_{s,\text{down}}}{\bar{n}_{s,\text{up}}} \right) = 0. \quad (2.20)$$

We compute the argument of the logarithm in Eq. 2.20 as the ratio of downstream to upstream rest-frame density, spatially averaged over the regions marked in Fig. 2.3. The lower bound of the

integral $v_{s,\text{up}}$ is computed as a density-weighted spatial average in the selected upstream region. The adiabatic index $\hat{\gamma}_s(v_s)$ is tabulated as discussed above. We numerically solve Eq. 2.20 for the predicted downstream dimensionless internal energy per particle $v_{s,\text{down}}^{\text{ad}}$ resulting from adiabatic compression. We refer to the corresponding dimensionless temperature as $\theta_{s,\text{down}}^{\text{ad}}$. We call the difference between the initial and the predicted dimensionless temperature or internal energy per particle due to adiabatic compression, i.e., $\Delta\theta_{s,\text{ad}} \equiv \theta_{s,\text{down}}^{\text{ad}} - \theta_{s,\text{up}}$ and $\Delta v_{s,\text{ad}} = v_{s,\text{down}}^{\text{ad}} - v_{s,\text{up}}$, as the “adiabatic” component of heating.

The irreversible heating, which is associated with a genuine increase in entropy, is the residual between the total heating and the adiabatic heating:

$$\Delta\theta_{s,\text{irr}} = (\theta_{s,\text{down}} - \theta_{s,\text{up}}) - \Delta\theta_{s,\text{ad}}, \quad (2.21)$$

$$\Delta v_{s,\text{irr}} = (v_{s,\text{down}} - v_{s,\text{up}}) - \Delta v_{s,\text{ad}}. \quad (2.22)$$

As in Section 2.4.3.2, we introduce efficiency ratios to characterize the irreversible and adiabatic heating of electrons,

$$M_{Te,\text{irr}} \equiv \frac{\Delta\theta_{e,\text{irr}}}{\sigma_i m_i / m_e}, \quad M_{Te,\text{ad}} \equiv \frac{\Delta\theta_{e,\text{ad}}}{\sigma_i m_i / m_e}, \quad (2.23)$$

$$M_{ue,\text{irr}} \equiv \frac{\Delta v_{e,\text{irr}}}{\sigma_i m_i / m_e}, \quad M_{ue,\text{ad}} \equiv \frac{\Delta v_{e,\text{ad}}}{\sigma_i m_i / m_e}, \quad (2.24)$$

and define analogous ratios for protons

$$M_{Ti,\text{irr}} \equiv \frac{\Delta\theta_{i,\text{irr}}}{\sigma_i}, \quad M_{Ti,\text{ad}} \equiv \frac{\Delta\theta_{i,\text{ad}}}{\sigma_i}, \quad (2.25)$$

$$M_{ui,\text{irr}} \equiv \frac{\Delta v_{i,\text{irr}}}{\sigma_i}, \quad M_{ui,\text{ad}} \equiv \frac{\Delta v_{i,\text{ad}}}{\sigma_i}. \quad (2.26)$$

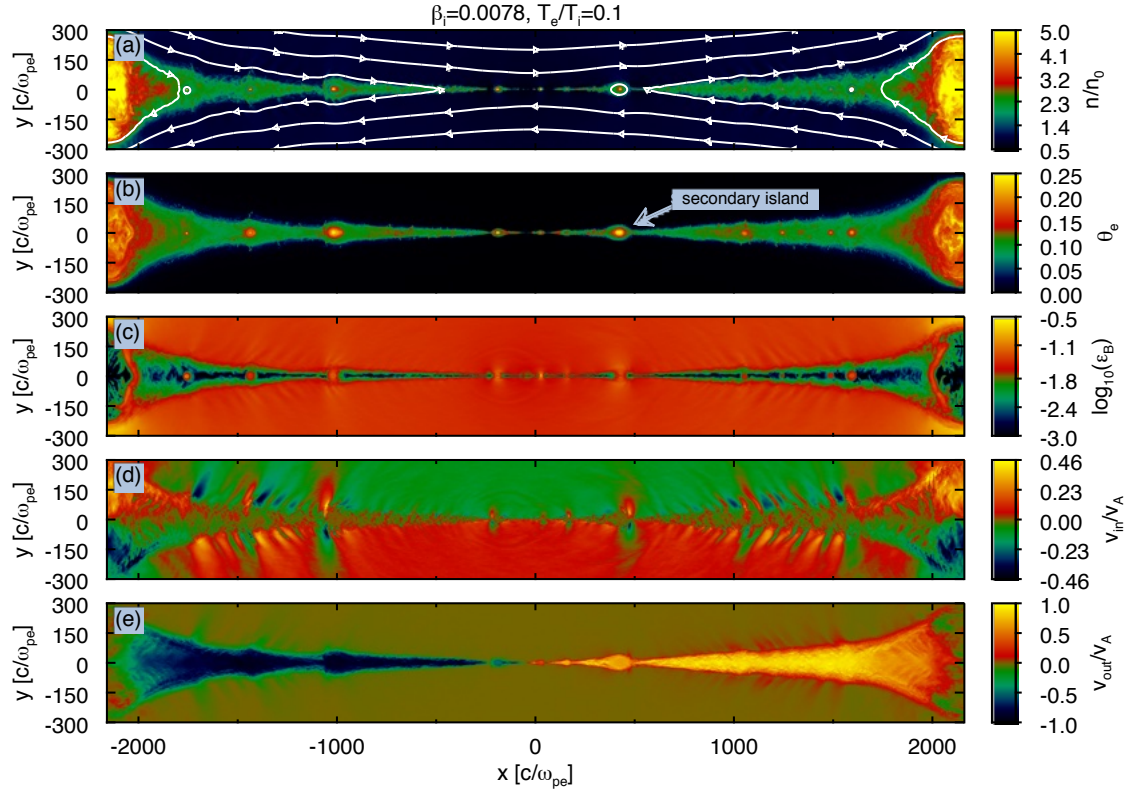


Figure 2.5: 2D structure at $t = 11250 \omega_{\text{pe}}^{-1} \approx 0.75 t_A$ from a representative low- β_i simulation (**A[0]** in Tab. 2.1) with $\beta_i = 0.0078$, $\sigma_w = 0.1$, $T_e/T_i = 0.1$ and $m_i/m_e = 25$. We present 2D plots of (a): particle density in units of the upstream initial value, n/n_0 , with overplotted magnetic field lines; (b): dimensionless electron temperature, θ_e ; (c): logarithm of the magnetic energy fraction, $\varepsilon_B = B_0^2/8\pi n_0 m_i c^2$; (d): inflow velocity, in units of Alfvén speed $v_{\text{in}}/v_A = \mathbf{v} \cdot \hat{\mathbf{y}}/v_A$; (e): outflow velocity, in units of Alfvén speed $v_{\text{out}}/v_A = \mathbf{v} \cdot \hat{\mathbf{x}}/v_A$. We show the full extent of the domain in the x direction ($L_x = 4318 c/\omega_{\text{pe}}$), and only a small fraction of the box close to the current sheet in the y direction. The primary island, which contains the particles initialized in the current sheet, can be seen at the boundaries ($x = \pm 2200 c/\omega_{\text{pe}}$). As shown in panel (a), the density reaches $n/n_0 \approx 2.3$ in the bulk of the outflow, with sharp increases up to $n/n_0 \approx 5$ in the core of secondary islands (e.g., at $x = -1000 c/\omega_{\text{pe}}$ and $x = 300 c/\omega_{\text{pe}}$). The primary island has a high density throughout its interior, $n/n_0 \approx 5$. Similarly, the temperature (panel (b)) is uniform $\theta_e \approx 0.1$ in the bulk of the outflow, with spikes up to $\theta_e \approx 0.25$ at the center of secondary islands. The primary island has a temperature $\theta_e \approx 0.15$ throughout its interior. In panel (c), we show that the magnetic energy fraction ε_B is extremely small in the outflow, $\varepsilon_B \lesssim 0.01$. The inflow velocity in panel (d) is a fraction of the Alfvén limit $|v_{\text{in}}|/v_A \approx 0.08$, and the outflow velocity in panel (e) approaches the Alfvén limit, $|v_{\text{out}}|/v_A \approx 1$.

2.5 Results

In this section, we describe our main results, focusing on the dependence of the heating efficiency on the plasma conditions. First, in Section 2.5.1, we present the dynamics of the reconnection layer,

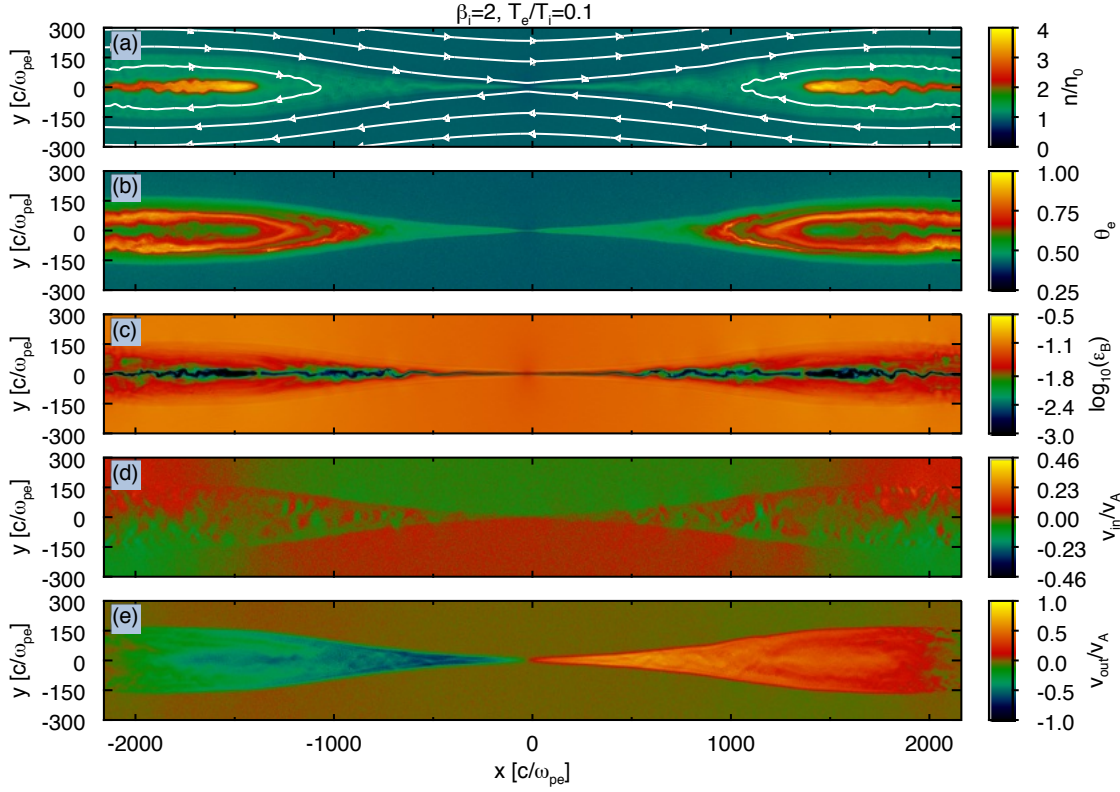


Figure 2.6: 2D structure at $t = 11250 \omega_{pe}^{-1} \approx 0.75 t_A$ from a representative high- β_i simulation (**A[4]** in Tab. 2.1) with $\beta_i = 2$, $\sigma_w = 0.1$, $T_e/T_i = 0.1$ and $m_i/m_e = 25$ (i.e., apart from β_i , with the same parameters as in Fig. 2.5). The panels show the same quantities as in Fig. 2.5. As shown in panel (a), the density is roughly $n/n_0 \approx 1.2$ in the bulk of the outflow, which is only slightly larger than the upstream density. In the primary island, the density reaches $n/n_0 \approx 4$. The electron temperature (panel (b)) is nearly uniform in the reconnection exhausts (i.e., within a distance of $\approx 700 c/\omega_{pe}$ from the central X-point), with $\theta_e \approx 0.6$. Within the primary island, the temperature reaches $\theta_e \approx 0.8$. In panel (c), we present the logarithm of magnetic energy fraction ε_B , showing that the reconnection layer is weakly magnetized ($\varepsilon_B \lesssim 0.01$). Panel (d) shows that the inflow velocity is nearly uniform in the upstream, with a typical value $|v_{in}|/v_A \approx 0.04$. Panel (e) shows that the outflow velocity in the reconnection exhausts is $|v_{out}|/v_A \approx 0.6$. At the center of the primary island, $x \approx \pm 2200 c/\omega_{pe}$, the plasma from the reconnection outflows comes to rest, $|v_{out}|/v_A \approx 0$.

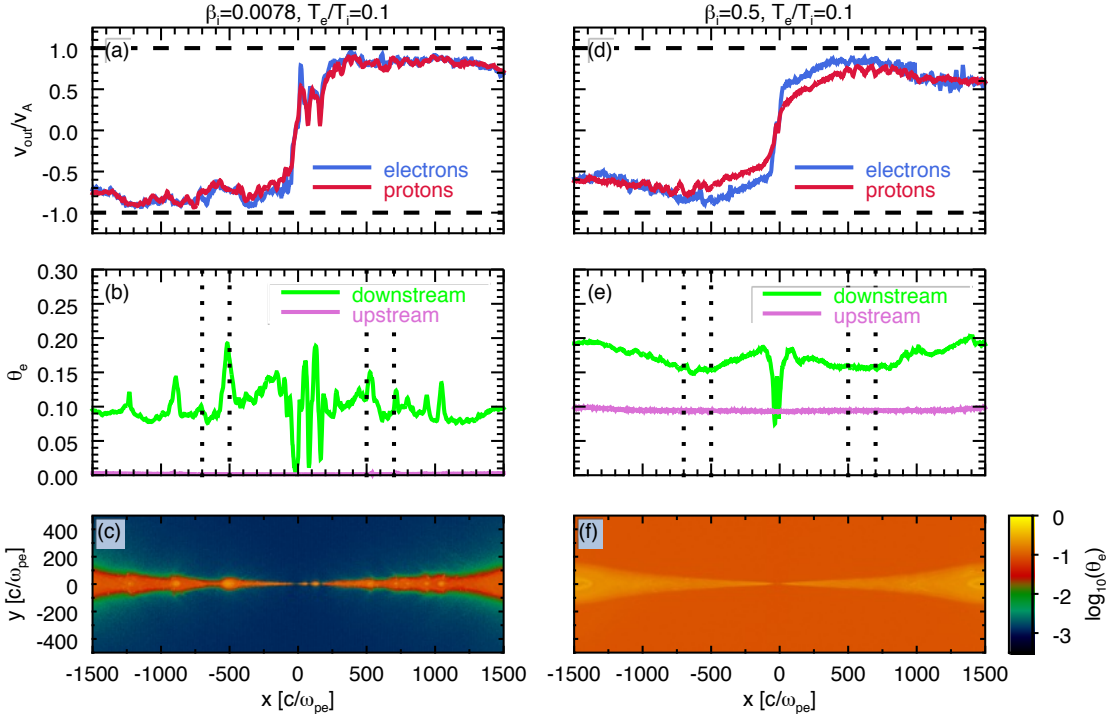


Figure 2.7: Comparison between a low- β_i (left column, with $\beta_i = 0.0078$, $\mathbf{A}[0]$ in Tab. 2.1) and a high- β_i (right column, with $\beta_i = 0.5$, $\mathbf{A}[3]$ in Tab. 2.1) simulation, at time $t = 9225 \omega_{pe}^{-1} \approx 0.65 t_A$. In both cases, $\sigma_w = 0.1$, $T_e/T_i = 0.1$ and $m_i/m_e = 25$. (a),(d): 1D profiles along x (averaged along y within the reconnection downstream, as identified by Eq. 2.7) of proton (red) and electron (blue) outflow velocity in units of the Alfvén speed, v_{out}/v_A ; (b),(e): 1D profiles along x of the upstream (magenta) and downstream (green) dimensionless electron temperature, θ_e (the two slabs in between the vertical dotted lines indicate the regions we use to calculate the downstream and upstream temperatures); (c),(f): 2D plots of $\log(\theta_e)$. In both the low- and high- β_i cases, the spatial profiles of outflow velocity and electron temperature show that the downstream region reaches a quasi-steady state.

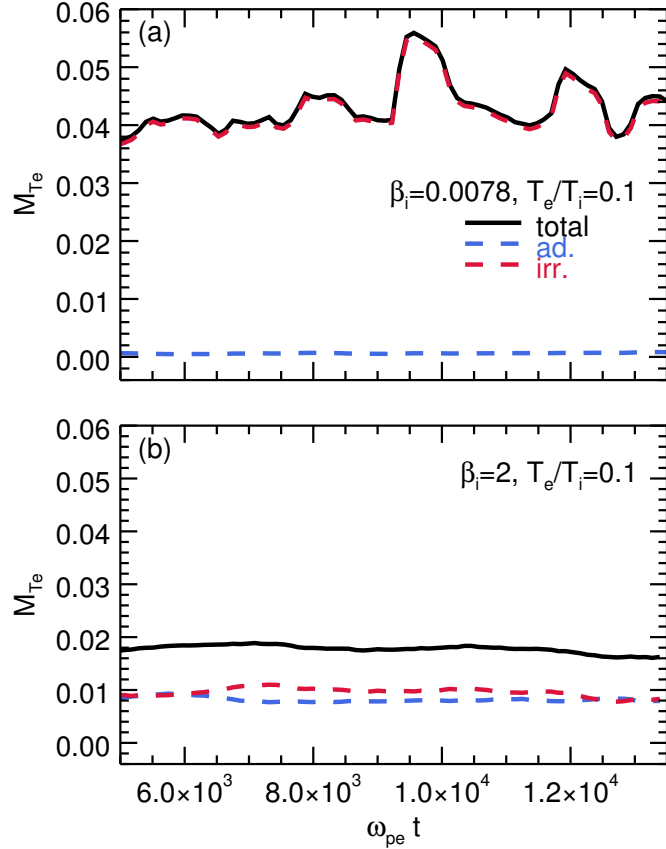


Figure 2.8: Time evolution of total ($M_{Te,tot}$; black solid), irreversible ($M_{Te,irr}$; red dashed), and adiabatic ($M_{Te,ad}$; blue dashed) heating efficiency, for a low- β_i simulation (top panel, with $\beta_i = 0.0078$) and a high- β_i case (bottom panel, with $\beta_i = 2$). In both cases, $\sigma_w = 0.1$, $T_e/T_i = 0.1$ and $m_i/m_e = 25$. The heating efficiencies are measured starting at $t \approx 5000 \omega_{pe}^{-1}$, at which point the two reconnection wavefronts recede past the location of the downstream region used for our computations (shown in Fig. 2.3 with the green contours). For the low- β_i case, the total heating efficiency oscillates around $M_{Te} \approx 0.04$, and it is dominated by genuine/irreversible heating (panel (a)). For high β_i , the total heating efficiency saturates at a smaller value, $M_{Te} \approx 0.016$. Here, adiabatic and irreversible heating equally contribute (panel (b)).

and describe the main differences between low- β_i and high- β_i cases, for our fiducial magnetization $\sigma_w = 0.1$ and mass ratio $m_i/m_e = 25$. Next, in Section 2.5.2, we discuss the inflow and outflow rates as a function of β_i and T_e/T_i . Then, in Section 2.5.3, we show the dependence of electron and proton heating on β_i and T_e/T_i , still for our fiducial magnetization $\sigma_w = 0.1$ and mass ratio $m_i/m_e = 25$. In Section 2.5.4, we extend our results for $T_e/T_i = 1$ and $\sigma_w = 0.1$ up to the physical mass ratio $m_i/m_e = 1836$, emphasizing the β_i -dependence of the particle heating efficiencies. Finally, in Section 2.5.5, we show how the heating physics changes when the magnetization σ_w extends above unity (i.e., in the regime of ultra-relativistic reconnection), for mass ratio $m_i/m_e = 1836$ and temperature ratio $T_e/T_i = 1$.

2.5.1 Reconnection physics as a function of β_i

The physics of reconnection shows a marked difference between low- and high- β_i regimes. In Figs. 2.5 and 2.6, we present various fluid quantities for representative low- and high- β_i simulations, respectively ($\beta_i = 0.0078$ in Fig. 2.5 and $\beta_i = 2$ in Fig. 2.6). In both cases, $\sigma_w = 0.1$, $T_e/T_i = 0.1$ and $m_i/m_e = 25$. At $t = 11250 \omega_{pe}^{-1} \approx 0.75 t_A$, we show 2D plots of: (a) the total density in the simulation frame in units of the initial density, n/n_0 ; (b) the dimensionless electron temperature θ_e ; (c) the magnetic energy fraction $\varepsilon_B = B^2/8\pi n_0 m_i c^2$; (d) the inflow velocity $v_{in}/v_A = \mathbf{v} \cdot \hat{\mathbf{y}}/v_A$ (v_A is the Alfvén speed), and (e) the outflow velocity $v_{out}/v_A = \mathbf{v} \cdot \hat{\mathbf{x}}/v_A$.

A striking difference between the simulations shown in Figs. 2.5 and 2.6 is that, while the reconnection outflow at high β_i is nearly homogeneous, a number of secondary magnetic islands appear at low β_i (see Fig. 2.5(a)). The secondary islands are over-dense, and at their center they can reach temperatures a few times larger than the bulk of the outflow (Fig. 2.5(b)). They also correspond to peaks in magnetic energy (Fig. 2.5(c)).

The difference in electron temperature between inflow and outflow regions is more pronounced in the low- than in the high- β_i case (compare Figs. 2.5(b) and 2.6(b)). However, as we demonstrate

in Section 2.5.3, the fraction of available magnetic energy converted into total electron heating is roughly comparable between the two cases.

The inflow velocity $v_{\text{in}}/v_A = \mathbf{v} \cdot \hat{\mathbf{y}}/v_A$ is shown in panel (d). For low- β_i , the inflow velocity is $|v_{\text{in}}|/v_A \approx 0.08$. It is nearly uniform in the upstream, with the exception of the regions ahead of the secondary islands, where the velocity reverses its sign relative to the ambient inflow (see, e.g., Fig. 2.5(d) at $x \approx -1100 c/\omega_{pe}$). This reversal occurs as the secondary island moves along the outflow direction, pushing aside the inflowing plasma. For high- β_i , the plasma inflow is remarkably uniform, with $|v_{\text{in}}|/v_A \approx 0.04$, which is half the value of the low- β_i case. The inflow velocity at high β_i shows no reversals near the reconnection exhausts, as there are no secondary islands.

The outflow velocity $v_{\text{out}}/v_A = \mathbf{v} \cdot \hat{\mathbf{x}}/v_A$ is shown in panel (e). For low- β_i , the outflow speed nearly reaches the Alfvén limit, $|v_{\text{out}}|/v_A \approx 1$, whereas for high- β_i it approaches a smaller value, $|v_{\text{out}}|/v_A \approx 0.6$. For both low and high β_i , the outflow velocity is nearly uniform in the reconnection exhausts, but it drops close to the periodic boundaries at $x \approx \pm 2200$, as the outflowing plasma accretes onto the primary island.

We show in Fig. 2.7 a direct comparison between one low- β_i and one high- β_i simulation. The left column in Fig. 2.7 refers to $\beta_i = 0.0078$ (the same as in Fig. 2.5), whereas $\beta_i = 0.5$ for the right column. In both cases, $\sigma_w = 0.1$, $T_e/T_i = 0.1$ and $m_i/m_e = 25$. In the top row, we show the profile along x of the outflow velocity, for protons (red) and electrons (blue). We find that electrons move slightly faster than protons in the vicinity of the central X-point, but at larger distances the speeds of the two species are the same, and they saturate at a fixed fraction of the Alfvén limit. We show in the middle row of panels the x -profile of the dimensionless electron temperature θ_e , in the upstream (magenta) and downstream (green). The secondary magnetic islands present in the low- β_i simulation (panel (c)) are correlated with spikes in the downstream electron temperature (see the peak at $x \approx -500 c/\omega_{pe}$ in Fig. 2.7(b)). Aside from the temperature spikes at low β_i , the

two panels in the middle row of Fig. 2.7 demonstrate that, far enough from the central X-point, the electron temperature is nearly uniform.

To estimate the reconnection heating efficiency, we measure the downstream temperature in the two slabs delimited by the vertical dotted lines in Fig. 2.7(b) and (e) (more precisely, within the green contours in Fig. 2.3). The time evolution of the total electron heating efficiency $M_{Te,tot}$, of the adiabatic contribution $M_{Te,ad}$ and of the irreversible component $M_{Te,irr}$ are shown in Fig. 2.8 with black, dashed blue and dashed red lines, respectively. The top panel refers to a low- β_i simulation with $\beta_i = 0.0078$, whereas the bottom panel refers to the high- β_i case $\beta_i = 2$. In both cases, $\sigma_w = 0.1$, $T_e/T_i = 0.1$ and $m_i/m_e = 25$. The horizontal axis in the figure starts from $t = 5000 \omega_{pe}^{-1}$, which corresponds to the time when the two reconnection wavefronts pass beyond the region that we employ for calculating the downstream quantities (as discussed above, after this time the measurements are no longer affected by our choice of initialization of the current sheet).¹ While the heating efficiencies are nearly constant in time for high β_i (bottom panel), the temporal profiles at low β_i (top panel) present quasi-periodic modulations. They mark the passage of secondary islands — whose temperature is typically hotter than the bulk outflow — through the region used for our computations. To minimize the temperature variations associated with secondary islands, we average the heating efficiencies over time, as described in Section 2.4.3.2. In doing so, the results we obtain are a reliable assessment of the steady-state heating physics in reconnection.

Panels (a) and (b) in Fig. 2.8 also demonstrate that the fractional contributions of adiabatic and irreversible heating to the total electron heating significantly depend on β_i , as we further discuss in Section 2.5.3. In the low- β_i regime, adiabatic heating is unimportant as compared to the irreversible part, whereas the two components are comparable at high β_i .

¹This time is typically in the range $t \approx 4000 - 5000 \omega_{pe}^{-1}$, with marginal dependence on β_i and on the initial sheet thickness Δ .

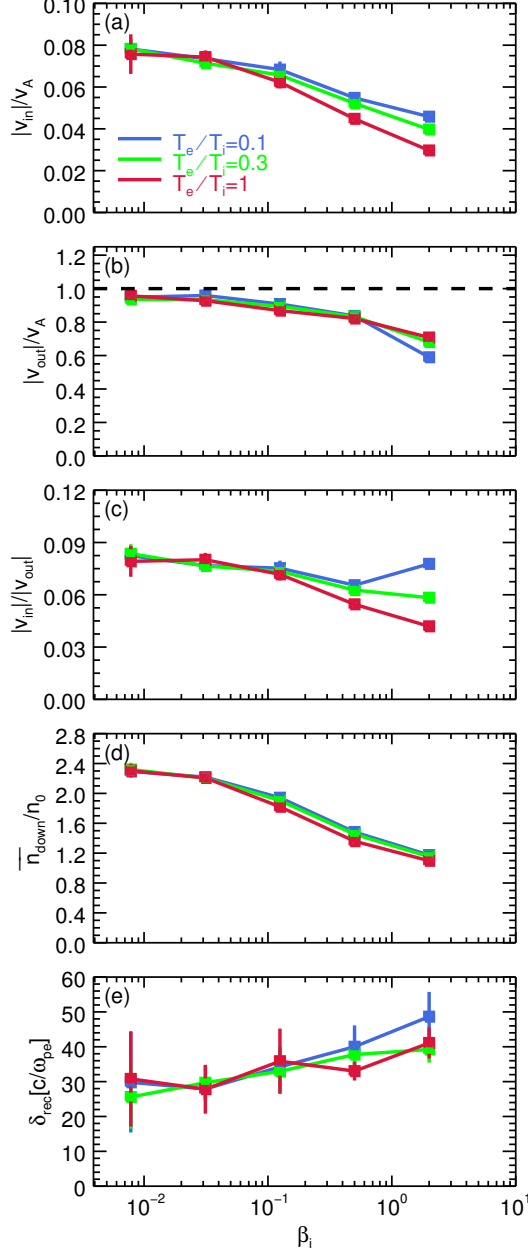


Figure 2.9: For temperature ratios $T_e/T_i = 0.1$ (blue), 0.3 (green), and 1 (red), β_i -dependence of (a): inflow velocity $|v_{in}|/v_A$; (b): outflow velocity $|v_{out}|/v_A$; (c): reconnection rate $|v_{in}|/|v_{out}|$; (d): downstream density in units of initial density in the upstream \bar{n}_{down}/n_0 ; (e): width of reconnection layer δ_{rec} . Error bars represent one standard deviation from the mean. The inflow velocity is averaged over a region of length $L_x/3 \approx 1440 c/\omega_{pe}$ in x and width $20 c/\omega_{pe}$ in y , located $|y| \sim 100 c/\omega_{pe}$ upstream of the central X-point. We have checked that the saturation value is insensitive to the choice of averaging region. The outflow velocity is computed as an average over the 20 cells with the largest $|\mathbf{v} \cdot \hat{\mathbf{x}}|$ located along the central region of the outflow ($|y| \lesssim 4 c/\omega_{pe}$). We have tested that the resulting outflow velocity is nearly insensitive to our averaging procedure. The regions used for measuring density in the upstream and downstream are described in Section 2.4.2. The width of the reconnection layer is measured at a distance $\sim 430 c/\omega_{pe}$ downstream of the central X-point. All quantities are time-averaged over $\sim 0.3 t_A \approx 4500 \omega_{pe}^{-1}$. Both inflow and outflow velocities tend to decrease with β_i , with weak dependence on T_e/T_i (noticeable only at high β_i). The density compression decreases with β_i . The width δ_{rec} of the layer increases with β_i , yet with large error bars.

2.5.2 Dependence of inflow and outflow velocity on β_i and T_e/T_i

In Fig. 2.9, we show the dependence on β_i and T_e/T_i of various fluid quantities, from a suite of simulations with fixed $\sigma_w = 0.1$ and $m_i/m_e = 25$. We present the (a) inflow velocity normalized to the Alfvén speed $|v_{\text{in}}|/v_A$; (b) outflow velocity normalized to the Alfvén speed $|v_{\text{out}}|/v_A$; (c) ratio of inflow to outflow velocity $|v_{\text{in}}|/|v_{\text{out}}|$; (d) downstream rest-frame density in units of the initial density in the upstream $\bar{n}_{\text{down}}/n_0$; (e) width of the reconnection region at a distance of $430 c/\omega_{pe}$ from the center of the layer. Blue, green, and red points denote simulations with upstream temperature ratios $T_e/T_i = 0.1, 0.3$, and 1, respectively.

As described in Section 2.4.3.2, the quantities we extract are time-averaged, typically over 0.3 Alfvénic crossing times, corresponding to $\sim 4500 \omega_{pe}^{-1}$. The points in Fig. 2.9 represent the time averages, with vertical error bars indicating one standard deviation. At low β_i , the inflow velocity is $|v_{\text{in}}|/v_A \approx 0.08$, independent of the upstream temperature ratio (panel (a)). In the high- β_i case, the inflow speed is smaller, $|v_{\text{in}}|/v_A \approx 0.04$, and shows a weak dependence on the temperature ratio, with higher temperature ratios attaining lower values of $|v_{\text{in}}|/v_A$.

The outflow velocity (panel (b)) nearly saturates the Alfvén limit at low β_i (the Alfvén limit is indicated with the horizontal dashed black line), whereas for high β_i it is sub-Alfvénic, $|v_{\text{out}}|/v_A \approx 0.75$. For low values of β_i , i.e., $\beta_i \lesssim 0.1$, the outflow velocity is nearly independent of the temperature ratio, whereas at high β_i it shows a weak dependence on T_e/T_i , with higher temperature ratios corresponding to greater outflow speeds.

The dependence of the reconnection rate $|v_{\text{in}}|/|v_{\text{out}}|$ on β_i and T_e/T_i (panel (c)) follows from the variations in inflow speed and outflow velocity that we have just discussed. At low β_i , the reconnection rate is $|v_{\text{in}}|/|v_{\text{out}}| \approx 0.08$ regardless of the temperature ratio, whereas at high β_i , and specifically for $\beta_i = 2$, the reconnection rate at $T_e/T_i = 1$ is $|v_{\text{in}}|/|v_{\text{out}}| \approx 0.04$, only half that of the $T_e/T_i = 0.1$ case. So, in the high- β_i regime reconnection proceeds slower for hotter upstream

electrons.

As β_i increases, the plasma is less prone to be compressed during the reconnection process. As shown in Fig. 2.9 (d), the downstream to upstream density ratio decreases as β_i increases. The value of $\bar{n}_{\text{down}}/n_0$ is nearly independent of the upstream temperature ratio. Though the ratio $\bar{n}_{\text{down}}/n_0$ approaches unity at high β_i , this does not necessarily imply that the fractional contribution of adiabatic heating to total heating is negligible at high β_i (we demonstrate this in Section 2.5.3).

Lastly, in panel (e) we show the β_i -dependence of the reconnection layer width δ_{rec} , in units of the electron skin depth c/ω_{pe} . We measure the width across the reconnection layer, as identified by Eq. 2.7, at a distance $\sim 430 c/\omega_{\text{pe}}$ downstream of the central X-point. The width shows strong variability in time at low β_i , as secondary islands pass through the region employed for our measurements (note the large error bars). Despite the uncertainty in the measurement, panel (e) shows a consistent trend of increasing reconnection layer width δ_{rec} with β_i . The measured values of δ_{rec} lie in the range $25 - 50 c/\omega_{\text{pe}}$, which is apparently close to the chosen current sheet thickness at initialization, $\Delta = 40 c/\omega_{\text{pe}}$. However, we demonstrate in Appendix 2.F that the measured reconnection layer width is independent of our choice of the initial sheet thickness. It follows that our measurement leads to a reliable assessment of the opening angle of the reconnection outflow, $\sim \delta_{\text{rec}}/(430 c/\omega_{\text{pe}}) \sim 0.1$.

2.5.3 Dependence of particle heating on β_i and T_e/T_i

In Fig. 2.10, we show the β_i and T_e/T_i dependence of electron (panel (a)) and proton (panel (b)) dimensionless temperature, and the ratio of proton-to-electron skin depth (panel (c); see Eq. 2.5). In each panel, solid and dashed lines indicate downstream and upstream quantities, respectively. As in Fig. 2.9, blue, green, and red points refer to electron-to-proton temperature ratios $T_e/T_i = 0.1, 0.3$, and 1, respectively. The upstream electron dimensionless temperatures lie in the range 10^{-3} to 10, as in Table 2.1; for protons, the dimensionless temperature in the upstream ranges from 4×10^{-4}

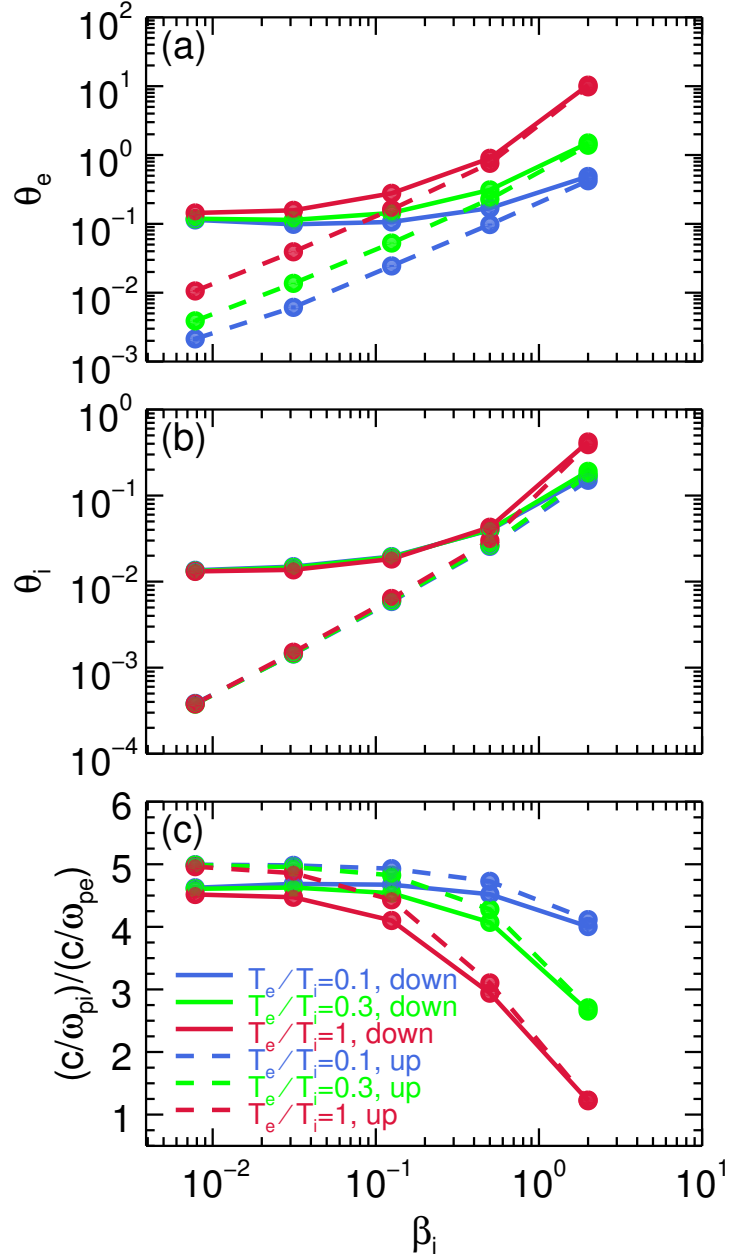


Figure 2.10: For upstream temperature ratios $T_e/T_i = 0.1$ (blue), 0.3 (green), and 1 (red), we present the β_i -dependence of various upstream (dashed) and downstream (solid) quantities; (a): electron dimensionless temperature, θ_e ; (b): proton dimensionless temperature, θ_i ; (c): proton-to-electron skin depth ratio, $(c/\omega_{pi})/(c/\omega_{pe})$. The simulations shown here use a mass ratio $m_i/m_e = 25$ and magnetization $\sigma_w = 0.1$.

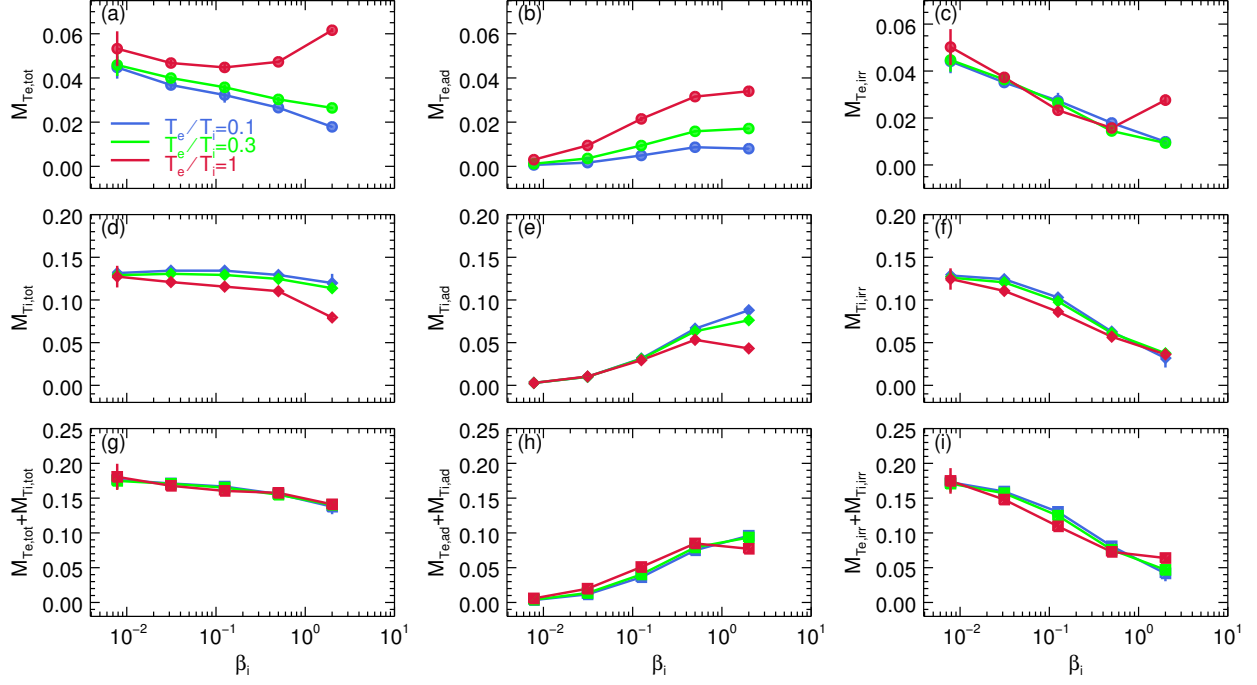


Figure 2.11: For upstream temperature ratios $T_e/T_i = 0.1$ (blue), 0.3 (green), and 1 (red), β_i -dependence of heating efficiencies; (a): electron total, $M_{Te,tot}$; (b): electron adiabatic, $M_{Te,ad}$; (c): electron irreversible, $M_{Te,irr}$; (d): proton total, $M_{Ti,tot}$; (e): proton adiabatic, $M_{Ti,ad}$; (f): proton irreversible, $M_{Ti,irr}$; (g): electron and proton total, $M_{Te,tot} + M_{Ti,tot}$; (h): electron and proton adiabatic, $M_{Te,ad} + M_{Ti,ad}$; (i): electron and proton irreversible, $M_{Te,irr} + M_{Ti,irr}$. The simulations shown here use a mass ratio $m_i/m_e = 25$ and magnetization $\sigma_w = 0.1$. Error bars, mostly smaller than the plotted symbols, represent one standard deviation from the mean. The decomposition of total heating into irreversible and adiabatic components shows that electron and proton heating at low β_i is accompanied by an increase in entropy, while heating in the high- β_i regime tends to be dominated by adiabatic compression.

to 0.4.

The range of temperatures in the downstream is smaller than in the upstream (compare the solid and dashed lines in Fig. 2.10(a) and (b)). At low β_i , the available magnetic energy is large compared to the particle thermal content in the upstream, so dissipation of the magnetic field leads to electron and proton temperatures in the downstream that are nearly independent of β_i . At high β_i , the energy transferred from the fields to the particles is much smaller than the initial particle thermal content, giving a minor increase of temperature from upstream to downstream. Even if the fractional increase in temperature is extremely small at high β_i , the fraction of available magnetic energy being converted into particle heating might still be as large as at low β_i . The rest of the section addresses this question.

We show the plasma- β_i and temperature ratio T_e/T_i dependence of electron and proton heating in Fig. 2.11. The simulations presented here are those referenced in Tab. 2.1, for which $m_i/m_e = 25$ and $\sigma_w = 0.1$. We indicate the total, adiabatic, and irreversible heating by $M_{Te,tot}$ (Eq. 2.16), $M_{Te,ad}$ and $M_{Te,irr}$ (Eqs. 2.23) for electrons, and by $M_{Ti,tot}$ (Eq. 2.18), $M_{Ti,ad}$ and $M_{Ti,irr}$ (Eqs. 2.25) for protons. Blue, green, and red points indicate simulations with upstream electron-to-proton temperature ratios of 0.1, 0.3, and 1, respectively. As in Section 2.5.2, filled points are the time-averaged results of our simulations, and vertical error bars indicate one standard deviation from the mean. The top, middle, and bottom rows show heating fractions of electrons, protons, and of the overall fluid, respectively, which we now discuss in turn.

In Fig. 2.11(a), we show the dependence of the total electron heating efficiency $M_{Te,tot}$ on β_i and T_e/T_i . Although the initial plasma β_i spans more than two orders of magnitude, and the initial temperature ratio an order of magnitude, even the most extreme values of $M_{Te,tot}$ differ by no more than a factor of ~ 4 . The value of $M_{Te,tot}$ in our $\beta_i \lesssim 0.5$ simulations, for which electrons stay non-relativistic both in the upstream and in the downstream, is ~ 0.04 , which is consistent with the

results of non-relativistic reconnection by [Shay et al. \(2014\)](#) for mass ratio $m_i/m_e = 25$.² As shown by [Shay et al. \(2014\)](#), the electron heating efficiency in non-relativistic reconnection is expected to decrease with increasing mass ratio; in Sections 2.5.4 and 2.5.6, we present the dependence of the electron and proton heating fractions in trans-relativistic reconnection on m_i/m_e , up to the physical value.

The total electron heating fraction $M_{Te,tot}$ is decomposed into adiabatic and irreversible components in panels (b) and (c). By comparing the two panels, we see that most of the heating in the low- β_i regime comes from irreversible processes, i.e., it is accompanied by a genuine increase in entropy, while heating at high β_i mostly results from adiabatic compression.

The electron adiabatic heating efficiency increases with the inflow temperature ratio T_e/T_i (Fig. 2.11(b)). The dependence is most apparent at high β_i , where adiabatic heating represents a significant contribution to the total heating. The dependence of adiabatic heating on temperature ratio can be simply understood through the adiabatic law $T/\bar{n}^{\hat{\gamma}-1} = \text{const}$. As electrons get compressed from upstream to downstream, the adiabatic heating fraction can be written as³

$$M_{Te,ad} = \frac{1}{2}\beta_i \frac{T_e}{T_i} \left[\left(\frac{\bar{n}_{\text{down}}}{n_0} \right)^{\hat{\gamma}_e - 1} - 1 \right]. \quad (2.27)$$

As shown in Fig. 2.9(d), the ratio of downstream to initial upstream density $\bar{n}_{\text{down}}/n_0$ is nearly independent of the upstream temperature ratio, so that $M_{Te,ad} \propto T_e/T_i$ at fixed β_i . Eq. 2.27 also provides insight into the β_i -dependence of adiabatic heating. It shows that, for a given temperature ratio, the adiabatic heating efficiency would scale linearly with β_i , if the compression ratio $\bar{n}_{\text{down}}/n_0$

²In [Shay et al. \(2014\)](#), the magnetization was $\sigma_w \approx 0.004 - 0.1$. However, as long as $\sigma_w \ll 1$ and all the species stay at non-relativistic temperatures, we expect the reconnection physics to be independent of the flow magnetization.

³Eq. 2.27 assumes that the adiabatic index is constant as electrons pass from upstream to downstream, which is a good approximation when electrons are ultra-relativistic in both regions (so, for high β_i and large T_e/T_i); still, in all the simulations used in Fig. 2.11, we find that the electron adiabatic index changes by no more than $\hat{\gamma}_{e,\text{up}} - \hat{\gamma}_{e,\text{down}} \approx 0.1$. In any case, Eq. 2.27 is presented only for illustrative purposes, and we properly account for the effect of a variable adiabatic index in our calculation of the heating fractions.

were to be fixed. As shown in Fig. 2.9(d), the downstream to upstream density ratio decreases with β_i , approaching unity at high β_i . However, the decrease of $\bar{n}_{\text{down}}/n_0$ with β_i is quite shallow, and insufficient to counteract the linear dependence on β_i in Eq. 2.27. It follows that at low β_i the effect of adiabatic heating is negligible, while at high β_i the role of adiabatic heating can be more important than that of irreversible heating.

This statement can be further justified by considering electron energization in the diffusion region as the main source of irreversible electron heating, following Le et al. (2016). In the diffusion region, the electron energy will increase by $eE_{\text{rec}}\ell_e$, where $E_{\text{rec}} \sim 0.1(v_A/c)B_0$ is the reconnection electric field (assuming a reconnection inflow rate of $\sim 0.1v_A/c$, see Fig. 2.9(a)) and ℓ_e is the distance traveled by electrons along the electric field (along z , in our geometry). For the sake of simplicity, let us now assume that β_i is sufficiently small that $w \sim n_0m_i c^2$ and so $\sigma_w \sim \sigma_i$ (this is the case for $\beta_i \lesssim 0.1$, at our reference magnetization $\sigma_w = 0.1$). The corresponding irreversible heating efficiency can be written in the case $\sigma_w \sim \sigma_i \lesssim 1$ as

$$M_{T_e,\text{irr}} \sim 0.1 \frac{\ell_e}{c/\omega_{pi}} \quad (2.28)$$

which does not depend explicitly on β_i . It follows that, as long as ℓ_e is a weak function of β_i , the adiabatic heating efficiency in Equation 2.27, which scales linearly with β_i , will be unimportant at low β_i , whereas it will dominate over irreversible heating at high β_i .

We remark that Equation 2.28 does not capture a number of important effects. First, by tracking individual particle orbits, we have found that the in-plane components of the electric field, that we have neglected above, can provide a significant contribution to the total electron energization (a comprehensive discussion of the physics of electron heating will be presented elsewhere). Second, we have neglected the β_i -dependence of the reconnection rate. Third, we have assumed $w \sim n_0m_i c^2$,

which is incorrect at high β_i . Fourth, we do not have a direct measure of ℓ_e , which would assess its dependence on the flow conditions. For these reasons, it is likely that the electron irreversible heating will be dependent on β_i .

In fact, the irreversible electron heating efficiency (shown in Fig. 2.11(c)) systematically decreases with β_i , and the trend is largely independent of the initial temperature ratio, apart from the case with $\beta_i = 2$ (rightmost points in Fig. 2.11(c)). Here, the irreversible heating fraction reaches $M_{Te,\text{irr}} \approx 0.03$ for $T_e/T_i = 1$, a factor of ~ 3 larger than for the $\beta_i = 2$ cases with lower temperature ratios, $T_e/T_i = 0.1$ and 0.3 .⁴ We attribute the peculiar behavior of this case to the fact that, among the $m_i/m_e = 25$ simulations presented in Fig. 2.11, the $\beta_i = 2, T_e/T_i = 1$ case is the only one for which the scale separation $(c/\omega_{pi})/(c/\omega_{pe})$ between protons and electrons approaches unity (see Fig. 2.10(c)). For the case $\beta_i = 2, T_e/T_i = 1$ in Fig. 2.11, this statement holds true for both the *upstream* and the *downstream* scale separation, since the reconnection process at high β_i does not appreciably change the plasma thermal content. However, as we further discuss in the next two subsections, where we investigate the dependence of our results on the mass ratio and the magnetization, we find that the necessary and sufficient condition for the electron and proton heating efficiencies to be comparable is that the *downstream* scale separation approaches unity. In retrospect, this is not surprising, since if $(c/\omega_{pi})/(c/\omega_{pe}) \rightarrow 1$ in the downstream, the fluid effectively behaves like an electron-positron plasma.

In Fig. 2.11 (second row of panels), we also explore the β_i -dependence of (d) total, (e) adiabatic, and (f) irreversible proton heating. As before, blue, green, and red points correspond to simulations with upstream T_e/T_i of 0.1, 0.3, and 1, respectively (we change the temperature ratio by varying the electron temperature, while the proton temperature at a given β_i is kept fixed). While the

⁴We have extensively checked this result, finding that it holds regardless of the simulation boundary conditions (periodic or outflow in the x direction, or double periodic; see Appendix 2.B) and the number of computational particles per cell.

initial dimensionless electron temperature in our simulations ranges from non-relativistic to ultra-relativistic values, protons always stay at non-relativistic or trans-relativistic energies, $\theta_i \approx 0.0004 - 0.5$ (this is true in both upstream and downstream). At low β_i , protons are heated more efficiently than electrons, typically by a factor of 2 – 3 at mass ratio $m_i/m_e = 25$ (compare panels (a) and (d), $M_{Te,tot} \approx 0.05$ while $M_{Ti,tot} \approx 0.13$). At larger values of m_i/m_e , the ratio of proton to electron heating is even larger, as we discuss in Sections 2.5.4 and 2.5.6. Once again, the notable exception is the high- β_i case with $\beta_i = 2$ and $T_e/T_i = 1$, where the electron and proton heating fractions are comparable, $M_{Te,tot} \approx 0.06$ and $M_{Ti,tot} \approx 0.08$. Similar to electrons, the irreversible component of proton heating decreases with β_i , and shows only weak dependence on the upstream temperature ratio T_e/T_i (panel (f)). As shown in panel (e), the fractional contribution of adiabatic heating to the total proton heating increases with β_i , as for electrons.

Finally, we show the total particle (i.e., sum of electron and proton) heating, as well as the corresponding adiabatic and irreversible components, in Fig. 2.11(g)-(i). Given that protons are heated more efficiently than electrons, the trends in the bottom row of Fig. 2.11 are primarily controlled by protons (again, with the exception of the case $\beta_i = 2$, $T_e/T_i = 1$). Panel (g) shows that the total particle heating efficiency is ~ 0.15 across all simulations, with a weakly declining trend with increasing β_i . Panels (h) and (i) show that, as discussed for electrons and protons individually, heating in the low- β_i regime is associated with an increase in entropy, while at high β_i it is dominated by adiabatic compression.

While we cast the heating fractions in Fig. 2.11 in terms of temperature differences between upstream and downstream, they may be expressed, alternatively, via differences in internal energy per particle; see Appendix 2.G.

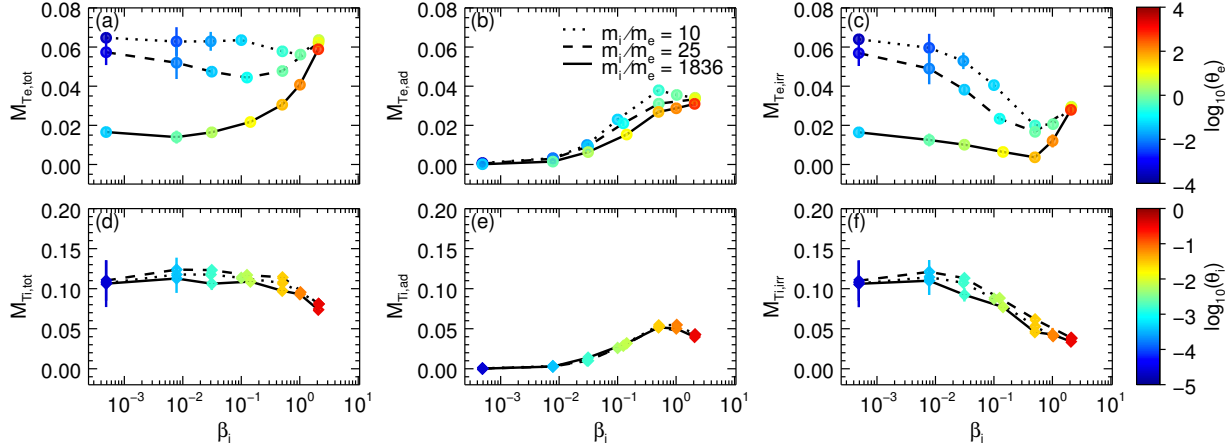


Figure 2.12: Mass ratio m_i/m_e dependence of heating efficiencies; (a): electron total, $M_{Te,tot}$; (b): electron adiabatic, $M_{Te,ad}$; (c): electron irreversible, $M_{Te,irr}$; (d): proton total, $M_{Ti,tot}$; (e): proton adiabatic, $M_{Ti,ad}$; (f): proton irreversible, $M_{Ti,irr}$, for $T_e/T_i = 1$ simulations with mass ratios $m_i/m_e = 10$ (dotted), 25 (dashed), and 1836 (solid); the legend is located in the upper part of panel (b). Points in panels (a)–(c) are colored according to electron dimensionless temperature in the upstream (color bar is to the right of (c)), and points in (d)–(f) according to proton dimensionless temperature in the upstream (color bar is to the right of (f)). The irreversible heating is remarkably independent of mass ratio at high $\beta_i (= 2)$, while at low β_i , the irreversible electron heating efficiency decreases with increasing mass ratio.

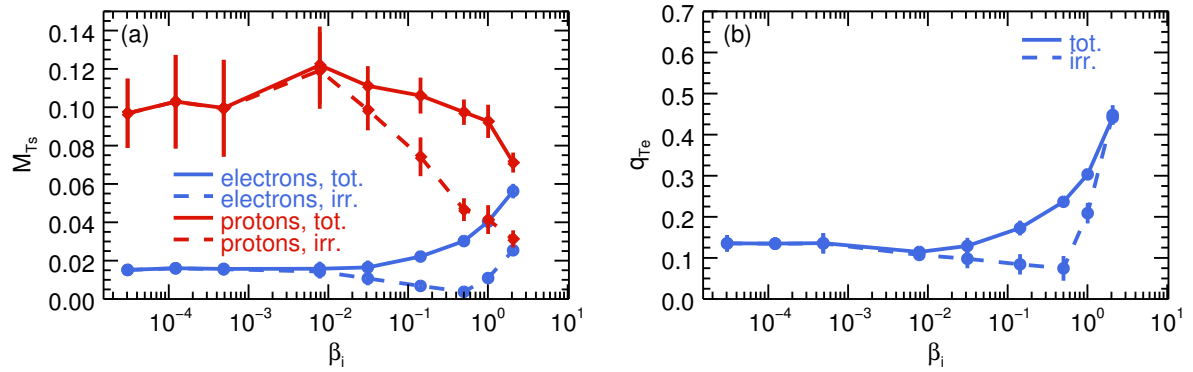


Figure 2.13: (a): β_i -dependence of electron total heating $M_{Te,tot}$ (solid blue), electron irreversible heating $M_{Te,irr}$ (dashed blue), proton total heating $M_{Ti,tot}$ (solid red), and proton irreversible heating $M_{Ti,irr}$ (dashed red); (b): β_i -dependence of electron-to-overall total heating ratio $q_{Te,tot}$ (solid blue) and electron-to-overall irreversible heating ratio $q_{Te,irr}$ (dashed blue), as defined in Eqs. 2.29, 2.30. Here, $\sigma_w = 0.1$, $T_e/T_i = 1$, and $m_i/m_e = 1836$.

2.5.4 Dependence of particle heating on m_i/m_e

We have extended our results up to the physical mass ratio $m_i/m_e = 1836$, and in this section we focus on the case with $T_e/T_i = 1$ (runs with $\sigma_w = 0.1$ and unequal temperature ratios are presented in Section 2.5.6). The separation between the electron scale c/ω_{pe} and the proton scale c/ω_{pi} is regulated by Eq. 2.5. For non-relativistic particles, the ratio of proton to electron skin depth is $\sqrt{m_i/m_e} \sim 40$, so that a large simulation domain is required to properly capture the proton physics. However, in the trans-relativistic regime of our simulations, the particles can approach (or exceed, in the case of electrons) relativistic temperatures. Here, the effective increase in electron inertia can bring the ratio of proton to electron skin depth close to unity (see Eq. 2.5). This condition holds, for example, in simulations **C[3]**, **C[4]**, and **B[4]**, when the mass ratio is increased to $m_i/m_e = 1836$ at fixed σ_w and β_i .

We show in Fig. 2.12 the dependence of total (a), adiabatic (b), and irreversible (c) electron heating on β_i , for mass ratios $m_i/m_e = 10, 25$, and 1836 . We fix the magnetization $\sigma_w = 0.1$, and the temperature ratio $T_e/T_i = 1$; the legend is shown in the upper part of panel (b). The points are colored according to the dimensionless temperature of upstream electrons (the corresponding colorbar is to the right of panel (c)), ranging from non-relativistic ($\theta_e \sim 10^{-4}$) to ultra-relativistic ($\theta_e \sim 10^3$) values. In agreement with earlier studies of non-relativistic reconnection by Dahlin et al. (2014) and Le et al. (2016), we find that the total electron heating efficiency at low β_i is a decreasing function of mass ratio. For the realistic mass ratio, at low β_i the total heating fraction $M_{Te,tot} \approx 0.016$ is in good agreement with the observed value in the magnetopause, $M_{Te,tot} = 0.017$ (Phan et al., 2013). At $\beta_i = 2$, the electron heating efficiency is remarkably insensitive to the mass ratio, with $M_{Te,tot} \approx 0.06$. As we have anticipated above, in this case the upstream and downstream skin depths of protons and electrons are comparable (once we account for the effects of relativistic inertia), so the physics should resemble that of an electron-positron plasma, regardless

of the mass ratio. The adiabatic heating efficiency (panel (b)) shows only a weak dependence on mass ratio, in agreement with Eq. 2.27. For realistic mass ratios, electron heating is governed by irreversible processes at low β_i , adiabatic heating dominates at intermediate $\beta_i \sim 0.1 - 1$, while the two components equally contribute at high $\beta_i \sim 2$.

We show the β_i -dependence of the proton heating fractions $M_{Ti,tot}$, $M_{Ti,ad}$, and $M_{Ti,irr}$ in panels (d), (e), and (f). The points are colored according to the upstream dimensionless proton temperature, θ_i (the scale is to the right of panel (f)). The upstream proton temperatures are non-relativistic or trans-relativistic, with $\theta_i \lesssim 0.5$. At fixed σ_w and β_i , the initial proton temperature stays the same, when we vary the mass ratio (as opposed to the electron temperature, which increases with mass ratio). So, the proton heating efficiencies are expected to remain unchanged, as long as the box size L_x is sufficiently large (in units of the proton skin depth c/ω_{pi}) to capture the physics of proton heating. In the bottom row of Fig. 2.12, the proton heating fractions $M_{Ti,tot}$, $M_{Ti,ad}$, and $M_{Ti,irr}$ are nearly independent of the mass ratio, which demonstrates that even for the realistic mass ratio, the box used here is sufficiently large to capture the physics of proton heating (and even more so, of electron heating). The results discussed in Section 2.5.3 for $m_i/m_e = 25$ and $T_e/T_i = 1$ are therefore still valid here: proton heating is dominated by irreversible processes at low β_i , whereas irreversible and adiabatic components equally contribute at high β_i ; the irreversible heating efficiency of protons is a decreasing function of β_i ; protons are heated more efficiently than electrons (although the total proton-to-electron heating ratio for $m_i/m_e = 1836$ is ~ 7 at low β_i , larger than the value measured for $m_i/m_e = 25$, since the electron heating efficiency decreases with mass ratio); the heating fractions of the two species approach comparable values at $\beta_i = 2$, with $M_{Ti,tot} \approx 0.08$ and $M_{Te,tot} \approx 0.06$.

In Fig. 2.13(a), we directly compare the β_i -dependence of electron and proton heating fractions $M_{Te,tot}$ (solid blue), $M_{Te,irr}$ (dashed blue), $M_{Ti,tot}$ (solid red), and $M_{Ti,irr}$ (dashed red) for $m_i/m_e =$

1836 , $\sigma_w = 0.1$, and $T_e/T_i = 1$.⁵ As anticipated above, the proton and electron total and irreversible heating fractions differ roughly by a factor of ~ 7 at low β_i , but they approach a similar value at $\beta_i = 2$ (≈ 0.03 for the irreversible component and ≈ 0.06 for the total). In Fig. 2.13(b), we show the β_i -dependence of the ratio of electron-to-overall total heating ratio (solid blue),

$$q_{Te,\text{tot}} = \frac{M_{Te,\text{tot}}}{M_{Te,\text{tot}} + M_{Ti,\text{tot}}}, \quad (2.29)$$

and similarly, the ratio of electron-to-overall irreversible heating ratio (dashed blue),

$$q_{Te,\text{irr}} = \frac{M_{Te,\text{irr}}}{M_{Te,\text{irr}} + M_{Ti,\text{irr}}}. \quad (2.30)$$

At low β_i , the electron-to-overall total heating ratio is $q_{Te,\text{tot}} \approx 0.14$, and it increases with β_i up to $q_{Te,\text{tot}} \approx 0.45$ at $\beta_i = 2$. The corresponding ratio of the irreversible components $q_{Te,\text{irr}}$ is comparable to $q_{Te,\text{tot}}$ at both low β_i (where adiabatic heating is negligible) and $\beta_i = 2$ (where adiabatic and irreversible contributions are similar), but for intermediate β_i we find that $q_{Te,\text{irr}}$ can be as low as 0.07 , smaller than $q_{Te,\text{tot}}$ by up to a factor of ≈ 3 .

2.5.5 Dependence of particle heating on magnetization

In the previous sections, we have focused on the case $\sigma_w = 0.1$; in Fig. 2.14, we show the β_i -dependence of the heating efficiencies for a suite of simulations with $\sigma_w = 0.1, 0.3, 1, 3$, and 10 .⁶ We fix the temperature ratio $T_e/T_i = 1$ and the mass ratio $m_i/m_e = 1836$. The panels are similar to those in Fig. 2.12: (a), (b), and (c) show the electron heating fractions $M_{Te,\text{tot}}$, $M_{Te,\text{ad}}$, and $M_{Te,\text{irr}}$;

⁵The error bars in Fig. 2.13(a) are larger for protons than electrons (for electrons, they are smaller than the size of the plot symbols), but the fractional error is the same. Additionally, the error bars are larger at low β_i . As described in 2.5.2, this results from the frequent formation of secondary islands at low β_i .

⁶At high σ_w , the rate of secondary island production is enhanced (Sironi et al., 2016). In the simulations with $\sigma_w = 1, 3, 10$, we employ outflow boundary conditions in order to evolve the system to longer times. This allows us to average the downstream quantities in the reconnection exhausts over a longer timespan, and obtain more reliable estimates.

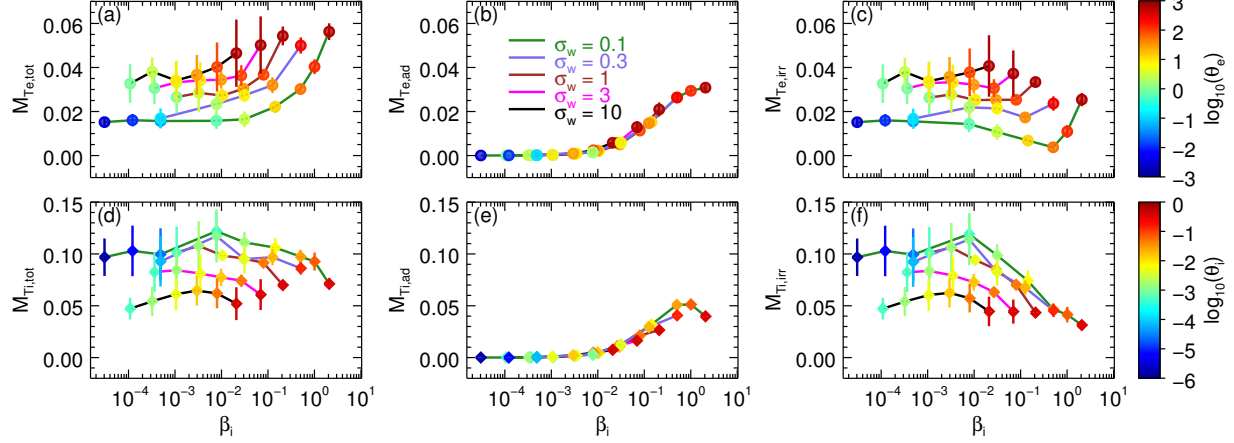


Figure 2.14: Dependence of the heating efficiencies on the magnetization σ_w (normalized to the enthalpy density), with a layout similar to that of Fig. 2.12; (a): electron total, $M_{Te,tot}$; (b): electron adiabatic, $M_{Te,ad}$; (c): electron irreversible, $M_{Te,irr}$; (d): proton total, $M_{Ti,tot}$; (e): proton adiabatic, $M_{Ti,ad}$; (f): proton irreversible, $M_{Ti,irr}$. We fix $T_e/T_i = 1$ and $m_i/m_e = 1836$, and vary the magnetization $\sigma_w = 0.1$ (green), 0.3 (purple), 1 (brown), 3 (magenta), 10 (black); the legend is located in the upper part of panel (b). Points in panels (a)–(c) are colored according to $\theta_{e,up}$ (color bar is to the right of (c)), and points in (d)–(f) according to $\theta_{i,up}$ (color bar is to the right of (f)).

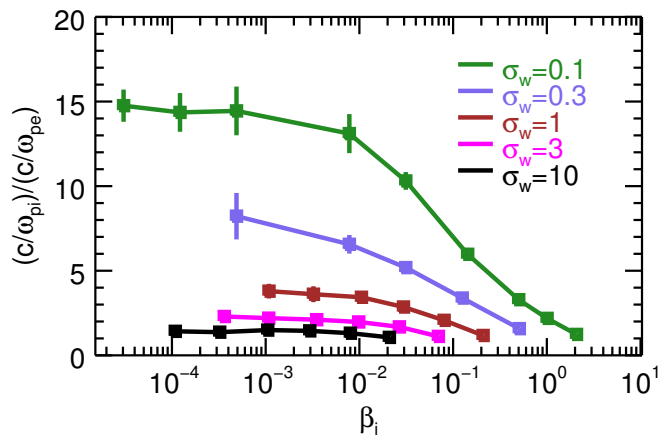


Figure 2.15: β_i -dependence of downstream proton-to-electron skin depth ratio, $(c/\omega_{pi})/(c/\omega_{pe})$ (see Eq. 2.5), for magnetizations $\sigma_w = 0.1$ (green), 0.3 (purple), 1 (brown), 3 (magenta), and 10 (black). For these simulations, the upstream electron-to-proton temperature ratio is $T_e/T_i = 1$, and $m_i/m_e = 1836$.

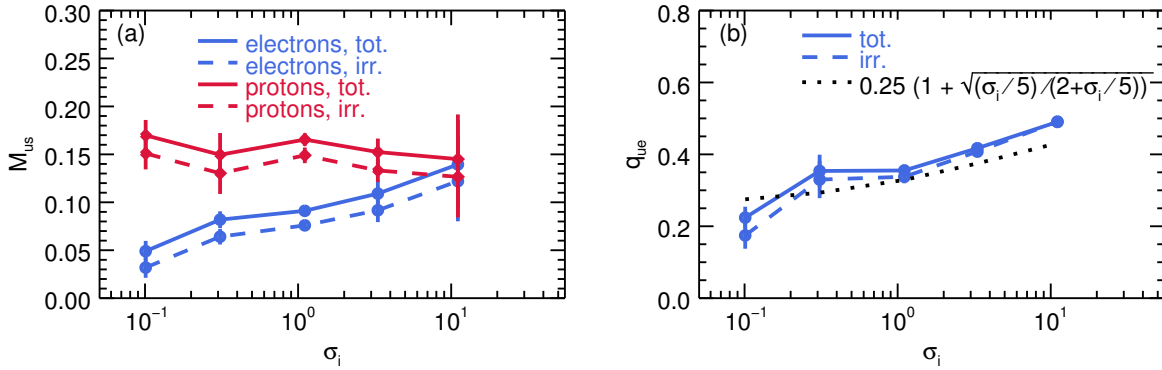


Figure 2.16: (a): Dependence on the magnetization σ_i (normalized to rest mass energy density) of electron total heating efficiency $M_{ue,\text{tot}}$ (solid blue), irreversible heating efficiency $M_{ue,\text{irr}}$ (dashed blue), proton total heating efficiency $M_{ui,\text{tot}}$ (solid red), and proton irreversible heating efficiency $M_{ui,\text{irr}}$ (dashed red). (b): Dependence on the magnetization σ_i of the electron-to-overall heating ratio $q_{ue,\text{tot}}$ (solid blue) as in Eq. 2.31, electron-to-overall irreversible heating ratio $q_{ue,\text{irr}}$ (dashed blue) as in Eq. 2.32, and empirical formula Eq. 2.33 (dotted black) obtained by Werner et al. (2016) in the case $\beta_i = 0.01$. Here, $\beta_i \approx 0.03$, $T_e/T_i = 1$, and $m_i/m_e = 1836$.

(d), (e), and (f) show the proton heating fractions $M_{Ti,\text{tot}}$, $M_{Ti,\text{ad}}$, and $M_{Ti,\text{irr}}$. The legend is in panel (b): green, purple, brown, magenta, and black curves connect the points having $\sigma_w = 0.1, 0.3, 1, 3$, and 10, respectively, to guide the eye. The points of panels (a)–(c) are colored according to the upstream dimensionless electron temperature θ_e , as indicated by the color bar to the right of panel (c). Similarly, in panels (d)–(f) the points are colored according to the upstream dimensionless proton temperature θ_i , as indicated by the color bar to the right of panel (f). For fixed β_i , T_e/T_i , and m_i/m_e , an increase in magnetization leads to an increase in the upstream dimensionless temperature of both electrons and protons, which can be seen by comparing the colors of data points in panel (a) or (d) at fixed β_i .

We note that the data points in Fig. 2.14 extend up to a maximum value of β_i that depends on σ_w . For our choice of defining the magnetization using the enthalpy density, rather than the rest-mass energy density, the ion β_i cannot exceed $\beta_{i,\text{max}} \sim 1/4\sigma_w$. For each value of σ_w , the points with the highest value of β_i are also those for which the proton-to-electron scale separation ratio $(c/\omega_{pi})/(c/\omega_{pe})$ is the smallest (see Fig. 2.15). We find that in the limit $\beta_i \rightarrow \beta_{i,\text{max}}$, the

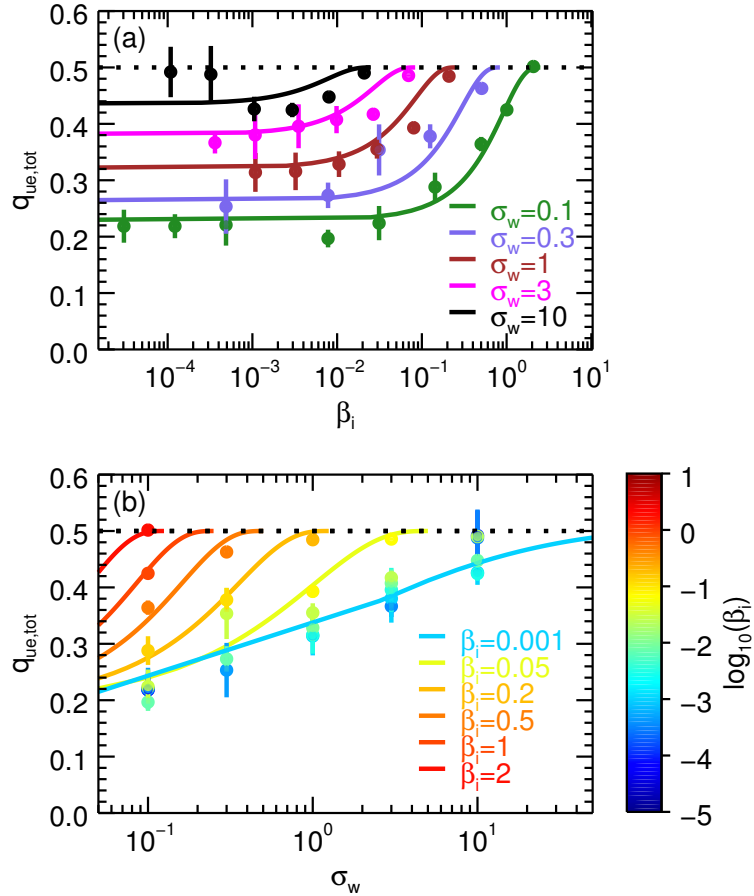


Figure 2.17: Comparison of the electron-to-overall heating ratio $q_{ue,tot}$ between our simulations with $m_i/m_e = 1836$ and $T_e/T_i = 1$ (filled circles with error bars) and the best fitting formula in Eq. 2.34 (solid curves). We show the dependence on (a) plasma- β_i and (b) magnetization σ_w . In panel (a), the different colors represent magnetizations $\sigma_w = 0.1$ (green), 0.3 (purple), 1 (brown), 3 (magenta), and 10 (black). In panel (b), the color coding of the curves is indicated in the legend (from cyan to red for increasing β_i), while the color of the filled points refers to the colorbar on the right. In both panels, the black dotted line at $q_{ue,tot} = 0.5$ shows the limit of comparable heating efficiencies between electrons and protons, expected when $\beta_i \rightarrow \beta_{i,\max}$ (regardless of σ_w) or $\sigma_w \gg 1$ (independently of β_i).

total electron heating efficiency shows a characteristic upturn (panel (a)), with a typical value $M_{Te,tot} \approx 0.05$ that is nearly independent of σ_w . In the low- β_i regime, the electron total heating efficiency approaches a σ_w -dependent plateau, with higher σ_w yielding larger electron efficiencies (panel (a)). The opposite holds for protons: higher magnetizations give smaller proton heating efficiencies (panel (d)). Indeed, for $\sigma_w = 10$ the electron and proton efficiencies are comparable in the whole range of β_i we have explored, in agreement with the results by Sironi et al. (2015).

As anticipated in Section 2.5.3, we find that the necessary and sufficient condition for having comparable electron and proton heating efficiencies is that the separation between the electron and proton scales in the downstream be of order unity (or equivalently, that the two species be relativistically hot, with comparable temperatures). As shown in Fig. 2.15, this can be achieved in two ways: (i) at high σ_w , regardless of β_i , the reconnection process transfers so much magnetic energy to the particles that both species become relativistically hot, with comparable temperatures; (ii) at low σ_w and in the limit $\beta_i \rightarrow \beta_{i,max}$, both electrons and protons already start relativistically hot in the upstream region (and more so, will be relativistically hot in the downstream).

Most of the σ_w -dependences that we have now presented for the total heating efficiencies $M_{Te,tot}$ and $M_{Ti,tot}$ also apply to the irreversible components $M_{Te,irr}$ and $M_{Ti,irr}$, since the adiabatic contribution is independent of the magnetization, at fixed β_i (see Eq. 2.27). However, since the magnetization affects the efficiency of irreversible heating at fixed β_i , while the adiabatic component remains the same, this can lead to a significant change in the relative contributions of irreversible and adiabatic heating. This can be seen, for example, at $\beta_i \approx 0.5$. For $\sigma_w = 0.1$, $M_{Te,irr}/M_{Te,tot} \approx 0.1$, whereas at $\sigma_w = 0.3$, we find $M_{Te,irr}/M_{Te,tot} \approx 0.5$.

To connect with the recent work of Werner et al. (2016), we show in Fig. 2.16 the dependence of electron and proton heating on the magnetization σ_i , defined with the rest-mass energy density (see Eq. 2.2). We fix temperature ratio $T_e/T_i = 1$, mass ratio $m_i/m_e = 1836$, and $\beta_i \approx 0.03$ (which

is close to the upstream plasma β_i employed in Werner et al. (2016), $\beta_i = 0.01$. In panel (a), we show the σ_i -dependence of the electron total (solid blue), electron irreversible (dashed blue), proton total (solid red), and proton irreversible (dashed red) heating fractions, phrased in terms of internal energy as in Werner et al. (2016), $M_{ue,tot}$, $M_{ue,irr}$, $M_{ui,tot}$, and $M_{ui,irr}$ (see Eqs. 2.15, 2.17). As σ_i increases, the downstream scale separation between protons and electrons gets reduced (see Fig. 2.15), and the two species approach comparable heating efficiencies (whereas the two differ by a factor of ~ 3 at low magnetization). This holds for both the total efficiencies $M_{ue,tot}$ and $M_{ui,tot}$ and the irreversible components $M_{ue,irr}$ and $M_{ui,irr}$, since the amount of adiabatic heating at fixed β_i does not depend on σ_w .

This is further illustrated in Fig. 2.16(b), where we show the σ_i -dependence of the electron-to-overall total heating fraction, phrased in terms of internal energy (solid blue),

$$q_{ue,tot} = \frac{M_{ue,tot}}{M_{ue,tot} + M_{ui,tot}}, \quad (2.31)$$

and the electron-to-overall irreversible heating ratio (dashed blue),

$$q_{ue,irr} = \frac{M_{ue,irr}}{M_{ue,irr} + M_{ui,irr}}. \quad (2.32)$$

Blue circles show the results of our simulations, and the black dotted line indicates the empirical formula suggested by Werner et al. (2016),

$$q_{ue,emp} = \frac{1}{4} \left(1 + \sqrt{\frac{\sigma_i/5}{2 + \sigma_i/5}} \right) \quad (2.33)$$

We find reasonable agreement between this empirical formula and our simulations, for $\beta_i \approx 0.03$. For low values of the magnetization, $q_{ue,tot} \approx q_{ue,irr} \approx 0.25$, but as σ_i increases toward the ultra-

relativistic limit, $q_{ue,\text{tot}}$ and $q_{ue,\text{irr}}$ approach ≈ 0.5 , i.e., electrons and protons are heated with comparable efficiencies. However, Fig. 2.14 shows that, at fixed magnetization, the heating efficiencies depend on β_i , a trend which cannot be properly captured by the empirical formula of Werner et al. (2016).

We then propose the following formula, which captures the dependence of the electron-to-overall heating ratio $q_{ue,\text{tot}}$ on both magnetization σ_w and proton β_i :

$$q_{ue,\text{fit}} = \frac{1}{2} \exp \left[\frac{-(1 - \beta_i/\beta_{i,\text{max}})^{3.3}}{1 + 1.2 \sigma_w^{0.7}} \right], \quad (2.34)$$

where $\beta_i \leq \beta_{i,\text{max}} = 1/4\sigma_w$. The formula in Eq. 2.34 has two desirable, and physically motivated, features. First, for $\beta_i \rightarrow \beta_{i,\text{max}}$, the electron-to-overall heating ratio approaches 0.5, independently of the magnetization. Second, for $\sigma_w \gg 1$, $q_{ue,\text{tot}} = 0.5$, regardless of β_i . In both these limits, the scale separation between electrons and protons in the downstream will be of order unity (as we have discussed above), which we have demonstrated is a necessary and sufficient condition for comparable heating efficiencies between electrons and protons.

In Fig. 2.17, we compare Eq. 2.34 to the results of simulations with $m_i/m_e = 1836$ and $T_e/T_i = 1$ (this is the same set of simulations presented earlier in this section, as well as in Section 2.5.4). In Fig. 2.17(a), we show the β_i -dependence of the electron-to-overall heating ratio $q_{ue,\text{tot}}$ for a range of σ_w (see the legend). The simulation results are shown by solid filled circles, while solid lines are based on Eq. 2.34. The curves are plotted up to the maximum allowed value of β_i , namely $\beta_{i,\text{max}} = 1/4\sigma_w$. The black dotted line at $q_{ue,\text{tot}} = 0.5$ shows the limit of comparable heating efficiencies for electrons and protons, which will be reached as $\beta_i \rightarrow \beta_{i,\text{max}}$, independently of σ_w . We find that both the simulation data and the fitting formula in Eq. 2.34 asymptote to a constant value for $\beta_i \ll \beta_{i,\text{max}}$, with smaller heating ratios at lower σ_w . In the non-relativistic limit $\sigma_w \ll 1$,

our formula prescribes that $q_{ue,\text{fit}} \rightarrow 0.18$, not very different from the value $q_{ue,\text{fit}} \approx 0.22$ obtained for $\sigma_w = 0.1$. This is consistent with the expectation that in the non-relativistic regime $\sigma_w \ll 1$, the heating efficiencies will be independent from the magnetization.

In Fig. 2.17(b), we show the dependence of the electron-to-overall heating ratio on the magnetization σ_w , for a range of β_i . The simulations results are shown by filled solid circles, which are colored according to the value of β_i in the upstream (the color scale is located to the right of Fig. 2.17(b)). We select a few representative values of β_i and plot the corresponding predictions based on Eq. 2.34 with the solid curves (see the legend in the plot). The curves are plotted up to $\sigma_{w,\text{max}}$, which for a fixed β_i is given by $\sigma_{w,\text{max}} \sim 1/4\beta_i$. In summary, Figs. 2.17(a) and (b) show that our proposed formula (Eq. 2.34) properly captures the magnetization and plasma β_i dependence of the electron-to-overall heating ratio over the whole range of σ_w and β_i explored in this work.

2.5.6 Dependence of particle heating on T_e/T_i for $m_i/m_e = 1836$

In Fig. 2.18, we present the dependence of electron and proton heating efficiencies on the proton beta β_i and the temperature ratio T_e/T_i for the realistic mass ratio $m_i/m_e = 1836$ (the figure layout is the same as in Fig. 2.11, where we had employed a reduced mass ratio $m_i/m_e = 25$). We fix $\sigma_w = 0.1$. Even at the realistic mass ratio, the conclusions drawn in the reduced mass ratio case $m_i/m_e = 25$ (see Section 2.5.3) still hold: electron and proton heating at low β_i is dominated by irreversible processes, while heating in the high- β_i regime is mostly a result of adiabatic compression; the irreversible component of electron heating is independent of T_e/T_i at $\beta_i \lesssim 1$ (Fig. 2.18 (c)); the proton irreversible heating shows only a weak dependence on temperature ratio (Fig. 2.18 (f)); protons are heated more efficiently than electrons (compare the top and middle rows).

For both electrons and protons, the adiabatic heating efficiencies for $m_i/m_e = 1836$ (Figs. 2.18(b) and (e)) are similar to those of the reduced mass ratio case. In fact, according to Eq. 2.27, the

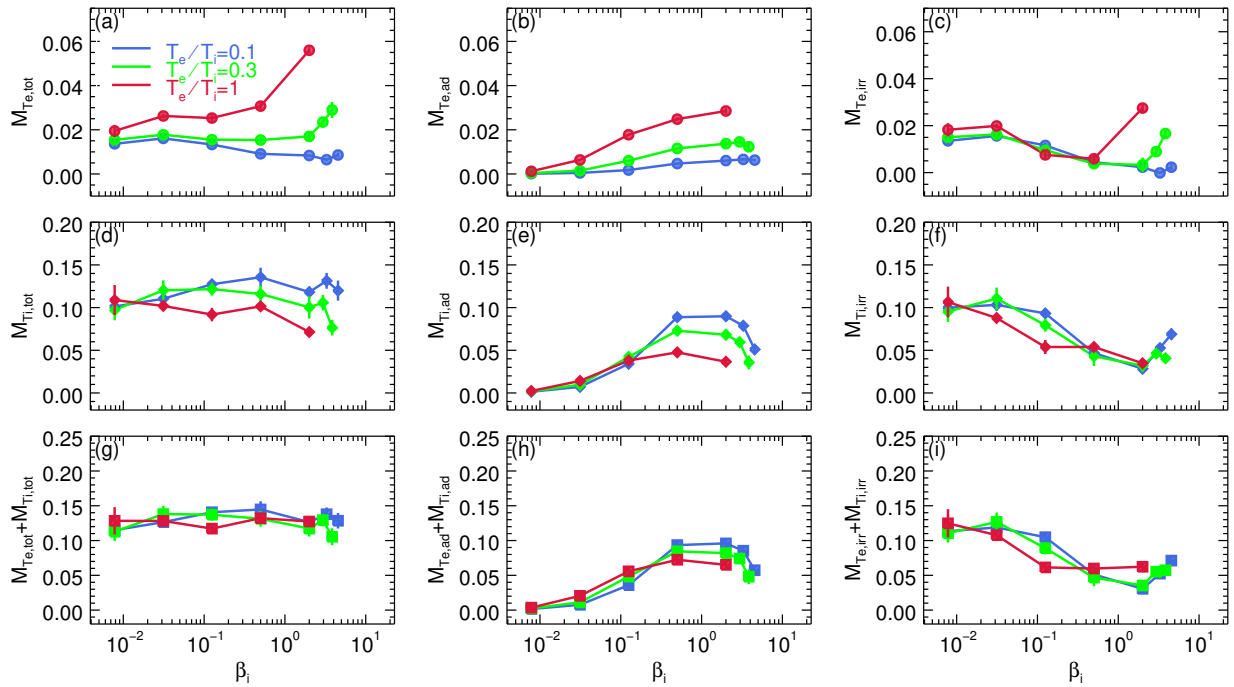


Figure 2.18: For mass ratio $m_i/m_e = 1836$, magnetization $\sigma_w = 0.1$ and upstream temperature ratios $T_e/T_i = 0.1$ (blue), 0.3 (green), and 1 (red), we present the β_i -dependence of heating efficiencies; (a): electron total, $M_{Te,tot}$; (b): electron adiabatic, $M_{Te,ad}$; (c): electron irreversible, $M_{Te,irr}$; (d): proton total, $M_{Ti,tot}$; (e): proton adiabatic, $M_{Ti,ad}$; (f): proton irreversible, $M_{Ti,irr}$; (g): electron and proton total, $M_{Te,tot} + M_{Ti,tot}$; (h): electron and proton adiabatic, $M_{Te,ad} + M_{Ti,ad}$; (i): electron and proton irreversible, $M_{Te,irr} + M_{Ti,irr}$.

adiabatic heating efficiency is independent of mass ratio.⁷ For protons, the adiabatic heating efficiency decreases at $\beta_i \gtrsim 2$; this is largely an effect of the decrease in the adiabatic index, as the protons transition from non-relativistic to relativistic temperatures.

For $m_i/m_e = 1836$, the irreversible heating of protons at low β_i is a factor of $\sim 5 - 7$ greater than that of electrons; in the $m_i/m_e = 25$ case, the ratio of proton-to-electron irreversible heating was smaller, $\sim 2 - 3$. As in the reduced mass ratio case, the simulation with $\beta_i = 2$ and $T_e/T_i = 1$ shows a sharp increase in irreversible electron heating as compared to the decreasing trend observed at lower β_i (Fig. 2.18 (c)), and the heating efficiencies of the two species become comparable. As we argued in Section 2.5.5, the electron and proton heating efficiencies are about equal if and only if the downstream scale separation is of order unity. Even for the highest values of β_i that we can explore (≈ 3.9 for $T_e/T_i = 0.1$, and ≈ 4.6 for $T_e/T_i = 0.3$), this condition is not realized for smaller temperature ratios $((c/\omega_{pi})/(c/\omega_{pe})) \gtrsim 3.2$ for $T_e/T_i = 0.1$, and $((c/\omega_{pi})/(c/\omega_{pe})) \gtrsim 1.8$ for $T_e/T_i = 0.3$), which explains why — despite the upturn in electron heating efficiency at high β_i (Fig. 2.18 (c)) — the ratio of irreversible proton to electron heating for $T_e/T_i = 0.1$ and 0.3 remains larger than unity.

2.6 Summary and discussion

In this work, we have presented the results of a series of 2D fully-kinetic PIC simulations to explore electron and proton heating by magnetic reconnection in the trans-relativistic regime. Here, protons are typically non-relativistic, yet electrons can be moderately relativistic or even ultra-relativistic. We vary the flow magnetization σ_w , the proton β_i and the electron-to-proton temperature ratio T_e/T_i , extending our results up to the physical mass ratio $m_i/m_e = 1836$.

We show that heating in the high- β_i regime is primarily dominated by adiabatic compression, while for low β_i the heating is genuine, in the sense that it is associated with an increase in entropy.

⁷While Eq. 2.27 is written for electrons, an analogous equation holds for the adiabatic heating of protons, if we replace $\beta_i T_e/T_i \rightarrow \beta_i$ and $\hat{\gamma}_e \rightarrow \hat{\gamma}_i$.

At our fiducial $\sigma_w = 0.1$, we find that for $\beta_i \lesssim 1$ the irreversible heating efficiency is independent of T_e/T_i (which we vary from 0.1 up to 1), for both electrons and protons. For $T_e/T_i = 1$, the fraction of inflowing magnetic energy converted to electron irreversible heating at realistic mass ratios decreases from $\sim 1.6\%$ down to $\sim 0.2\%$ as β_i ranges from $\beta_i \sim 10^{-2}$ up to $\beta_i \sim 0.5$, but then it increases up to $\sim 3\%$ as β_i approaches ~ 2 . Protons are heated much more efficiently than electrons at low and moderate β_i (by a factor of ~ 7), whereas the electron and proton heating efficiencies become comparable at $\beta_i \sim 2$ if $T_e/T_i = 1$. We find that comparable heating efficiencies between electrons and protons are achieved when the scale separation between the two species in the reconnection exhaust approaches unity, so that the electron-proton plasma effectively resembles an electron-positron fluid. This occurs at high β_i for low magnetizations, or regardless of β_i at high magnetizations (i.e., in the regime $\sigma_w \gg 1$ of ultra-relativistic reconnection). We propose a fitting formula (Eq. 2.34) that captures the magnetization and plasma- β_i dependence of the electron-to-overall heating ratio over the whole range of σ_w and β_i explored in this work.

The low- and high- β_i cases differ with respect to secondary island formation. The formation of secondary islands is suppressed at high β_i , which leads to a homogeneous reconnection outflow. Secondary islands occur frequently at low β_i and high magnetizations.

We also measure the inflow speed for our fiducial magnetization $\sigma_w = 0.1$, finding that it decreases from $v_{\text{in}}/v_A \approx 0.08$ down to 0.04 as β_i ranges from $\beta_i \sim 10^{-2}$ up to $\beta_i \sim 2$ (here, v_A is the Alfvén speed). Similarly, the outflow speed saturates at the Alfvén velocity for low β_i , but it decreases with increasing β_i down to $v_{\text{out}}/v_A \approx 0.7$ at $\beta_i \sim 2$. The inflow (outflow, respectively) speed is independent of T_e/T_i at low β_i , with only a minor tendency for lower (higher, respectively) speeds at larger T_e/T_i in the high- β_i regime.

This investigation provides important insights into the physics of low-luminosity accretion flows, such as the accretion disk of Sgr A*. Collisionless accretion flows are often assumed to be two-

temperature, and our results indeed show that in the trans-relativistic regime relevant to hot accretion flows and accretion disk coronae, magnetic reconnection preferentially heats protons more than electrons. Our results — and in particular, our fitting formula in Eq. 2.34 — can be used to provide general relativistic MHD simulations of accretion flows with the sub-grid physics of energy partition between electrons and protons (Ressler et al., 2015, 2017b; Sadowski et al., 2017). This ingredient is of fundamental importance in producing emission models that can be compared with the forthcoming observations by the Event Horizon Telescope (Doeleman et al., 2008).

To conclude, we note a few lines of investigation that have not been considered in the current work. First, we limited our focus to the case of symmetric, anti-parallel reconnection. The more general case of guide-field reconnection will be a topic of future investigation. Second, while we have provided a quantitative description of energy partition between electrons and protons, we have not addressed the question of the underlying heating mechanism. A detailed study of the heating mechanism is deferred to future work. Lastly, we have focused on thermal heating, as opposed to nonthermal acceleration. The dependence of nonthermal acceleration efficiency on magnetization is the focus of Werner et al. (2016), though the dependence on β_i and T_e/T_i remains unexplored.

Acknowledgements

This work is supported in part by NASA via the TCAN award grant NNX14AB47G and by the Black Hole Initiative at Harvard University, which is supported by a grant from the Templeton Foundation. LS acknowledges support from DoE DE-SC0016542, NASA Fermi NNX16AR75G, NSF ACI-1657507, and NSF AST-1716567. The simulations were performed on Habanero at Columbia, on the BHI cluster at the Black Hole Initiative, and on NASA High-End Computing (HEC) resources. The authors acknowledge computational support from NSF via XSEDE resources (grants TG-AST80026N and TG-AST120010).

2.A Convergence with respect to domain size

For most of the simulations presented in the main body of this work, we employ a domain size of $L_x \approx 4000 c/\omega_{pe}$. However, as we demonstrate in this appendix, the heating efficiencies are insensitive to the domain size. While we have extensively checked for convergence with boxes ranging in size from $L_x \approx 500 c/\omega_{pe}$ up to $L_x \approx 5000 c/\omega_{pe}$, we focus here on a low- β_i case and a high- β_i case, and compare domains of size $L_x \approx 2000 c/\omega_{pe}$ and $L_x \approx 4000 c/\omega_{pe}$.

We show in Fig. 2.19 the electron heating fractions $M_{Te,tot}$, $M_{Te,ad}$, $M_{Te,irr}$ (panels (a), (b), and (c)) and proton heating fractions $M_{Ti,tot}$, $M_{Ti,ad}$, $M_{Ti,irr}$ (panels (d), (e), and (f)). Green circles indicate simulations with $L_x \approx 2000 c/\omega_{pe}$, and blue triangles $L_x \approx 4000 c/\omega_{pe}$. The comparison is performed for two cases: $\beta_i = 0.0078$, $T_e/T_i = 0.1$ and $\beta_i = 2$, $T_e/T_i = 1$. For both the low- and high- β_i simulations, $\sigma_w = 0.1$ and $m_i/m_e = 25$. For each pair of simulations (at low and high β_i), the downstream and upstream dimensionless temperatures that enter into the heating fractions are measured at the same physical distance (in units of the electron skin depth) downstream of the central X-point. The electron and proton heating fractions show minimal dependence on the box size.

In Fig. 2.20, we show — for box sizes $L_x \approx 2000 c/\omega_{pe}$ (green) and $L_x \approx 4000 c/\omega_{pe}$ (blue) — the spatial profiles along the outflow direction (i.e., along x , and averaged along y in the cells identified by Eq. 2.7 as belonging to the reconnection downstream) of: (a) dimensionless electron temperature θ_e for $\beta_i = 0.0078$, $T_e/T_i = 0.1$; (b) dimensionless proton temperature θ_i for $\beta_i = 0.0078$, $T_e/T_i = 0.1$; (c) dimensionless electron temperature θ_e for $\beta_i = 2$, $T_e/T_i = 1$; (d) dimensionless proton temperature θ_i for $\beta_i = 2$, $T_e/T_i = 1$. The simulations shown in Fig. 2.20 correspond to the same simulations presented in Fig. 2.19. The dimensionless temperature profiles are shown at $t \approx 1 t_A$; this corresponds to $t \approx 6900 \omega_{pe}^{-1}$ for $L_x \approx 2000 c/\omega_{pe}$, and to $t \approx 14000 \omega_{pe}^{-1}$ for $L_x \approx 4000 c/\omega_{pe}$. The horizontal axes range from $x \approx -700 c/\omega_{pe}$ to $+700 c/\omega_{pe}$, which accounts for most of the

smaller box, but only a fraction of the larger one. For low β_i , the region used for our measurements is located at $x \approx \pm 630 c/\omega_{pe}$, whereas it is at $x \approx \pm 350 c/\omega_{pe}$ for high β_i ; in each case, the chosen distance is far enough from the central X-point that the temperature profiles attain a quasi-uniform value, and far enough from the domain boundaries to be unaffected by the primary island (Section 2.4).

In Figs. 2.20(a) and (b), which correspond to the low- β_i case, the dimensionless temperature profiles show similar spatial dependence within $x \approx \pm 630 c/\omega_{pe}$, and for the high- β_i profiles shown in (c) and (d), the temperatures agree within $x \approx \pm 350 c/\omega_{pe}$. For the high- β_i case, the large and small boxes show some discrepancy beyond $x \approx \pm 400 c/\omega_{pe}$, which is an effect of the large primary island extending from the domain boundary into the outflow region.

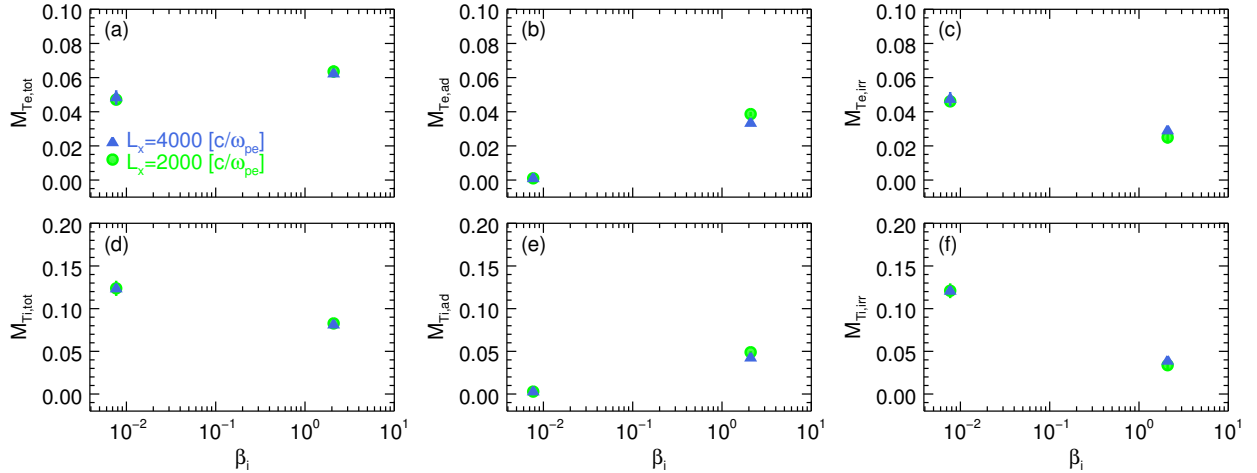


Figure 2.19: Comparison between domain sizes $L_x \approx 2000 c/\omega_{pe}$ (green circles) and $L_x \approx 4000 c/\omega_{pe}$ (blue triangles) of the following heating fractions; (a): electron total, $M_{Te,tot}$; (b): electron adiabatic, $M_{Te,ad}$; (c): electron irreversible, $M_{Te,irr}$; (d): proton total, $M_{Ti,tot}$; (e): proton adiabatic, $M_{Ti,ad}$; (f): proton irreversible, $M_{Ti,irr}$. We present a low- β_i case with $\beta_i = 0.0078$, $T_e/T_i = 0.1$, and a high- β_i case with $\beta_i = 2$, $T_e/T_i = 1$; in both cases, the mass ratio is $m_i/m_e = 25$ and $\sigma_w = 0.1$.

2.B Outflow versus periodic boundary conditions

We have compared the results of our main simulations, which are periodic in x , to a second set that employs outflow boundary conditions, similar to what is described in Sironi et al. (2016). In Fig. 2.21, we show the time evolution of the electron heating fractions $M_{Te,tot}$, $M_{Te,ad}$, and $M_{Te,irr}$

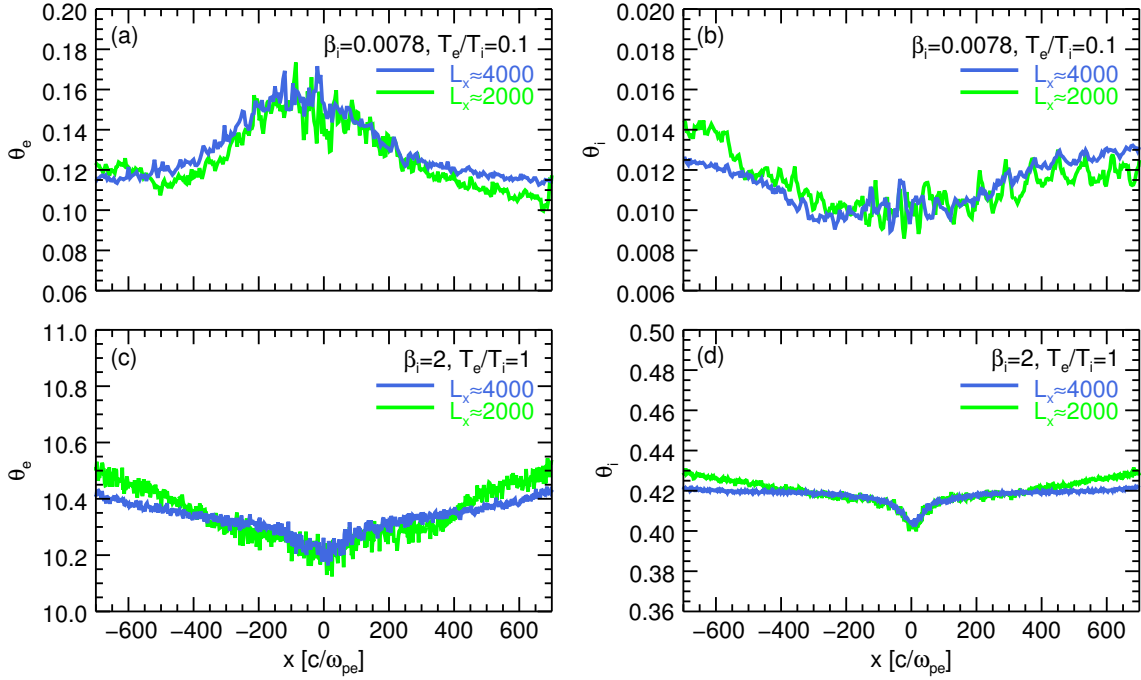


Figure 2.20: Spatial profiles along the reconnection outflow of (a): dimensionless electron temperature θ_e for $\beta_i = 0.0078$, $T_e/T_i = 0.1$; (b): dimensionless proton temperature θ_i for $\beta_i = 0.0078$, $T_e/T_i = 0.1$; (c): dimensionless electron temperature θ_e for $\beta_i = 2$, $T_e/T_i = 1$; (d): dimensionless proton temperature θ_i for $\beta_i = 2$, $T_e/T_i = 1$. The mass ratio is $m_i/m_e = 25$ and $\sigma_w = 0.1$. The spatial profiles are extracted from simulations with domain size $L_x \approx 2000 c/\omega_{pe}$ (green), and $L_x \approx 4000 c/\omega_{pe}$ (blue). These spatial profiles are from the same simulations shown in Fig. 2.19, at time $t \approx 1t_A$.

in a low- β_i simulation (Fig. 2.21(a)–(c)) and a high- β_i case (Fig. 2.21(d)–(f)), for both outflow (blue) and periodic (red) boundary conditions. For the periodic simulations the domain size is $L_x = 4318 c/\omega_{pe}$, whereas for the outflow runs $L_x \approx 2600 c/\omega_{pe}$. Up to ~ 1 Alfvénic crossing time, which corresponds to $t \approx 1.4 \times 10^4 \omega_{pe}^{-1}$ for the periodic simulations and $t \approx 8.5 \times 10^3 \omega_{pe}^{-1}$ for the outflow runs, we find good agreement between the periodic and outflow simulations. At later times, the pile-up of particles and magnetic flux in the primary magnetic island sitting at the boundary leads to the eventual suppression of reconnection in periodic simulations, whereas the outflow runs can be evolved for multiple Alfvénic crossing times.

In Fig. 2.22, we compare the dependence of the electron total heating fraction $M_{Te,tot}$ on β_i and T_e/T_i for periodic and outflow simulations with $m_i/m_e = 25$ and $\sigma_w = 0.1$. The periodic

simulations are indicated by blue, green, and red circles, corresponding to upstream temperature ratios of $T_e/T_i = 0.1, 0.3$, and 1, respectively. The results of outflow simulations are shown by dark yellow ($T_e/T_i = 0.1$), magenta ($T_e/T_i = 0.3$), and cyan ($T_e/T_i = 1$) triangles. The points corresponding to periodic runs are connected by solid lines, whereas the outflow cases are linked by dashed lines. With regard to the β_i - and T_e/T_i -dependence of the electron total heating fraction, $M_{Te,\text{tot}}$, the outflow and periodic cases show good agreement. The agreement for adiabatic and irreversible heating fractions is also good.

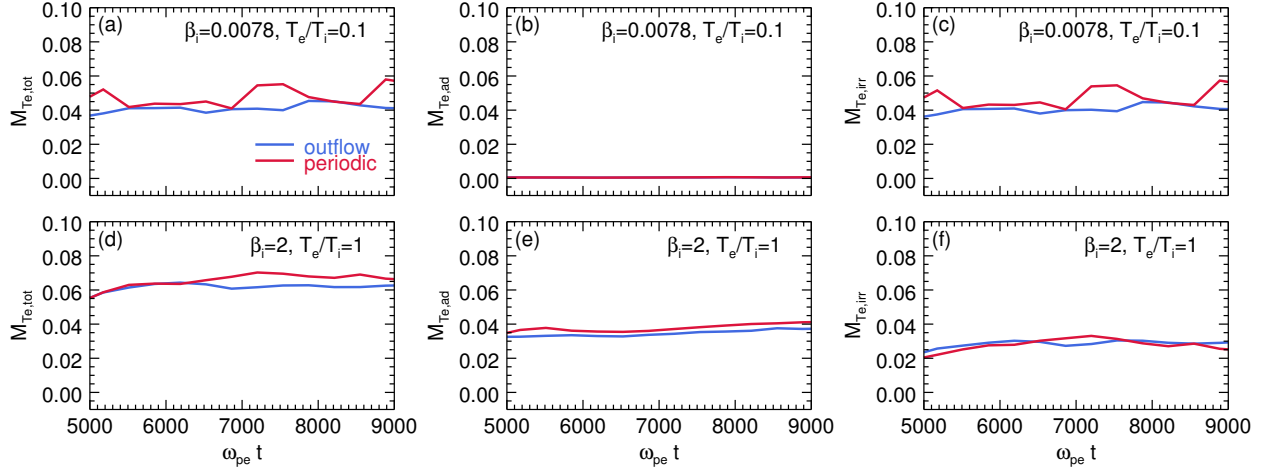


Figure 2.21: Comparison between outflow (blue) and periodic (red) simulations with $\sigma_w = 0.1$ and $m_i/m_e = 25$. We show the time evolution of (a): electron total heating fraction, $M_{Te,\text{tot}}$ for $\beta_i = 0.0078$, $T_e/T_i = 0.1$; (b): electron adiabatic heating fraction, $M_{Te,\text{ad}}$ for $\beta_i = 0.0078$, $T_e/T_i = 0.1$; (c): electron irreversible heating fraction, $M_{Te,\text{irr}}$ for $\beta_i = 0.0078$, $T_e/T_i = 0.1$; (d): electron total heating fraction, $M_{Te,\text{tot}}$ for $\beta_i = 2$, $T_e/T_i = 1$ (e): electron adiabatic heating fraction, $M_{Te,\text{ad}}$ for $\beta_i = 2$, $T_e/T_i = 1$ (f): electron irreversible heating fraction, $M_{Te,\text{irr}}$ for $\beta_i = 2$, $T_e/T_i = 1$. The heating fractions are shown in the interval $t = 5 \times 10^3 \omega_{pe}^{-1} - 9 \times 10^3 \omega_{pe}^{-1}$, which corresponds to $t \approx 0.36 t_A - 0.64 t_A$ for the periodic simulations and $t \approx 0.6 t_A - 1 t_A$ for the outflow ones. The curves have been shifted in time to account for slightly different onsets of reconnection in periodic vs. outflow cases, due to different initialization of the current sheet.

2.C Convergence with respect to spatial resolution

To properly capture the electron physics, adequate spatial resolution of the electron skin depth c/ω_{pe} , or equivalently, temporal resolution of the inverse electron plasma frequency ω_{pe}^{-1} , is necessary. In most of our simulations, we use $c/\omega_{pe} = 4$ cells; since we fix $c = 0.45$ cells/timestep, the

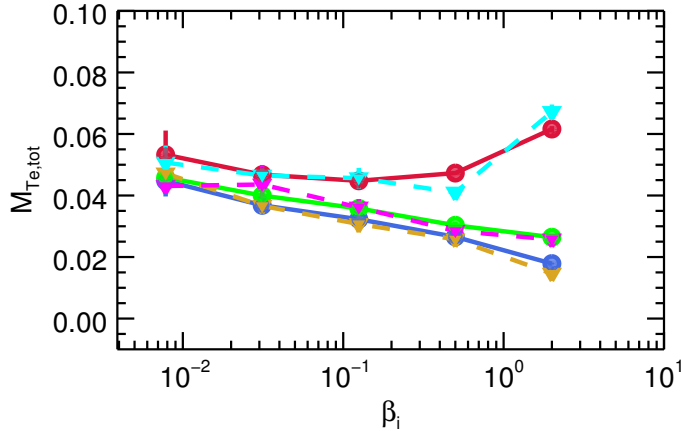


Figure 2.22: Comparison of outflow and periodic simulations (with $\sigma_w = 0.1$ and $m_i/m_e = 25$), in terms of the dependence of $M_{Te,tot}$ on β_i and T_e/T_i . Circles connected by solid lines show the results of periodic simulations, and inverted triangles connected by dashed lines indicate outflow simulations. For periodic runs, blue, green, and red correspond to runs with upstream temperature ratios $T_e/T_i = 0.1, 0.3$, and 1 ; for periodic, dark yellow, magenta, and cyan denote $T_e/T_i = 0.1, 0.3$, and 1 .

temporal resolution in our simulations is $\Delta t \approx 0.1 \omega_{pe}^{-1}$. In this appendix, we show that even at finer spatial (also, temporal) resolution, i.e. $c/\omega_{pe} = 8$ cells $\rightarrow \Delta t \approx 0.05 \omega_{pe}^{-1}$, the heating fractions are essentially unchanged relative to those obtained in simulations with $c/\omega_{pe} = 4$ cells.

In Fig. 2.23, we show the heating fractions for electrons (panels (a), (b), and (c)) and protons (panels (d), (e), and (f)). For the cases $\beta_i = 0.0078, T_e/T_i = 1$ and $\beta_i = 2, T_e/T_i = 1$, we compare a simulation with $c/\omega_{pe} = 4$ cells (denoted by green circles) to one with $c/\omega_{pe} = 8$ cells (indicated by blue triangles). In both sets of simulations, we employ $m_i/m_e = 1836$ and magnetization $\sigma_w = 0.1$. To ensure that the simulations with $c/\omega_{pe} = 8$ cells contain the same number of electron skin depths as those with $c/\omega_{pe} = 4$ cells, it is necessary to double the size of the simulation domain in x (in units of cells). For the simulations with $c/\omega_{pe} = 4$ cells, we use $L_x \approx 8000$ cells, and for $c/\omega_{pe} = 8$ cells, we use $L_x \approx 1.6 \times 10^4$ cells; in both cases, the physical extent of the domain in x is $L_x \approx 4318 c/\omega_{pe}$. For both choices of the spatial resolution, the electron heating fractions (total, adiabatic, and irreversible) show good agreement. The proton heating fractions show good agreement, too.

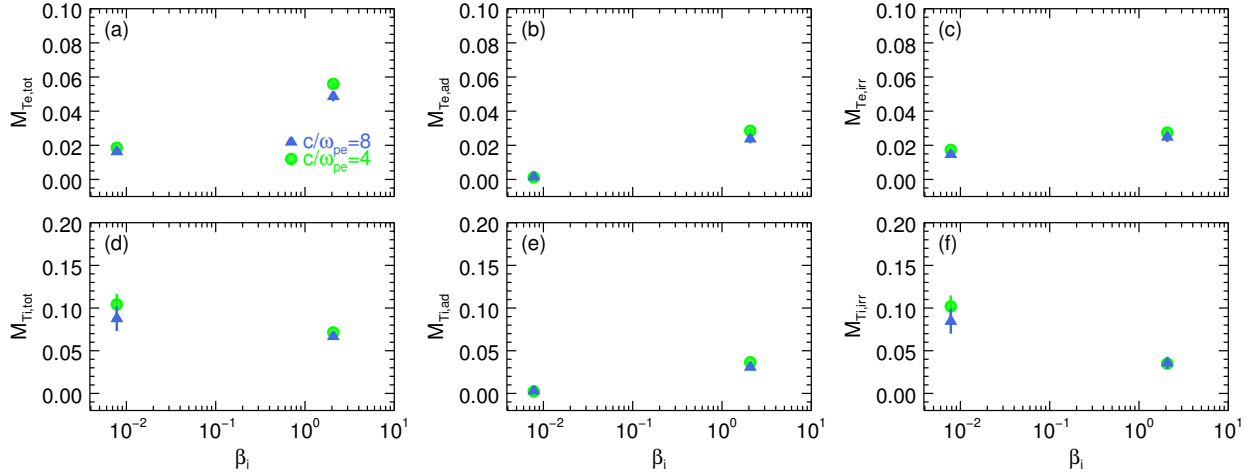


Figure 2.23: Comparison between simulations with $c/\omega_{pe} = 4$ cells $\rightarrow \Delta t \approx 0.1\omega_{pe}^{-1}$ (green circles) and $c/\omega_{pe} = 8$ cells $\rightarrow \Delta t \approx 0.05\omega_{pe}^{-1}$ (blue triangles) of the following heating fractions; (a): electron total, $M_{Te,tot}$; (b): electron adiabatic, $M_{Te,ad}$; (c): electron irreversible, $M_{Te,irr}$; (d): proton total, $M_{Ti,tot}$; (e): proton adiabatic, $M_{Ti,ad}$; (f): proton irreversible, $M_{Ti,irr}$. We present a low- β_i case with $\beta_i = 0.0078$, $T_e/T_i = 1$, and a high- β_i case with $\beta_i = 2$, $T_e/T_i = 1$; in both cases, we employ the realistic mass ratio $m_i/m_e = 1836$ and $\sigma_w = 0.1$.

2.D Control of numerical heating

In simulations with high β_i and low temperature ratios, numerical effects can lead to an artificial increase in the upstream electron temperature, at the expense of protons. The rate of numerical heating is proportional to the temperature difference between the two species, hence the high- β_i simulations with $T_e/T_i = 0.1$ exhibit the strongest degree of numerical heating (Melzani et al., 2013). As the temperature difference between electrons and protons in the upstream and downstream regions is not necessarily the same, the rate of numerical heating in the two regions may be different. If not adequately kept under control, this can affect our measured heating efficiencies.

In Fig. 2.24, we compare two simulations with $m_i/m_e = 25$, $\sigma_w = 0.1$, $\beta_i = 2$, and $T_e/T_i = 0.1$, which is the case where numerical heating is the most serious. One has $N_{ppc} = 16$ (dashed lines), and the other $N_{ppc} = 64$ (solid lines). In both cases, the size of the domain is $L_x = 4318 c/\omega_{pe}$. In panel (a), we show the time evolution of the dimensionless electron temperature in the upstream (magenta) and downstream (green) for $N_{ppc} = 16$ (dashed) and $N_{ppc} = 64$ (solid). The vertical

black dotted line indicates the time at which primary reconnection wavefronts recede past the region selected for our measurements (see Section 2.4). The dimensionless electron temperature in both the upstream and downstream increases with time, however the amount of numerical heating is significantly less with $N_{\text{ppc}} = 64$ than with $N_{\text{ppc}} = 16$. For example, the former shows a shift in downstream temperature (green) from $t \approx 4 \times 10^3 \omega_{\text{pe}}^{-1}$ to $1.5 \times 10^4 \omega_{\text{pe}}^{-1}$ of only $\Delta\theta_e \approx 0.02$, but for $N_{\text{ppc}} = 16$ the temperature shift is about six times larger. The magenta lines show the analogous comparison for upstream temperatures. For both choices of N_{ppc} , the initial value of dimensionless electron temperature in the upstream is the same, but by $t = 1.5 \times 10^4 \omega_{\text{pe}}^{-1}$, they differ by $\Delta\theta_e \approx 0.15$.

In panel Fig. 2.24(b), we show the time evolution of the total electron heating fraction $M_{T_e,\text{tot}}$ for $N_{\text{ppc}} = 64$ (solid blue) and 16 (dashed blue). Although numerical heating can significantly shift the measured values of dimensionless temperature in the downstream and upstream (panel (a)), we find that the heating fractions are much less sensitive to the value of N_{ppc} , with $N_{\text{ppc}} = 16$ already giving good results. The heating fractions we measure are proportional to the difference between the downstream and upstream temperatures (or internal energy per particle), and it appears that the numerical heating in the downstream and upstream regions nearly cancels out in the difference. Although we use $N_{\text{ppc}} = 64$ in simulations with $\beta_i = 2$, the agreement with the $N_{\text{ppc}} = 16$ case demonstrates that the impact of numerical heating is negligible for our measured heating fractions.

We have tested the effect of numerical heating in a small box ($L_x \approx 1080 c/\omega_{\text{pe}}$) with up to $N_{\text{ppc}} = 256$, however the difference (as regard to heating fractions) with respect to simulations with $N_{\text{ppc}} = 64$, our standard choice for all $\beta_i = 2$ simulations, is again, negligible.

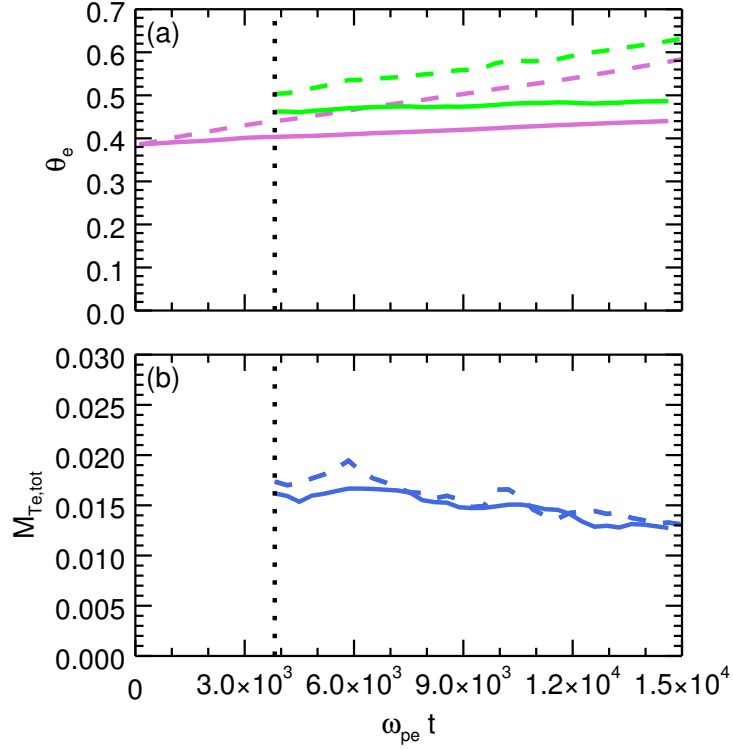


Figure 2.24: Comparison of two simulations with $N_{ppc} = 16$ (dashed lines) and $N_{ppc} = 64$ (solid lines), having the same physical parameters: $\beta_i = 2$, $T_e/T_i = 0.1$, $\sigma_w = 0.1$, and $m_i/m_e = 25$. We present the time evolution of (a): dimensionless electron temperature, θ_e in the upstream (magenta) and downstream (green); (b): total electron heating fraction, $M_{Te,tot}$. The upstream and downstream regions show an increase in electron temperature as time evolves, caused by numerical heating. The impact of numerical heating is significantly reduced by employing $N_{ppc} = 64$. The measured value of $M_{Te,tot}$ is, however, largely unaffected by numerical heating (panel (b)).

2.E Anisotropy in the downstream

We characterize the anisotropy in our simulations with ratios of the diagonal components of the stress-energy tensor,

$$r_x = T_{xx}/T_{\text{tot}} \quad (2.35)$$

$$r_y = T_{yy}/T_{\text{tot}} \quad (2.36)$$

$$r_z = T_{zz}/T_{\text{tot}}, \quad (2.37)$$

as seen in the fluid rest frame; here, $T_{\text{tot}} = (T_{xx} + T_{yy} + T_{zz})/3$. As we show below, we typically measure anisotropies on the order of 5 – 10% in the downstream, i.e., the reconnected plasma is nearly isotropic.

In Fig. 2.25, we show for $\sigma_w = 0.1$ and $m_i/m_e = 25$ the time evolution of the anisotropy ratios r_x (red), r_y (green), and r_z (blue), for three temperature ratios $T_e/T_i = 0.1, 0.3$, and 1, and five values of $\beta_i = 0.0078, 0.031, 0.13, 0.5$, and 2 (β_i and T_e/T_i of the respective simulation are indicated at the top of each panel). From top to bottom, β_i increases; from left to right, T_e/T_i increases. The temporal evolution starts from $\omega_{pe}t = 4 \times 10^3$, when the downstream region reaches a quasi-steady state. We find that the downstream pressures along the two directions transverse to the outflow ($\hat{\mathbf{y}}$ and $\hat{\mathbf{z}}$) are nearly identical, and slightly smaller than the pressure along the outflow direction ($\hat{\mathbf{x}}$, in our setup), which agrees with the findings of [Shay et al. \(2014\)](#).

2.F Convergence of the layer width when varying the initial sheet thickness

In Fig. 2.9(e), we showed the T_e/T_i - and β_i -dependence of the reconnection layer width δ_{rec} . As mentioned in Section 2.3, we set the initial current sheet thickness to be $\Delta = 40 c/\omega_{pe}$. A natural question is whether the measured value of δ_{rec} is affected by the sheet thickness at initialization, or by the self-consistent reconnection physics alone. To demonstrate that the measured values of δ_{rec} do not depend on the initial current sheet thickness Δ , we show in Fig. 2.26 the time evolution of δ_{rec} for $\Delta = 30$ (red), 40 (green), and $60 c/\omega_{pe}$ (blue). Here, the box size is $L_x = 2159 c/\omega_{pe}$, $\beta_i = 2$, $T_e/T_i = 1$, $\sigma_w = 0.1$, and $m_i/m_e = 25$. The reconnection width is measured at $215 c/\omega_{pe}$ downstream of the central X-point. The $\Delta = 40, 60 c/\omega_{pe}$ curves have been shifted in time to account for the delayed onset of reconnection caused by the thicker initial current sheet. The time evolution of δ_{rec} in Fig. 2.26 is shown starting at $t = 5000 \omega_{pe}^{-1}$, beyond which δ_{rec} reaches a quasi-steady value. The three simulations converge to a similar value $\delta_{\text{rec}} \approx 25 c/\omega_{pe}$, independent of the current sheet thickness at initialization.

The values in this plot should not be directly compared to those in panel (e) of Fig. 2.9. Here, we extract δ_{rec} at a distance of $\approx 215 c/\omega_{\text{pe}}$ downstream of the central X-point (in order to avoid the influence of the primary island sitting at the boundary), whereas in the larger box used in Fig. 2.9, δ_{rec} was measured at $430 c/\omega_{\text{pe}}$ from the center. Still, the results from the two experiments yield the same opening angle for the reconnection outflow.

2.G Heating efficiencies in terms of internal energy per particle

In the main body of the text, we phrased most of the heating fractions in terms of differences in temperature between downstream and upstream, but they can also be expressed in terms of differences in internal energy per particle. In Fig. 2.27, which is analogous to Fig. 2.11, we show the T_e/T_i - and β_i -dependence of: electron heating fractions $M_{ue,\text{tot}}, M_{ue,\text{ad}}, M_{ue,\text{irr}}$ (panels (a), (b), (c)); ion heating fractions $M_{ui,\text{tot}}, M_{ui,\text{ad}}, M_{ui,\text{irr}}$ (panels (d), (e), (f)); and total particle heating fractions $M_{ue,\text{tot}} + M_{ui,\text{tot}}, M_{ue,\text{ad}} + M_{ui,\text{ad}}, M_{ue,\text{irr}} + M_{ui,\text{irr}}$ (panels (g), (h), (i)). As before, blue, green, and red lines denote temperature ratios $T_e/T_i = 0.1, 0.3$, and 1, and the simulations have $m_i/m_e = 25$ and $\sigma_w = 0.1$. Since the protons here are non-relativistic in both the upstream and downstream, the points in panels (d) of Figs. 2.27 and 2.11 typically differ by a factor of $\hat{\gamma}_i - 1 = 2/3$ (excluding the $\beta_i = 2$ cases, for which the protons are mildly relativistic, with $\theta_{i,\text{up}} \approx 0.4$), where $\hat{\gamma}_i = 5/3$ is the adiabatic index for a non-relativistic gas. The relationship between the two options for measuring the heating fractions of electrons, $M_{Te,\text{tot}}$ and $M_{ue,\text{tot}}$ in panels (a) of Figs. 2.27 and 2.11, is not as simple because the electrons can be non-, trans- or ultra-relativistic. For example, at $\beta_i = 2, T_e/T_i = 1$, the upstream and downstream dimensionless electron temperatures are $\theta_{e,\text{up}} \approx \theta_{e,\text{down}} \approx 10$, and the adiabatic index is $\hat{\gamma}_e \approx 4/3$ in both the upstream and downstream. The ratio of $M_{Te,\text{tot}}$ to $M_{ue,\text{tot}}$ is then $M_{Te,\text{tot}}/M_{ue,\text{tot}} \approx 1/3 = \hat{\gamma}_e - 1$ for $\hat{\gamma}_e = 4/3$. However, at low β_i , electrons are less relativistic, and the ratio $M_{Te,\text{tot}}/M_{ue,\text{tot}}$ is typically larger because the adiabatic index is larger. Still, we remark that all of the conclusions presented in the paper hold

when the heating efficiencies are measured using the internal energy per particle, rather than the temperature.

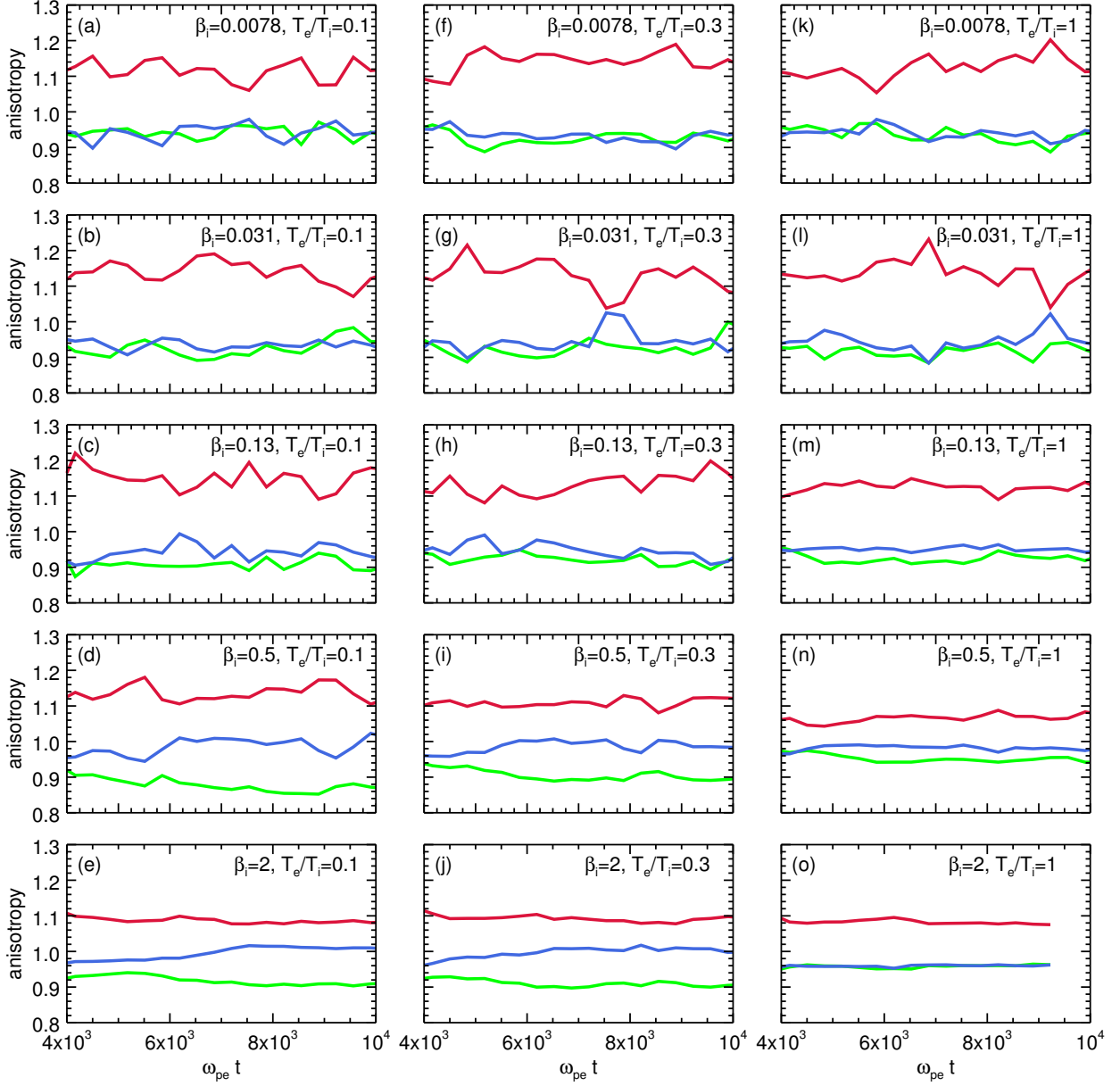


Figure 2.25: Time evolution of the anisotropy ratios in the reconnection downstream for a range of β_i (increasing from top to bottom, as indicated in the legends) and T_e/T_i (0.1 in the left column, 0.3 in the middle column, 1 in the right column). Here, $\sigma_w = 0.1$ and $m_i/m_e = 25$. Red, green, and blue curves correspond to the ratios r_x , r_y , and r_z (Eqs. 2.35–2.37). Time evolution is shown starting at $\omega_{pe}t = 4 \times 10^3$, at which point the downstream region used for our heating measurements reaches a quasi-steady state.

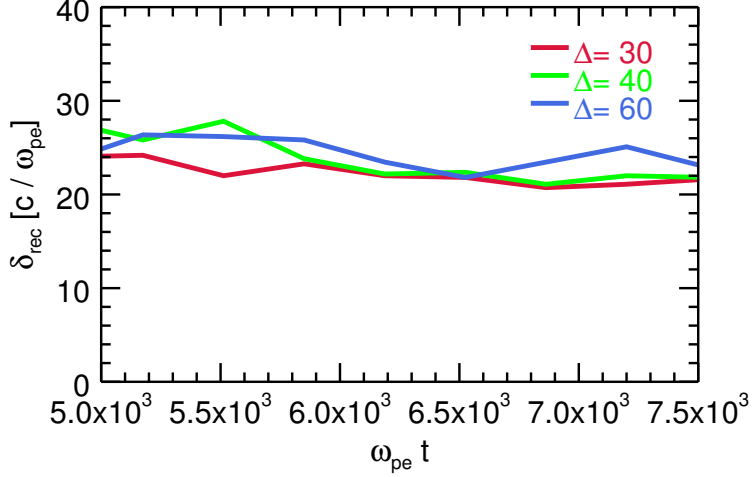


Figure 2.26: Time evolution of the reconnection layer width δ_{rec} for a simulation with box size $L_x = 2159 c/\omega_{\text{pe}}$, $\beta_i = 2$, $T_e/T_i = 1$, $\sigma_w = 0.1$, and $m_i/m_e = 25$. The value of δ_{rec} is measured at $215 c/\omega_{\text{pe}}$ from the center. It does not depend on the choice of the initial current sheet thickness, $\Delta = 30, 40, 60 c/\omega_{\text{pe}}$, shown by the red, green, and blue curves, respectively.

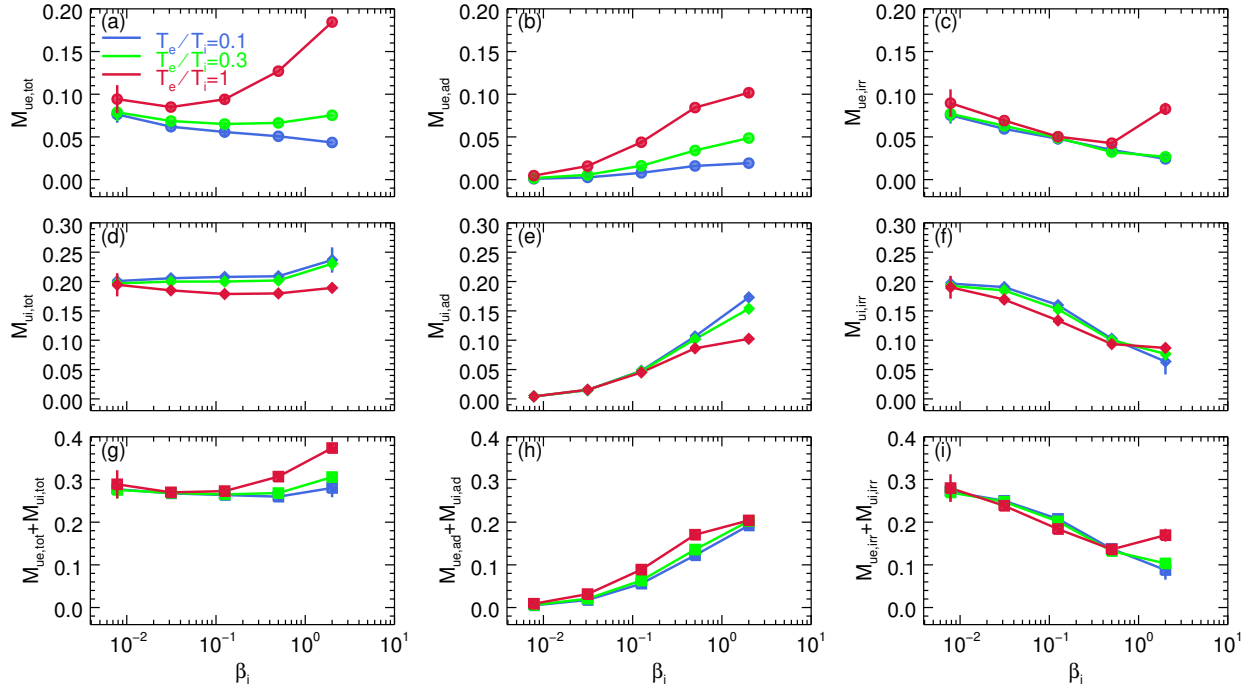


Figure 2.27: The layout here is analogous to Fig. 2.11, but for the internal energies, u_e, u_i instead of temperatures, T_e, T_i . Plasma β_i - and T_e/T_i -dependence of various heating efficiencies; (a): electron total, $M_{ue,\text{tot}}$; (b): electron adiabatic, $M_{ue,\text{ad}}$; (c): electron irreversible, $M_{ue,\text{irr}}$; (d): proton total, $M_{ui,\text{tot}}$; (e): proton adiabatic, $M_{ui,\text{ad}}$; (f): proton irreversible, $M_{ui,\text{irr}}$; (g): electron and proton total, $M_{ue,\text{tot}} + M_{ui,\text{tot}}$; (h): electron and proton adiabatic, $M_{ue,\text{ad}} + M_{ui,\text{ad}}$; (i): electron and proton irreversible, $M_{ue,\text{irr}} + M_{ui,\text{irr}}$. The simulations shown here use a mass ratio $m_i/m_e = 25$ and magnetization $\sigma_w = 0.1$. As in earlier plots, blue, green, and red points correspond to simulations with upstream T_e/T_i ratios of 0.1, 0.3, and 1.

3. Electron and proton heating in transrelativistic guide field magnetic reconnection

*Text in this chapter was originally published in:
ApJ, 873, 2, (2019; Rowan, M., Sironi, L., & Narayan, R.).*

3.1 Abstract

The plasma in low-luminosity accretion flows, such as the one around the black hole at the center of M87 or Sgr A* at our Galactic Center, is expected to be collisionless and two-temperature, with protons hotter than electrons. Here, particle heating is expected to be controlled by magnetic reconnection in the transrelativistic regime $\sigma_w \sim 0.1\text{--}1$, where the magnetization σ_w is the ratio of magnetic energy density to plasma enthalpy density. By means of large-scale 2D particle-in-cell simulations, we explore for a fiducial $\sigma_w = 0.1$ how the dissipated magnetic energy gets partitioned between electrons and protons, as a function of β_i (the ratio of proton thermal pressure to magnetic pressure) and of the strength of a guide field B_g perpendicular to the reversing field B_0 . At low β_i ($\lesssim 0.1$), we find that the fraction of initial magnetic energy per particle converted into electron irreversible heat is nearly independent of B_g/B_0 , whereas protons get heated much less with increasing B_g/B_0 . As a result, for large B_g/B_0 , electrons receive the overwhelming majority of irreversible particle heating ($\sim 93\%$ for $B_g/B_0 = 6$). This is significantly different than the antiparallel case $B_g/B_0 = 0$, in which electron irreversible heating accounts for only $\sim 18\%$ of the total particle heating (Rowan et al., 2017). At $\beta_i \sim 2$, when both species start already relativistically hot (for our fiducial $\sigma_w = 0.1$), electrons and protons each receive $\sim 50\%$ of the irreversible particle heating, regardless of the guide field strength. Our results provide important insights into the plasma physics of electron and proton heating in hot accretion flows around supermassive black holes.

3.2 Introduction

When black holes accrete at much below the Eddington limit they tend to be radiatively inefficient, and the resulting accretion flows become extremely hot (see [Yuan & Narayan 2014](#) for a review). Hot accretion flows are particularly common in the large population of low-luminosity active galactic nuclei ([Ho 2008](#)). Two members of this population, viz., Sagittarius A* (Sgr A*)—the black hole at the center of our Galaxy—and the supermassive black hole in M87, are primary targets of the Event Horizon Telescope (EHT, [Doeleman et al. 2008, 2009](#)), and are of special interest at the present time. These systems, and many others like them, can be modeled within the framework of advection-dominated accretion flows (ADAFs, [Narayan & Yi 1995a](#); alternatively, radiatively inefficient accretion flows, RIAFs, [Stone et al. 1999](#); [Igumenshchev et al. 2003](#); [Beckwith et al. 2008](#)). However, detailed models, suitable for comparison with observations, require an understanding of electron heating in the accreting plasma, given that the observed emission is powered by electrons; yet, a detailed understanding of electron microphysics is currently lacking.

The key feature of a hot accretion flow is that the accreting gas heats up close to the virial temperature, causing the flow to puff up into a geometrically thick configuration and the plasma to become optically thin. Because of the low gas density, the plasma is largely collisionless, i.e., Coulomb collisions between charged particles are negligible. Furthermore, at radii inside a few hundred $R_S \equiv 2GM/c^2$, where M is the mass of the black hole and R_S is the Schwarzschild radius, the plasma becomes two-temperature, with the protons substantially hotter than the electrons ([Yuan et al., 2003](#)). The two-temperature nature of the gas in an ADAF is a generic prediction for several reasons: first, electrons radiate much more efficiently than protons. Second, coupling between protons and electrons via Coulomb collisions is inefficient at low densities. Lastly, compressive heating favors nonrelativistic protons over relativistic electrons.

Despite these strong reasons, the plasma could still be driven to a single-temperature state if there

were additional modes of energy transfer (beyond Coulomb collisions) from protons to electrons. Several mechanisms of energy transfer in collisionless accretion flows have been proposed, including weak shocks, turbulence, and magnetic reconnection (Quataert & Gruzinov, 1999; Howes, 2010; Yuan et al., 2002; Sironi & Narayan, 2015; Sironi, 2015; Werner et al., 2016; Rowan et al., 2017; Kawazura et al., 2019; Zhdankin et al., 2019). In the present work, we focus on the last of these possibilities, i.e., magnetic reconnection.

Magnetic reconnection plays an important role in the energy dynamics of numerous astrophysical systems, for example, relativistic jets, hot accretion flows (ADAFs), and coronae above stellar and accretion disk photospheres. Many of these systems tend to be magnetically dominated, in the sense that $\beta_i \equiv P_{\text{gas}}/P_{\text{mag}} \lesssim 1$ (here, $P_{\text{gas}} \equiv n_0 k_B T_{i0}$ is the thermal pressure of protons, with density n_0 and temperature T_{i0} , and $P_{\text{mag}} \equiv B_0^2/8\pi$ is the magnetic pressure, with B_0 the magnitude of the reconnecting magnetic field). As a result, the magnetic field is the primary (or at least major) energy reservoir, and energy dissipation may proceed via reconnection. Although hot accretion flows and disk coronae are magnetically dominated (i.e., low-beta plasmas), the magnetization $\sigma_w \equiv 2P_{\text{mag}}/w$ is typically small, with $\sigma_w \lesssim 1$; here, $w \equiv (\rho_{e0} + \rho_{i0})c^2 + \hat{\gamma}_{e0}u_{e0} + \hat{\gamma}_{i0}u_{i0}$ is the enthalpy density per unit volume, and $\rho_{e0} = m_e n_0$, $\rho_{i0} = m_i n_0$, $\hat{\gamma}_{e0}$, $\hat{\gamma}_{i0}$, and u_{e0}, u_{i0} are the rest-mass densities, adiabatic indices, and internal energy densities, respectively, of electrons and protons. This regime of $\beta_i \lesssim 1$ and $\sigma_w \lesssim 1$, termed *transrelativistic*, provides a unique context for the study of magnetic reconnection, as protons are generally nonrelativistic, whereas electrons can be moderately or even ultra-relativistic (Melzani et al., 2014; Werner et al., 2016; Ball et al., 2018).

In a previous work, we explored electron and proton heating in transrelativistic reconnection, for the idealized case of antiparallel fields (Rowan et al., 2017, hereafter RSN17). The important question of electron and proton heating has been addressed by others as well, especially in the case of antiparallel reconnection (Melzani et al., 2014; Shay et al., 2014; Werner et al., 2016; Hoshino, 2018).

The more general, and astrophysically relevant, case of reconnection includes a guide magnetic field component perpendicular to the plane of the reconnecting field lines. In fact, recent work suggests that turbulent heating at microscopic dissipation scales may be ultimately mediated by reconnection (Boldyrev & Loureiro, 2017; Loureiro & Boldyrev, 2017; Mallet et al., 2017; Comisso & Sironi, 2018; Shay et al., 2018). In turbulent systems like accretion flows, turbulent eddies get naturally stretched into thin current sheets, which at small scales become susceptible to the tearing mode instability, which in turn drives reconnection. At sufficiently small scales, one may then expect that energy dissipation in turbulence is mediated by reconnection. At these small scales, the guide field has the same strength as at large scales, yet the strength of the reversing fields becomes smaller at progressively smaller scales in the turbulent cascade. Our work, which focuses on guide field reconnection (up to the regime of strong guide fields), has then broader implications for energy dissipation in a turbulent cascade.

In nonrelativistic reconnection, it has been demonstrated through direct measurements, fully-kinetic and gyrokinetic simulations, and analytical theory, that the strength of the guide field heavily impacts the energy partition between electrons and protons. In the strong guide field limit, electrons receive a larger fraction of dissipated magnetic energy than protons (Dahlin et al., 2014; Numata & Loureiro, 2015; Eastwood et al., 2018). However, for the transrelativistic electron-proton plasma relevant to hot accretion flows and disk coronae, the question is under-explored, yet crucially important for obtaining predictions that can be compared to observations.

To explore the effect of a guide field in transrelativistic reconnection, we use fully-kinetic particle-in-cell (PIC) simulations, which are capable of capturing the fundamental plasma physics that controls electron and proton heating in collisionless systems. The PIC method captures from first principles the interplay between charged particles and electromagnetic fields at the basis of reconnection, thereby resolving plasma processes that are out of reach for large-scale magnetohydrodynamic

simulations of accretion disks.

In this paper, we investigate the effect of a guide field on electron and proton heating via reconnection in the transrelativistic regime. We study the dependence of the heating efficiency on the initial plasma properties, by varying the guide field strength and the proton- β_i . For our main runs, we choose $\sigma_w = 0.1$ as our fiducial magnetization, and the initial electron-to-proton temperature ratio is set to $T_{e0}/T_{i0} = 1$. In a few selected cases, we also vary the temperature ratio ($T_{e0}/T_{i0} = 0.1$ and 0.3), as well as the magnetization ($\sigma_w = 1$). We employ the realistic mass ratio in all our simulations.

The rest of this paper is organized as follows. In Section 3.3, we describe the setup and initial conditions of our simulations. Next, in Section 3.4, we explain our technique for measuring electron and proton heating at late times, when the energy of bulk motions driven by reconnection has thermalized. Then, in Section 3.5, we summarize the main results of electron and proton heating in guide field reconnection. We conclude in Section 3.6.

3.3 Simulation setup

We use the electromagnetic PIC code **TRISTAN-MP** (Spitkovsky, 2005), which is a parallel version of **TRISTAN** (Buneman, 1993), to perform numerical simulations of magnetic reconnection. Our simulations are two-dimensional (2D) in space, however all three components of particle momenta and electromagnetic fields are evolved. In this section, we describe the setup for our simulations of guide field reconnection. The simulation setup is similar to that described in Sironi & Spitkovsky (2014), RSN17, and Ball et al. (2018) for the study of antiparallel reconnection.

Simulation coordinates are as follows: the xy plane is the simulation plane; the antiparallel field is along x , and the inflow direction is along y ; a guide component of magnetic field points in the z direction. The initial field configuration is sketched in Fig. 3.1.

The profile of the antiparallel component of magnetic field is set as $\mathbf{B}_{ap} = -B_0 \tanh(2\pi y/\Delta_{cs}) \hat{\mathbf{x}}$.

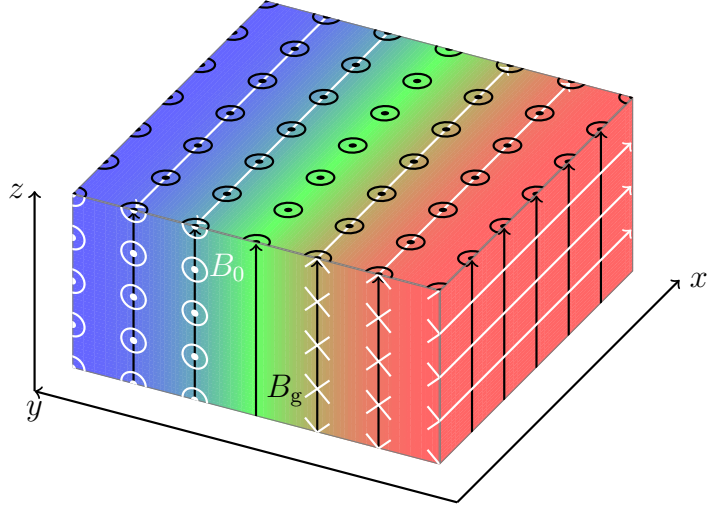


Figure 3.1: Illustration of the initial setup for simulations of guide field reconnection. The antiparallel component of reconnecting field lines, shown by white arrows and aligned along x , reverses from the red to the blue region. A guide component of magnetic field, shown by black arrows, is superposed perpendicular to the plane of antiparallel reconnection (the xy plane). At initialization, the thermal pressure of hot and overdense plasma (green region) balances against magnetic pressure from outside the current layer. While our simulations are two-dimensional in space, particle momenta and electromagnetic fields are evolved in all three dimensions.

The parameter Δ_{cs} controls the width over which the antiparallel field \mathbf{B}_{ap} reverses; we usually set $\Delta_{\text{cs}} = 30 c/\omega_{\text{pe}}$, where c/ω_{pe} is the electron skin depth,

$$\frac{c}{\omega_{\text{pe}}} = \sqrt{\frac{\gamma_{e0} m_e c^2}{4\pi n_0 e^2}}. \quad (3.1)$$

Here, $\gamma_{e0} m_e$ is the electron mass (including relativistic inertia), $\gamma_{e0} = 1 + u_{e0}/(n_0 m_e c^2)$, u_{e0} is the initial electron internal energy density, n_0 is the number density of electrons (as well as protons) in the inflow, and e is the electron charge. In all simulations, we use $c/\omega_{\text{pe}} = 4$ (we refer to RSN17 for tests of convergence with respect to the choice of c/ω_{pe}). The magnitude of the antiparallel magnetic field B_0 is controlled via the magnetization

$$\sigma_w = \frac{B_0^2}{4\pi w}, \quad (3.2)$$

where

$$w = n_0(m_e + m_i)c^2 + \hat{\gamma}_{e0}u_{e0} + \hat{\gamma}_{i0}u_{i0} \quad (3.3)$$

is the specific enthalpy density of the inflowing plasma; $\hat{\gamma}_{e0}$, $\hat{\gamma}_{i0}$ are the initial adiabatic indices, and u_{e0} , u_{i0} are the initial internal energy densities of electrons and protons. This definition of magnetization differs (only when plasma is relativistically hot) from the one commonly used in studies of nonrelativistic reconnection,

$$\sigma_i = \frac{B_0^2}{4\pi n_0 m_i c^2}. \quad (3.4)$$

For nonrelativistic temperatures $\sigma_w \cong \sigma_i$, however for relativistically hot plasma, Eq. (3.2) includes the effects of relativistic inertia in the denominator, so that $\sigma_w < \sigma_i$ in general. In our simulations, we fix $\sigma_w = 0.1$ (except for a few cases with $\sigma_w = 1$, which we explore in Sec. 3.5.4).

In addition to the antiparallel field, a guide magnetic field component is initialized perpendicular to the plane of antiparallel field lines, i.e., $\mathbf{B}_g = B_g \hat{\mathbf{z}}$. The strength of the guide field is parametrized by the ratio

$$b_g = B_g/B_0, \quad (3.5)$$

where B_g is the magnitude of the guide field (uniform throughout the domain) and B_0 is the magnitude of the antiparallel field. We vary b_g from 0 to 6 (i.e., from the antiparallel case to the strong guide field regime).

Particles in the upstream region are initialized according to a Maxwell-Jüttner distribution,

$$f_{\text{MJ}}(\gamma, \theta_{s0}) \propto \gamma \sqrt{\gamma^2 - 1} \exp(-\gamma/\theta_{s0}), \quad (3.6)$$

where θ_{s0} , $s \in \{\text{e}, \text{i}\}$, is the initial dimensionless temperature of the respective particle species: $\theta_{e0} = k_B T_{e0}/m_e c^2$ and $\theta_{i0} = k_B T_{i0}/m_i c^2$. The combination of proton dimensionless temperature θ_{i0} and magnetization σ_i determines the value of proton- β_i ,

$$\beta_i = \frac{8\pi n_0 k_B T_{i0}}{B_0^2} = \frac{2\theta_{i0}}{\sigma_i}. \quad (3.7)$$

Our simulations have β_i in the range 5×10^{-4} to 2. For each value, we explore a range of b_g between and 6.

Magnetic pressure within the current sheet is smaller than that on the outside. To ensure pressure balance, a population of hot and overdense particles is initialized in the current sheet. From the pressure equilibrium condition, the temperature of overdense particles in the current sheet, T_{cs} , is given by $k_B T_{cs}/m_i c^2 = \sigma_i/2\eta$, where η is the overdensity of particles in the current sheet, relative to that of the inflowing plasma, n_0 . We use $\eta = 3$. Electrons and protons in the current sheet are assumed to have the same temperature.

Parameters associated with each of the main runs are indicated in Tab. 3.1. In these simulations, we employ the physical mass ratio, $m_i/m_e = 1836$, and an initial electron-to-proton temperature ratio in the upstream of $T_{e0}/T_{i0} = 1$. In two cases (see Sec. 3.5.4), we also consider $T_{e0}/T_{i0} = 0.1$ and 0.3, to illustrate the dependence of our results on temperature ratio.

Reconnection is triggered at the center of the box ($x \sim 0$, $y \sim 0$), by artificially removing the pressure of the hot particles initialized in the current sheet. This leads to the formation of an X-point. From this central X-point, the tension of reconnected field lines ejects the plasma to

the left and to the right, along x . We use periodic boundary conditions along x , so the outflows from the two sides (i.e., the moving plasma ejected along x by the field line tension) meet at the boundary, where their collision forms a large magnetic island (we shall call it “primary island” or “boundary island”). Here, particles and magnetic flux accumulate, as more plasma reconnects and is ejected along the outflows (this is discussed in detail in Sec. 3.4.1). Along the y boundaries, we use two moving injectors (each receding from $y = 0$ at the speed of light) to introduce fresh plasma and magnetic field; the domain is enlarged when the injectors reach the y boundaries. We refer to [RSN17](#) for further details.

In the present work, we measure electron and proton heating at late times, when the particle internal energies have reached quasi-steady values.¹ The primary island is the site where we extract our heating measurements, which requires to run the simulations for a sufficient time such that the outflows from opposite sides of the central X-point meet at the boundary and form the island. The choice of extracting our heating efficiencies from particles residing in the primary island has advantages and disadvantages. The main disadvantage is that it does not allow to directly probe the heating that results solely from reconnection physics (which was the focus of [RSN17](#)), as it includes, e.g., heating due to shocks generated by the colliding reconnection outflows. On the other hand, our choice is the most appropriate for modeling realistic macroscopic systems, since reconnection outflows are expected to eventually come to rest, and their bulk energy to thermalize (e.g., this is expected in systems like accretion flows, for which the dynamical time and length scales are much larger as compared to that of the reconnection microphysics).

We run our simulations up to $t/t_A \approx 3\text{--}4$, where $t_A = L_x/v_A$ is the Alfvénic crossing time for a box of length L_x along the x direction; $v_A = c\sqrt{\sigma_w/(1 + \sigma_w)}$ is the Alfvén speed.² In all the

¹Thanks to our choice of periodic boundary conditions along x , we are able to track the particle energies for extended times, and thus assess the time-asymptotic heating efficiency.

²Note that this definition does not include the effective inertia of the guide field, which could be accounted for by defining an effective Alfvén speed as $v_{A,\text{eff}} = c\sqrt{\sigma_w/[1 + \sigma_w(1 + b_g^2)]}$.

cases considered here (even the high guide field cases $b_g \gtrsim 3$, for which the onset of reconnection is delayed due to the large magnetic pressure in the current sheet), we find that evolving the system for around 3–4 Alfvénic crossing times is sufficient for the measured temperatures in the primary island to attain quasi-steady values. The procedure for measuring the heating efficiency is further described in Sec. 3.4.

We find that the time-asymptotic heating efficiencies (especially for protons) are sensitive to the x -extent of the domain, if the box is not large enough. In this case, plasma that is ejected along x , away from the center, does not have enough time to reach the expected terminal velocity before stopping at the boundaries. It follows that particle heating in the primary island (which also includes the contribution from thermalization of bulk outflow energy) can be artificially inhibited if the domain is too small. We find that a box size $L_x \approx 2160 c/\omega_{pe}$ is large enough to guard against this effect, and this is the value we use in our simulations; convergence of our heating results with respect to the domain size L_x is discussed in App. 4.A. In units of the proton skin depth,

$$\frac{c}{\omega_{pi}} \approx \frac{c}{\omega_{pe}} \sqrt{\frac{m_i}{m_e}} \left(1 + \frac{\theta_{e0}}{\hat{\gamma}_{e0} - 1}\right)^{-1/2} \left(1 + \frac{\theta_{i0}}{\hat{\gamma}_{i0} - 1}\right)^{1/2}, \quad (3.8)$$

the adopted box size corresponds to at least $L_x \approx 51 c/\omega_{pi}$, with this lower limit achieved at low β_i . For higher values of β_i , the proton skin depth approaches the electron skin depth, and the x -extent of the domain approaches $L_x \approx 2160 c/\omega_{pi}$. For each value of β_i , the box size L_x , in units of c/ω_{pi} , is listed in Tab. 3.1.

We use a sufficient number of computational particles per cell N_{ppc} to ensure that numerical heating is negligible with respect to measured heating efficiencies (see Sec. 3.5.3; we refer also to RSN17 for convergence tests). For β_i in the range 5×10^{-4} to 0.5, we use $N_{ppc} = 16$, and for $\beta_i = 2$, we use a larger value, $N_{ppc} = 64$.

Run ID:	b5e-4.bg0	b3e-2.bg0	b5e-1.bg0	b2.bg0
β_i	4.9×10^{-4}	0.031	0.5	2.0
b_g	0	0	0	0
θ_{i0}	2.4×10^{-5}	0.0016	0.031	0.39
θ_{e0}	0.045	2.9	55	690
σ_i	0.1	0.1	0.12	0.36
N_{ppc}	16	16	16	64
c/ω_{pi}	170	58	14	5.0
r_{Le0}	0.063	0.5	2.0	4.0
r_{Li0}	2.6	7.2	6.7	4.9
$L_x[c/\omega_{pi}]$	51	149	617	1728
Run ID:	b5e-4.bg3e-1	b3e-2.bg3e-1	b5e-1.bg3e-1	b2.bg3e-1
b_g	0.3	0.3	0.3	0.3
r_{Le0}	0.060	0.48	1.9	3.8
r_{Li0}	2.5	6.9	6.4	4.7
Run ID:	b5e-4.bg6e-1	b3e-2.bg6e-1	b5e-1.bg6e-1	b2.bg6e-1
b_g	0.6	0.6	0.6	0.6
r_{Le0}	0.053	0.43	1.7	3.4
r_{Li0}	2.2	6.2	5.8	4.2
Run ID:	b5e-4.bg1	b3e-2.bg1	b5e-1.bg1	b2.bg1
b_g	1	1	1	1
r_{Le0}	0.045	0.35	1.4	2.8
r_{Li0}	1.8	5.1	4.7	3.5
Run ID:	b5e-4.bg3	b3e-2.bg3	b5e-1.bg3	b2.bg3
b_g	3	3	3	3
r_{Le0}	0.02	0.16	0.63	1.3
r_{Li0}	0.82	2.3	2.1	1.6
Run ID:	b5e-4.bg6	b3e-2.bg6	b5e-1.bg6	b2.bg6
b_g	6	6	6	6
r_{Le0}	0.010	0.082	0.33	0.66
r_{Li0}	0.43	1.2	1.1	0.81

Table 3.1: Parameters and values associated with our main simulations, described in Sec. 3.3. The *Run ID* for each simulation is composed of the value of proton- β_i and guide field strength b_g . The electron and proton Larmor radii (r_{Le0} and r_{Li0}) are measured in the upstream. Parameters listed for antiparallel simulations (those ending in $bg\theta$), but not stated for nonzero guide field cases, are implied to be the same. In all cases, $L_x = 2160 c/\omega_{pe}$, $c/\omega_{pe} = 4$, $m_i/m_e = 1836$, $T_{e0}/T_{i0} = 1$, and $\sigma_w = 0.1$.

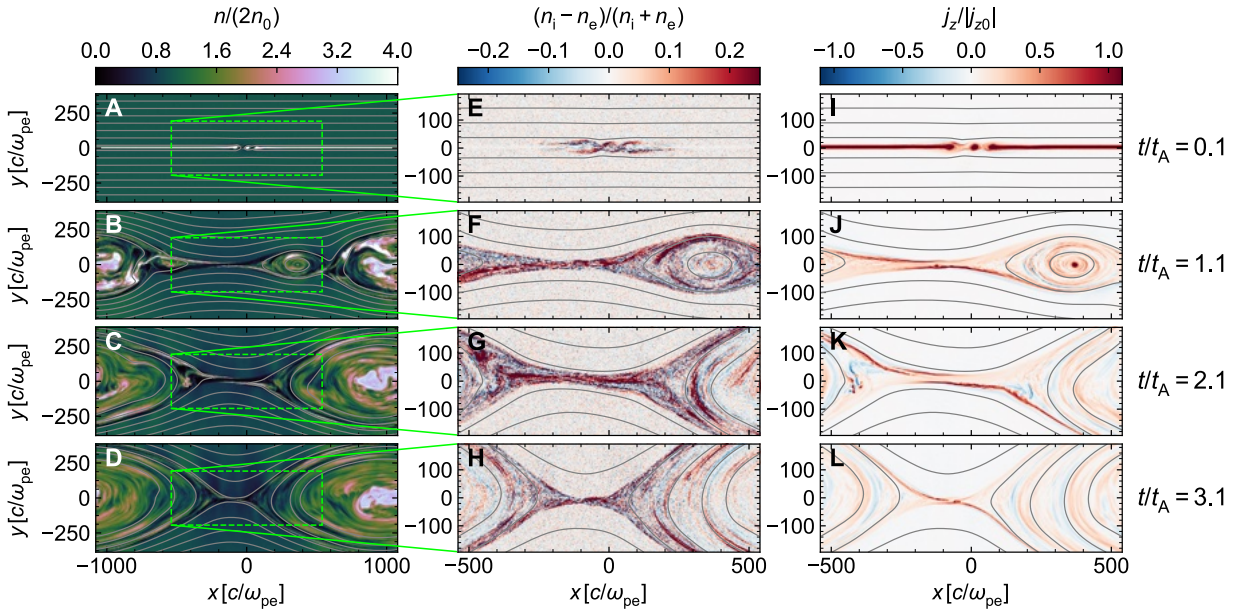


Figure 3.2: Time evolution of a simulation with $\beta_i = 5 \times 10^{-4}$ and $b_g = 1$ (b5e-4.bg1 in Tab. 3.1). The first, second, and third columns show particle number density (in units of initial number density in the upstream), charge non-neutrality, and electric current density along z , in units of initial z -current in the reconnection layer; the quantities shown here are computed in the simulation frame. The snapshots are shown at $t/t_A = 0.1, 1.1, 2.1$, and 3.1 (equivalently, $t\omega_{pe} \approx 7.1 \times 10^2, 7.8 \times 10^3, 1.5 \times 10^4$ and 2.2×10^4) in the first through fourth rows, as indicated on the right hand side.

3.4 Measurement of late-time heating

In Sec. 3.4.1 we discuss the time evolution of the reconnection layer, and in Sec. 3.4.2 we discuss the measurement of late-time heating in the primary island.

3.4.1 Time evolution of the reconnection layer

In Fig. 3.2, we show snapshots covering the time range $t/t_A = 0.1\text{--}3.1$ for a simulation with $\beta_i = 5 \times 10^{-4}$ and moderate guide field, $b_g = 1$ (run b5e-4.bg1 in Tab. 3.1). In the first, second, and third columns, respectively, we show the number density n (in units of total upstream density, $2n_0$), the degree of charge non-neutrality (i.e., the ratio of charge density to particle number density, $(n_i - n_e)/(n_i + n_e)$), and the z -component of current density, normalized to the initial value in the current layer, j_z/j_{z0} ; the gray contours show magnetic field lines.

The time evolution is illustrated from the first to the fourth row (e.g., panels A–D). After reconnection is triggered at $x \sim 0$, an X-point forms. From the central X-point, two reconnection

fronts, dragged by magnetic tension, recede from the center; for the simulation shown in Fig. 3.2, the speed of recession is $0.31 c \approx \sqrt{\sigma_w} c$, so the expected Alfvén limit is saturated. Since we use periodic boundary conditions, the receding fronts meet at $x = \pm 1080 c/\omega_{pe}$ after about one Alfvénic crossing time (second row), and merge into a volume of particles and magnetic flux that continues to grow as reconnection proceeds. As anticipated, we refer to this structure as the *primary island*; it is the main site where we extract our heating measurements, since this is where particles ejected from the outflow region eventually end up. Up to the runtimes of our simulations, the primary island tends to maintain an oblong shape (elongated along x), a feature that is more prominent for stronger guide fields.

Secondary islands, as opposed to the primary island, form frequently at low β_i in the exhaust region (or equivalently, in the outflow region); the formation of secondary islands is suppressed at high β_i (Daughton & Karimabadi, 2007; Uzdensky et al., 2010; RSN17). We find that simulations with high guide fields are characterized by a relative absence of secondary islands, as compared to simulations with the same β_i but weaker guide fields.

The current layer in guide field reconnection is characterized by left-right and top-bottom asymmetry, especially in the exhaust region, immediately downstream of the central X-point. Electrons and protons are ejected from the X-point toward different directions: for our magnetic geometry, electrons to the upper-left and lower-right quadrants, whereas protons are sent to the upper-right and lower-left ones (see panels E–H, which zoom into the central region of panels A–D) (Zenitani & Hoshino, 2008). The z -current (third column) is inhomogeneous in the immediate downstream (see panels I–L); there is some enhancement along the walls of the exhaust (at the interface with the upstream), in particular along the directions that electrons leave the X-point.

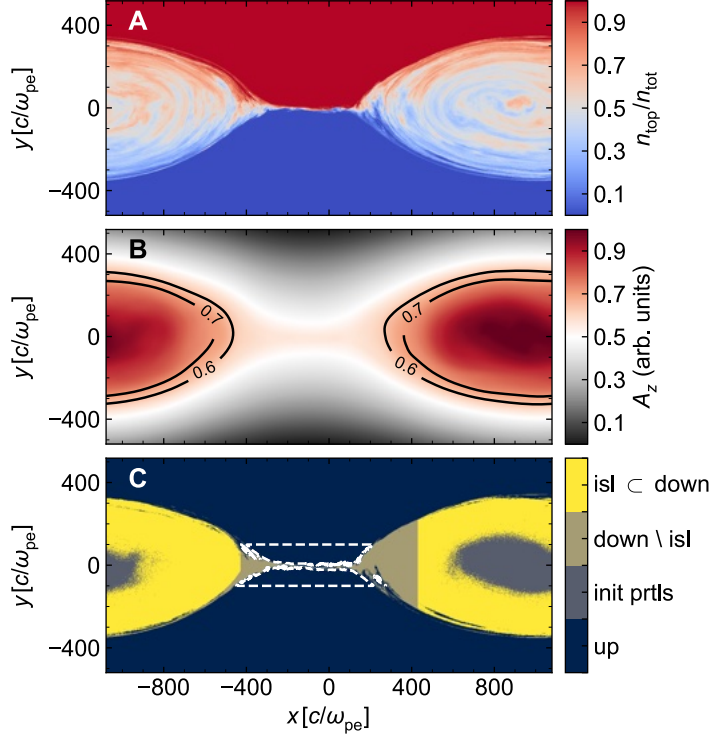


Figure 3.3: 2D plots (from simulation b5e-4.bg1 in Tab. 3.1) of (A) ratio of top-to-total particle number density, (B) the z -component of magnetic vector potential, and (C) separation into island (yellow), non-island downstream (tan), and upstream (navy) regions; cells containing particles that are part of the hot overdense population left over from initialization are excluded from the island region, and typically reside at the island core (grey region at the center of the yellow island region in panel C). In panel B, two contours corresponding to $A_z = 0.6$ and 0.7 are plotted (solid black lines) to illustrate the typical shape of magnetic field lines in the primary island (here, units are arbitrary; A_z is normalized to be between 0 and 1). The dashed white contours in panel (C) show the parts of the upstream used to measure inflow quantities. The yellow region that we use for the computation of heating efficiencies in the primary island is defined by criteria (i), (ii) and (iii) described in the text.

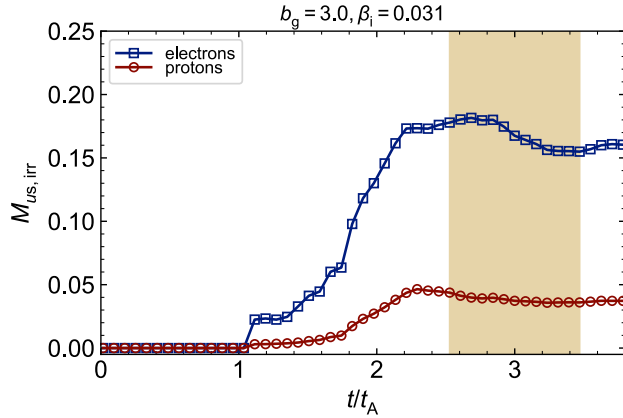


Figure 3.4: Time dependence of irreversible heating fractions $M_{ue,\text{irr}}$ (blue) and $M_{ui,\text{irr}}$ (red) for simulation `b3e-2.bg3`. The yellow shaded region indicates the time interval used to compute the time-averaged values.

3.4.2 Measurement of particle heating in the primary island

To assess the heating efficiency at late times, we focus on the change in particle internal energy, as particles travel from the inflow region (i.e., the upstream) to the far downstream, and eventually enter the primary island (these different regions are defined in more detail below). Internal energy and temperature in each cell of the simulation domain are calculated as in [RSN17](#); here we briefly review the method, but we refer the reader to [RSN17](#) for more details.

The internal energy is computed by treating the plasma as a perfect, isotropic fluid,³ whose stress-energy tensor is:

$$T_s^{\mu\nu} = (e_s + p_s) U_s^\mu U_s^\nu - p_s g^{\mu\nu}, \quad (3.9)$$

where $e_s = \bar{n}_s m_s c^2 + u_s$, p_s , U_s^μ , and $g^{\mu\nu}$ are the rest-frame energy density, pressure, dimensionless four-velocity, and flat-space Minkowski metric, and the subscript s denotes the particle species; \bar{n}_s is the rest-frame particle number density. From Eq. (3.9), the dimensionless internal energy per

³Though we assume isotropy here, our measurements are not significantly affected by this assumption, as we discuss in Sec. 3.5.6.

particle in the fluid rest frame v_s can be written as

$$v_s = \frac{(T_s^{00}/n_s m_s c^2 - \Gamma_s) \Gamma_s}{1 + \hat{\gamma}_s(v_s)(\Gamma_s^2 - 1)}. \quad (3.10)$$

Here,⁴ T_s^{00} is the lab-frame energy density, n_s is the lab-frame particle number density, Γ_s is the Lorentz factor computed from the local fluid velocity, $\hat{\gamma}_s$ is the adiabatic index, and the subscript $s \in \{e, i\}$ indicates the type of particle (electron or proton). Note that the adiabatic index $\hat{\gamma}_s(v_s)$ is a function of the specific internal energy. Given a mapping between the specific internal energy and adiabatic index, Eq. (3.10) can be solved iteratively for v_s . For adiabatic index, we use a function of the form

$$\hat{\gamma}_s(v_s) = \frac{A + B v_s}{C + D v_s}, \quad (3.11)$$

where $A \approx 1.176$, $B \approx 1.258$, $C \approx 0.706$, and $D \approx 0.942$. The numerical coefficients satisfy $A/C = 5/3$ and $B/D = 4/3$ in the nonrelativistic ($v_s \rightarrow 0$) and ultra-relativistic ($v_s \rightarrow \infty$) limits, respectively; see Eq. 14 of [RSN17](#) for additional details. The adiabatic index in Eq. (4.90) is used to convert between specific dimensionless internal energy and dimensionless temperature:

$$\theta_s = [\hat{\gamma}_s(v_s) - 1]v_s.$$

In the following, we refer to “downstream” as the combination of the outflow region and the primary island. We select only part of the downstream to compute the late-time particle heating, in particular part of the primary island, which is far from the central X-point. The region is selected

⁴To employ Eqs. 3.9 and 3.10, one must choose which frame to boost to; the rest-frame stress-energy tensor is computed from the lab-frame one via Lorentz transformations, $T^{\alpha'\beta'} = \Lambda^{\alpha'}_{\mu}(\mathbf{v}_{\text{fl}})\Lambda^{\beta'}_{\nu}(\mathbf{v}_{\text{fl}})T^{\mu\nu}$, where \mathbf{v}_{fl} is the local fluid velocity. This does not necessarily ensure that $T^{0'i'} = T^{i'0'} = 0$, so we have tested a more precise, also more expensive, calculation, i.e., solving for \mathbf{v} from $T^{\alpha'\beta'} = \Lambda^{\alpha'}_{\mu}(\mathbf{v})\Lambda^{\beta'}_{\nu}(\mathbf{v})T^{\mu\nu}$, subject to the constraints $T^{0'i'} = T^{i'0'} = 0$ (by symmetry of the stress-energy tensor, these are three equations). The solution of these equations yields a boost $\Lambda(\mathbf{v})$ which ensures $T^{0'i'} = 0$. However, whether we boost to the frame defined by \mathbf{v}_{fl} or \mathbf{v} , our results are unchanged.

based on three criteria: (*i*) the mixing between particles originating from the top ($y > 0$) and bottom ($y < 0$) of the domain must exceed a chosen threshold (and be less than the complementary threshold): $d_{\text{th}} < n_{\text{top}}/n_{\text{tot}} < 1 - d_{\text{th}}$ (RSN17), (*ii*) the z -component of the magnetic vector potential must exceed a value, $A_z > A_{z,\text{th}}$, which is related to the mixing threshold identified in (*i*) (Li et al., 2017b; Ball et al., 2018), and (*iii*) cells containing particles that were part of the hot, overdense population initialized in the current sheet (see Sec. 3.3) are excluded, since their properties depend on arbitrary choices at initialization. The use of the above criteria for selection of the “island” region is illustrated in Fig. 3.3. Panel A shows the ratio of density of particles originating from the top of the domain, n_{top} , to the total density n_{tot} . The part of the downstream that has mixed, according to (*i*) above, is shown in panel C by the combination of grey, yellow and tan regions.

To select the island area, which is a subset of the mixed region, we find cells at the boundary $x = \pm 1080 c/\omega_{\text{pe}}$ that satisfy $d_{\text{th}} < n_{\text{top}}/n_{\text{tot}} < 1 - d_{\text{th}}$, and of those cells, we select the ones at the upper and lower edges of the island (along $\pm y$). In these cells, we compute the average value of the vector potential $A_{z,\text{th}}$, to serve as a second threshold for selection of the island region (panel B). The island cells are then identified as those where there is sufficient mixing (criterion (*i*)), and where $A_z > A_{z,\text{th}}$ (criterion (*ii*)). We also impose a strict spatial cutoff on the island region, to ensure that it is distinct from the exhaust even at late times (see RSN17 for details). This criterion corresponds in panel C of Fig. 3.3 to excluding the tan regions at $|x| < 430 c/\omega_{\text{pe}}$. Finally, from the island region, we exclude any cells where the density of the hot, overdense particles used for initialization (see Sec. 3.3) is greater than zero (criterion (*iii*)), so that the measured heating does not depend on particles whose properties are set by hand as initial conditions. These initial particles generally reside in the island center (see the grey core in panel C). The region that satisfies all our criteria (which we shall call “island region” for brevity) is shown in panel C of Fig. 3.3 as the yellow area.

The method of island selection outlined here is a robust and consistent way of selecting cells that are far downstream of the central X-point, for all guide field strengths we consider, and it is relatively insensitive to the choice of threshold value d_{th} . For example, $A_{z,\text{th}}$ differs by no more than 10% for d_{th} in the range 0.003–0.3; the overall measured values of particle heating in the island show comparable sensitivity to the choice of d_{th} , at a level of around 15% for d_{th} in the range 0.003–0.3. For island selection, we find that $d_{\text{th}} = 0.3$ is suitable.

To assess particle heating, we measure the change in particle internal energies, as they travel from the inflow to the island region (described above). The upstream region is defined such that $n_{\text{top}}/n_{\text{tot}} < d_{\text{th},\text{up}}$ or $n_{\text{top}}/n_{\text{tot}} > 1 - d_{\text{th},\text{up}}$ (so, a complementary definition to the mixing criterion (i) above). We employ a threshold value $d_{\text{th},\text{up}} = 3 \times 10^{-5}$; the fact that $d_{\text{th},\text{up}} < d_{\text{th}}$ provides a thin (\sim few c/ω_{pe}) buffer region between the downstream (tan and yellow areas combined in panel C of Fig. 3.3) and the upstream (navy region in panel C of Fig. 3.3). We further select only those upstream cells lying within $\pm 100 c/\omega_{\text{pe}}$ of $y = 0$ (as delimited by the dashed white contours in panel C of Fig. 3.3).

With the inflow and island regions suitably identified, overall heating fractions can be computed as the difference between the dimensionless internal energies in the island and inflow regions, normalized to the inflowing magnetic energy per particle (Shay et al., 2014; RSN17):

$$M_{ue,\text{tot}} \equiv \frac{v_{e,\text{isl}} - v_{e,\text{up}}}{\sigma_i m_i / m_e}, \quad (3.12)$$

$$M_{ui,\text{tot}} \equiv \frac{v_{i,\text{isl}} - v_{i,\text{up}}}{\sigma_i}. \quad (3.13)$$

These dimensionless ratios indicate the fraction of magnetic energy per particle in the inflow that is converted to particle heating, by the time the particle reaches the island, far downstream of the central X-point. As in RSN17, the heating fractions in Eqs. 3.12 and 3.13 can be decomposed into

adiabatic-compressive and irreversible components,

$$M_{ue,\text{tot}} = M_{ue,\text{ad}} + M_{ue,\text{irr}}, \quad (3.14)$$

$$M_{ui,\text{tot}} = M_{ui,\text{ad}} + M_{ui,\text{irr}}. \quad (3.15)$$

The adiabatic heating fractions represent the heating that results solely from an increase in internal energy due to adiabatic compression of the plasma as it travels from the inflow to the island; for electrons, the adiabatic heating fraction is approximately⁵ (RSN17)

$$M_{ue,\text{ad}} \approx \frac{1}{2} \beta_i \frac{T_{e0}}{T_{i0}} \left[\left(\frac{n_{\text{isl}}}{n_0} \right)^{\hat{\gamma}_e - 1} - 1 \right]. \quad (3.16)$$

where n_{isl} is the typical electron density in the island. The irreversible heating fractions are associated with a genuine increase in the entropy of the particles, and are of primary interest to us. The measured heating fractions we present in Sec. 3.5 are typically time-averaged over one Alfvénic crossing time ($\approx 7100 \omega_{pe}^{-1}$).

A representative temporal evolution of electron and proton irreversible heating fractions, $M_{ue,\text{irr}}$ and $M_{ui,\text{irr}}$, is shown in Fig. 3.4. The time evolution of the heating fractions is shown from $t/t_A = 0$ to $t/t_A \approx 3.5$; at late times, the heating fractions achieve a steady state (i.e., both the electron and proton irreversible heating fractions are relatively flat after $t/t_A \approx 2.5$). Time-averaged heating fractions are computed during this steady state; the points used for time-averaging are indicated by the shaded region in Fig. 3.4.

⁵This is an approximation because Eq. (3.16) assumes a constant adiabatic index $\hat{\gamma}_e$; in reality, when calculating $M_{ue,\text{ad}}$, we properly account for the possibility of a changing adiabatic index, as is appropriate for electrons that start nonrelativistic in the upstream, but are heated to ultra-relativistic temperatures by the time they reach the island.

3.5 Results

In this section, we discuss our measurements of electron and proton heating in the primary island, and their dependence on guide field strength b_g and upstream proton- β_i . In Sec. 3.5.1, we focus on one low and one high β_i case, and explore the effect of guide field strengths b_g in the range 0.3–6. Next, in Sec. 3.5.2, we show the dependence of the reconnection rate on β_i and the guide field. In Sec. 3.5.3, we present comprehensive results of electron and proton heating, extracted from a suite of simulations that span the whole parameter space $b_g = 0\text{--}6$ and $\beta_i = 5 \times 10^{-4}\text{--}2$. Here, we focus on the case of equal initial electron and proton temperatures in the upstream, $T_{e0}/T_{i0} = 1$. For these simulations, the magnetization is $\sigma_w = 0.1$. In Sec. 3.5.4, we present several results of irreversible electron heating from simulations with temperature ratios in the range $T_{e0}/T_{i0} = 0.1\text{--}1$, as well as several cases with $\sigma_w = 1$. Next, in Sec. 3.5.5, we provide a fitting function for the electron irreversible heating efficiency, based on the simulation results presented in Secs. 3.5.3 and 3.5.4. Then, in Sec. 3.5.6, we discuss the degree of anisotropy in the particle distribution (as a function of b_g and β_i), and its effect on the accuracy of our results. Lastly, in Sec. 3.5.7, we discuss an application of the guiding-center formalism to dissect the mechanisms responsible for electron heating at low β_i .

3.5.1 Electron and proton heating: weak vs. strong guide field

Electron and proton heating via reconnection shows substantial differences in the limits of strong and weak guide field. Fig. 3.5 shows 2D snapshots at $t/t_A = 2.7$ of electron (panels A–C) and proton (panels D–F) temperature,⁶ and corresponding 1D profiles (panels G–I), for three simulations with a relatively low $\beta_i = 0.03$ and guide field strengths $b_g = 0.3, 1$, and 6, increasing from left to right. The simulations here correspond to runs `b3e-2.bg3e-1`, `b3e-2.bg1`, and `b3e-2.bg6` in Tab. 3.1.

⁶Here, we phrase our results in terms of temperature, rather than internal energy; however, similar conclusions hold regardless of which quantity is considered (in this section as well as in the rest of the paper).

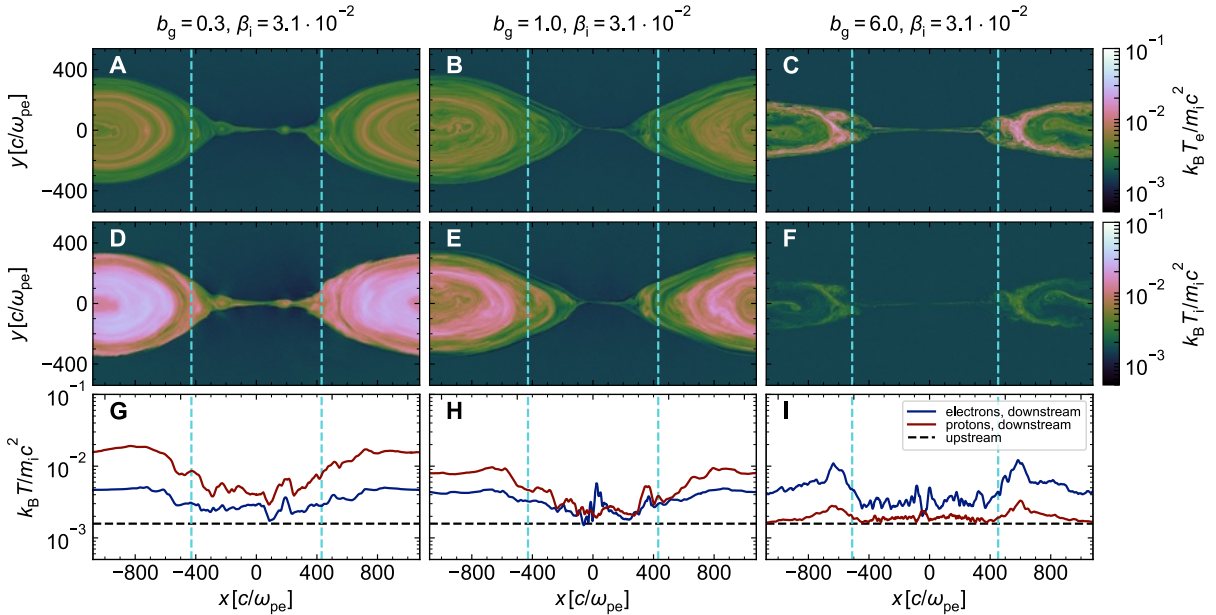


Figure 3.5: Comparison of electron and proton heating for guide fields $b_g = 0.3$ (first column), $b_g = 1$ (second column), and $b_g = 6$ (third column); $\beta_i \approx 0.03$ for these simulations, which correspond to b3e-2.bg3e-1, b3e-2.bg1, and b3e-2.bg6 in Tab. 3.1. The first, second, and third rows show 2D plots of electron temperature, 2D plots of proton temperature, and 1D profiles (averaged along y , for cells in the downstream) of electron (blue) and proton (red) temperature. In the bottom row, the dashed black line shows the initial temperature in the upstream. Vertical cyan dashed lines indicate the x boundaries of the island region; no cells between the cyan lines are counted as part of the island region. Note that the electron and proton temperatures are both normalized to $m_i c^2$. The snapshots are shown at time $t/t_A = 2.7$ (equivalently, $t\omega_{pe} \approx 2 \times 10^4$). 1D profiles are slightly smoothed for clarity. An animated version of this figure is available from the online journal.

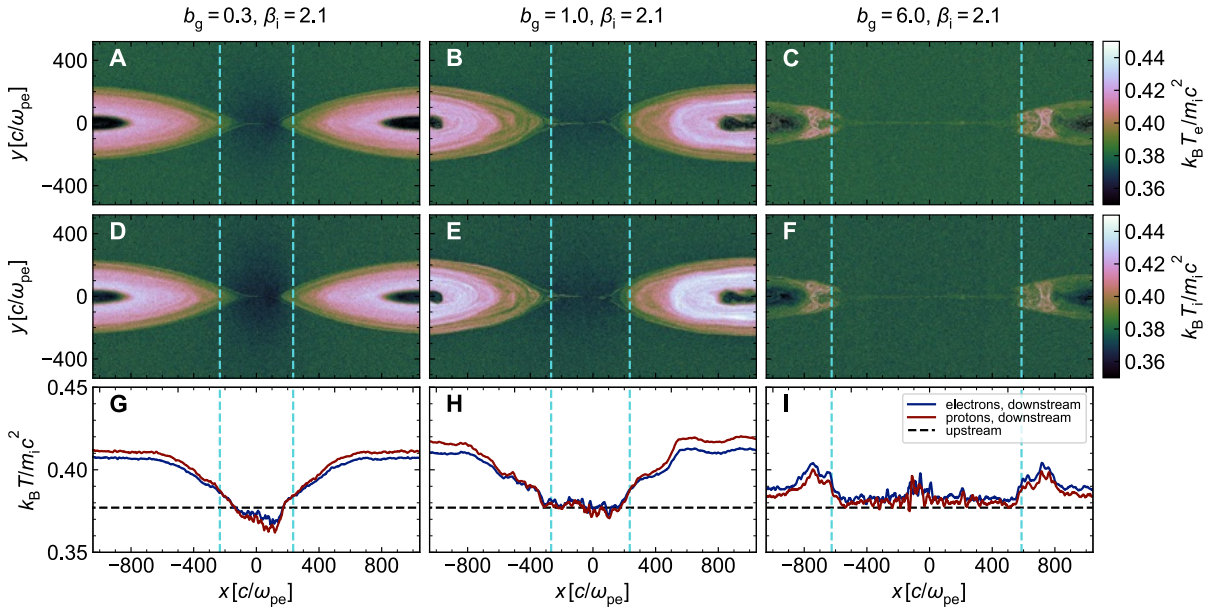


Figure 3.6: The layout is similar to Fig. 3.5. Comparison of electron and proton heating for guide fields $b_g = 0.3$ (first column), $b_g = 1$ (second column), and $b_g = 6$ (third column), but for $\beta_i \approx 2$; these are simulations `b2.bg3e-1`, `b2.bg1`, and `b2.bg6` in Tab. 3.1. The first, second, and third rows show 2D plots of electron temperature, 2D plots of proton temperature, and 1D profiles of electron (blue) and proton (red) temperature; here, temperatures are normalized to $m_i c^2$. The meaning of dashed black and cyan lines is as in Fig. 3.5. The snapshots are at time $t/t_A = 3.1$ ($t\omega_{pe} \approx 2.2 \times 10^4$). 1D profiles are slightly smoothed for clarity. An animated version of this figure is available from the online journal.

The first and second rows show the spatial dependence of electron (panels A–C) and proton (panels D–F) heating. At low b_g (run `b3e-2.bg3e-1`), the electron and proton temperatures are relatively uniform in the exhaust and island regions. For intermediate guide field strengths (run `b3e-2.bg1`), the electron and proton heating is less uniform in the island, and shows marked asymmetry in the exhaust region (see panels B and E, in between the cyan lines). For the strong guide field case (run `b3e-2.bg6`), electrons reach a maximum temperature of roughly $k_B T_e/m_i c^2 \approx 0.02$ along the upper-left and lower-right edges of the outflow; on the other hand, proton heating along the exhaust is essentially isolated to the upper-right and lower-left edges. Throughout the entire downstream (for run `b3e-2.bg6`), the proton temperature rarely exceeds $k_B T_i/m_i c^2 \approx 5 \times 10^{-3}$.

The 2D plots in panels A–F also illustrate that the primary island becomes more oblong with increasing guide field. For $b_g = 0.3$, the aspect ratio of the island (length along the layer to width orthogonal to it) is about 7 : 4, whereas at $b_g = 6$, it is twice as large, 7 : 2. In the cases with strong guide field the primary islands do not circularize up to the run times of our simulations.

The bottom row of Fig. 3.5 shows the 1D profiles of electron (blue) and proton (red) temperatures, both in units of $m_i c^2$, averaged along y for cells within the downstream region (including the yellow and tan regions in panel C of Fig. 3.3, and excluding the grey area in the island core that contains particles left over from initialization). The edges of the primary island are shown by vertical cyan lines. Horizontal black dashed lines indicate the initial temperature of particles in the far upstream. In the weak guide field case $b_g = 0.3$ (panel G), protons are heated substantially more than electrons, similar to the case of antiparallel reconnection (see Melzani et al. (2014), Werner et al. (2016), RSN17). As the strength of the guide field increases (panels H and I), proton heating in both the exhaust region and the primary island is strongly suppressed. The electron temperature, on the other hand, is largely unaffected; for $b_g = 0.3, 1$, and 6, the electron temperature in the island is always around $k_B T_e/m_i c^2 \approx 5 \times 10^{-3}$.

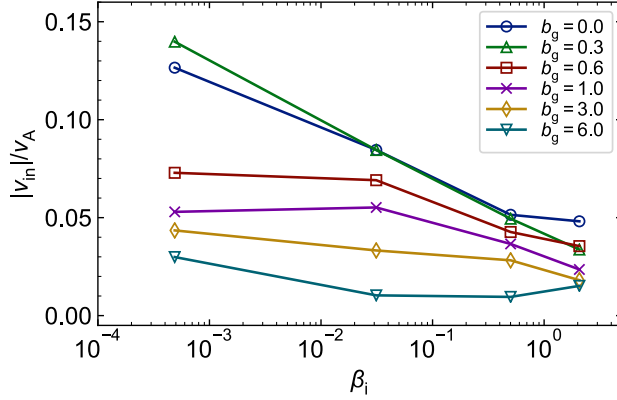


Figure 3.7: Reconnection rate, i.e., the upstream inflow velocity in units of the Alfvén velocity, for the main simulations in Tab. 3.1. Blue, green, red, purple, yellow, and teal points indicate simulations with guide fields 0, 0.3, 0.6, 1, 3, and 6 (solid lines are included to guide the eye). The inflow velocity is averaged in time from $t/t_A \approx 0.7$ to 1 ($t\omega_{pe}$ from 5000 to 7100), and spatially over the upstream region (similar to what is delimited in Fig. 3.3 by the dashed white lines, but see text for details).

Fig. 3.6 is similar to Fig. 3.5, but corresponds to a set of simulations with $\beta_i = 2$ (runs `b2.bg3e-1`, `b2.bg1`, and `b2.bg6` in Tab. 3.1). As we discuss below, this value of $\beta_i = 2$ is close to $\beta_{i,\max} = 2.5$ (see Eq. (3.18)), implying that electrons and protons both start with relativistic temperatures. In stark contrast to the low β_i case, at $\beta_i = 2$ the electron and proton temperatures in the island region are roughly equal, regardless of the guide field strength ($b_g = 0.3\text{--}6$). Still, the 2D temperature structure within the island differs between low and high guide field cases. At high β_i and low or intermediate guide field (runs `b2.bg3e-1` and run `b2.bg1`), the electron and proton temperatures in the island are typically uniform (similar to the low β_i , low b_g case in panels A and D of Fig. 3.5). However, at high β_i and high guide field (run `b2.bg6`), the electron and proton temperatures are less uniform (relative to runs `b2.bg3e-1` and `b2.bg1`; see panels C and F of Fig. 3.5), with electron and proton temperatures greatest near the interfaces between the primary island and the outflows (i.e., $x = \pm 700 c/\omega_{pe}$).

3.5.2 Reconnection rate

Fig. 3.7 shows the β_i and b_g dependence of the reconnection rate, $|v_{in}|/v_A$. The inflow speed $|v_{in}|$ is computed as a spatial average over a specific region of the upstream,⁷ and temporal average from $t/t_A \approx 0.7$ to 1 (when reconnection is roughly in steady state). Each point corresponds to the measurement from a different simulation, and those with the same guide field strength b_g are connected by a solid line. For these simulations, $m_i/m_e = 1836$, $T_{e0}/T_{i0} = 1$, and $\sigma_w = 0.1$.

In most cases, reconnection proceeds at or below the value often reported in the literature, i.e. $|v_{in}|/v_A \lesssim 0.1$ (Cassak et al., 2017); however, for low β_i and weak guide field ($b_g \lesssim 0.3$), the reconnection rate exceeds this fiducial value, with $|v_{in}|/v_A$ in the range 0.1–0.15. For $b_g \lesssim 0.3$, the reconnection rate shows a relatively weak scaling with β_i , decreasing from $|v_{in}|/v_A \approx 0.1$ –0.15 to $|v_{in}|/v_A \approx 0.05$, only a factor of 2–3, as β_i increases from 5×10^{-4} to 2 (Numata & Loureiro, 2015, RSN17, Ball et al., 2018). For guide fields $b_g \gtrsim 1$, the β_i dependence of the reconnection rate is even weaker, and $|v_{in}|/v_A$ typically varies from 0.01 to 0.07. We find that the presence of a guide field tends to suppress the reconnection rate, which is a dependence similar to that found by Melzani et al. (2014) for electron-ion relativistic reconnection, Ricci et al. (2003), Huba (2005), TenBarge et al. (2013), and Liu et al. (2014) for electron-ion nonrelativistic reconnection, and Hesse & Zenitani (2007) and Werner & Uzdensky (2017) for electron-positron plasma. The decrease in the reconnection rate with b_g is more pronounced at lower values of β_i .

3.5.3 Electron and proton heating: b_g and β_i dependence

Fig. 3.8 shows the b_g and β_i dependence of electron (panel A) and proton (panel B) dimensionless temperature. Each solid line shows the volume-averaged temperature in the island for a set of simulations with the same value of b_g , and the black diamonds, connected with a dashed line, show the upstream temperature for each value of β_i (for simulations with fixed β_i , the upstream

⁷Specifically, in the region where $100 c/\omega_{pe} < |y| < 120 c/\omega_{pe}$ and $|x| < 360 c/\omega_{pe}$.

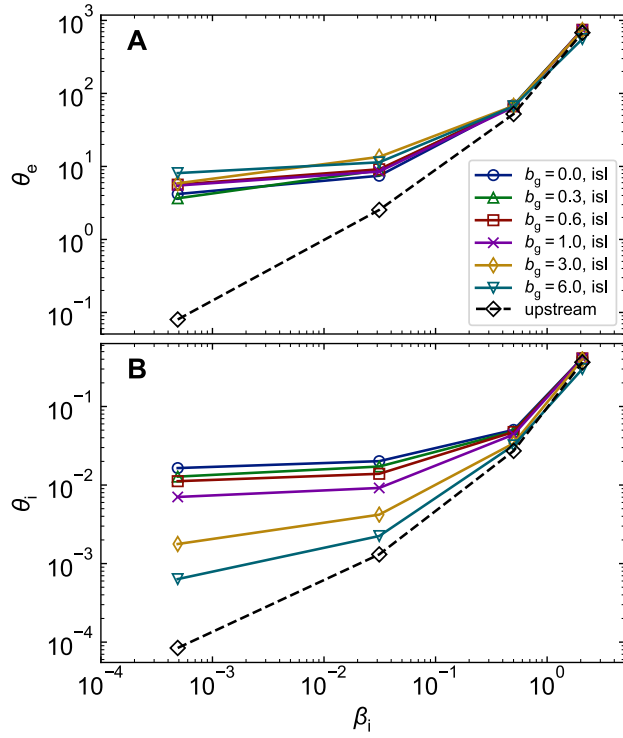


Figure 3.8: Dimensionless (A) electron and (B) proton temperatures, in units of $m_e c^2$ and $m_i c^2$, respectively, measured in the island region (yellow region in Fig. 3.3). The color scheme is the same as in Fig. 3.7, with different colors indicating simulations with different guide field strength. The black diamond points show the temperature in the upstream region. The measured temperatures are averaged over $\sim 1 t_A$ (equivalently, $\sim 7100 \omega_{pe}^{-1}$).

temperature is the same, independent of b_g). As discussed in Sec. 3.3, the numerical resolution is sufficient to keep numerical heating under control; temperatures measured in the inflow region are about the same as the ones at initialization, throughout the duration of our simulations.⁸ The simulations presented here are the same as those in Sec. 3.5.2, so they employ $m_i/m_e = 1836$, $T_{e0}/T_{i0} = 1$, and $\sigma_w = 0.1$.

The upstream electron dimensionless temperatures range from nonrelativistic, $\theta_e \approx 0.08$, up to ultra-relativistic, $\theta_e \approx 700$; the temperatures in the downstream region range from moderately to ultra-relativistic, $\theta_e \approx 6\text{--}700$.⁹ For all values of β_i , the electron temperature in the island appears to be nearly independent of the guide field strength (Fig. 3.8, panel A). The guide field simulations show the same scaling with β_i as the antiparallel case (blue circles), with the electron temperature increasing from about $\theta_e \approx 6$ at $\beta_i \sim 5 \times 10^{-4}$ up to $\theta_e \approx 700$ at $\beta_i \sim 2$. Additionally, the electron temperature shows only a relatively weak dependence on β_i , for $\beta_i \lesssim 0.5$. From $\beta_i \sim 5 \times 10^{-4}$ up to 0.5, the electron temperature in the island changes by no more than a factor of 10 (the dependence is even weaker for $\beta_i \lesssim 3 \times 10^{-2}$). At high β_i , the electron temperature in the island appears to be nearly the same as that in the upstream. However, the increase in temperature from upstream to downstream corresponds to a substantial fraction (typically $\sim 30\%$) of the inflowing magnetic energy per electron (see Fig. 3.9 below, panel A). These two statements are not in contradiction, since for high β_i the available magnetic energy is only a small fraction of the initial thermal energy.

In Fig. 3.8, panel B, we show the proton dimensionless temperature in the island, for the same simulations shown in panel A. At low β_i , protons show a clear decrease in island temperature with

⁸Due to numerical heating, the measured upstream temperature $\theta_e \approx 0.08$ for the $\beta_i = 5 \times 10^{-4}$ runs differs from the expected initialized electron temperature, $\theta_{e0} = 0.045$ (see Tab. 3.1). However, the difference is much smaller (less than $\sim 15\%$) in runs with higher β_i . Although the upstream numerical heating for $\beta_i = 5 \times 10^{-4}$ is large compared to the temperature at initialization, the resulting upstream temperature is still much smaller than the downstream temperature, so it has no effect on the heating fractions presented below. The basic reason is that for low β_i , the available magnetic energy (a fraction of which will be transferred to the particles) is much larger than the initial particle thermal energy.

⁹This is a consequence of our choice of $\sigma_w = 0.1$; for $\sigma_w \ll 1$, the bulk of electrons will not attain ultra-relativistic energies.

increasing guide field strength; for antiparallel reconnection ($b_g = 0$) and $\beta_i \sim 5 \times 10^{-4}$, the proton dimensionless temperature in the island is $\theta_i \approx 0.02$, but decreases to $\theta_i \approx 6 \times 10^{-4}$ for strong guide field, $b_g = 6$. As β_i increases, the proton heating in the island shows a weaker dependence on guide field strength. Similar to electron heating in the island at high β_i , θ_i is nearly independent of b_g at high β_i . The proton dimensionless temperatures, in both the upstream and the island region, are generally nonrelativistic, $\theta_i \lesssim 1$. In summary, when comparing panels A and B, a striking difference is that the electron dimensionless temperature in the island is independent of the guide field strength, whereas the proton dimensionless temperature appreciably decreases with increasing b_g .

In Fig. 3.9 we present the scaling of electron and proton heating with guide field strength b_g and proton- β_i . The first and second rows show the electron and proton heating fractions, respectively (see Eqs. 3.12–3.15); the total heating (first column) is decomposed into adiabatic-compressive and irreversible components, shown in the second and third columns, respectively. In each panel, the corresponding heating fraction is plotted as a function of β_i for guide field strengths in the range 0–6.

The first row in Fig. 3.9 shows the scaling of the electron total, adiabatic, and irreversible heating fractions ($M_{ue,tot}$, $M_{ue,ad}$, and $M_{ue,irr}$) with respect to b_g and β_i . At low β_i , the electron total heating fraction within the island does not show a strong scaling with the strength of the guide field (consistent with Fig. 3.8). For $\beta_i \lesssim 0.03$, $M_{ue,tot} \sim 0.1$. At high β_i , the total heating is suppressed by strong guide fields, $b_g \gtrsim 3$. Some insight into this trend is provided by decomposing the total heating fraction $M_{ue,tot}$ into adiabatic and irreversible parts, $M_{ue,ad}$ (panel B) and $M_{ue,irr}$ (panel C). For low β_i , compressive heating is negligible; however, at higher values of β_i , compressive heating is more significant, but tends to decrease with stronger guide fields, which is in qualitative agreement with Li et al. (2018). This result is physically intuitive, as the plasma becomes less

compressible when the magnetic pressure of the guide field is larger (and in fact, we notice that the primary island is less dense for stronger guide fields).

To summarize, we find that the electron compressive heating fraction in panel (B) steadily increases with β_i and strongly decreases with b_g . Both trends for $M_{ue,ad}$ can be easily understood from Eq. (3.16), given that stronger guide fields give smaller density compressions. In contrast, the electron irreversible heating fraction (panel C) is largely independent of both b_g and β_i , and it is around $M_{ue,irr} \sim 0.1$. The combination of irreversible and compressive heating explains why the total heating at low β_i is independent of both β_i and b_g , whereas at high β_i it is lower for larger b_g (due to the corresponding trend in compressive heating).

The second row in Fig. 3.9 shows the proton heating fractions $M_{ui,tot}$, $M_{ui,ad}$, and $M_{ui,irr}$ (panels D, E, and F). The proton total heating in the island differs sharply from the electron total heating (panel A). The proton total heating shows a strong dependence on the strength of the guide field; for antiparallel reconnection, $M_{ui,tot} \approx 0.3$ regardless of β_i , but the total heating is significantly suppressed as b_g increases. For $b_g = 6$ and $\beta_i \lesssim 0.5$, $M_{ui,tot}$ is negligible. The proton compressive heating (panel E) shows a trend similar to that of the electron compressive heating (panel B); for both electrons and protons, the compressive heating is controlled by density in the upstream, density in the island region, and upstream temperature (here, we focus on the case $T_{e0}/T_{i0} = 1$); since these quantities are similar for electrons and protons, the compressive heating for both species shows the same trend. The proton irreversible heating (panel F) is similar to the proton total heating (panel A) for $\beta_i \lesssim 0.03$, because compressive heating is negligible in this regime. For $\beta_i \gtrsim 0.03$, the proton irreversible heating is less sensitive to the guide field strength, and by $\beta_i = 2$, $M_{ui,irr} \approx 0.08$ regardless of b_g , similarly to the electron irreversible heating.

The electron and proton irreversible heating fractions $M_{ue,irr}$ and $M_{ui,irr}$ can be used to compute the ratio of electron irreversible heating to total irreversible particle heating liberated during

reconnection ([RSN17](#)),

$$q_{ue,\text{irr}} \equiv \frac{M_{ue,\text{irr}}}{M_{ue,\text{irr}} + M_{ui,\text{irr}}}. \quad (3.17)$$

In Fig. 3.10, we present the β_i and b_g dependence of $q_{ue,\text{irr}}$, the *electron irreversible heating efficiency*. For all $\beta_i \lesssim 2$, $q_{ue,\text{irr}}$ increases with the guide field strength. For antiparallel reconnection, electrons ultimately receive $\sim 18\%$ of the irreversible heat transferred to particles. As the guide field increases, so does the fraction of irreversible heating transferred to electrons; for $b_g = 1$, $q_{ue,\text{irr}} \approx 45\%$, and by $b_g = 6$, electrons receive the vast majority of magnetic energy that is converted to irreversible particle heating, with $q_{ue,\text{irr}} \approx 93\%$. At $\beta_i = 2 \sim \beta_{i,\text{max}}$, $q_{ue,\text{irr}} \approx 50\%$, independently of b_g ; $\beta_{i,\text{max}}$ is the maximum possible value of β_i , given σ_w and T_{e0}/T_{i0} , and is defined as

$$\beta_{i,\text{max}} = \frac{0.5}{\sigma_w + \sigma_w T_{e0}/T_{i0}}. \quad (3.18)$$

This equation is derived by expressing β_i as a function of T_{e0}/T_{i0} , σ_w , and θ_i , then taking the limit $\theta_i \rightarrow \infty$. For the simulations presented here, with $m_i/m_e = 1836$, $T_{e0}/T_{i0} = 1$, and $\sigma_w = 0.1$, we find $\beta_{i,\text{max}} = 2.5$. Note that for $\beta_i \sim \beta_{i,\text{max}}$, electrons and protons start relativistically hot in the upstream, and the scale separation $(c/\omega_{pe})/(c/\omega_{pi})$ is of order unity ([RSN17](#)); in this case, electrons and protons behave nearly the same, which explains why for $\beta_i \sim \beta_{i,\text{max}}$ we obtain energy equipartition, i.e., we find that $q_{ue,\text{irr}} \approx 50\%$, independently of b_g .

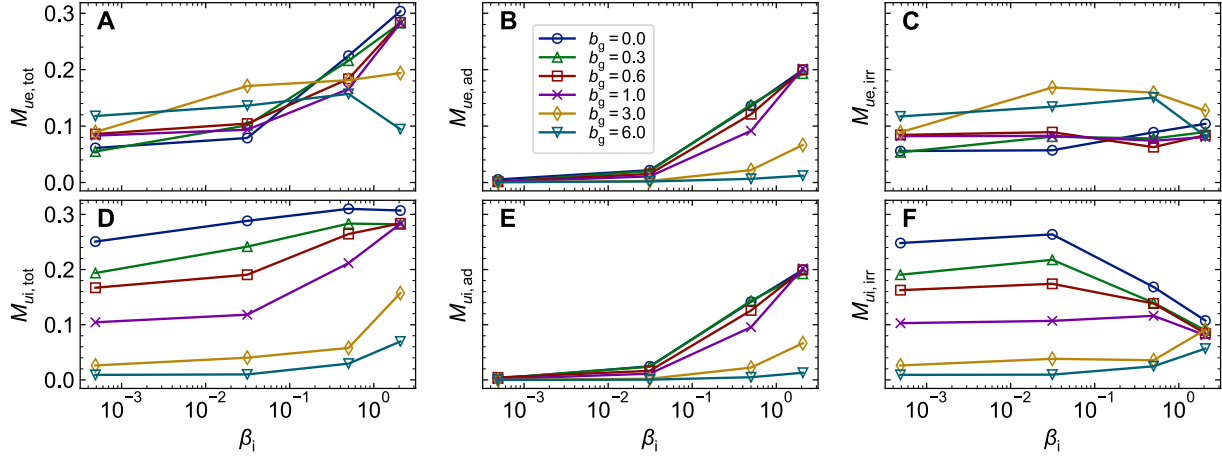


Figure 3.9: Guide field b_g and proton- β_i dependence of electron (A) total, (B) adiabatic, (C) irreversible heating; proton (D) total, (E) adiabatic, and (F) irreversible heating. The heating fractions are defined in Sec. 3.4 (see Eqs. 3.12–3.15). For these simulations, $m_i/m_e = 1836$, $\sigma_w = 0.1$, and $T_{e0}/T_{i0} = 1$.

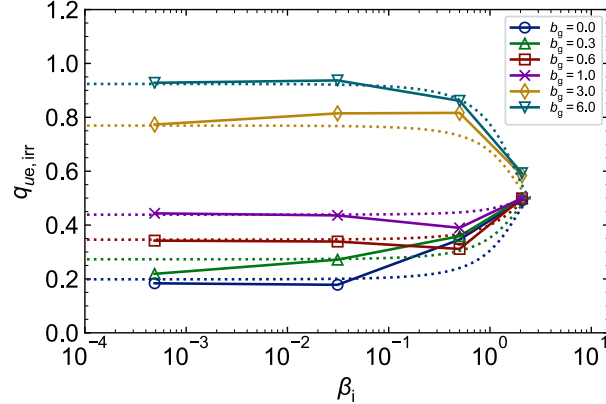


Figure 3.10: Guide field and proton- β_i dependence of electron irreversible heating efficiency, $q_{ue,irr}$ (see Eq. (3.17)). The values plotted here are computed from $M_{ue,irr}$ and $M_{ui,irr}$ shown in panels C and F of Fig. 3.9. Dotted lines show the fitting function in Eq. (3.19) for b_g in the range 0–6.

3.5.4 Electron irreversible heating efficiency: T_{e0}/T_{i0} and σ_w dependence

For simplicity, we focused in Sec. 3.5.3 on electron heating for cases with representative magnetization $\sigma_w = 0.1$ and temperature ratio $T_{e0}/T_{i0} = 1$. A full exploration of the dependence of electron and proton heating on β_i , b_g , σ_w , and T_{e0}/T_{i0} is beyond the scope of this work. Nevertheless, for a limited range of b_g and β_i , we present in Fig. 3.11 the electron irreversible heating efficiencies when we vary the electron-to-proton temperature ratio T_{e0}/T_{i0} in the range 0.1–1 (panels A and B), as

well as for several simulations with $\sigma_w = 1$ (panel C). The physical parameters of these runs are given in Tab. 3.2.

The effect of varying the initial electron-to-proton temperature ratio for antiparallel reconnection ($b_g = 0$) is demonstrated in panel A of Fig. 3.11. At low β_i , the electron irreversible heating efficiency shows nearly no dependence on β_i or temperature ratio. At high β_i , the dependence on temperature ratio can be understood via the dependence of $\beta_{i,\max}$ on T_{e0}/T_{i0} . According to Eq. (3.18), decreasing the temperature ratio for fixed σ_w leads to an increase in $\beta_{i,\max}$, and so (as discussed in Sec. 3.5.2) in the value of $\beta_i \sim \beta_{i,\max}$ where equipartition between electrons and protons is realized.

The effect of varying the temperature ratio for $b_g = 0.3$ and $b_g = 6$ is shown in panel B. As for antiparallel reconnection, there is no significant dependence on T_{e0}/T_{i0} at low β_i , for each of the two b_g values. While $\beta_{i,\max} = 2.5$ for $T_{e0}/T_{i0} = 1$, for $T_{e0}/T_{i0} = 0.3$ we expect $\beta_{i,\max} \approx 3.85$, so equipartition between electrons and protons, which should hold regardless of b_g at $\beta_i \sim \beta_{i,\max}$, is expected at higher β_i than probed in panel (B).

The effect of varying the magnetization and guide field strength is shown in panel C of Fig. 3.11. At low β_i , the electron irreversible heating efficiency has a weaker dependence on guide field for $\sigma_w = 1$ than for $\sigma_w = 0.1$. For $\beta_i \sim \beta_{i,\max} \propto \sigma_w^{-1}$ (see Eq. (3.18)), irreversible heating of electrons and protons is in equipartition, and this conclusion holds regardless of σ_w or b_g .

Run ID:	b8e-3.bg0.t1e-1	b3e-2.bg0.t1e-1	b1e-1.bg0.t1e-1	b5e-1.bg0.t1e-1	b2.bg0.t1e-1	
β_i	7.8×10^{-3}	0.031	0.13	0.5	2	
b_g	0	0	0	0	0	
σ_w	0.1	0.1	0.1	0.1	0.1	
T_{e0}/T_{i0}	0.1	0.1	0.1	0.1	0.1	
Run ID:	b8e-3.bg0.t3e-1	b3e-2.bg0.t3e-1	b1e-1.bg0.t3e-1	b5e-1.bg0.t3e-1	b2.bg0.t3e-1	
β_i	7.8×10^{-3}	0.031	0.13	0.5	2	
b_g	0	0	0	0	0	
σ_w	0.1	0.1	0.1	0.1	0.1	
T_{e0}/T_{i0}	0.3	0.3	0.3	0.3	0.3	
Run ID:	b3e-2.bg3e-1.t3e-1	b5e-1.bg3e-1.t3e-1	b2.bg3e-1.t3e-1	b3e-2.bg6.t3e-1	b5e-1.bg6.t3e-1	b2.bg6.t3e-1
β_i	0.031	0.5	2	0.031	0.5	2
b_g	0.3	0.3	0.3	6	6	6
σ_w	0.1	0.1	0.1	0.1	0.1	0.1
T_{e0}/T_{i0}	0.3	0.3	0.3	0.3	0.3	0.3
Run ID:	b8e-3.bg3e-1.s1	b3e-2.bg3e-1.s1	b2e-1.bg3e-1.s1	b8e-3.bg6.s1	b3e-2.bg6.s1	b2e-1.bg6.s1
β_i	7.8×10^{-3}	0.031	0.2	7.8×10^{-3}	0.031	0.2
b_g	0.3	0.3	0.3	6	6	6
σ_w	1	1	1	1	1	1
T_{e0}/T_{i0}	1	1	1	1	1	1

Table 3.2: Physical parameters for simulations with unequal temperature ratios, as well as $\sigma_w = 1$, described in Sec. 3.5.4.

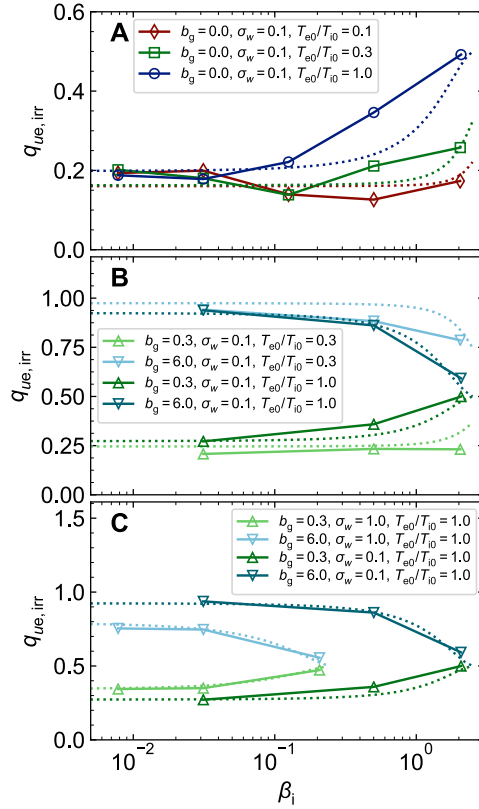


Figure 3.11: Similar to Fig. 3.10, but for the simulations listed in Tab. 3.2 rather than Tab. 3.1 (fiducial cases with $\sigma_w = 0.1, T_{e0}/T_{i0} = 1$ are also shown for reference); dependence of electron irreversible heating efficiency, $q_{ue,irr}$, for (A) $T_{e0}/T_{i0} = 0.1$ up to 1 and antiparallel reconnection, (B) unequal initial electron and proton temperatures in the upstream, $T_{e0}/T_{i0} = 0.3$, for two guide field cases, $b_g = 0.3$ and 6, and (C) $\sigma_w = 1$, again for $b_g = 0.3$ and 6. As before, dotted lines show the fitting function in Eq. (3.19).

3.5.5 Fitting function

For use as a sub-grid model of electron heating in magnetohydrodynamic simulations (as in Ressler et al. (2017a); Chael et al. (2018); Ryan et al. (2018)), we provide the following fitting formula, motivated by the simulation results presented in Secs. 3.5.3 and 3.5.4:

$$q_{ue,\text{irr,fit}}(\beta_i, b_g, T_{e0}/T_{i0}, \sigma_w) = \frac{1}{2} (\tanh(0.33 b_g) - 0.4) \\ \times 1.7 \tanh\left(\frac{(1 - \beta_i/\beta_{i,\text{max}})^{1.5}}{(0.42 + T_{e0}/T_{i0})\sigma_w^{0.3}}\right) + \frac{1}{2}, \quad (3.19)$$

where $\beta_{i,\text{max}}$ is in Eq. (3.18) in terms of σ_w and T_{e0}/T_{i0} .

The fitting function in Eq. (3.19) has the following limits: for low β_i , $q_{ue,\text{irr,fit}}$ asymptotes to a (σ_w - and b_g -dependent) value that does not depend on β_i . The asymptotic low- β_i limit tends to the equipartition value $q_{ue,\text{irr,fit}} \sim 0.5$ for $\sigma_w \gg 1$ (i.e., in the limit of ultra-relativistic reconnection), regardless of b_g . Still at $\beta_i \ll 1$, electrons receive most of the irreversible heat if $b_g \gtrsim 1.3$. For $b_g \gg 1$, $\sigma_w \ll 1$ and $\beta_i \ll 1$, we get $q_{ue,\text{irr,fit}} \approx 1.0$, i.e., all of the irreversible heat goes to electrons. At $\beta_i \sim \beta_{i,\text{max}}$, the fitting function returns $q_{ue,\text{irr,fit}} \approx 0.5$, independent of b_g , σ_w , and T_{e0}/T_{i0} . For b_g in the range 0–6, the fitting function in Eq. (3.19) is plotted in Figs. 3.10 and 3.11 as dotted lines, showing that it matches well the trends obtained from the simulations.

Predictions of the reconnection-mediated heating model presented here differ from those of heating via a Landau-damped turbulent cascade (Howes, 2010; Kawazura et al., 2019; Zhdankin et al., 2019). In Fig. 3.12 we show a comparison between reconnection-based heating (Eq. (3.19)) for the antiparallel ($b_g = 0$, panel A) and strong guide field ($b_g = 6$, panel B) cases, and the turbulence-based heating prescription of Kawazura et al. (2019) (panel C), over the range of plasma conditions we have investigated. First, one notices that turbulence-based heating is much more similar to heating via reconnection in the strong guide field limit, rather than in the antiparallel case. In fact, for the latter (in contrast to the first two), protons are heated much more than electrons at low β_i .

However, some differences persist even between turbulent heating and heating via strong guide field reconnection. In fact, the turbulence-based heating model is nearly insensitive to the initial temperature ratio T_{e0}/T_{i0} , whereas for guide field reconnection, an increase in T_{e0}/T_{i0} decreases $\beta_{i,\max}$ (see Eq. (3.18)), which in turn decreases the value of β_i at which electrons and protons achieve equipartition, i.e., $q_{ue,\text{irr}} \sim 0.5$. More generally, relativistic effects leave a unique fingerprint in our results at $\beta_i \sim \beta_{i,\max}$,¹⁰ where both species start as relativistically hot, and in the limit $\sigma_w \gg 1$. In either case, protons and electrons receive equal amount of the dissipated energy, i.e., $q_{ue,\text{irr}} \sim 0.5$, regardless of the guide field strength.

3.5.6 Temperature anisotropy

Guide field reconnection can result in highly anisotropic electron distribution functions at late times (Dahlin et al., 2014; Numata & Loureiro, 2015). Yet, to determine the dimensionless internal energy per particle in the fluid rest frame, we have assumed an isotropic stress-energy tensor at every location in the upstream and in the downstream. Eq. (3.10) relies on this assumption. In addition, we have implicitly assumed isotropy in our prediction for the amount of adiabatic heating.

To assess whether isotropy is a reasonable assumption, we show in Fig. 3.13 the electron temperature anisotropy $T_{e,\parallel}/T_{e,\perp}$ in the island (\parallel and \perp refer to orientations relative to the local magnetic field); the simulations here are similar to the production runs listed in Tab. 3.1, but cover β_i more densely in the range 8×10^{-3} up to 2.

For weak guide fields ($b_g \lesssim 0.3$), the electron temperature is isotropic, $T_{e,\parallel}/T_{e,\perp} \approx 1$ (see RSN17). For $b_g \gtrsim 0.6$ and $\beta_i \lesssim 0.5$, we find substantial anisotropy, with temperature ratios in the range $T_{e,\parallel}/T_{e,\perp} \approx 2\text{--}27$. In these cases, isotropy is certainly not a valid assumption. As discussed above, this will affect our inferred internal energy (since, in principle, Eq. (3.10) cannot be employed) and the predicted degree of adiabatic heating. As regard to the internal energy, in a few cases we have

¹⁰We remark that $\beta_{i,\max}$ may be much larger or much smaller than unity, depending primarily on σ_w .

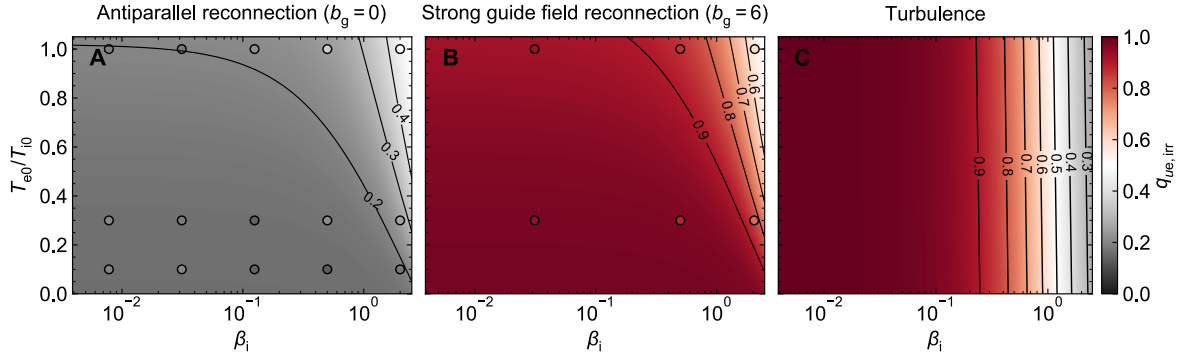


Figure 3.12: Comparison of electron irreversible heating efficiency, $q_{ue,\text{irr}}$ (defined in Eq. (3.17)) for (A) antiparallel reconnection ($b_g = 0$), (B) strong guide field reconnection ($b_g = 6$), and (C) the turbulent heating prescription of Kawazura et al. (2019) (see Eq. 2 therein), in the β_i - T_{e0}/T_{i0} parameter space. Circles in panels A and B show parameters probed directly by the simulations discussed in Sec. 3.5.4, colors in panels A and B employ the fitting function in Eq. (3.19).

calculated all the components of the stress energy tensor in the simulation frame. By transforming into the comoving frame, we do not need to rely on any assumption of isotropy. In general, we have found the inferred internal energies differ from Eq. (3.10) only at the $\sim 10\%$ level.

As regard to adiabatic heating, we have discussed in Sec. 3.5.3 that compressive heating is suppressed by strong guide fields, as well as at low values of β_i . Therefore, in the majority of cases that show substantial temperature anisotropy, adiabatic heating constitutes a negligible fraction of the total heating, so the degree of anisotropy has only a negligible effect on the inferred irreversible heating. A notable exception here is the run with $\beta_i \approx 0.1$ and $b_g = 1$, for which compressive heating accounts for about 33% of the total heating, and the measured anisotropy in the island is non-negligible, $T_{e,\parallel}/T_{e,\perp} \approx 2$; of all our simulations, this one has the greatest systematic uncertainty on the compressive heating, and consequently on the inferred irreversible heating.

3.5.7 Mechanisms of electron heating in guide field reconnection

The orbit of a charged particle in electromagnetic fields may be approximated as the superposition of two motions: fast circular motion about a point, the *guiding center*, and a slow drift of the guiding center itself. This approximation is valid when the particle's gyroperiod is short compared

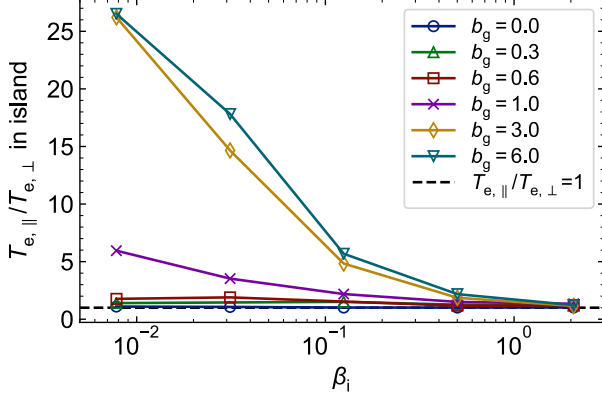


Figure 3.13: Ratio of electron parallel-to-perpendicular temperature in the island region. For reference, the black dashed line indicates temperature isotropy, $T_{e,\parallel}/T_{e,\perp} = 1$. Parallel (\parallel) and perpendicular (\perp) are in reference to the direction of the local magnetic field. The simulations shown here are similar to those listed in Tab. 3.1, but cover β_i in the narrower range 8×10^{-3} –2.

to the timescale of variation of the fields, and also when the particle's Larmor radius is small compared to the field gradient length scale. When valid, the guiding center approximation can provide valuable insight into the mechanisms responsible for particle energization (see e.g., Dahlin et al. (2014); Sironi & Narayan (2015); Wang et al. (2016)). In this section, we use the guiding center approximation to investigate the mechanisms of electron heating for $\beta_i \sim 0.01$, as a function of the guide field strength. Details of the guiding center decomposition are discussed in App. 4.B.

We track $\sim 10^4$ electrons starting initially in the upstream region (see Fig. 3.14, panel A), and compute the contributions $\Delta\epsilon_{E\parallel}$ and $\Delta\epsilon_{\text{curv}}$, which correspond to energy changes due to the parallel electric field and curvature drift, respectively. For clarity we focus in our discussion only on the E -parallel and curvature drift terms, which tend to dominate for the cases we investigate here (we have directly verified this, and it agrees with findings of Dahlin et al. (2014) for nonrelativistic reconnection). While the simulation timestep is $\Delta t \approx 0.1 \omega_{pe}^{-1}$, the time interval we use here for outputs of the field and electron properties for the guiding center analysis is around $\Delta t_{\text{out}} \approx 3 \omega_{pe}^{-1}$. To ensure that this time resolution is sufficient for a guiding center reconstruction, we compare the actual evolution of the electron energy (computed on the fly by the simulation) to

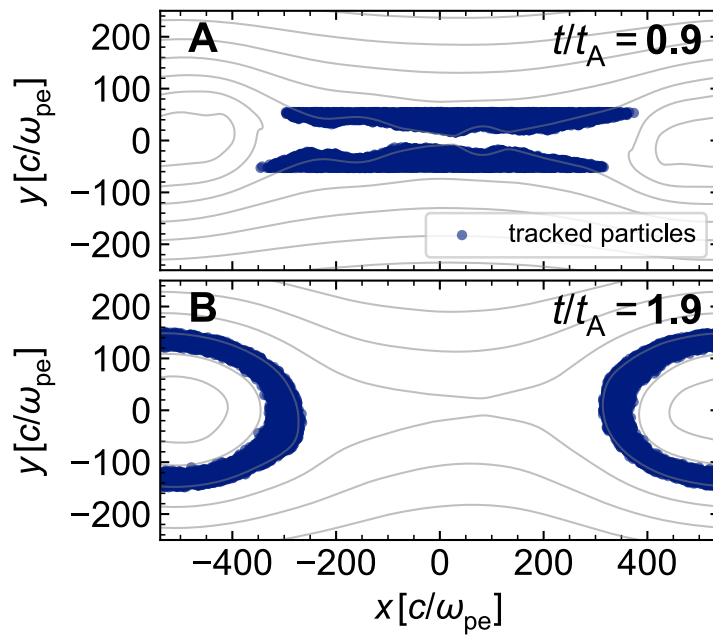


Figure 3.14: Representative (A) initial and (B) final locations of electrons in simulations used for the guiding center analysis outlined in Sec. 3.5.7. For the simulation shown here, $b_g = 0.1$, $\beta_i \approx 7.8 \times 10^{-3}$, $\sigma_w = 0.1$, $m_i/m_e = 1836$, and $T_{e0}/T_{i0} = 1$. In this case, a sample of about 1.5×10^4 particles is tracked as they propagate from the upstream to the island region.

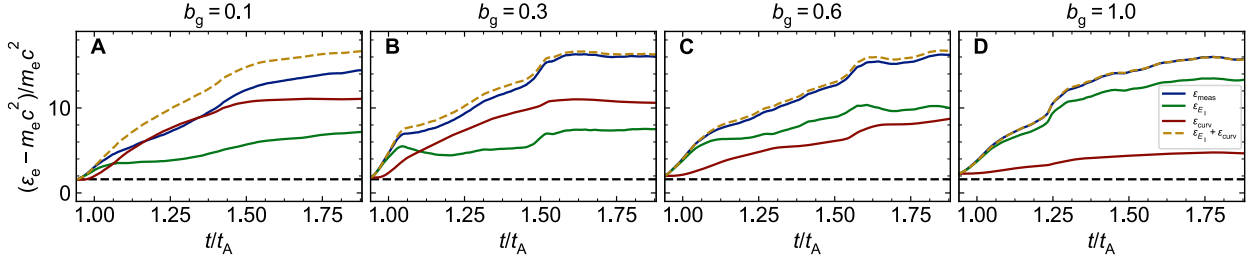


Figure 3.15: Average energy gain per electron for the population of tracked particles (see Fig. 3.14), for guide field strengths b_g in the range 0.1–1, shown in panels A–D. The measured change in energy (blue) is compared to energization due to the parallel electric field (green) and curvature drift (red) terms, as well as their sum (dashed yellow). The initial dimensionless electron internal energy in the upstream, $v_{e0} \approx 1.6$, is shown by the horizontal dashed black line.

the value calculated from the downsampled field and particle information. For the time range over which we track particles ($\sim 3700 \omega_{pe}^{-1} \approx 1 t_A$ for these simulations), the energy gain computed from downsampled field and particle information shows excellent agreement with the actual value evolved at the time resolution of the simulation.

To study electron heating via the guiding center theory, we use four simulations for which $\beta_i = 7.8 \times 10^{-3}$ and $b_g \in \{0.1, 0.3, 0.6, 1\}$. Here, we use a smaller box size, $L_x \approx 1080 c/\omega_{pe}$ (the domain size dependence of our results is discussed in App. 4.A). Apart from the domain size, the parameters are the same as in the main guide field simulations (i.e., $m_i/m_e = 1836$, $\sigma_w = 0.1$, $T_{e0}/T_{i0} = 1$, $c/\omega_{pe} = 4$ cells, $N_{ppc} = 16$). The heating fractions extracted from these simulations are roughly the same as in the production runs of Tab. 3.1.

Electrons are tracked from $t/t_A \approx 0.9$ to 1.9 (equivalently, $t\omega_{pe} \approx 3330$ to 7030). The tracked particles are selected at the initial time to lie in the upstream region, within roughly $\pm 50 c/\omega_{pe}$ of $y = 0$ (see Fig. 3.14, panel A; grey contours show magnetic field lines). The selected electrons are tracked for $\sim 3700 \omega_{pe}^{-1} \approx 1 t_A$, at which point they typically reside in the island region (panel B).

Fig. 3.15 shows the time evolution of electron energy gains, for guide fields $b_g = 0.1, 0.3, 0.6$, and 1 in panels A, B, C, and D, respectively (the strength of the guide field increases from left to right). The energy gain is presented in dimensionless form with rest mass subtracted, i.e.,

$(\varepsilon_e - m_e c^2)/m_e c^2 \cong v_e$.¹¹ In each panel, the blue line corresponds to the electron energy gain measured directly in the simulations. The E -parallel and curvature terms are shown in green and red, respectively, and the yellow dashed curve is their sum. The good agreement between dashed yellow and blue lines is an indication that our output time resolution is adequate for the guiding center reconstruction. The black dashed line shows the specific internal energy in the far upstream ($v_{e0} \approx 1.6$), which matches well the starting point of the curves.

For weak guide fields, $b_g \lesssim 0.6$, the energy gains due to E -parallel and curvature terms are comparable, consistent with the findings of Dahlin et al. (2014). For strong guide fields, energization due to the parallel electric field dominates; in this case, the magnetic field in the current sheet is approximately straight (since it is dominated by the out-of-plane field), so heating due to the curvature term is negligible. Though the mechanisms responsible for energization of electrons differ for weak and strong guide fields, the overall energy gain is about the same in all cases, $(\varepsilon_e - m_e c^2)/m_e c^2 \cong v_e \approx 14.5$ (see also Fig. 3.8, panel A). The temporal evolution of electron heating (both the total heating, as well as E -parallel and curvature contributions) saturates at late times, when most of the particles reside in the primary island.

Fig. 3.16 shows the 2D spatial distribution of power associated with the E -parallel (panels A–D) and curvature (panels E–H) energization terms. For every tracked electron at each time, we deposit the corresponding E -parallel and curvature powers at the location where the particle instantaneously resides (power is deposited into spatial bins of length and width equal to $2c/\omega_{pe}$; note that the colorbar range in Fig. 3.16 depends on this binning, so the units are arbitrary), and then we average over the number of tracked electrons. Grey lines show the magnetic field lines at $t/t_A \approx 1.9$, for reference. For weak guide fields ($b_g \lesssim 0.3$), energization due to the parallel electric field is patchy (Dahlin et al. (2014)), with heating spread over the exhaust region as well

¹¹This is not an equality because $\varepsilon_e - m_e c^2$ includes bulk kinetic energy, in addition to internal energy. However, in the primary island the latter greatly dominates over the former.

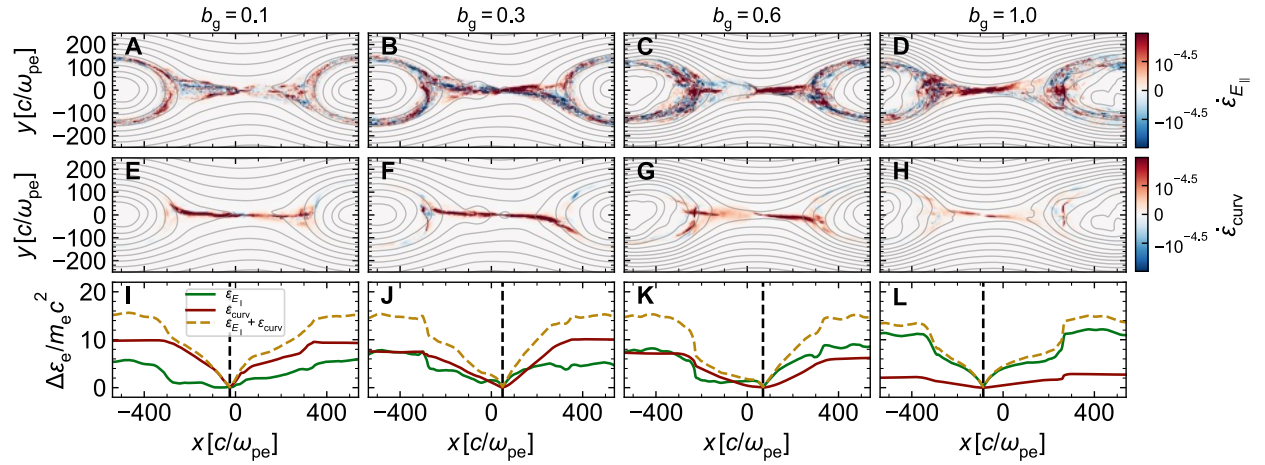


Figure 3.16: 2D spatial dependence of energy changes due to (A–D) E -parallel and (E–H) curvature drift terms in the guiding center approximation, and (I–L) 1D profiles of E -parallel heating (green), curvature drift heating (red), and their sum (dashed yellow). From left to right, the guide field increases from 0.1 to 1. The first and second rows show the per-particle average power deposited from $t/t_A = 0.9$ up to 1.9 ($t\omega_{pe} \approx 3330$ to 7030 in these simulations; the domain size $L_x \approx 1080 c/\omega_{pe}$ used here is a factor of two smaller than for the runs in Tab. 3.1, a choice that is justified in App. 4.A). For reference, magnetic field lines at $t/t_A = 1.9$ are shown in grey, but note that they are not static from $t/t_A = 0.9$ to 1.9. In the third row, 1D profiles are computed from 2D profiles by summing first along y , then summing cumulatively along x , starting from the vertical dashed black line (which represents roughly the location of the central X-point) and proceeding outward along $\pm x$.

as the island. On average, there is a net energy gain, however, parallel electric fields can also locally cool the electrons (blue patches in panel A). Heating due to the curvature drift is localized predominantly along the walls of the exhaust, in particular on the upper left and lower right (as in panel B, for $b_g = 0.3$), where outflowing electrons tend to get focused (see also Fig. 3.2, panel F).

As the strength of the guide field increases, the relative importance of the curvature drift energization decreases (panels G–H), and the E -parallel heating becomes dominant (panels C–D). A substantial amount of heating due to the parallel electric field is localized in the exhaust region, however energization continues into the island.

While the guiding center formalism makes no distinction between adiabatic and irreversible heating, we can infer based on our results for low β_i guide field reconnection (see Fig. 3.9, first row) that the E -parallel and curvature drift terms in this case (having $\beta_i \sim 0.01$) contribute predominantly to the irreversible heating of electrons. Since compressive heating is negligible at $\beta_i \approx 8 \times 10^{-3}$ (see Fig. 3.9, panel B; also, Eq. (3.16)), irreversible heating in the low β_i regime represents the main contribution to total electron heating. It follows that, in this low β_i regime, the guiding center decomposition assesses contributions to irreversible heating.

To clarify the spatial dependence of E -parallel and curvature drift heating, we show in the last row of Fig. 3.16 (panels I–L) the 1D cumulative sum along $\pm x$ (as in Dahlin et al. (2014)), starting from the vertical dashed line, of the E -parallel (solid green) and curvature (solid red) energization rates displayed in the first and second rows; their sum is shown by the dashed yellow line. This shows that heating continues throughout the exhaust region, and at the interface between the outflow and the primary island. Little additional heating happens inside the primary island.

3.6 Summary and discussion

By means of fully-kinetic large-scale 2D PIC simulations, we have investigated guide field reconnection in the transrelativistic regime most relevant to black hole coronae and hot accretion flows.

In particular, we have focused on the fundamental question of electron and proton heating via reconnection, differentiating between adiabatic-compressive and irreversible components. All our simulations employ the realistic mass ratio, $m_i/m_e = 1836$.

We find that the energy partition between electrons and protons can vary substantially depending on the strength of the guide field. For a strong guide field $b_g = B_g/B_0 \sim 6$ and low proton beta $\beta_i \lesssim 0.5$, around 10% of the free magnetic energy per particle is converted to irreversible electron heating (regardless of β_i), whereas the efficiency of irreversible proton heating is much smaller, of order $\sim 1\%$ (these values refer to our fiducial magnetization $\sigma_w = 0.1$ and temperature ratio $T_{e0}/T_{i0} = 1$). It follows that the energy partition at high guide fields differs drastically from the antiparallel limit ($b_g = 0$), in which electrons receive only $\sim 6\%$ of the free magnetic energy per particle, and proton irreversible heating is around four times as much, $\sim 24\%$ (RSN17).

While the energy partition between electrons and protons changes drastically with the guide field strength at low β_i , at $\beta_i \sim 2$ ($\approx \beta_{i,\max}$, for $\sigma_w = 0.1$ and $T_{e0}/T_{i0} = 1$), the irreversible heating of electrons and protons is in approximate equipartition, regardless of the guide field strength. That is, as $\beta_i \rightarrow \beta_{i,\max}$ (when both species start relativistically hot), electrons and protons each receive roughly the same amount of energy, $\sim 10\%$ of the free magnetic energy per particle in the upstream.

In addition to a comprehensive investigation of the guide field dependence of electron and proton energy partition for our fiducial cases with $\sigma_w = 0.1$ and $T_{e0}/T_{i0} = 1$, we study several cases with larger magnetization, $\sigma_w = 1$, and smaller temperature ratios, $T_{e0}/T_{i0} = 0.1, 0.3$. Motivated by our extensive exploration of the parameter space (Tab. 3.1 and (Tab. 3.2)), we provide a fitting function (Eq. (3.19)), which captures the approximate dependence of electron irreversible heating efficiency on β_i, b_g, σ_w , and T_{e0}/T_{i0} . This fitting function can be used for sub-grid models of low-luminosity accretion flows such as Sgr A* at the Galactic Center.

As we have said, for strong guide fields and low β_i , electrons receive most of the irreversible heat

that is transferred to the particles. This is similar to recent findings of electron and proton heating in magnetized turbulence (see Fig. 3.12, which compares with Kawazura et al. 2019), suggesting a fundamental connection between reconnection and turbulence, as indeed supported by recent theoretical works (Boldyrev & Loureiro, 2017; Loureiro & Boldyrev, 2017; Mallet et al., 2017; Comisso & Sironi, 2018; Shay et al., 2018). Still, some key differences between our reconnection-based heating prescription and turbulence-based heating prescriptions (Howes, 2010; Kawazura et al., 2019) persist: for $\beta_i \sim \beta_{i,\max}$, when both electrons and protons start relativistic, reconnection leads to equipartition between the two species independently of the guide field strength, whereas for the prescription of, e.g., Kawazura et al. (2019), protons receive the majority of the irreversible heating at high β_i . Also, for reconnection-based heating, the transition to equipartition happens not at $\beta_i \sim 1$, but generally at $\beta_i \sim \beta_{i,\max}$, which can differ from unity if $\sigma_w \ll 1$ or $\sigma_w \gg 1$.

We have also used a guiding center analysis to study the mechanisms responsible for electron heating as a function of the guide field strength, for a representative low- β_i case with $\beta_i \sim 0.01$. The E -parallel and curvature drift terms dominate the energy change of electrons, and their relative importance shifts depending on the strength of the guide field; for weak to moderate guide fields, $0.1 \lesssim b_g \lesssim 0.6$, the energy gains due to E -parallel and curvature drift are comparable, but for a strong guide field, $b_g \gtrsim 1$, electron energization is dominated by E -parallel heating. Though the mechanisms of electron heating differ depending on the strength of the guide field, the net increase in electron energy remains about the same.

We conclude by remarking on some simplifying assumptions of the present work, as well as discussing future lines of inquiry. First, in our investigation of guide field reconnection, we have focused primarily on one value of the magnetization, $\sigma_w = 0.1$, and equal temperature ratios in the upstream, $T_{e0}/T_{i0} = 1$,¹² to simplify the parameter space investigation. The dependence of

¹²The fitting function Eq. (3.19), however, also incorporates results from additional simulations with $\sigma_w = 1$ and $T_{e0}/T_{i0} = 0.1, 0.3$, for both low and high guide field regimes.

energy partition via reconnection on guide field strength for other values of the magnetization remains under-explored, especially for the low β_i regime, where we find that the proton irreversible heating efficiency depends strongly on the guide field strength. Similarly, the effect of the upstream temperature ratio T_{e0}/T_{i0} in guide field reconnection is under-explored.

A second simplification is that we have used 2D simulations, which may differ from 3D as regard to particle heating. In 3D reconnection, in place of magnetic islands, twisted tubes of magnetic flux will develop; to understand the differences as regard to heating, a comparison between 2D and 3D transrelativistic reconnection will be important, especially in the low- β_i regime, where secondary magnetic islands are copiously generated.

Finally, in our guiding center analysis, we have focused on electron heating in the low β_i regime, where the assumption that the magnetic field varies negligibly over the electron radius of gyration is easily satisfied. At high β_i , this assumption is less robust, and the guiding center theory may be not applicable. Additional theoretical work will be necessary to provide insight into the physics of electron and proton heating in these regimes.

Acknowledgements

This work is supported in part by NASA via the TCAN award grant NNX14AB47G and by the Black Hole Initiative at Harvard University, which is supported by a grant from the Templeton Foundation. LS acknowledges support from DoE DE-SC0016542, NASA Fermi NNX-16AR75G, NASA ATP NNX-17AG21G, NSF ACI1657507, and NSF AST-1716567. The simulations were performed on Habanero at Columbia, on the BHI cluster at the Black Hole Initiative, and on NASA High-End Computing (HEC) resources. This research also used resources of the National Energy Research Scientific Computing Center, a DOE Office of Science User Facility supported by the Office of Science of the U.S. Department of Energy under Contract No. DE-AC02-05CH11231.

3.A Convergence of irreversible heating fractions with respect to domain size L_x

The main focus of this paper is the irreversible heating of electrons and protons. In principle, the measured values may depend on the domain size L_x if, for example, the computational box is so small that the reconnection outflows do not have the chance to reach the asymptotic Alfvén limit. In this case, the bulk energy of the outflows would be artificially suppressed, which could in turn suppress the particle irreversible heating. In this appendix, we present a set of lower resolution ($c/\omega_{pe} = 2$ instead of $c/\omega_{pe} = 4$) simulations with varying domain sizes, $L_x = 1080 c/\omega_{pe}$, $2160 c/\omega_{pe}$ (our fiducial choice), and $4176 c/\omega_{pe}$, to explore the box size dependence of the electron and proton irreversible heating fractions, $M_{ue,\text{irr}}$ and $M_{ui,\text{irr}}$. For these simulations, $b_g = 1$, $m_i/m_e = 1836$, $\sigma_w = 0.1$, $\beta_i = 0.125$, and $T_{e0}/T_{i0} = 1$. In Fig. 3.17, we show the time dependence of electron (panel A) and proton (panel B) irreversible heating fractions for the three simulations with varying L_x .

For box sizes $L_x \gtrsim 2160 c/\omega_{pe}$, the electron irreversible heating converges to $M_{ue,\text{irr}} \approx 0.11$. With respect to electron irreversible heating, even the smaller box with $L_x \gtrsim 1080 c/\omega_{pe}$ differs by only $\sim 10\%$ compared to the larger boxes. This justifies the fiducial domain size $L_x = 2160 c/\omega_{pe}$ that we use to study electron heating in guide field reconnection, and also the choice of $L_x = 1080 c/\omega_{pe}$ in Sec. 3.5.7, where we use the guiding center theory to study electron energization. The proton irreversible heating depends more strongly on the box size, but still shows reasonable agreement between the fiducial box size ($L_x = 2160 c/\omega_{pe}$) and larger boxes ($L_x = 4176 c/\omega_{pe}$). In contrast, smaller boxes underestimate the proton heating fraction (green line).

3.B Guiding center formalism

Here, we review the details of guiding center formalism (Northrop, 1961, 1963a,b). The guiding center method provides an approximation to particle motion along a magnetic field line, in the limit that the inverse Larmor frequency $\omega^{-1} \equiv mc/qB$ is small compared to the timescale that

Domain size convergence test

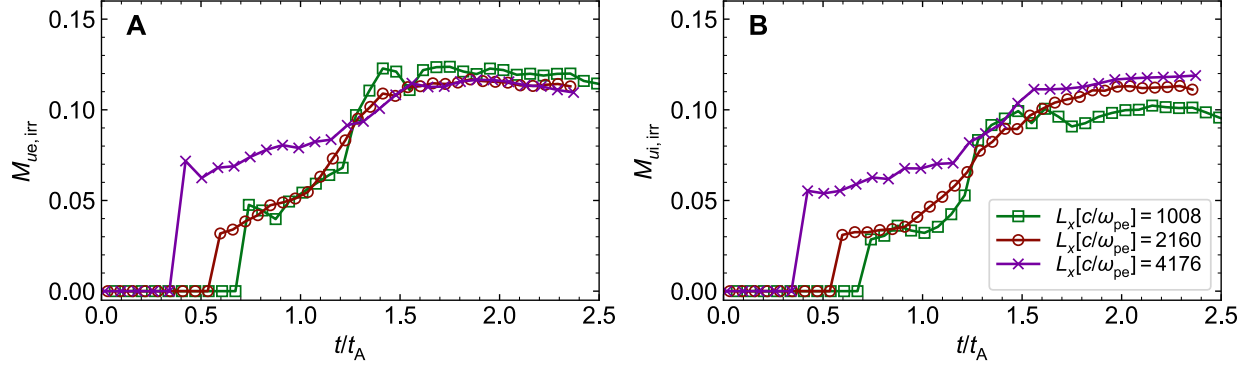


Figure 3.17: Test of convergence for (A) electron and (B) proton irreversible heating fractions, with respect to domain size L_x . We show measured irreversible heating fractions from simulations with $L_x = 1080 c/\omega_{pe}$, $2160 c/\omega_{pe}$, and $4176 c/\omega_{pe}$. For these simulations, $b_g = 1$, $m_i/m_e = 1836$, $\sigma_w = 0.1$, $\beta_i = 0.125$, and $T_{e0}/T_{i0} = 1$.

characterizes variation in the magnetic field, or equivalently, that the magnetic field does not vary significantly over the Larmor (gyration) radius, $\rho \equiv v_\perp/\omega$, where v_\perp is the particle velocity perpendicular to the magnetic field. To study the motion of a particle due to an electromagnetic field, we start with the Lorentz force law:

$$\ddot{\mathbf{r}} = \frac{q}{m} \left(\mathbf{E}(\mathbf{r}) + \frac{\dot{\mathbf{r}}}{c} \times \mathbf{B}(\mathbf{r}) \right), \quad (3.20)$$

where \mathbf{r} denotes the location of the particle. Eq. 3.20 is written in the nonrelativistic limit, but the effect of relativistic inertia can be inferred from the substitution $m \rightarrow \gamma m$, where γ is the particle's Lorentz factor. Define two vectors, \mathbf{R} and $\boldsymbol{\rho}$, corresponding to the location of the guiding center and the location of the particle relative to the guiding center, respectively. Then $\mathbf{r} = \mathbf{R} + \boldsymbol{\rho}$. The guiding center coordinates are illustrated in Fig. 3.18.

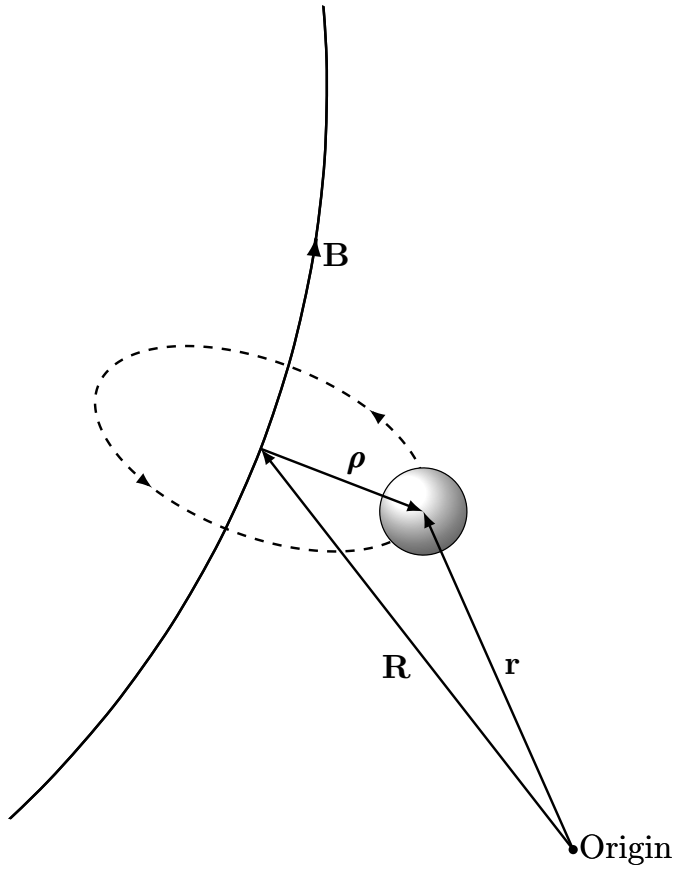


Figure 3.18: Illustration of the guiding center coordinates; in the guiding center formalism, the orbit of a particle is decomposed into rapid circular motion about a point, the guiding center (located at \mathbf{R}), and motion along the magnetic field \mathbf{B} .

A Taylor expansion in ρ about the guiding center \mathbf{R} , ignoring higher order terms in the expansion parameter $\epsilon \equiv m/q$, yields

$$\ddot{\mathbf{R}} + \ddot{\boldsymbol{\rho}} = \frac{q}{m} \left(\mathbf{E}(\mathbf{R}) + (\boldsymbol{\rho} \cdot \nabla) \mathbf{E}(\mathbf{R}) + \frac{\dot{\mathbf{R}} + \dot{\boldsymbol{\rho}}}{c} \times (\mathbf{B}(\mathbf{R}) + (\boldsymbol{\rho} \cdot \nabla) \mathbf{B}(\mathbf{R})) \right) + \mathcal{O}(\epsilon^2) \quad (3.21)$$

It is necessary to retain the final term in parentheses $\sim \dot{\boldsymbol{\rho}}\boldsymbol{\rho}$, because it is in fact of order ϵ .

Define a set of orthogonal basis vectors, $\hat{\mathbf{e}}_1 = \mathbf{B}/B$, $\hat{\mathbf{e}}_2$ which points toward the center of curvature of the magnetic field line, and $\hat{\mathbf{e}}_3 = \hat{\mathbf{e}}_1 \times \hat{\mathbf{e}}_2$, which is orthogonal to the previous two unit vectors.

With these unit vectors, the particle location, velocity, and acceleration can be written as

$$\boldsymbol{\rho} = \rho(\hat{\mathbf{e}}_2 \sin \theta + \hat{\mathbf{e}}_3 \cos \theta) \quad (3.22)$$

$$\dot{\boldsymbol{\rho}} = \omega \rho (\hat{\mathbf{e}}_2 \cos \theta - \hat{\mathbf{e}}_3 \sin \theta) + \frac{d}{dt}(\rho \hat{\mathbf{e}}_2) \sin \theta + \frac{d}{dt}(\rho \hat{\mathbf{e}}_3) \cos \theta \quad (3.23)$$

$$\begin{aligned} \ddot{\boldsymbol{\rho}} &= -\omega^2 \rho (\hat{\mathbf{e}}_2 \sin \theta + \hat{\mathbf{e}}_3 \cos \theta) + \dot{\omega} \rho (\hat{\mathbf{e}}_2 \cos \theta - \hat{\mathbf{e}}_3 \sin \theta) \\ &\quad + 2\omega \left(\frac{d}{dt}(\rho \hat{\mathbf{e}}_2) \cos \theta - \frac{d}{dt}(\rho \hat{\mathbf{e}}_3) \sin \theta \right) \\ &\quad + \frac{d^2}{dt^2}(\rho \hat{\mathbf{e}}_2) \sin \theta + \frac{d^2}{dt^2}(\rho \hat{\mathbf{e}}_3) \cos \theta \end{aligned} \quad (3.24)$$

where $\theta = \int \omega dt$, where ω . Note that $\dot{\boldsymbol{\rho}}$ contains terms of order 1, because $\omega \rho \sim (1/\epsilon)\epsilon \equiv 1$. The second and third terms in Eq. 3.23 are of order ϵ so they can be ignored upon substitution into Eq. 3.21. The terms in Eq. 3.24 are of order $1/\epsilon, 1, 1$, and ϵ , respectively, so only the first three terms need to be kept when substituting into Eq. 3.21.

Inserting Eqs. 3.22, 3.23, and 3.24 into Eq. 3.21, and evaluating the time-average over the gyration period $\int_0^{2\pi} (\dots) d\theta$, one obtains

$$\ddot{\mathbf{R}} = \frac{q}{m} \left(\mathbf{E}(\mathbf{R}) + \frac{\dot{\mathbf{R}}}{c} \times \mathbf{B}(\mathbf{R}) \right) + \frac{q}{mc} \langle \dot{\boldsymbol{\rho}} \times (\boldsymbol{\rho} \cdot \nabla) \mathbf{B}(\mathbf{R}) \rangle. \quad (3.25)$$

The angle brackets here denote the time-average; evaluating the time-average for the final term yields

$$\langle \dot{\boldsymbol{\rho}} \times (\boldsymbol{\rho} \cdot \nabla) \mathbf{B}(\mathbf{R}) \rangle = \frac{1}{2} \omega \rho^2 (\hat{\mathbf{e}}_2 \times (\hat{\mathbf{e}}_3 \cdot \nabla) \mathbf{B}(\mathbf{R}) - \hat{\mathbf{e}}_3 \times (\hat{\mathbf{e}}_2 \cdot \nabla) \mathbf{B}(\mathbf{R})). \quad (3.26)$$

The coefficient on the right hand side is the adiabatic moment:

$$\frac{1}{2}\omega\rho^2 = \frac{1}{2}\frac{qB}{mc} \left(\frac{mcv_{\perp}}{qB} \right)^2 = \frac{\frac{mv_{\perp}^2}{2B}c}{q} \equiv \frac{\mu c}{q} \quad (3.27)$$

Eq. 3.25 simplifies with the following vector identities:

$$\hat{\mathbf{e}}_2 \times (\hat{\mathbf{e}}_3 \cdot \nabla) \mathbf{B}(\mathbf{R}) = (\hat{\mathbf{e}}_3 \times \hat{\mathbf{e}}_1) \times (\hat{\mathbf{e}}_3 \cdot \nabla) \mathbf{B} \quad (3.28)$$

$$= \hat{\mathbf{e}}_1 (\hat{\mathbf{e}}_3 \cdot (\hat{\mathbf{e}}_3 \cdot \nabla) \mathbf{B}) - \hat{\mathbf{e}}_3 (\hat{\mathbf{e}}_1 \cdot (\hat{\mathbf{e}}_3 \cdot \nabla) \mathbf{B}) \quad (3.29)$$

The last term can be rewritten as

$$\hat{\mathbf{e}}_1 \cdot (\hat{\mathbf{e}}_3 \cdot \nabla) \mathbf{B} = \hat{\mathbf{e}}_1 \cdot (\hat{\mathbf{e}}_3 \cdot \nabla) (\hat{\mathbf{e}}_1 B) \quad (3.30)$$

$$= \hat{\mathbf{e}}_3 \cdot \nabla B + \frac{B}{2} (\hat{\mathbf{e}}_3 \cdot \nabla) \hat{\mathbf{e}}_1^2 \quad (3.31)$$

$$= \hat{\mathbf{e}}_3 \cdot \nabla B, \quad (3.32)$$

then

$$(\hat{\mathbf{e}}_2 \times (\hat{\mathbf{e}}_3 \cdot \nabla) \mathbf{B}) = \hat{\mathbf{e}}_1 (\hat{\mathbf{e}}_3 \cdot (\hat{\mathbf{e}}_3 \cdot \nabla) \mathbf{B}) - \hat{\mathbf{e}}_3 (\hat{\mathbf{e}}_3 \cdot \nabla B) \quad (3.33)$$

and similarly

$$(\hat{\mathbf{e}}_3 \times (\hat{\mathbf{e}}_2 \cdot \nabla) \mathbf{B}) = -\hat{\mathbf{e}}_1 (\hat{\mathbf{e}}_2 \cdot (\hat{\mathbf{e}}_2 \cdot \nabla) \mathbf{B}) + \hat{\mathbf{e}}_2 (\hat{\mathbf{e}}_2 \cdot \nabla B). \quad (3.34)$$

The two first terms in Eqs. 3.33 and 3.34 contain terms appearing in $\nabla \cdot \mathbf{B}$, which is clear if the

divergence operator is written as

$$\nabla = \hat{\mathbf{e}}_1(\hat{\mathbf{e}}_1 \cdot \nabla) + \hat{\mathbf{e}}_2(\hat{\mathbf{e}}_2 \cdot \nabla) + \hat{\mathbf{e}}_3(\hat{\mathbf{e}}_3 \cdot \nabla) \quad (3.35)$$

$$\Rightarrow \nabla \cdot \mathbf{B} = \hat{\mathbf{e}}_1 \cdot (\hat{\mathbf{e}}_1 \cdot \nabla) \mathbf{B} + \hat{\mathbf{e}}_2 \cdot (\hat{\mathbf{e}}_2 \cdot \nabla) \mathbf{B} + \hat{\mathbf{e}}_3 \cdot (\hat{\mathbf{e}}_3 \cdot \nabla) \mathbf{B}, \quad (3.36)$$

but

$$\hat{\mathbf{e}}_1 \cdot (\hat{\mathbf{e}}_1 \cdot \nabla) \mathbf{B} = \hat{\mathbf{e}}_1 \cdot \frac{\partial \mathbf{B}}{\partial \ell} = \frac{\partial B}{\partial \ell} \quad (3.37)$$

where ℓ denotes the distance along the magnetic field line. Now, subtract Eq. 3.34 from Eq. 3.33 to obtain

$$(\hat{\mathbf{e}}_2 \times (\hat{\mathbf{e}}_3 \cdot \nabla) \mathbf{B} - \hat{\mathbf{e}}_3 \times (\hat{\mathbf{e}}_2 \cdot \nabla) \mathbf{B}) = \hat{\mathbf{e}}_1(\hat{\mathbf{e}}_3 \cdot (\hat{\mathbf{e}}_3 \cdot \nabla) \mathbf{B}) + \hat{\mathbf{e}}_1(\hat{\mathbf{e}}_2 \cdot (\hat{\mathbf{e}}_2 \cdot \nabla) \mathbf{B}) \quad (3.38)$$

$$- \hat{\mathbf{e}}_2(\hat{\mathbf{e}}_2 \cdot \nabla B) - \hat{\mathbf{e}}_3(\hat{\mathbf{e}}_3 \cdot \nabla B) \quad (3.39)$$

$$= \hat{\mathbf{e}}_1(\hat{\mathbf{e}}_1 \cdot (\hat{\mathbf{e}}_1 \cdot \nabla) \mathbf{B} + \hat{\mathbf{e}}_2 \cdot (\hat{\mathbf{e}}_2 \cdot \nabla) \mathbf{B} + \hat{\mathbf{e}}_3 \cdot (\hat{\mathbf{e}}_3 \cdot \nabla) \mathbf{B}) \quad (3.40)$$

$$- \hat{\mathbf{e}}_1(\hat{\mathbf{e}}_1 \cdot (\hat{\mathbf{e}}_1 \cdot \nabla) \mathbf{B}) - \hat{\mathbf{e}}_2(\hat{\mathbf{e}}_2 \cdot \nabla B) - \hat{\mathbf{e}}_3(\hat{\mathbf{e}}_3 \cdot \nabla B) \quad (3.41)$$

$$= \hat{\mathbf{e}}_1(\nabla \cdot \mathbf{B}) - \hat{\mathbf{e}}_1 \frac{\partial B}{\partial \ell} - \hat{\mathbf{e}}_2(\hat{\mathbf{e}}_2 \cdot \nabla B) - \hat{\mathbf{e}}_3(\hat{\mathbf{e}}_3 \cdot \nabla B) \quad (3.42)$$

$$= -\nabla B, \quad (3.43)$$

where we have used $\nabla \cdot \mathbf{B} = 0$. Using this simplification in Eq. 3.25, we find that

$$\ddot{\mathbf{R}} = \frac{q}{m} \left(\mathbf{E}(\mathbf{R}) + \frac{\dot{\mathbf{R}}}{c} \times \mathbf{B}(\mathbf{R}) \right) - \frac{\mu}{m} \nabla B(\mathbf{R}) + \mathcal{O}(\epsilon). \quad (3.44)$$

This is the equation of motion for the guiding center, with fields evaluated at the location of the guiding center.

Eq. (3.44) separates into perpendicular and parallel components. In particular, solving for the perpendicular and parallel components of the guiding center velocity $\dot{\mathbf{R}}$ provides a form that is useful in evaluating the particle energy gain per unit time, dW/dt . To get the perpendicular component, cross on the right with $\hat{\mathbf{e}}_1$:

$$\ddot{\mathbf{R}} \times \hat{\mathbf{e}}_1 = \frac{q}{m} \left[\mathbf{E}(\mathbf{R}) \times \hat{\mathbf{e}}_1 + \left(\frac{\dot{\mathbf{R}}}{c} \times \mathbf{B}(\mathbf{R}) \right) \times \hat{\mathbf{e}}_1 \right] - \frac{\mu}{m} (\nabla B(\mathbf{R}) \times \hat{\mathbf{e}}_1) + \mathcal{O}(\epsilon) \quad (3.45)$$

The last term in square brackets is rewritten as

$$\left(\frac{\dot{\mathbf{R}}}{c} \times \mathbf{B}(\mathbf{R}) \right) \times \hat{\mathbf{e}}_1 = \mathbf{B} \left(\hat{\mathbf{e}}_1 \cdot \frac{\dot{\mathbf{R}}}{c} \right) - \frac{\dot{\mathbf{R}}}{c} (\hat{\mathbf{e}}_1 \cdot \mathbf{B}) \quad (3.46)$$

$$= \left(\hat{\mathbf{e}}_1 \left(\hat{\mathbf{e}}_1 \cdot \frac{\dot{\mathbf{R}}}{c} \right) - \frac{\dot{\mathbf{R}}}{c} \right) B, \quad (3.47)$$

then we can solve Eq. 3.45 for the perpendicular component of the guiding center velocity,

$$\dot{\mathbf{R}} - \hat{\mathbf{e}}_1 \left(\hat{\mathbf{e}}_1 \cdot \dot{\mathbf{R}} \right) \equiv \dot{\mathbf{R}}_{\perp} = \frac{c\mathbf{E}(\mathbf{R}) \times \hat{\mathbf{e}}_1}{B} - \frac{mc}{q} \frac{\ddot{\mathbf{R}} \times \hat{\mathbf{e}}_1}{B} - \frac{\mu c}{q} \frac{\nabla B(\mathbf{R}) \times \hat{\mathbf{e}}_1}{B} + \mathcal{O}(\epsilon^2) \quad (3.48)$$

$$= \frac{\hat{\mathbf{e}}_1}{B} \times \left(-c\mathbf{E} + \frac{\mu c}{q} \nabla B + \frac{mc}{q} \ddot{\mathbf{R}} \right) + \mathcal{O}(\epsilon^2). \quad (3.49)$$

Note that

$$\ddot{\mathbf{R}} = \frac{d}{dt} \dot{\mathbf{R}} = \frac{d}{dt} \left(\hat{\mathbf{e}}_1 \left(\hat{\mathbf{e}}_1 \cdot \dot{\mathbf{R}} \right) + \dot{\mathbf{R}}_{\perp} \right), \quad (3.50)$$

but at zeroth order in ϵ , $\dot{\mathbf{R}}_{\perp} = c\mathbf{E} \times \hat{\mathbf{e}}_1/B$, then

$$\dot{\mathbf{R}}_{\perp} = \frac{\hat{\mathbf{e}}_1}{B} \times \left[-c\mathbf{E} + \frac{\mu c}{q} \nabla B + \frac{mc}{q} \frac{d}{dt} \left(v_{\parallel} \hat{\mathbf{e}}_1 + \frac{c\mathbf{E} \times \hat{\mathbf{e}}_1}{B} \right) \right] + \mathcal{O}(\epsilon^2) \quad (3.51)$$

The last term in the square brackets is the drift velocity, $\mathbf{u}_E \equiv c\mathbf{E} \times \mathbf{B}/B^2$.

The perpendicular velocity of the guiding center, as written in Eq. 3.51, is useful in analyzing the energy gain of the particle per time. Intuitively, the energy of a particle, averaged over gyration, is the sum of three terms:

$$W = \frac{1}{2}m\dot{\mathbf{R}}_{\parallel}^2 + \frac{1}{2}m\dot{\mathbf{R}}_{\perp}^2 + \mu B \quad (3.52)$$

The first and second terms are the parallel and perpendicular energies of the guiding center motion, respectively. The last term is the rotational energy of the particle about the guiding center. We have

$$W = q \int \mathbf{E} \cdot (\dot{\mathbf{R}}_{\parallel} + \dot{\mathbf{R}}_{\perp}) dt + \mu B \quad (3.53)$$

$$\Rightarrow \frac{dW}{dt} = q(\dot{\mathbf{R}}_{\parallel} + \dot{\mathbf{R}}_{\perp}) \cdot \mathbf{E} + \mu \frac{\partial B}{\partial t} \quad (3.54)$$

Using Eq. 3.51, we obtain

$$\frac{dW}{dt} = qv_{\parallel}E_{\parallel} + q\dot{\mathbf{R}}_{\perp} \cdot \mathbf{E} + \mu \frac{\partial B}{\partial t} \quad (3.55)$$

$$= qv_{\parallel}E_{\parallel} + q \left(\frac{\hat{\mathbf{e}}_1}{B} \times \left[-c\mathbf{E} + \frac{\mu c}{q}\nabla B + \frac{mc}{q} \frac{d}{dt} \left(v_{\parallel}\hat{\mathbf{e}}_1 + \frac{c\mathbf{E} \times \hat{\mathbf{e}}_1}{B} \right) \right] \right) \cdot \mathbf{E} + \mu \frac{\partial B}{\partial t} \quad (3.56)$$

$$= qv_{\parallel}E_{\parallel} + q \left(\frac{c\mathbf{E} \times \hat{\mathbf{e}}_1}{B} + \frac{\mu c \hat{\mathbf{e}}_1 \times \nabla B}{qB} + \frac{mc \hat{\mathbf{e}}_1}{qB} \times \frac{d}{dt} \left(v_{\parallel}\hat{\mathbf{e}}_1 + \frac{c\mathbf{E} \times \hat{\mathbf{e}}_1}{B} \right) \right) \cdot \mathbf{E} + \mu \frac{\partial B}{\partial t} \quad (3.57)$$

$$= qv_{\parallel}E_{\parallel} + q \left(\frac{\mu c (\hat{\mathbf{e}}_1 \times \nabla B) \cdot \mathbf{E}}{qB} + \frac{mc \hat{\mathbf{e}}_1}{qB} \times \frac{d}{dt} (v_{\parallel}\hat{\mathbf{e}}_1 + \mathbf{u}_E) \cdot \mathbf{E} \right) + \mu \frac{\partial B}{\partial t} \quad (3.58)$$

$$= qv_{\parallel}E_{\parallel} + q \left(\frac{\mu c \mathbf{E} \times \hat{\mathbf{e}}_1}{qB} \cdot \nabla B + \frac{mc \mathbf{E} \times \hat{\mathbf{e}}_1}{qB} \cdot \frac{d}{dt} (v_{\parallel}\hat{\mathbf{e}}_1 + \mathbf{u}_E) \right) + \mu \frac{\partial B}{\partial t} \quad (3.59)$$

$$= qv_{\parallel}E_{\parallel} + \mu \mathbf{u}_E \cdot \nabla B + \left(m \mathbf{u}_E \cdot \frac{d}{dt} (v_{\parallel}\hat{\mathbf{e}}_1 + \mathbf{u}_E) \right) + \mu \frac{\partial B}{\partial t} \quad (3.60)$$

$$= qv_{\parallel}E_{\parallel} + \mu \mathbf{u}_E \cdot \nabla B + m \mathbf{u}_E \cdot \frac{d\mathbf{u}_E}{dt} + m \mathbf{u}_E \cdot \frac{d}{dt} (v_{\parallel}\hat{\mathbf{e}}_1) + \mu \frac{\partial B}{\partial t} \quad (3.61)$$

$$= \underbrace{\left[qv_{\parallel}E_{\parallel} + mv_{\parallel}\mathbf{u}_E \cdot \frac{d\hat{\mathbf{e}}_1}{dt} \right]}_{\text{parallel}} + \underbrace{\left[\mu \mathbf{u}_E \cdot \nabla B + \mu \frac{\partial B}{\partial t} + m \mathbf{u}_E \cdot \frac{d\mathbf{u}_E}{dt} \right]}_{\text{perpendicular}} \quad (3.62)$$

For example, the energy change of an electron, time-averaged over the gyration period, and to first order in the expansion parameter m_e/e , is (restoring the effect of relativistic inertia via the substitution $m_e \rightarrow \gamma m_e$)

$$\begin{aligned} \frac{1}{e} \frac{d\varepsilon_e}{dt} &= \underbrace{\left[-v_{\parallel}E_{\parallel} + \frac{\gamma m_e}{e} v_{\parallel} \mathbf{u}_E \cdot \frac{d\hat{\mathbf{b}}}{dt} \right]}_{\text{parallel}} \\ &+ \underbrace{\left[\frac{1}{\gamma e} \mu \mathbf{u}_E \cdot \nabla B + \frac{1}{\gamma e} \mu \frac{\partial B}{\partial t} + \frac{\gamma m_e}{e} \mathbf{u}_E \cdot \frac{d\mathbf{u}_E}{dt} \right]}_{\text{perpendicular}} + \mathcal{O}\left(\frac{m_e}{e}\right)^2 \end{aligned} \quad (3.63)$$

where $\varepsilon_e = \gamma m_e c^2$, $-e$ is the electron charge, $\mu = \gamma^2 v_{\perp}^2 m_e / 2B$ is the adiabatic moment of the electron, $\hat{\mathbf{b}} = \hat{\mathbf{e}}_1 = \mathbf{B}/B$ is the direction of the local B -field, and $\mathbf{u}_E = c\mathbf{E} \times \mathbf{B}/B^2$ is the drift velocity; electric and magnetic fields are to be evaluated at the location of the guiding center. The underbrackets indicate terms that are associated with parallel and perpendicular energy changes.

Several of the terms have direct physical significance, and provide insight into the mechanisms responsible for particle energization; the first of the terms labeled ‘parallel’ in Eq. (3.63), for example, corresponds to acceleration by the electric field, parallel to the local B -field. The physical significance of several of the other terms is discussed below.

The terms in Eq. 3.63 can be further analyzed using the relation between Lagrangian and Eulerian derivatives:

$$\frac{d}{dt} = \frac{\partial}{\partial t} + (v_{\parallel} \hat{\mathbf{b}} + \mathbf{u}_E) \cdot \nabla \quad (3.64)$$

Take the second term on the first line of Eq. (3.63):

$$\frac{\gamma m_e}{e} v_{\parallel} \mathbf{u}_E \cdot \frac{d\hat{\mathbf{b}}}{dt} = \frac{\gamma m_e}{e} v_{\parallel} \mathbf{u}_E \cdot \left(\frac{\partial}{\partial t} + (v_{\parallel} \hat{\mathbf{b}} + \mathbf{u}_E) \cdot \nabla \right) \hat{\mathbf{b}} \quad (3.65)$$

$$= \frac{\gamma m_e}{e} v_{\parallel} \mathbf{u}_E \cdot \frac{\partial \hat{\mathbf{b}}}{\partial t} + \frac{\gamma m_e}{e} v_{\parallel} \mathbf{u}_E \cdot (\mathbf{u}_E \cdot \nabla) \hat{\mathbf{b}} + \frac{\gamma m_e}{e} v_{\parallel}^2 \mathbf{u}_E \cdot (\hat{\mathbf{b}} \cdot \nabla) \hat{\mathbf{b}} \quad (3.66)$$

The last term here is the well-known ‘curvature drift’,

$$\frac{\gamma m_e}{e} v_{\parallel}^2 \mathbf{u}_E \cdot (\hat{\mathbf{b}} \cdot \nabla) \hat{\mathbf{b}} = \frac{\gamma m_e}{e} c v_{\parallel}^2 \mathbf{E} \cdot \frac{\hat{\mathbf{b}} \times [(\hat{\mathbf{b}} \cdot \nabla) \hat{\mathbf{b}}]}{B} \quad (3.67)$$

$$\equiv -\mathbf{E} \cdot \mathbf{v}_{\text{curv.}} \quad (3.68)$$

which describes the Fermi-like acceleration of particles due to the magnetic tension of curved field lines (Drake et al., 2006, 2010). Here, we have defined the curvature drift velocity, $\mathbf{v}_{\text{curv.}}$. This can be interpreted as the velocity, in the direction orthogonal to the plane of curvature, that is required

to provide centripetal force on a particle following a curved magnetic field line:

$$\mathbf{F}_{\text{curv}} = \frac{\gamma m_e v_{\parallel}^2}{R_{\text{curv}}^2} \mathbf{R}_{\text{curv}} \quad (3.69)$$

$$\Rightarrow \mathbf{v}_{\text{curv}} = -\frac{c}{e} \frac{\mathbf{F}_{\text{curv}} \times \mathbf{B}}{B^2} = -\frac{\gamma m_e c v_{\parallel}^2}{e R_{\text{curv}}^2} \frac{\mathbf{R}_{\text{curv}} \times \mathbf{B}}{B^2}, \quad (3.70)$$

which can be expressed in terms of the derivative of the unit vector $\hat{\mathbf{b}}$ along the magnetic field line. To see this, consider an infinitesimal change in the unit vector $d\hat{\mathbf{b}}$ as a particle subtends angle α along a curved field whose radius of curvature is R_{curv} . Then $d\hat{\mathbf{b}} = -\alpha \mathbf{R}_{\text{curv}}/R_{\text{curv}}$, and the distance traveled along the arc is $d\ell = R_{\text{curv}}\alpha$, but by definition

$$\frac{d\hat{\mathbf{b}}}{d\ell} = (\hat{\mathbf{b}} \cdot \nabla) \hat{\mathbf{b}}, \quad (3.71)$$

therefore

$$(\hat{\mathbf{b}} \cdot \nabla) \hat{\mathbf{b}} = -\frac{\mathbf{R}_{\text{curv}}}{R_{\text{curv}}^2}. \quad (3.72)$$

Substitute this into Eq. 3.70 to obtain

$$\mathbf{v}_{\text{curv}} = -\frac{\gamma m_e c v_{\parallel}^2}{e} \frac{\hat{\mathbf{b}} \times [(\hat{\mathbf{b}} \cdot \nabla) \hat{\mathbf{b}}]}{B}, \quad (3.73)$$

as in the definition (Eqs. 3.67, 3.68).

On the second line of Eq. (3.63), the first term expresses energy change due to the ‘ ∇B -drift’,

$$\frac{1}{\gamma} \frac{\mu}{e} \mathbf{u}_E \cdot \nabla B = \frac{1}{\gamma} \frac{\mu}{e} c \mathbf{E} \cdot \frac{\hat{\mathbf{b}} \times \nabla B}{B} \quad (3.74)$$

$$\equiv -\mathbf{E} \cdot \mathbf{v}_{\nabla B}. \quad (3.75)$$

which defines the ∇B -drift velocity.

To elucidate the physical origin of the ∇B -drift, consider the orbit of an electron in an inhomogeneous magnetic field $\mathbf{B} = B(\mathbf{R}_\perp)\hat{\mathbf{b}}$. Assume that the magnetic field varies only in the $\hat{\mathbf{e}}_2$ direction, and that the particle has no initial velocity along the direction $\hat{\mathbf{b}}$. The force on the electron, in the $\hat{\mathbf{e}}_3$ direction, is (neglecting relativistic inertia)

$$m_e \ddot{p}_2 = e \dot{p}_3 B \quad (3.76)$$

Taylor expanding B about the guiding center, and inserting the Eqs. of motion for the particle (3.23, 3.24),

$$m_e \ddot{p}_2 = \frac{e}{c} v_\perp \cos \theta [B + \rho \cos \theta (\partial_2 B)]. \quad (3.77)$$

We employ a time-average over the gyroperiod to compute the average force:

$$\langle m_e \ddot{p}_2 \rangle = \frac{ev_\perp \rho}{2c} \partial_2 B = -\frac{m_e v_\perp^2}{2B} \partial_2 B. \quad (3.78)$$

In general, this force may be written as

$$\langle m_e \ddot{p} \rangle = -\mu \nabla B. \quad (3.79)$$

Then, the ∇B -drift velocity is

$$\mathbf{v}_{\nabla B} = -\frac{\mu c}{e} \frac{\hat{\mathbf{b}} \times \nabla B}{B}, \quad (3.80)$$

which is the definition as provided in Eqs. 3.74 and 3.75 (for an electron with relativistic mass

γm_e).

The second term on the second line of Eq. (3.63) corresponds to the induction effect of a time-varying field due to $\nabla \times \mathbf{E}$ acting about the circle of gyration (Northrop, 1963b). Finally, the last term on the second line of Eq. (3.63), when expanded, contains another term with a well-known physical interpretation. To extract this term, expand the Lagrangian derivative:

$$\frac{\gamma m_e}{e} \mathbf{u}_E \cdot \frac{d\mathbf{u}_E}{dt} = \frac{\gamma m_e}{e} \mathbf{u}_E \cdot \left(\frac{\partial}{\partial t} + (v_{||} \hat{\mathbf{b}} + \mathbf{u}_E) \cdot \nabla \right) \mathbf{u}_E \quad (3.81)$$

$$= \frac{\gamma m_e}{e} \mathbf{u}_E \cdot \frac{\partial \mathbf{u}_E}{\partial t} + \frac{\gamma m_e}{e} \mathbf{u}_E \cdot (\mathbf{u}_E \cdot \nabla) \mathbf{u}_E + \frac{\gamma m_e}{e} v_{||} \mathbf{u}_E \cdot (\hat{\mathbf{b}} \cdot \nabla) \mathbf{u}_E. \quad (3.82)$$

This first term corresponds to ‘polarization drift’, which is driven by time-variation in the electric field:

$$\frac{\gamma m_e}{e} \mathbf{u}_E \cdot \frac{\partial \mathbf{u}_E}{\partial t} = \frac{\gamma m_e}{e} c \mathbf{E} \cdot \frac{\hat{\mathbf{b}} \times \frac{\partial \mathbf{u}_E}{\partial t}}{B} \quad (3.83)$$

$$\equiv -\mathbf{E} \cdot \mathbf{v}_{\text{pol}}. \quad (3.84)$$

To clarify the physical significance of polarization drift, consider an electron in perpendicular \mathbf{E} and \mathbf{B} fields. The electron has drift velocity

$$\mathbf{u}_E = \frac{c \mathbf{E} \times \mathbf{B}}{B^2}. \quad (3.85)$$

If the electric field is time varying, then (neglecting relativistic inertia)

$$m_e \dot{\mathbf{u}}_E = \frac{c \dot{\mathbf{E}} \times \mathbf{B}}{B^2}, \quad (3.86)$$

which is a force on the electron, perpendicular to both the \mathbf{E} and \mathbf{B} fields. It is not supplied by

\mathbf{E} because $\mathbf{E} \perp \mathbf{u}_\mathbf{E}$; instead, the electron develops a velocity \mathbf{v}_{pol} in the same direction as \mathbf{E} to balance the magnetic force on the electron,

$$m_e \dot{\mathbf{u}}_\mathbf{E} = -\frac{e}{c} \mathbf{v}_{\text{pol}} \times \mathbf{B} \quad (3.87)$$

$$\Rightarrow \frac{1}{\omega} \dot{\mathbf{u}}_\mathbf{E} \times \hat{\mathbf{b}} = -(\hat{\mathbf{b}} \times (\mathbf{v}_{\text{pol}} \times \hat{\mathbf{b}})) = -\mathbf{v}_{\text{pol}} \quad (3.88)$$

$$\Rightarrow \mathbf{v}_{\text{pol}} = \frac{1}{\omega} \left(\hat{\mathbf{b}} \times \frac{\partial \mathbf{u}_\mathbf{E}}{\partial t} \right). \quad (3.89)$$

Upon substitution $m_e \rightarrow \gamma m_e$ to account for relativistic inertia, this is the definition of polarization drift velocity as provided in Eqs. 3.83 and 3.84.

In practice, many terms in the expansion of Eq. (3.63) can be ignored, as their contribution to the electron energy gain is negligible. In Sec. 3.5.7, we employ the guiding center analysis, as detailed in Dahlin et al. (2014), to assess the mechanisms responsible for energy gain in guide field reconnection. Formally, the electromagnetic fields are to be evaluated at the location of the guiding center, however if the electron Larmor radius is sufficiently small, relative to the gradient length scale of the magnetic field, then the measured value at the guiding center is similar to that at the particle location. For the simulations described in Sec. 3.5.7, we find that this is a reasonable assumption.

4. Kelvin-Helmholtz I

4.1 Introduction

The Kelvin-Helmholtz (KH) instability is driven by the transfer of momentum across the interface of two fluids in relative motion. This instability was discovered first by Von Helmholtz & Monats (1868), who studied mixing between fluid layers of differing density. Lord Kelvin (1871) studied formally the passage of wind over water as a shearing flow. Chandrasekhar (1961) and Dyson (1960), among many others, have studied the KH instability at the interface of air currents in Earth's atmosphere.

The KH instability, with an especially rich history in geophysical literature, is a generic phenomenon. It has been shown to have a rich interplay with magnetic reconnection, for example; Faganello et al. (2008, 2012) used numerical simulations of the KH instability to show that reconnection may be induced as a byproduct of unstable KH growth at the interface of Earth's magnetosphere and the solar wind. It is interesting to ask whether a similar mechanism may operate in other astrophysical contexts, for example at the interface of a black hole's jet and the surrounding wind/corona (Hamlin & Newman, 2013).

In this chapter, we focus on a KH problem motivated by the interaction of astrophysical jets with the surrounding disk wind. In the typical case of an accreting black hole, the jet is highly magnetized, relativistic, and of low density, while the wind has lower magnetization, moves more slowly, and has higher density (e.g., Yuan & Narayan (2014)). Numerical general-relativistic magnetohydrodynamic simulations show some evidence for KH instability at the interface (Hardee, 2004; Mizuno et al., 2006; Hardee et al., 2007). The outline is as follows: In Sec. 4.2, we describe two KH problems, and for each carry out a linear analysis of the KH instability. Next, in Sec. 4.3, we describe relativistic magnetohydrodynamic simulations that we use to test the linear analysis. We

conclude in Sec. 4.4.

4.2 Problem descriptions and linear analysis

Here, we study the evolution of waves at the interface of two relativistic magnetized fluids in relative motion (Bodo et al., 2004; Osmanov et al., 2008). The growth of such waves is governed by the equations of relativistic magnetohydrodynamics (RMHD), and so a standard linear analysis of the shear flow problem, within the framework of RMHD, leads to a description of the waves allowed at the interface separating the two (relativistic and magnetized) fluids (Anile, 1990; Bodo et al., 2004). In the following sections, we describe two shear flow problem setups in detail, then investigate the linear instability of RMHD waves for each setup.

For conciseness of notation in Sec. 4.2.1, we adopt naturalized Gaussian units, with $c = 4\pi = k_B = 1$.

4.2.1 Shearing flow problem descriptions

We consider two related problems of magnetized shear flow: first, the classical case in which two identical fluids move with equal and opposite velocities (henceforth referred to as the ‘symmetric’ setup), and second, a case motivated by astrophysical jets, wherein weakly magnetized plasma rushes past magnetized plasma (which we refer to as the ‘jet’ setup, because of the physical similarity to what one may observe sitting in the rest frame of a jet). In the following sections, Secs. 4.2.1.1 and 4.2.1.2, we elaborate on the symmetric and jet setups.

4.2.1.1 Symmetric shearing flow: problem description

For the problem of symmetric shearing flow, we consider a (dimensionless) velocity profile with an infinitely thin transition width between the two sides of the flow:

$$\mathbf{v}(y) = \begin{cases} (+\beta_{sh}, 0, 0) & \text{if } y > 0, \\ (-\beta_{sh}, 0, 0) & \text{if } y < 0. \end{cases} \quad (4.1)$$

The parameter β_{sh} here parametrizes the velocity of either side of the flow, as viewed in the laboratory frame; notice that the total velocity jump between the sides with $y < 0$ and $y > 0$ (which we refer to as y_- and y_+ , respectively) is, in the laboratory frame, $2\beta_{\text{sh}}.$ ¹ Following the notation of Osmanov et al. (2008), we use subscripts $-$ and $+$ refer to quantities on sides y_- and $y_+.$ A magnetic field oriented along $+x$, i.e., parallel to the direction of motion, permeates the plasma:

$$\mathbf{B}(y) = (B_{x0}, 0, 0). \quad (4.2)$$

For symmetry, the two sides of the flow are assumed to have equal proper mass densities $\tilde{\rho}_{0-} = \tilde{\rho}_{0+}$, and to be in pressure balance along y , i.e. the yy component of the stress-energy tensor $T_{\text{tot}}^{yy}(y)$ is constant along $y.$

In its generality, the symmetric shear flow problem described here is the subject of a vast and deep literature, with seminal work originating as early as the late nineteenth century (Von Helmholtz & Monats, 1868; Lord Kelvin, 1871). Our focus then in investigating the symmetric setup is to make connection with previous studies, notably those regarding analysis of the KH instability in RMHD (Ferrari et al., 1980; Bodo et al., 2004; Osmanov et al., 2008; Hamlin & Newman, 2013; Mignone et al., 2018).

4.2.1.2 Astrophysical jet: problem description

As a companion setup to the symmetric case described above, we consider a second problem motivated by astrophysical jets, with y_- of the shear flow magnetized (the ‘jet’), and y_+ (possibly) weakly magnetized (the ‘wind’). To describe the field profiles, we imagine sitting in the rest frame of the magnetized jet; then the jet plasma is at rest, and the relative motion of the wind is along

¹The difference in velocity between jet and wind sides, as viewed in either the jet or wind frame, is in general not equal to $2\beta_{\text{sh}}$, due to standard relativistic formulae for velocity addition.

$+x$:

$$\mathbf{v}(y) = \begin{cases} (\beta_{\text{sh}}, 0, 0) & \text{if } y > 0, \\ (0, 0, 0) & \text{if } y < 0. \end{cases} \quad (4.3)$$

Note that in our description here of the jet problem, β_{sh} parametrizes the full difference in velocity between sides y_- and y_+ ; this differs from the definition of β_{sh} in the symmetric setup (where β_{sh} is half the difference in velocity between y_- and y_+). However, the meaning of β_{sh} in the remainder of this chapter will either be unambiguous based on the context, or will be stated explicitly.

The profile of the magnetic field is

$$\mathbf{B}(y) = \begin{cases} (0, 0, b_w B_0) & \text{if } y > 0, \\ (B_0, 0, b_j B_0) & \text{if } y < 0, \end{cases} \quad (4.4)$$

where we allow for guide components of magnetic field on the jet and wind sides via the parameters b_w and b_j , respectively. The (fluid frame rest-mass) density ratio of jet to wind is inferred from general relativistic MHD simulations to lie roughly in the range 10^2 – 10^5 (see e.g., [Tchekhovskoy et al. \(2011\)](#); [Duran et al. \(2017\)](#)), but it is not known with precision. We consider a density profile of the form:

$$\rho(y) = \begin{cases} \rho_{0w} & \text{if } y > 0, \\ \rho_{0j} & \text{if } y < 0. \end{cases} \quad (4.5)$$

In both the symmetric and jet problems described above, we make the simplifying assumption that the profiles of velocity and magnetic field (as well as mass density, for $\rho_{0w} \neq \rho_{0j}$) have an infinitely thin transition width. A more physical assumption (also, more challenging analytically), is

that the field profiles vary smoothly over some finite length; the growth rate of the KH instability in MHD, for fluids separated by a hyperbolic tangent profile, was worked out by [Chandrasekhar \(1961\)](#). Introduction of a smoothly varying velocity profile has the effect of suppressing KH modes with wavelengths less than the transition width (neglecting factors of order unity ([Berlok & Pfrommer, 2011](#))). The growth rates of the KH instability that we discuss in the following sections, assuming discontinuous profiles, should then be understood as upper limits to growth rates that can be obtained in simulations, where spatial resolution of the transition is itself limited.

4.2.2 Relativistic MHD equations

The equations of relativistic MHD follow from conservation of energy-momentum and mass; in covariant form, the governing equations of RMHD may be written compactly as ([Dixon, 1978](#); [Anile, 1990](#))

$$\partial_\mu T_{\text{tot}}^{\mu\nu} = 0, \quad (4.6)$$

$$\partial_\mu(\rho u^\mu) = 0, \quad (4.7)$$

where $T_{\text{tot}}^{\mu\nu}$ is the stress-energy tensor (consisting of fluid and electromagnetic components, $T_{\text{tot}}^{\mu\nu} = T_{\text{fl}}^{\mu\nu} + T_{\text{em}}^{\mu\nu}$), $u^\mu = (\gamma, \gamma \mathbf{v})$ is the fluid four-velocity, and

$$T_{\text{fl}}^{\mu\nu} = w u^\mu u^\nu + p g^{\mu\nu}, \quad (4.8)$$

$$T_{\text{em}}^{\mu\nu} = F^{\mu\alpha} F_\alpha^\nu - \frac{1}{4} g^{\mu\nu} F_{\alpha\beta} F^{\alpha\beta}. \quad (4.9)$$

Here, $w = \rho h$ is the fluid enthalpy density (in the rest frame of the fluid); ρ is mass density; $h = 1 + \theta \Gamma_{\text{ad}} / (\Gamma_{\text{ad}} - 1)$ is specific enthalpy, assuming a perfect fluid; θ is the fluid dimensionless temperature; Γ_{ad} is the adiabatic index of the fluid; p is the fluid pressure (assumed isotropic); $g^{\mu\nu} = \text{diag}(-1, 1, 1, 1)$ is the metric; and $F^{\mu\nu}$ is the electromagnetic tensor, obeying the Gauss-

Faraday law $\partial_{[\alpha} F_{\mu\nu]} = 0$ and Gauss-Ampère law $\partial_\mu F^{\mu\nu} = -J^\nu$. The equations of RMHD (Eqs. 4.8 and 4.9) may be written in three-dimensional form as (Mignone et al., 2018)

$$\frac{\partial(\rho\gamma)}{\partial t} + \nabla \cdot (\rho\gamma\mathbf{v}) = 0, \quad (\text{Continuity Eqn.}) \quad (4.10)$$

$$\frac{\partial}{\partial t}(w\gamma^2\mathbf{v}) + \nabla \cdot (w\gamma^2\mathbf{v}\mathbf{v}) + \nabla p - \mathbf{J} \times \mathbf{B} = 0, \quad (\text{Momentum Eqn.}) \quad (4.11)$$

$$\frac{\partial\mathbf{E}}{\partial t} - \nabla \times \mathbf{B} + \mathbf{J} = 0, \quad (\text{Ampère's law}) \quad (4.12)$$

$$\frac{\partial\mathbf{B}}{\partial t} + \nabla \times \mathbf{E} = 0, \quad (\text{Faraday's law}) \quad (4.13)$$

$$\frac{\partial}{\partial t}(w\gamma^2 - p) + \nabla \cdot (w\gamma^2\mathbf{v}) - \mathbf{J} \cdot \mathbf{E} = 0, \quad (\text{Energy Eqn.}) \quad (4.14)$$

where \mathbf{E} and \mathbf{B} are the electric and magnetic fields, and \mathbf{J} is the current. Constraints on the divergence of the electric and magnetic fields come from the temporal components of the Gauss-Ampère and Gauss-Faraday laws,

$$\nabla \cdot \mathbf{E} = \rho_q, \quad (4.15)$$

$$\nabla \cdot \mathbf{B} = 0, \quad (4.16)$$

where ρ_q is the charge density.

4.2.3 Linear analysis of instability

To proceed with linearization of Eqs. 4.10–4.14, wherein small perturbations about the background fields are introduced, we choose to work in the rest frame of the fluid, where the background electric field vanishes. Eqs. 4.10–4.14 are then linearized by introducing small perturbations to the

background fields,

$$\rho = \rho_0 + \rho_1 + \mathcal{O}(\epsilon^2), \quad (4.17)$$

$$p = p_0 + p_1 + \mathcal{O}(\epsilon^2), \quad (4.18)$$

$$\mathbf{v} = 0 + \mathbf{v}_1 + \mathcal{O}(\epsilon^2), \quad (4.19)$$

$$\mathbf{B} = \mathbf{B}_0 + \mathbf{B}_1 + \mathcal{O}(\epsilon^2), \quad (4.20)$$

$$\mathbf{E} = 0 + \mathbf{E}_1 + \mathcal{O}(\epsilon^2), \quad (4.21)$$

and by assuming that the perturbed variables take the form of plane waves: $X_1 \propto \epsilon e^{i(\mathbf{k} \cdot \mathbf{x} - \omega t)}$, where X_1 is any of the perturbed variables $\rho_1, p_1, \mathbf{v}_1$, or \mathbf{B}_1 ; ϵ is a small amplitude, ω is the frequency, and $\mathbf{k} = (k, l, m)$ is the wavevector (both the frequency and wavevector are complex). The wavevector component k is the part of \mathbf{k} parallel to the shear velocity, l is the component of \mathbf{k} perpendicular to the jet-wind interface, and m is the component of \mathbf{k} lying on the interface and perpendicular to the shearing plane. The angle of propagation of the wave, relative to the shearing plane and lying in the interface, is controlled by

$$f \equiv \frac{m}{k}. \quad (4.22)$$

We consider this as a free parameter during our exploration of the KH instability in jets, in Secs. 4.2.3.3 and 4.2.4.

The perturbation to the electric field \mathbf{E}_1 is eliminated from the linearized equations in the ideal limit (i.e. infinite conductivity), which requires the current to vanish at all orders in ϵ , from which we deduce $\mathbf{E}_1 = -\mathbf{v}_1 \times \mathbf{B}_0$.

Linearization of Eqs. 4.10–4.14 yields

$$-i\omega\rho_1 + i\rho_0\mathbf{k}\cdot\mathbf{v}_1 = 0, \quad (4.23)$$

$$-i\omega w_0\mathbf{v}_1 + i\mathbf{k}p_1 - ((i\mathbf{k}\times\mathbf{B}_1 - i\omega\mathbf{v}_1\times\mathbf{B}_0)\times\mathbf{B}_0) = 0, \quad (4.24)$$

$$-i\omega\mathbf{B}_1 - (i\mathbf{k}\times(\mathbf{v}_1\times\mathbf{B}_0)) = 0, \quad (4.25)$$

$$-i\omega\left(\left(\frac{\partial w_0}{\partial p_0} - 1\right)p_1 + \frac{\partial w_0}{\partial\rho_0}\rho_1\right) + w_0i\mathbf{k}\cdot\mathbf{v}_1 = 0; \quad (4.26)$$

note that Ampère's law (Eq. 4.12) is eliminated from Eqs. 4.10–4.14 by solving for \mathbf{J} and substituting into the remaining equations prior to linearization, which leads to the equations Eqs. 4.23–4.26. Introducing the state vector $\psi = (\rho_1, p_1, \mathbf{B}_1, \mathbf{v}_1)$, Eqs. 4.10–4.14 may be cast as a matrix equation $\mathbf{X}\psi = 0$, which has nontrivial solutions if

$$\det(\mathbf{X}) = 0. \quad (4.27)$$

One must also enforce the divergence-free constraint, $\mathbf{k}\cdot\mathbf{B}_1 = 0$.

In the following sections, we apply the technique outlined above to determine the growth rates of RMHD waves for the ‘symmetric’ and ‘jet’ geometries described in Sec. 4.2.1. In this analysis, the notation becomes more concise by introducing the Alfvén speed v_A and sound speed c_s , which we define as (Komissarov, 1999; Osmanov et al., 2008; Mignone et al., 2018)

$$v_A = \sqrt{\frac{\mathbf{B}_0^2}{w_0 + \mathbf{B}_0^2}}, \quad (4.28)$$

$$c_s = \sqrt{\frac{w_0 - \frac{\partial w_0}{\partial p_0}\rho_0}{\frac{\partial w_0}{\partial p_0} - 1}} \frac{1}{w_0}. \quad (4.29)$$

The equation $\det(\mathbf{X}) = 0$ yields a dispersion relation governing relativistic MHD waves, as viewed

in the frame comoving with the fluid. Defining the magnetization $\sigma_w = \mathbf{B}_0^2/w_0$, and recalling that (for a perfect fluid) $w_0 = \rho_0 h_0 = \rho_0(1 + \theta_0 \Gamma_{\text{ad}}/(\Gamma_{\text{ad}} - 1))$, the Alfvén speed and sound speed may be written as

$$v_A = \sqrt{\frac{\sigma_w}{1 + \sigma_w}}, \quad (4.30)$$

$$c_s = \sqrt{\frac{\Gamma_{\text{ad}} \theta_0}{h_0}}. \quad (4.31)$$

4.2.3.1 Symmetric shear flow: relativistic MHD dispersion relation

For the symmetric shear flow setup described in Sec. 4.2.1.1, a longitudinal magnetic field $\mathbf{B}_0 = (B_{x0}, 0, 0)$ permeates the plasma (the dispersion relation for this problem has been derived by Osmanov et al. (2008), whose derivation we follow in this section). In this case, Eq. 4.27 (enforcing also $\nabla \cdot \mathbf{B}_1 = 0$, i.e. $\mathbf{k} \cdot \mathbf{B}_1 = 0$, and employing the definitions Eqs. 4.28–4.31) reduces to (Komissarov, 1999; Osmanov et al., 2008)

$$\begin{aligned} & \tilde{\omega}_{\pm} \cdot (\tilde{\omega}_{\pm}^2 - \tilde{k}_{\pm}^2 v_{A\pm}^2) \cdot (\tilde{\omega}_{\pm}^4 - \tilde{\omega}_{\pm}^2 (c_{s\pm}^2 (\tilde{k}_{\pm}^2 + (1 - v_{A\pm}^2) (\tilde{l}_{\pm}^2 + \tilde{m}_{\pm}^2))) \\ & + v_{A\pm}^2 (\tilde{k}_{\pm}^2 + \tilde{l}_{\pm}^2 + \tilde{m}_{\pm}^2)) + \tilde{k}_{\pm}^2 v_{A\pm}^2 c_{s\pm}^2 (\tilde{k}_{\pm}^2 + \tilde{l}_{\pm}^2 + \tilde{m}_{\pm}^2)) = 0, \end{aligned} \quad (4.32)$$

where the overtilde indicates rest-frame quantities (the overtilde is omitted for the Alfvén speed $v_A = B_{x0}/\sqrt{w_0 + B_{x0}^2}$, which is in this case invariant under boosts in the x direction, and so is the same whether viewed from y_- or y_+ ; the overtilde is omitted also for the sound speed, which is only well-defined in the fluid rest frame); as in Sec. Sec. 4.2.1.1, subscripts $-$ and $+$ refer to the $y < 0$ and $y > 0$ sides of the shear.

The first root of the dispersion relation Eq. 4.32, $\tilde{\omega}_{\pm} = 0$, is important in smoothly varying shear layers, as opposed to the discontinuous profile we consider presently, and is discussed in

detail by Blumen et al. (1975);² see also Bodo et al. (2004). The second factor in Eq. 4.32 gives $\tilde{\omega}_\pm = \pm \tilde{k}_\pm v_{A\pm}$ and corresponds to the propagation of Alfvén waves. This again is not of interest to us. The final factor in Eq. 4.32 describes the propagation of magnetosonic modes; in anticipation that the phase velocities $\tilde{\omega}_\pm$ corresponding to these magnetosonic modes may have imaginary parts, we select the third factor from Eq. 4.32 to study instability at the interface of the shear layer.

To express the growth rate of the instability as viewed in the laboratory frame, we derive two equations for $(l_+/l_-)^2$, which allows us to eliminate $(l_+/l_-)^2$ and arrive at the laboratory frame dispersion relation, which depends only on the sound speed, Alfvén speed, shear flow β_{sh} , wavevectors k, m , and phase velocity ω . To boost Eqs. 4.32 to the laboratory frame, we use the Lorentz transformations

$$\tilde{\omega}_\pm = \frac{\omega \mp k\beta_{sh}}{\sqrt{1 - \beta_{sh}^2}}, \quad \tilde{k}_\pm = \frac{k \mp \omega\beta_{sh}}{\sqrt{1 - \beta_{sh}^2}}, \quad \tilde{l}_\pm = l_\pm, \quad \tilde{m}_\pm = m, \quad (4.33)$$

²Blumen et al. (1975) showed that for a smoothly varying (as opposed to discontinuous) shear layer of compressible fluid, the neutrally stable mode corresponding to $\tilde{\omega}_\pm = 0$ in Eq. 4.32 is indeed unstable to perturbations; the stability properties of long-wavelength perturbations at smoothly-varying interfaces differ significantly from the properties of long-wavelength perturbations at discontinuous shear interfaces.

and solve for $(l_+/l_-)^2$, which yields

$$\begin{aligned}
(l_+/l_-)^2 = & (1 - \beta_{\text{sh}}^2)(c_s^2(1 - v_A^2)(\omega + k\beta_{\text{sh}})^2 - c_s^2 v_A^2(k + \omega\beta_{\text{sh}})^2 + v_A^2(\omega + k\beta_{\text{sh}})^2) \\
& \cdot (c_s^2(v_A^2(k - \omega\beta_{\text{sh}})^2((k - \omega\beta_{\text{sh}})^2 + (1 - \beta_{\text{sh}}^2)m^2) - (\omega - k\beta_{\text{sh}})^2((k - \omega\beta_{\text{sh}})^2 \\
& + (1 - \beta_{\text{sh}}^2)m^2(1 - v_A^2))) + (\omega - k\beta_{\text{sh}})^4 - v_A^2(\omega - k\beta_{\text{sh}})^2((k - \omega\beta_{\text{sh}})^2 + (1 - \beta_{\text{sh}}^2)m^2)) \\
& / ((1 - \beta_{\text{sh}}^2)(v_A^2(\omega - k\beta_{\text{sh}})^2 - c_s^2(k^2(v_A^2 - \beta_{\text{sh}}^2(1 - v_A^2)) + 2\beta_{\text{sh}}k(1 - 2v_A^2)\omega \\
& - \omega^2(1 - (1 + \beta_{\text{sh}}^2)v_A^2)))c_s^2(v_A^2(k + \omega\beta_{\text{sh}})^2((k + \omega\beta_{\text{sh}})^2 - (\beta_{\text{sh}}^2 - 1)m^2) \\
& - (\omega + k\beta_{\text{sh}})^2((k + \omega\beta_{\text{sh}})^2 + (1 - \beta_{\text{sh}}^2)m^2(1 - v_A^2))) + (\omega + k\beta_{\text{sh}})^4 \\
& - v_A^2(\omega + k\beta_{\text{sh}})^2((k + \omega\beta_{\text{sh}})^2 + (1 - \beta_{\text{sh}}^2)m^2))).
\end{aligned} \tag{4.34}$$

We derive a second equation for $(l_+/l_-)^2$ by considering the y and z components of the linearized RMHD momentum equations, Eqs. 4.24, along with the induction equations Eqs. 4.25:

$$\tilde{k}_\pm B_{x0} \widetilde{B_{y1\pm}} - l_\pm B_{x0} B_{x1\pm} - l_\pm \tilde{p}_{1\pm} + \widetilde{v_{y1\pm}} \widetilde{\omega}_\pm (B_{x0}^2 + \tilde{\rho}_{0\pm} h_{0\pm}) = 0, \tag{4.35}$$

$$m B_{x0} B_{x1\pm} - \widetilde{v_{z1\pm}} \widetilde{\omega}_\pm (B_{x0}^2 + \tilde{\rho}_{0\pm} h_{0\pm}) - \tilde{k}_\pm B_{x0} \widetilde{B_{z1\pm}} + m \tilde{p}_{1\pm} = 0, \tag{4.36}$$

$$l_\pm \widetilde{v_{y1\pm}} B_{x0} + m \widetilde{v_{z1\pm}} B_{x0} - \widetilde{\omega}_\pm B_{x1\pm} = 0, \tag{4.37}$$

$$\tilde{k}_\pm \widetilde{v_{y1\pm}} B_{x0} + \widetilde{\omega}_\pm \widetilde{B_{y1\pm}} = 0, \tag{4.38}$$

$$\tilde{k}_\pm \widetilde{v_{z1\pm}} B_{x0} + \widetilde{\omega}_\pm \widetilde{B_{z1\pm}} = 0. \tag{4.39}$$

By eliminating $m, \widetilde{B_{y1\pm}}, \widetilde{B_{z1\pm}}, \widetilde{v_{x1\pm}}$, and $\widetilde{v_{z1\pm}}$ from Eqs. 4.35–4.39, applying the Lorentz transformations Eqs. 4.33, and employing pressure balance ($p_- = p_+$), along with the displacement

matching condition at the interface of the shear flow ($y = 0$), namely

$$\frac{\widetilde{v_{y1}}_-}{\omega + k\beta_{sh}} = \frac{\widetilde{v_{y1}}_+}{\omega - k\beta_{sh}}, \quad (4.40)$$

we obtain a second equation for l_+/l_- ,

$$\frac{l_+}{l_-} = \frac{v_A^2(\omega^2 - k^2)(1 - \beta_{sh}^2) + (\omega - k\beta_{sh})^2(1 - v_A^2)}{v_A^2(\omega^2 - k^2)(1 - \beta_{sh}^2) + (\omega + k\beta_{sh})^2(1 - v_A^2)}. \quad (4.41)$$

Together, Eqs. 4.34 and 4.41 yield the desired dispersion relation governing RMHD modes coupled at the interface of the shear flow for the symmetric shear problem. In squaring Eq. 4.41 to seek numerically the complex roots of the dispersion relation, four spurious solutions are introduced; trial solutions must be rejected if they do not satisfy Eq. 4.41, so that only the physical solutions are retained. In computing solutions to the dispersion relation, we also enforce the condition $\text{Im}(l_+) > 0$ and $\text{Im}(l_-) < 0$, which ensures that the wave amplitude approaches zero as $y \rightarrow \pm\infty$.

When discussing solutions to the dispersion relation, it will be convenient to recast the phase velocities as dimensionless numbers (Osmanov et al., 2008),

$$\phi_{v_A} \equiv \frac{\omega}{v_A \sqrt{k^2 + m^2}}, \quad \phi_{c_s} \equiv \frac{\omega}{c_s \sqrt{k^2 + m^2}}. \quad (4.42)$$

If the quantity ϕ_{v_A} (or ϕ_{c_s} , which is especially convenient if discussing unmagnetized shearing flow) has a positive imaginary part, we have an unstable mode, whereas a negative imaginary part indicates a stable mode.

In the remainder of this section, and also in Sec. 4.3.3, we make frequent reference to the ‘growth rate’ $\text{Im}(\phi_{v_A})$, which is a condensed notation we use to indicate the following: from the set of four physically viable ϕ_{v_A} that, for a given choice of physical parameters, satisfy 1) the dispersion

relation, and 2) the ‘decaying’ boundary condition as $y \rightarrow \pm\infty$, select the maximum of the four imaginary parts; thus the notation $\text{Im}(\phi_{v_A}) > 0$ indicates instability, and $\text{Im}(\phi_{v_A}) < 0$ corresponds to stability.

The dispersion relation Eqs. 4.34 and 4.41 is written in terms of physical parameters v_A and c_s , but other parameterizations are possible. Yet another choice of parameters is

$$\mathcal{M}_r = \frac{\beta_{sh}}{c_s} \frac{\sqrt{1 - c_s^2}}{\sqrt{1 - \beta_{sh}^2}}, \quad (4.43)$$

$$\zeta = \frac{v_A}{c_s}, \quad (4.44)$$

which are the relativistic Mach number and Alfvénic Mach number, respectively (Chiu, 1973; Konigl, 1980; Bodo et al., 2004; Osmanov et al., 2008). An alternate parametrization, familiar from studies of magnetized plasmas (reconnection, turbulence, and shocks, for example) is in terms of ion plasma-beta and magnetization (defined with the in-plane component of magnetic field),

$$\beta_{ix} = \frac{2p_{0i}}{B_{x0}^2}, \quad (4.45)$$

$$\sigma_{wx} = \frac{B_{x0}^2}{w_0}, \quad (4.46)$$

where $p_{0i} = \rho_{0i}\theta_{0i}$ is the thermal pressure of ions (ρ_{0i} and θ_{0i} are the mass density and dimensionless temperature of ions, respectively; we consider a two fluid picture, with $p_{0i} = p_{0e}$), and the magnetic field and enthalpy are as defined in Secs. 4.2.2 and 4.2.3. To write Eqs. 4.34 and 4.41 in terms of β_i and σ_w , one also requires an equation of state relating dimensionless temperature and adiabatic index; to this end, we use a precise fitting formula to the Synge (1957) equation of state (Service, 1986); see Eq. 4.90 in Sec. 4.A. Our main results in Secs. 4.2.3.3 and 4.3.3 are phrased in terms of ion plasma-beta and magnetization.

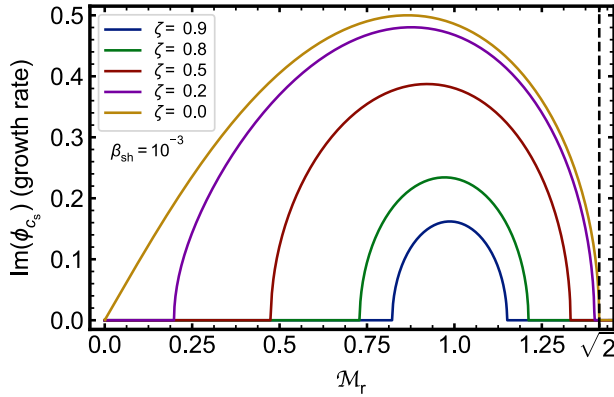


Figure 4.1: Relativistic Mach number dependence of the growth rate in relativistic MHD for symmetric shear flow, for different values of the Alfvénic Mach number, $\zeta \equiv v_A/c_s$. A vertical black dashed line at $M_r = \sqrt{2}$ indicates the classical stability bound.

To connect with results in the literature, we show in Fig. 4.1 the dependence of the growth rate $\text{Im}(\phi_{c_s})$ on relativistic Mach number for shear-aligned modes ($m = 0$), computed via the dispersion relation (Eqs. 4.34 and 4.41; our Fig. 4.1 can be compared with Fig. 1 in [Ferrari et al. \(1980\)](#), and Fig. 4 in [Bodo et al. \(2004\)](#)). The yellow curve in Fig. 4.1 corresponds to the nonrelativistic hydrodynamic limit, in which the system is stable to perturbations for Mach numbers above $\sqrt{2}$ ([Ferrari et al., 1980](#); [Bodo et al., 2004](#); [Hamlin & Newman, 2013](#)); see Sec. 4.2.3.2 for further discussion. This classical bound is indicated in Fig. 4.1 by a vertical black dashed line. Taken together, the sequence of colored lines demonstrates some of the basic physics of the KH instability in the presence of a shear-aligned magnetic field; as the Alfvénic Mach number increases (equivalently, as the magnitude of the in-plane magnetic field increases at fixed temperature), the range of M_r over which the system is unstable decreases, and also the maximum growth rate within the range of unstable M_r decreases. Heuristically, the effect of the magnetic field is similar to the stabilizing effect of a surface tension; as the strength of the magnetic field increases, the energy required by the wave to propagate along the direction of the magnetic field, and in doing so, bend the field lines, increases ([Chandrasekhar, 1961](#); [Hamlin & Newman, 2013](#)).

4.2.3.2 Symmetric shear flow: nonrelativistic HD dispersion relation

In the limit of vanishing magnetic fields, and nonrelativistic β_{sh} and c_s , roots of the dispersion relation Eqs. 4.34 and 4.41 simplify considerably (as a further simplification, we consider only modes which propagate along the direction of the shearing flow, i.e. modes with $m = 0$). With $v_A = 0$ and $m = 0$, Eq. 4.34 reduces to

$$\left(\frac{l_+}{l_-}\right)^2 = \frac{(\omega - k\beta_{\text{sh}})^2 - c_s^2(k - \omega\beta_{\text{sh}})^2}{(\omega + k\beta_{\text{sh}})^2 - c_s^2(k + \omega\beta_{\text{sh}})^2}. \quad (4.47)$$

Similarly, Eq. 4.34 simplifies:

$$\frac{l_+}{l_-} = \frac{(\omega - k\beta_{\text{sh}})^2}{(\omega + k\beta_{\text{sh}})^2}. \quad (4.48)$$

Eqs. 4.47 and 4.48 may be solved for ω , which yields (using Eq. 4.42) an analytic expression for the dimensionless phase velocity. For nonrelativistic β_{sh} and c_s , the (physically viable) solutions are

$$\phi_{c_s} = 0, \quad (4.49)$$

$$\phi_{c_s} = \sqrt{1 + \left(\frac{\beta_{\text{sh}}}{c_s}\right)^2} \pm \sqrt{1 + 4\left(\frac{\beta_{\text{sh}}}{c_s}\right)^2}. \quad (4.50)$$

As discussed in Sec. 4.2.3.1, the first solution Eq. 4.49 in fact corresponds to an unstable mode when one considers a smoothly varying shear profile. From the second set of solutions Eqs. 4.50, only the one with a minus sign can have a positive imaginary part, and it corresponds to an unstable mode; in particular, this root is purely imaginary when

$$\frac{\beta_{\text{sh}}}{c_s} < \sqrt{2}, \quad (4.51)$$

which demonstrates the classical result that the symmetric shear flow is unstable for $\mathcal{M}_c < \sqrt{2}$, where $\mathcal{M}_c \equiv \beta_{sh}/c_s$ is the classical Mach number (Chandrasekhar, 1961). This bound is plotted in Fig. 4.1 as a vertical black dashed line, and explains why the yellow curve (corresponding to Alfvénic Mach number $\zeta = 0$ and $\beta_{sh} = 10^{-3}$) indicates stability beyond $\mathcal{M}_c \approx \mathcal{M}_r = \sqrt{2}$; Bodo et al. (2004) have shown that the classical limit persists even for relativistic shearing flows, when one considers the appropriate Mach number, i.e. the system is unstable for $\mathcal{M}_r < \sqrt{2}$.

4.2.3.3 Astrophysical jet: relativistic MHD dispersion relation

Here, we derive the dispersion relation for the jet problem described in Sec. 4.2.1.1. The method of solution is similar to that presented in Sec. 4.2.3.1 for the symmetric shear problem, so here we focus on key results, and on any steps in the solution which differ from what is presented in Sec. 4.2.1.1.

For the jet setup, we consider a magnetic field which differs between the two sides of the shear, y_+ and y_- (the ‘wind’ and ‘jet’, respectively). On the wind side, the magnetic field is $\mathbf{B}_{0+} = (0, 0, b_w B_0)$, and on the jet side the magnetic field is $\mathbf{B}_{0-} = (B_0, 0, b_j B_0)$, which are both of the form $\mathbf{B}_{0\pm} = (B_{x0\pm}, 0, B_{z0\pm})$. Substitution of $\mathbf{B}_{0\pm}$ into Eq. 4.27, along with the divergence-free constraint, yields a dispersion relation governing RMHD waves in the fluid rest frame:³

$$\begin{aligned} \tilde{\omega}_\pm \cdot (\tilde{\omega}_\pm^2 - \tilde{k}_{\parallel\pm}^2 \tilde{v}_{A\pm}^2) \cdot & \left(\tilde{\omega}_\pm^4 - \tilde{\omega}_\pm^2 \left(\frac{\widetilde{B_{x0\pm}}^2 + \widetilde{B_{z0\pm}}^2}{|\widetilde{\mathbf{B}_0}|_\pm^2} |\widetilde{\mathbf{k}}|_\pm^2 \tilde{v}_{A\pm}^2 + c_{s\pm}^2 \left(|\widetilde{\mathbf{k}}|_\pm^2 - \frac{\tilde{v}_{A\pm}^2}{|\widetilde{\mathbf{B}_0}|_\pm^2} (\widetilde{B_{z0\pm}}^2 (\tilde{k}_\pm^2 + \tilde{l}_\pm^2) \right. \right. \right. \\ & \left. \left. \left. - 2 \widetilde{B_{x0\pm}} \widetilde{B_{z0\pm}} \tilde{k}_\pm \tilde{m}_\pm + \widetilde{B_{x0\pm}}^2 (\tilde{l}_\pm^2 + \tilde{m}_\pm^2) \right) \right) \right) + \tilde{k}_{\parallel\pm}^2 \widetilde{|\mathbf{k}|}_\pm^2 c_{s\pm}^2 \tilde{v}_{A\pm}^2 \Big) = 0. \end{aligned} \quad (4.52)$$

Similar to Eq. 4.32, the first factor in Eq. 4.52 corresponds to a marginally stable mode ($\tilde{\omega}_\pm = 0$), the second factor corresponds to Alfvén waves ($\tilde{\omega}_\pm = \pm \tilde{k}_{\parallel\pm} \tilde{v}_{A\pm}$), and the third factor gives the

³Even for quantities (apart from c_s) which transform trivially under a boost along x , such as \tilde{l}_\pm , \tilde{m}_\pm , and $\widetilde{B_{x0}}$, we do not suppress overtilde, to clarify that this equation applies generally in the fluid rest frame.

magnetosonic modes. Selecting the third factor in Eq. 4.52, we may solve for $\tilde{l}_\pm^2 (= l_\pm^2)$, then use appropriate Lorentz transforms to express each of l_+^2 and l_-^2 in terms of jet-frame quantities (note that, as described in Sec. 4.2.1.1, we choose the jet frame as the lab frame, so the equation for l_-^2 transforms trivially). To express the (wind-side) \tilde{l}_+^2 in terms of jet frame quantities, we employ standard Lorentz transformations,

$$\begin{aligned} \tilde{\omega}_+ &= \frac{\omega - k\beta_{\text{sh}}}{\sqrt{1 - \beta_{\text{sh}}^2}}, & \tilde{k}_+ &= \frac{k - \omega\beta_{\text{sh}}}{\sqrt{1 - \beta_{\text{sh}}^2}}, & \tilde{l}_+ &= l, & \tilde{m}_+ &= m, & \widetilde{B_{z0+}} &= B_{z0+}\sqrt{1 - \beta_{\text{sh}}^2}. \end{aligned} \quad (4.53)$$

The result, which we express in terms of our canonical choice of variables ϕ_{v_A} , β_{ix} , σ_{wx} , β_{sh} , b_j , b_w , ρ_{0j} , ρ_{0w} , k , and the ratio of wavevectors $f \equiv m/k$, is a rather lengthy equation; it is presented in full in Sec. 4.A (along with other calculational details). For the present discussion, we represent the solution as a placeholder function F_1 which simply indicates the quantities upon which $(l_+/l_-)^2$ depends:⁴

$$(l_+/l_-)^2 = F_1(\phi_{v_A}, k, \beta_{ix}, \sigma_{wx}, \rho_{0j}, \rho_{0w}, \beta_{\text{sh}}, b_j, b_w, f). \quad (4.54)$$

We obtain a second equation for $(l_+/l_-)^2$ from the linearized relativistic MHD momentum and induction equations (Eqs. 4.23–4.26), along with total pressure balance (to first order); on the jet

⁴In Sec. 4.A, we have derived the explicit form of Eq. 4.54 assuming an arbitrary mass ratio m_i/m_e in the plasma, but for the present discussion, we assume the two species to have equal masses, $m_i/m_e = 1$.

side, these read

$$kb_j B_0 B_{z1} - mb_j B_0 B_{x1} + kp_1 - v_{x1} \omega (b_j B_0)^2 + v_{z1} \omega b_j B_0^2 - \rho_0 h_0 v_{x1} \omega = 0, \quad (4.55)$$

$$\begin{aligned} k B_0 B_{y1} - l B_0 B_{x1} - lb_j B_0 B_{z1} + mb_j B_0 B_{y1} - lp_1 + v_{y1} \omega B_0^2 \\ + v_{y1} \omega (b_j B_0)^2 + \rho_0 h_0 v_{y1} \omega = 0, \end{aligned} \quad (4.56)$$

$$k B_0 B_{z1} - m B_0 B_{x1} - mp_1 - v_{x1} \omega b_j B_0^2 + v_{z1} \omega B_0^2 + \rho_0 h_0 v_{z1} \omega = 0, \quad (4.57)$$

$$mv_{x1} b_j B_0 - lv_{y1} B_0 - mv_{z1} B_0 + \omega B_{x1} = 0, \quad (4.58)$$

$$kv_{y1} B_0 + mv_{y1} b_j B_0 + \omega B_{y1} = 0, \quad (4.59)$$

$$kv_{x1} b_j B_0 + lv_{y1} b_j B_0 - kv_{z1} B_0 - \omega B_{z1} = 0, \quad (4.60)$$

$$p_{\text{tot1}} - (p_1 + B_{x1} B_0 + B_{z1} b_j B_0) = 0, \quad (4.61)$$

and on the wind side (in the frame comoving with the wind),

$$\tilde{k}_+ \widetilde{B_{z0+}} \widetilde{B_{z1+}} - m \widetilde{B_{z0+}} B_{x1+} + \tilde{k}_+ \tilde{p}_{1+} - \widetilde{v_{x1+}} \widetilde{\omega}_+ \widetilde{B_{z0+}}^2 - \widetilde{\rho_0}_+ h_{0+} \widetilde{v_{x1+}} \widetilde{\omega}_+ = 0, \quad (4.62)$$

$$l_+ \widetilde{B_{z0+}} \widetilde{B_{z1+}} - m \widetilde{B_{z0+}} \widetilde{B_{y1+}} + l_+ \tilde{p}_{1+} - \widetilde{v_{y1+}} \widetilde{\omega}_+ \widetilde{B_{z0+}}^2 - \widetilde{\rho_0}_+ h_{0+} \widetilde{v_{y1+}} \widetilde{\omega}_+ = 0, \quad (4.63)$$

$$m \tilde{p}_{1+} - \widetilde{\rho_0}_+ h_{0+} \widetilde{v_{z1+}} \widetilde{\omega}_+ = 0, \quad (4.64)$$

$$-m \widetilde{v_{x1+}} \widetilde{B_{z0+}} - \widetilde{\omega}_+ B_{x1+} = 0, \quad (4.65)$$

$$-m \widetilde{v_{y1+}} \widetilde{B_{z0+}} - \widetilde{\omega}_+ \widetilde{B_{y1+}} = 0, \quad (4.66)$$

$$\tilde{k}_+ \widetilde{v_{x1+}} \widetilde{B_{z0+}} + l_+ \widetilde{v_{y1+}} \widetilde{B_{z0+}} - \widetilde{\omega}_+ \widetilde{B_{z1+}} = 0, \quad (4.67)$$

$$\widetilde{p_{\text{tot1+}}} - (\widetilde{p_{1+}} + \widetilde{B_{z1+}} \widetilde{B_{z0+}}) = 0. \quad (4.68)$$

By solving Eqs. 4.55–4.61 and 4.62–4.68 for l and l_+ , respectively, and using the Lorentz transforma-

mations 4.53, along with the displacement matching condition at the interface,

$$\frac{v_{y1}}{\omega} = \frac{\widetilde{v_{y1+}}}{\frac{\omega - k\beta_{sh}}{\sqrt{1-\beta_{sh}^2}}}, \quad (4.69)$$

the ratio of wavevectors l_+/l is obtained. The result may be expressed as a function of ϕ_{v_A} , k , β_{ix} , σ_{wx} , ρ_{0j} , ρ_{0w} , β_{sh} , b_j , b_w , and f ($= m/k$, which controls the angle of propagation of the wave in the xz plane). The result, which we indicate by the function F_2 ,

$$l_+/l = F_2(\phi_{v_A}, k, \beta_{ix}, \sigma_{wx}, \rho_{0j}, \rho_{0w}, \beta_{sh}, b_j, b_w, f), \quad (4.70)$$

is stated explicitly in Sec. 4.A (see Eq. 4.85). Together, Eqs. 4.54 and 4.70 provide the desired dispersion relation. To study the growth rate of unstable modes in the jet problem, we compute (numerically) solutions to the equation

$$F_1(\phi_{v_A}, k, \beta_{ix}, \sigma_{wx}, \rho_{0j}, \rho_{0w}, \beta_{sh}, b_j, b_w, f) = F_2(\phi_{v_A}, k, \beta_{ix}, \sigma_{wx}, \rho_{0j}, \rho_{0w}, \beta_{sh}, b_j, b_w, f)^2. \quad (4.71)$$

The dependence on k cancels between the two sides of Eq. 4.71, so solutions ϕ_{v_A} are finally computed as roots of an equation of the form

$$F_3(\phi_{v_A}, \beta_{ix}, \sigma_{wx}, \rho_{0j}, \rho_{0w}, \beta_{sh}, b_j, b_w, f) = 0. \quad (4.72)$$

As described in Sec. 4.2.3.1, squaring F_2 (which is equal to l_+/l) in Eqn. 4.71 introduces four nonphysical roots which do not satisfy Eq. 4.70, so we reject these solutions. We also reject solutions that do not satisfy the boundary condition $\text{Im}(l_+) > 0$ and $\text{Im}(l) < 0$; this is a statement that the wave amplitude must approach zero as $y \rightarrow \pm\infty$.

Parameter	Eqn.	Description
β_{ix}	Eq. 4.45	$p_{0i}/(B_{x0}^2/2)$, the ion plasma-beta defined with respect to in-plane magnetic field; ratio of ion thermal pressure to in-plane magnetic pressure on jet side
σ_{wx}	Eq. 4.46	B_{x0}^2/w_0 , magnetization defined with respect to in-plane magnetic field; controls ratio of $(2\times)$ in-plane magnetic pressure to plasma enthalpy density in the jet
β_{sh}	Eq. 4.3	Speed of wind relative to the jet
b_j	Eq. 4.4	$B_{z0,j}/B_{x0,j}$, strength of guide field in the jet (as measured in the jet/lab frame), in units of in-plane magnetic field $B_{x0,j}$ (in the jet)
b_w	Eq. 4.4	$B_{z0,w}/B_{x0,j}$, strength of guide field in the wind (as measured in the jet/lab frame), in units of in-plane magnetic field $B_{x0,j}$ (in the jet)
ρ_{0j}	Eq. 4.5	Mass density of the jet (in the fluid rest frame)
ρ_{0w}	Eq. 4.5	Mass density of the wind (in the fluid rest frame)
f	Eq. 4.22	m/k , the ratio of wave vectors in the plane of the shear interface (that is, the xz plane); controls propagation angle of perturbation

Table 4.1: Listing of parameters used to specify the initial state for the astrophysical jet problem.

4.2.4 Astrophysical jet: numerical results

To explore the parameter dependence of the KH instability in the astrophysical jet problem, we compute the growth rate $\text{Im}(\phi_{v_A})$ for different selections of our standard variables β_{ix} , σ_{wx} , β_{sh} , b_j , b_w , ρ_{0j} , ρ_{0w} , and f ; for easy reference, these are listed in Tab. 4.1, along with short descriptions.

4.2.4.1 β_{ix} , σ_{wx} , and β_{sh} dependence of instability for propagation perpendicular to the jet-side magnetic field

As a first case, we consider a limit which is similar to pure hydrodynamic (HD) flow; we compute the growth rate $\text{Im}(\phi_{v_A})$ in the $\beta_{ix}\sigma_{wx}$ -plane, for β_{sh} in the range 0.1–0.9 ($b_j = 20$ and $b_w = 0$ are held fixed). We assume a ratio of wind-side density to jet-side density of $\rho_{0w}/\rho_{0j} = 100$. The parameter f is chosen to be zero, so that the perturbation propagates perpendicular to the magnetic field in the jet, i.e. $\mathbf{k} \cdot \mathbf{B}_{0-} = 0$; this choice is motivated by analogy to the symmetric shear problem, in which the growth rate is maximized when the wave propagates perpendicular to the magnetic field (Chandrasekhar, 1961; Miura & Pritchett, 1982; Hamlin & Newman, 2013).⁵ The result of the calculation in which we assume that $\mathbf{k} \cdot \mathbf{B}_{0-} = 0$ is satisfied is shown in Fig. 4.2; the grayed-out

⁵Chandrasekhar (1961), for example, proved that for the symmetric shear problem in MHD (and for a tangential discontinuity), perturbations grow as $\text{Im}(\phi_{v_A}) = \frac{1}{v_A} \sqrt{\frac{\beta_{sh}^2}{\rho} - \frac{(\hat{\mathbf{k}} \cdot \mathbf{B}_0)^2}{\rho}}$, which is maximized for $\hat{\mathbf{k}} \cdot \mathbf{B}_0 = 0$.

region indicates a region of the parameter space that is physically inaccessible, according to the definitions of β_{ix} and σ_{wx} (see Sec. 4.A for further details). Setting $\mathbf{k} \cdot \mathbf{B}_{0-} = 0$ is somewhat similar to HD because the perturbation propagates perpendicular to the magnetic field, so it does not experience the restoring force of magnetic tension that it would, were it propagating with some component parallel to the magnetic field. In fact, under a Lorentz boost by $+\beta_{sh}/2$ along x , the present case is similar to the symmetric shear problem in HD with $f = 0$ (i.e. wave propagation parallel to the direction of shear flow), which corresponds to the yellow curve in Fig. 4.1. Due to the physical similarity to the symmetric KH problem, we may expect the present case to exhibit a stability bound that is analogous to the classical one, $\mathcal{M}_c > \sqrt{2}$ (see Eq. 4.51). Indeed, if one recasts the jet dispersion relation Eqs. 4.84 and 4.85 in terms of v_A and c_s ,⁶ and considers the unmagnetized case $v_A = 0$ (and also $f = 0$), the dispersion relation may be written (to fourth order in c_s and β_{sh}) as a fifth-degree polynomial in ϕ_{c_s} ,

$$\beta_{sh}^4 - 4c_s\beta_{sh}^3\phi_{c_s} + 6c_s^2\beta_{sh}^2\phi_{c_s}^2 - \beta_{sh}^4\phi_{c_s}^2 - 4c_s^3\beta_{sh}\phi_{c_s}^3 + 4c_s\beta_{sh}^3\phi_{c_s}^3 - 5c_s^2\beta_{sh}^2\phi_{c_s}^4 + 2c_s^3\beta_{sh}\phi_{c_s}^5 = 0, \quad (4.73)$$

whose physically viable solutions are

$$\phi_{c_s} = \frac{1}{2} \frac{\beta_{sh}}{c_s}, \quad (4.74)$$

$$\phi_{c_s} = \frac{\beta_{sh} + \sqrt{\beta_{sh}^2 \pm 4c_s(c_s - \sqrt{c_s^2 + \beta_{sh}^2})}}{2c_s}. \quad (4.75)$$

The solution with the minus sign in Eq. 4.75 becomes pure imaginary if

$$\frac{\beta_{sh}}{c_s} < 2\sqrt{2}, \quad (4.76)$$

⁶Here, c_s is defined with respect to the jet-side plasma.

which is equivalent⁷ to the classical bound Eq. 4.51 (see also Ferrari et al. (1980), Fig. 1, panel (a)). Even for the large guide-field case presented in Fig. 4.2, the bound Eq. 4.76 may offer some physical insight as to the meaning of the stable region at sufficiently low σ_{wx} ; due to pressure balance at the interface of the wind and jet, and because the wind side is in the present case unmagnetized (as $b_w = 0$), the Alfvén velocity v_A and wind-side sound speed $c_{s,w}$ are related by $c_{s,w} = v_A \sqrt{\Gamma_{ad,w}/2} = v_A \sqrt{5/6} \sqrt{\rho_{0j}/\rho_{0w}}$, assuming nonrelativistic temperatures. By writing v_A in terms of σ_{wx} and substituting into Eq. 4.76, one obtains a (β_{sh} -dependent) limit on σ_{wx} , below which the system is stable to perturbations, i.e.

$$\sigma_{wx} \lesssim \sigma_{wx,crit} = \frac{3}{20} \frac{\rho_{0w}}{\rho_{0j}} \frac{\beta_{sh}^2}{1 + b_j^2}. \quad (4.77)$$

While this argument is only heuristic in nature (in that it captures roughly, up to a constant numerical factor, the scaling with β_{sh} of the lower bound of the unstable region with respect to σ_{wx} ; this lower bound is clear in Fig. 4.2), it may offer some physical intuition as to the origin of the stable region at sufficiently low σ_{wx} (and low β_{ix}) that is evident in Fig. 4.2.

4.2.4.2 β_{sh} , v_{ms} , σ_{wx} , and β_{iz} dependence of instability

In Fig. 4.3, we present the growth rate of the instability in the $v_{ms}\beta_{sh}$ plane, where v_{ms} is the magnetosonic speed,

$$v_{ms} \equiv \sqrt{\frac{c_s^2 + v_A^2}{1 + v_A^2}}. \quad (4.78)$$

Parameterizing the growth rate in the variables v_{ms} and β_{sh} , as an alternative to σ_{wx} and β_{ix} in Fig. 4.2, allows for a convenient transition between the HD limit and the magnetized limit that is our

⁷One must account for a Lorentz boost by $+\beta_{sh}/2$ along x ; β_{sh} in the jet problem is the total difference in velocity between the two sides of the shear flow, whereas β_{sh} in the symmetric problem represents half of the total velocity difference.

main focus in the jet problem; note that for small v_A , the magnetosonic speed $v_{ms} \approx c_s$, whereas for $v_A \approx 1$, $v_{ms} \approx v_A$.⁸ The growth rate is computed for $\beta_{iz} \in \{0.01, 1, 100\}$ (β_{iz} is the ratio of ion thermal pressure to magnetic pressure, computed with only the out-of-plane component of magnetic field) and $\sigma_{wx} \in \{0, 0.1, 1\}$. The guide field in the wind is $b_w = 0$; in-plane perturbations ($f = 0$) are considered; and the ratio of wind-side density to jet-side density is 100. Note that by fixing β_{iz} , σ_{wx} , and v_{ms} , both the (in-plane) ion plasma-beta β_{ix} and guide-field parameter b_j are determined. As in Fig. 4.2, the physically inaccessible regions are shaded gray.

A larger value of σ_{wx} corresponds to stronger in-plane magnetic field B_{x0} (on the jet side; the in-plane magnetic field is zero on the wind side), whereas smaller values of σ_{wx} correspond to weaker in-plane magnetic field; β_{iz} is an indicator of both the strength of the out-of-plane magnetic field, as well as the temperature on the jet side. In the language of σ_{wx} and β_{iz} , the HD limit corresponds to $\sigma_{wx} \ll 1$ and $\beta_{iz} \gg 1$. Of the cases presented in Fig. 4.3, panel C (with $\beta_{iz} = 100$ and $\sigma_{wx} = 0$) is closest to the HD limit. For this case, the magnetosonic speed is approximately equal to the sound speed, which has a largest possible value of $1/\sqrt{3}$; this is roughly where the gray-shaded region of nonphysical parameter space begins.

As shown in panel C, the jet system is unstable when $\beta_{sh} \lesssim v_{ms}$, even as β_{sh} approaches zero; which parallels the pure HD case (see, e.g., the yellow curve in Fig. 4.1). As the strength of the in-plane magnetic field increases, the magnetic tension increases, and requires progressively larger shear velocities to activate the instability (this can be seen by tracking, in the sequence of panels C-F-I, the location of the lower instability bound, i.e. the boundary furthest to the left delimiting the unstable region in β_{sh}). Indeed, for this high- β_{iz} case, the Alfvén speed is about equal to $\sqrt{\sigma_{wx}/(1 + \sigma_{wx})}$; for panels C, F, and I, the Alfvén speeds are 0, ~ 0.3 , and ~ 0.7 , which are approximately equal to the lowest possible values of β_{sh} required to activate the instability (for

⁸Even when c_s equals its maximum value $1/\sqrt{3}$, $v_{ms} \approx 0.82$, which is not too different from $v_A \approx 1$.

$\sigma_{wx} = 0, 0.1$, and 1 , respectively). This stability bound at $\beta_{sh} \approx v_A$ is analogous to the stability bound at sufficiently low (relativistic) Mach number \mathcal{M}_r shown in Fig. 4.1. Note that in Fig. 4.1, there is a ζ -dependent ($\zeta \equiv v_A/c_s$ is the Alfvénic Mach number) stable region, located roughly at $\zeta \approx \mathcal{M}_r$; considering the nonrelativistic limit for simplicity, this corresponds to a stability bound at $\beta_{sh} \approx v_A$. Physically, the condition that the instability is suppressed for $\beta_{sh} \lesssim v_A$ corresponds to magnetic tension suppressing growth of the perturbation, if the perturbation does not have enough energy to propagate along the magnetic field. As the magnetic tension increases (along the direction of wave propagation), the minimum energy required to activate the instability, and correspondingly the minimum shear β_{sh} (which is the source of free energy supplying growth of the perturbation), increases.

Panels A, B, D, E, and F (in Fig. 4.3) are also shown to satisfy (roughly) the criterion for instability ($\beta_{sh} > \sqrt{\sigma_{wx}/(1 + \sigma_{wx})}$); for smaller values of β_{iz} ($= 1, 0.01$), this bound appears to hold when $v_{ms} \approx v_A$, which is true as v_{ms} decreases toward the nonphysical gray region (this implies c_s is minimized). In addition to decreasing the area of the $v_{ms}\beta_{sh}$ plane over which the instability is active, increasing the in-plane magnetic tension decreases the magnitude of the growth rate. Even at $\sigma_{wx} = 1$, an upper bound for instability exists, evidently as a deformation of the line $v_{ms} \propto \beta_{sh}$ in the HD limit (panel C).

For the sequence of panels C-B-A ($\sigma_{wx} = 0$, and $\beta_{iz} = 100, 1$, and 0.01), the shape of the unstable region is largely unchanged (apart from the physically accessible region, whose upper limit approaches the maximum possible value of the magnetosonic speed, $v_{ms,max} = \sqrt{(3 + \sqrt{3})/6}$), because decreasing β_{iz} allows for larger magnetic fields, and in turn larger Alfvénic velocities). The magnitude of the growth rate $\text{Im}(\phi_{v_A})$ decreases, but this is largely due to the chosen normalization $\phi_{v_A} \equiv \omega/(kv_A)$, and should not be interpreted as a statement that the growth rate of the instability is intrinsically smaller at low β_{iz} .

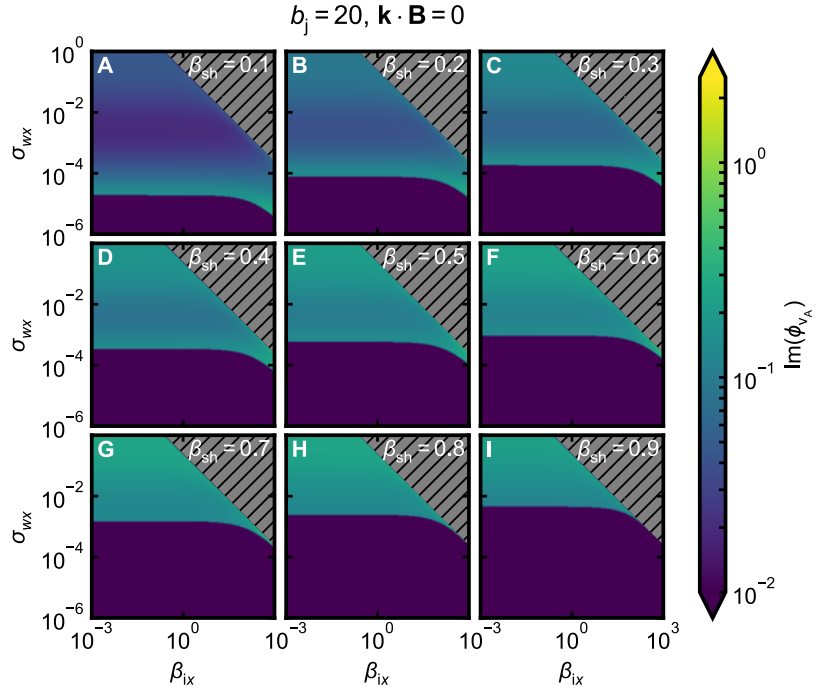


Figure 4.2: β_{ix} and σ_{wx} dependence of instability in the jet problem for β_{sh} in the range 0–0.9; for this case, the guide-field parameter in the jet is $b_j = 20$, and the perturbation propagates perpendicular to the magnetic field. Dark regions are stable, blue regions are unstable, and hatched gray regions are physically inaccessible regions of the $\beta_{ix}\sigma_{wx}$ plane (see Sec. 4.A).

4.2.4.3 β_{ix} , σ_{wx} , β_{sh} , and b_j dependence of instability

In Figs. 4.4, 4.5, 4.6, and 4.7, we present a series of calculations of the growth rate $\text{Im}(\phi_{v_A})$ for jet guide fields $b_j = 0, 0.3, 1$, and 3 , respectively; growth rates are computed in the $\beta_{ix}\sigma_{wx}$ plane (as in Fig. 4.2), for β_{sh} in the range 0.1–0.9 (the layout is similar to that of 4.2). As before, the density ratio is fixed to $\rho_{0w}/\rho_{0j} = 100$, but here we consider perturbations with $f = 0$.

We focus first on Fig. 4.4, with $b_j = 0$; this corresponds to purely in-plane magnetic field. The sequence of panels A–I demonstrates that as β_{sh} increases, the instability is suppressed; by $\beta_{sh} = 0.9$, the magnitude of instability has decreased, and the region of instability shrinks.

Comparing the two cases $b_j = 0$ (Fig. 4.4) and $\mathbf{k} \cdot \mathbf{B} = 0$, $b_j = 20$ (Fig. 4.2), one notices a substantial difference in the unstable region, especially at low β_{ix} . In Fig. 4.4, the unstable region at low β_{ix} covers only a sliver of the range of σ_{wx} , whereas in Fig. 4.2, there is evidently no upper

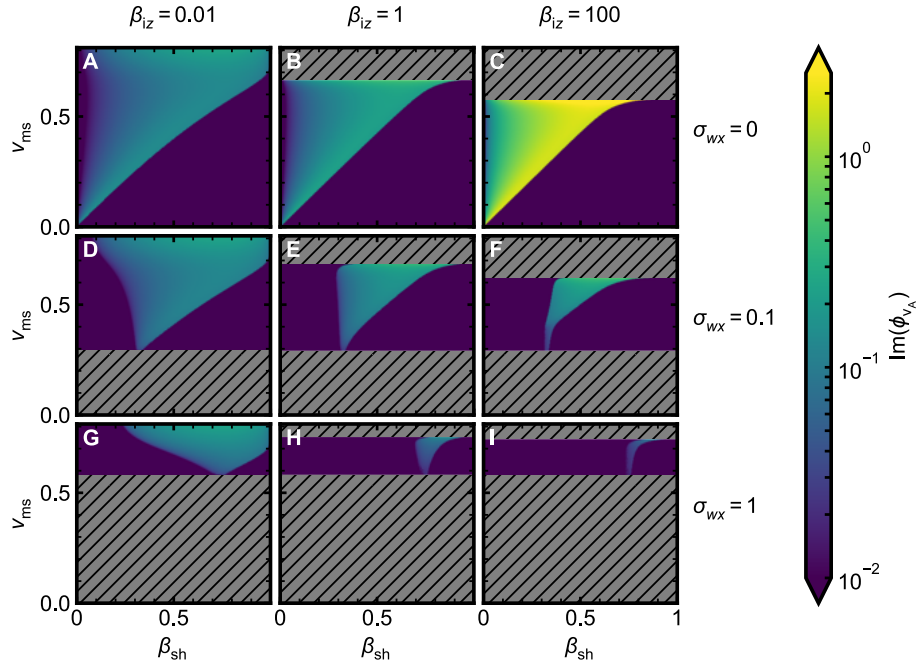


Figure 4.3: β_{sh} and v_{ms} dependence of instability in the jet problem for β_{iz} in the range 0.01–100 and σ_{wx} in the range 0–1.

stability bound in σ_w (the unstable region extends to at least $\sigma_{wx} = 1$ in all panels of Fig. 4.2).

A physical reason for this remarkable difference in upper stability bounds when comparing the $b_j = 0$ and $\mathbf{k} \cdot \mathbf{B} = 0$ cases is that for the former, the wave propagates along the magnetic field, and thus the instability depends on the magnetic tension; in particular, for σ_{wx} sufficiently large, the restoring force of the magnetic field inhibits the instability (for fixed β_{sh} , and independently of β_{ix} when β_{ix} is small). On the other hand, for the case with $b_j = 20$ and $\mathbf{k} \cdot \mathbf{B} = 0$, the wave propagates perpendicular to the magnetic field, and is therefore insensitive to the effect of increasing σ_{wx} (regardless of σ_{wx} , the perturbation propagates perpendicular to the magnetic field, for all points computed in Fig. 4.2).

Figs. 4.5–4.7 show the β_{ix} , σ_{wx} , and β_{sh} dependence of the instability, for jet guide fields $b_j = 0.3, 1$, and 3 , which helps to clarify the transition from the extreme case of in-plane propagation parallel to the magnetic field (Fig. 4.4), to in-plane propagation perpendicular to the magnetic

field (Fig. 4.2). Comparing the sequence of figures (Fig. 4.5)–(Fig. 4.6)–(Fig. 4.7) shows that for increasing guide field, the lower stability bound decreases, and the upper stability bound increases, so that the unstable region extends to cover a larger range in σ_{wx} . By $b_j = 3$, panels D–I (Fig. 4.7) indicate instability for σ_{wx} as large as 10^2 , similar to the extreme case presented in Fig. 4.2, for which the perturbation propagates perpendicular to the magnetic field.

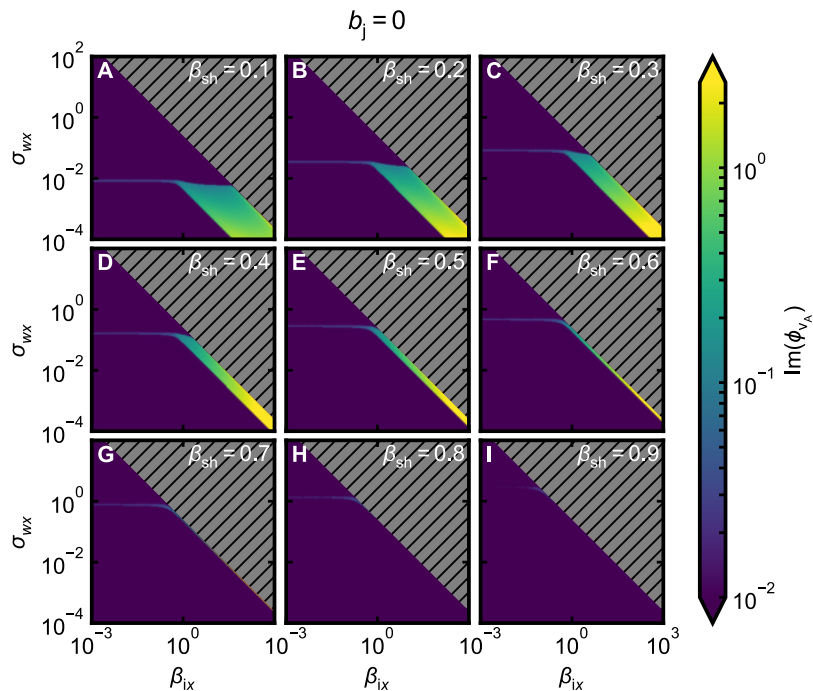


Figure 4.4: β_{ix} and σ_{wx} dependence of instability in the jet problem for β_{sh} in the range 0–0.9; the guide-field parameter in the jet is $b_j = 0$.

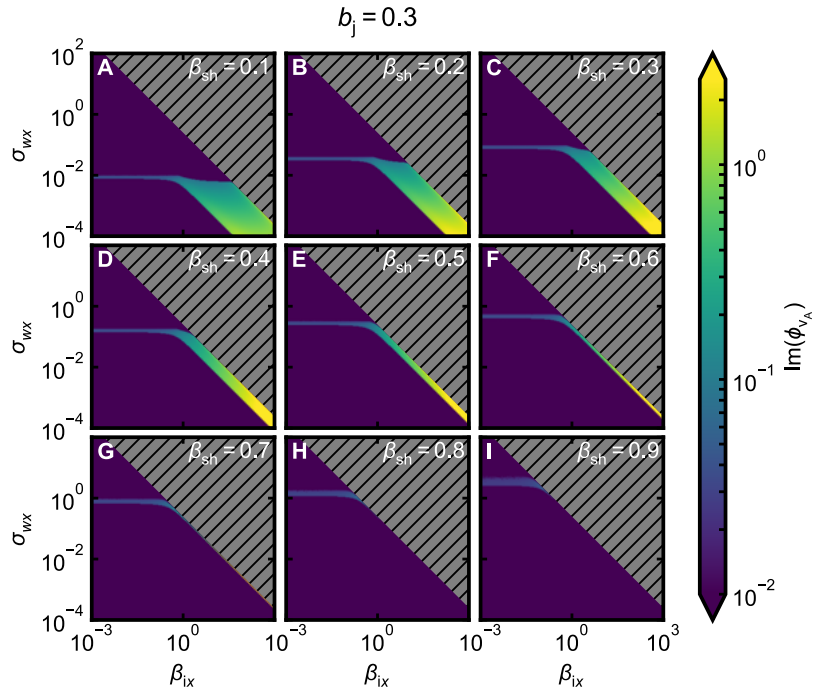


Figure 4.5: The layout is similar to that of Fig. 4.4; β_{ix} and σ_{wx} dependence of instability in the jet problem for β_{sh} in the range 0–0.9; the guide-field parameter in the jet is $b_j = 0.3$.

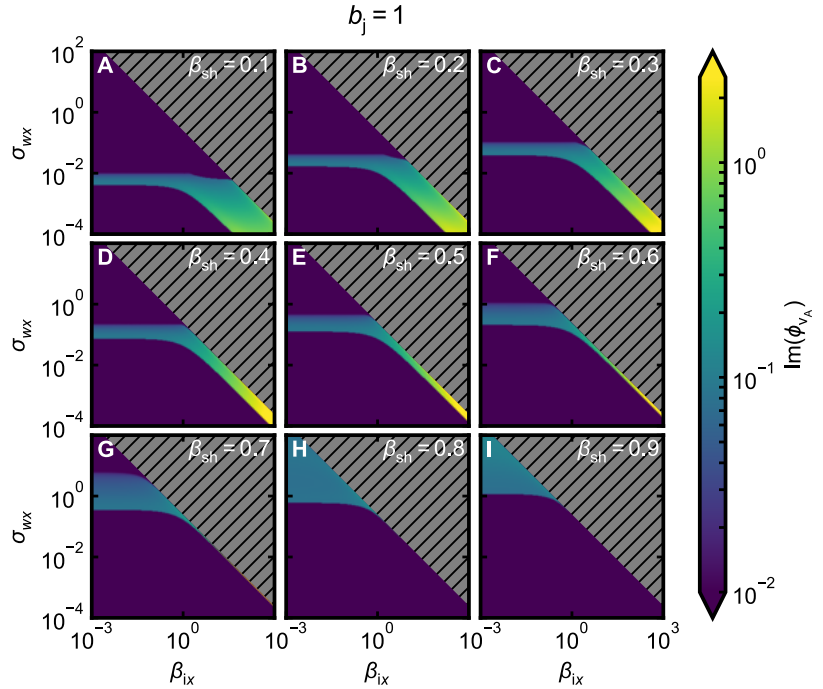


Figure 4.6: The layout is similar to that of Fig. 4.4; β_{ix} and σ_{wx} dependence of instability in the jet problem for β_{sh} in the range 0–0.9; the guide-field parameter in the jet is $b_j = 1$.

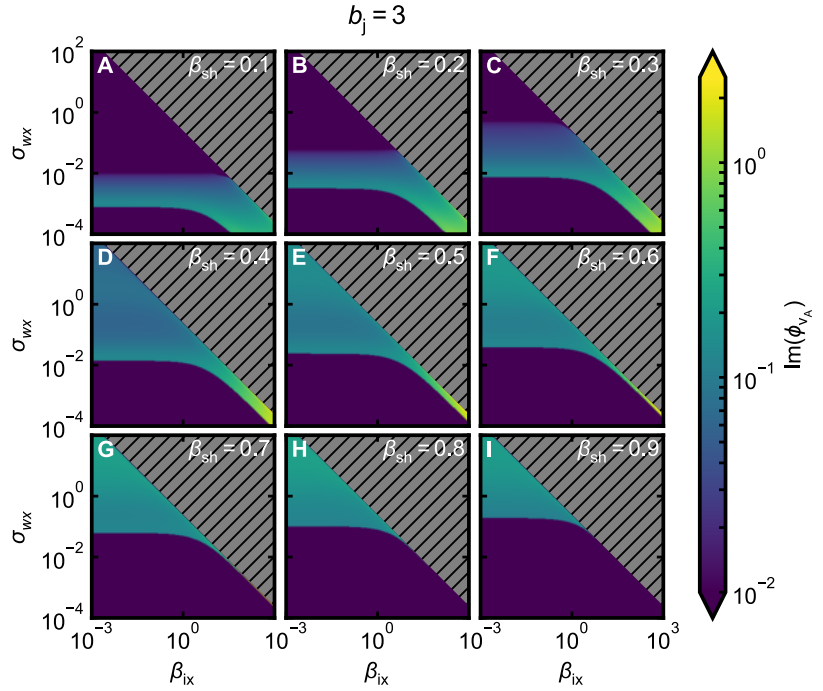


Figure 4.7: The layout is similar to that of Fig. 4.4; β_{ix} and σ_{wx} dependence of instability in the jet problem for β_{sh} in the range 0–0.9; the guide-field parameter in the jet is $b_j = 3$.

4.2.4.4 ρ_{0w}/ρ_{0j} dependence of instability

In Fig. 4.8, we show the dependence of the growth rate on the ratio of wind-side density to jet-side density, computed via numerical solution of Eqs. 4.84 and 4.85. For this calculation, $\beta_{sh} = 0.8$, $\beta_{ix} = 10^{-4}$, $\sigma_{wx} = 1$, $b_j = 3$, and $b_w = 0.3$; the parameters of the calculation are listed in the upper right of the figure.

The shape of the curve resembles one that follows from the classically known result for the KH growth rate, allowing for different densities on either side of the interface (see e.g., [Chandrasekhar \(1961\)](#)):

$$\text{Im}(\phi) \propto \sqrt{\frac{\rho_1 \rho_2}{(\rho_1 + \rho_2)^2}}, \quad (4.79)$$

where $\text{Im}(\phi)$ is a dimensionless growth rate, and ρ_1 and ρ_2 are the densities of the two fluids.⁹

According to Fig. 4.8, the magnitude of the instability decreases as the ratio ρ_{0w}/ρ_{0j} increases, but even at $\rho_{0w}/\rho_{0j} = 1000$, the growth rate decreases by only a factor of ~ 3 relative to the growth rate at $\rho_{0w}/\rho_{0j} = 1$. This observation has important astrophysical implications, as realistic density ratios ρ_{0w}/ρ_{0j} may limit the regions of the jet which are strongly KH unstable.

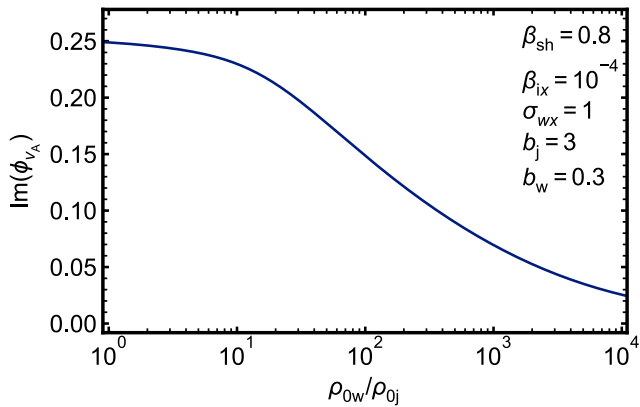


Figure 4.8: Dependence of instability growth rate, in the jet problem, on the ratio of densities between wind and jet.

4.3 Relativistic MHD simulation

All the discussion so far was based on analytic methods and linear stability analysis. As a reality check, we use numerical simulations of the symmetric KH setup, as well as the astrophysical jet problem (described in Secs. 4.2.1.1 and 4.2.1.2, respectively), to measure instability growth rates and compare with predictions of the dispersion relations, Eqs. 4.34, 4.41 and Eqs. 4.84, 4.85. To simulate the KH instability in relativistic MHD, we use the publicly available code **PLUTO** ([Mignone et al., 2011](#)). We perform both two-dimensional and three-dimensional simulations; the latter of

⁹We note that, according to Eq. 4.79, the growth rate in the symmetric KH problem decreases by a factor of ~ 16 as the density ratio increases from $\rho_1/\rho_2 = 1$ to $\rho_1/\rho_2 = 1000$; this differs from the result computed for the jet setup in Fig. 4.8, where the growth rate decreases by a factor of ~ 4 as the density ratio increases from $\rho_{0w}/\rho_{0j} = 1$ to $\rho_{0w}/\rho_{0j} = 1000$. To account for this difference, we remark that Eq. 4.79 does not account for the effect of magnetic fields; as shown in Sec. 4.2.4.3, magnetic fields modify the parameter dependence of the instability relative to the unmagnetized case.

these allows for testing of the f dependence of the dispersion relations.

4.3.1 Simulation setup

Here, we describe the simulation setup for the jet problem (the setup for the symmetric shear problem is similar). The setup described here is based on the one presented in Sec. 6.6 of [Mignone et al. \(2011\)](#).

Simulation coordinates are as follows: xy is the 2D simulation plane, with $x \in [0, 1]$ and $y \in [-1, 1]$. The x dimension is typically resolved with 1280 cells, whereas the y dimension is resolved with 2560 cells (for 2D simulations). The domain is periodic along x , and outflowing along y (for 3D simulations, the domain is also periodic along z).

We initialize a smoothly varying shear profile in which the flow is along x and the flow velocity varies with y , as well as a small perturbation to the y velocity:

$$\mathbf{v}(x, y) = \left\{ \frac{\beta_{sh}}{2} \left(1 + \tanh \left(\frac{y}{\alpha} \right) \right), \epsilon \sin(k_{x0}x) \exp \left(\frac{-y^2}{\beta^2} \right), 0 \right\}. \quad (4.80)$$

Here, β_{sh} is the velocity difference between jet and wind, $\epsilon = 10^{-5}$ is the amplitude of the perturbation, and we take $\alpha = 0.005$, and $\beta = 0.1$ as fiducial numerical choices; in general, we choose α to ensure that the transition of v_x across y is resolved with at least 13 cells along the y direction. The choice of α is further discussed in Sec. 4.B.

The magnetic field profile is also smoothly varying, and contains an in-plane component on the jet side, as well as out-of-plane components on both the jet and wind sides:

$$\mathbf{B}(x, y) = \left\{ B_0 \left(1 - \frac{1}{2} \left(1 + \tanh \left(\frac{y}{\alpha} \right) \right) \right), 0, B_0 \left(b_w + \frac{1}{2} (b_j - b_w) \left(1 - \tanh \left(\frac{y}{\alpha} \right) \right) \right) \right\}. \quad (4.81)$$

b_j and b_w are the guide-field parameters controlling the strength of the z component of magnetic

field. The profile of thermal pressure is chosen to ensure that total pressure is constant along y ,

$$p(x, y) = p_j + \frac{1}{2}(B_0^2 + b_j^2 B_0^2) - \frac{1}{2}(B_x(x, y)^2 + B_y(x, y)^2 + B_z(x, y)^2), \quad (4.82)$$

where p_j is the chosen jet thermal pressure, which is controlled by the initial choice of jet-side ion plasma-beta and magnetization. This choice of thermal pressure profile sets $p(x, y) = p_j$ on the jet side (sufficiently far from the transition, $y \lesssim 0$), and on the wind side $p(x, y) = p_j + \frac{1}{2}(B_0^2 + b_j^2 B_0^2 - b_w^2 B_0^2)$ (for $y \gtrsim 0$). The profile of initial mass density is

$$\rho(x, y) = \rho_{0w} + \frac{1}{2}(\rho_{0j} - \rho_{0w}) \left(1 - \tanh\left(\frac{y}{\alpha}\right)\right). \quad (4.83)$$

4.3.2 Simulation results: astrophysical jet

Here, we compare the growth rate of the KH instability, computed via the dispersion relation Eq. 4.72 (written in full in Eqs. 4.84 and 4.85), with measurements of the growth rate in relativistic MHD simulations. To start, we briefly outline the method for extracting growth rates of the KH instability from simulations.

We measure the growth rate of the instability via growth of the quantity $|\tilde{v}_y(k_{x0})|^2$ in time, which is the amplitude squared of the Fourier transformed velocity field v_y (for simplicity of discussion, we consider v_y to be a two-dimensional field). By means of a Fast Fourier Transform (FFT), we compute $|\tilde{v}_y(k_x, k_y)|^2$ at each output step of the simulation; the arguments k_x and k_y can be any of the allowed wave vectors on the (discretized) domain: $k_x = (2\pi/L_x), 2 \cdot (2\pi/L_x), \dots, n_x \cdot (2\pi/L_x)$ (n_x is the number of grid points in x), and similarly for k_y . At each output step, we measure the amplitude squared at the wavevector $\mathbf{k} = (k_{x0}, k_{y1})$, where k_{x0} is the wavevector of the initialized perturbation and k_{y1} is the wavevector of the longest wavelength perturbation in y (this choice typically captures the peak in \mathbf{k} -space of the initialized perturbation). Prior to computing the

FFT, we apply a Gaussian Filter to the field $v_y(x, y)$; the filter is centered at the interface of the shear, with a width that is 20% of the domain in y (this procedure helps to reduce noise).

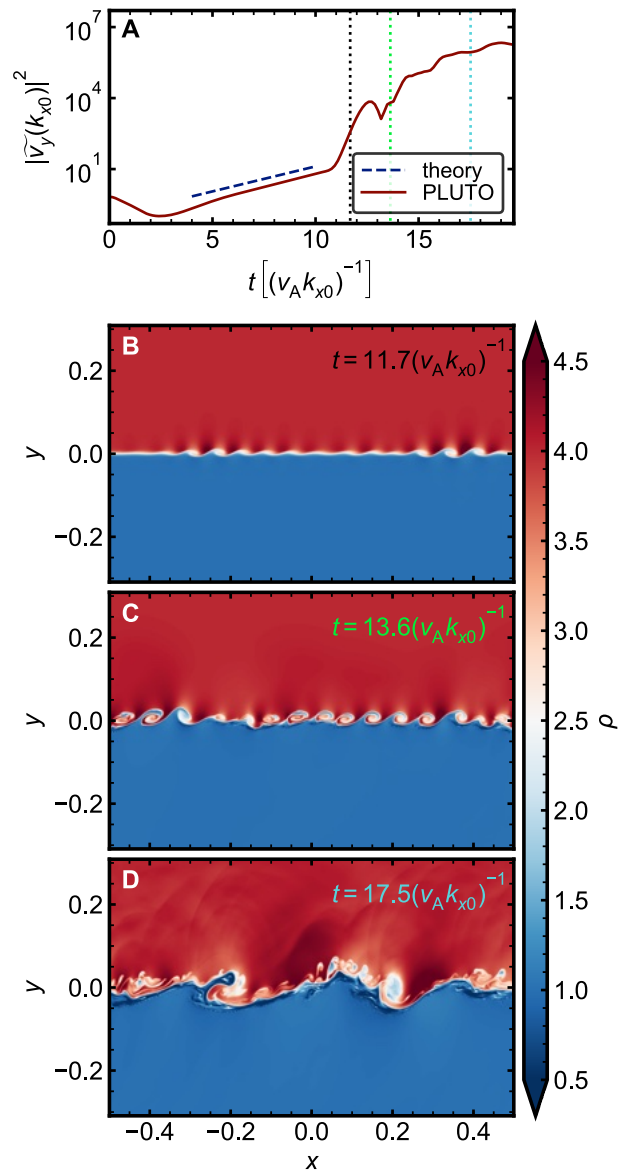


Figure 4.9: For a jet simulation with $\beta_{ix} = 0.078$, $\sigma_{wx} = 1$, $\beta_{sh} = 0.8$, $b_j = 3$, $b_w = 0.3$, $f = 0$, and $\rho_{0w}/\rho_{0j} = 4$, (A) Time evolution of Fourier amplitude, (B)–(D) 2D snapshots of the density at times indicated in the upper right of each snapshot; these are indicated also by color coded vertical lines in panel A.

4.3.2.1 Example simulation with **PLUTO**

As an example, we show in Fig. 4.9 the growth of $|\tilde{v}_y(k_{x0})|^2$ in a simulation of the KH instability via the jet setup (the simulation parameters are $\beta_{ix} = 0.078$, $\sigma_{wx} = 1$, $\beta_{sh} = 0.8$, $b_j = 3$, $b_w = 0.3$, $f = 0$, and $\rho_{0w}/\rho_{0j} = 4$). The red curve (see panel A) shows the time evolution of the amplitude squared $|\tilde{v}_y(k_{x0})|^2$. There is an initial ‘dip’ from around $t = 0 (v_A k_{x0})^{-1}$ to $t = 2.5 (v_A k_{x0})^{-1}$. This is common to many of our simulations, and we believe the reason for this feature is that our initialized perturbations do not correspond to an exact eigenmode of the system. From around $t = 5 (v_A k_{x0})^{-1}$ to $t = 10 (v_A k_{x0})^{-1}$, the quantity $|\tilde{v}_y(k_{x0})|^2$ shows a linear growth phase, before entering a nonlinear phase around $t = 11 (v_A k_{x0})^{-1}$. To measure the the growth rate, we fit a line to the measured curve during the linear growth phase; the slope yields twice the growth rate. The blue dashed line in panel A of Fig. 4.9 shows the predicted growth rate, as computed using Eqs. 4.84 and 4.85.

Panels B–D of Fig. 4.9 show the time evolution of mass density during the nonlinear phase (the times of these snapshots, indicated in the upper right of each panel, is color coded to match vertical dashed lines in panel A). Earlier on (panels B and C; times $t = 11.7 (v_A k_{x0})^{-1}$ and $t = 13.6 (v_A k_{x0})^{-1}$), smaller wavelength perturbations have grown to macroscopic scales; note that roots of the jet dispersion relation are constant, $\phi_{v_A} \equiv \omega/(v_A \sqrt{k^2 + m^2}) = \text{const.}$; thus, modes with larger wavevectors grow and saturate prior to those with lower wavevectors. By comparing panels C and D, this is evident; at $t = 13.6 (v_A k_{x0})^{-1}$ around fifteen small wavelengths fit in the box along x , but not until $t = 17.5 (v_A k_{x0})^{-1}$ has the wave with $k_x \approx 3 \cdot (2\pi/L)$ grown to a macroscopic scale.

4.3.2.2 Comparison of simulation growth rates with analytical predictions

The β_{ix} dependence of the growth rate $\text{Im}(\phi_{c_s})$, for the jet problem, is shown in Fig. 4.10; $\beta_{sh} = 0.165$ and $\sigma_{wx} = 0.01$ are fixed; in this simplified case, the other parameters are set to $b_j = 0$, $b_w =$

0 , $f = 0$, and $\rho_{0w}/\rho_{0j} = 1$, which allows us to isolate the role of β_{ix} for a case with nonrelativistic shear and no guide field. The blue line shows the growth rate as predicted from the dispersion relation (Eqs. 4.84 and 4.85), and the red circles show growth rates measured in simulations.

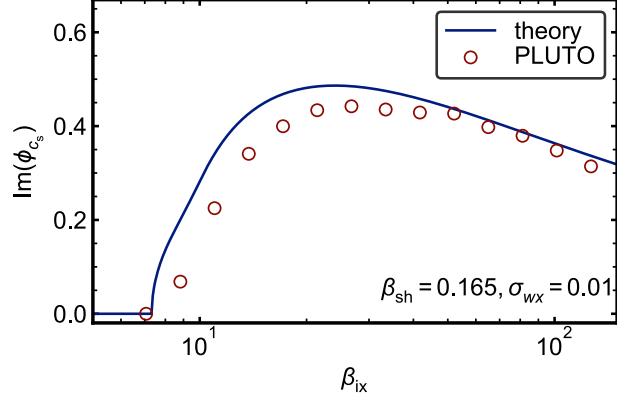


Figure 4.10: β_{ix} dependence of growth rate, for the jet problem; comparison between simulations and numerically computed solutions to the dispersion relation. For the simulations shown here, $\beta_{sh} = 0.165$, $\sigma_{wx} = 0.01$, $b_j = 0$, $b_w = 0$, $\rho_{0w}/\rho_{0j} = 1$, and $f = 0$.

Decreasing from high β_{ix} down to $\beta_{ix} \rightarrow 0$ (which corresponds to increasing the in-plane magnetic field), the instability is inhibited at around $\beta_{ix} = 7$. With regard to the shape of the predicted curve, the linear theory and numerical simulations show adequate agreement.

On the other hand, the simulations tend to underestimate the growth rate, however this is expected because the analytical prediction assumes a sharp velocity discontinuity, whereas the simulations employ a tangential shear profile; in this case, the prediction should be interpreted as an upper limit to the growth rate measured in simulations. Convergence of measured growth rates to predicted growth rates, with respect to the numerical parameter α (see Sec. 4.3.1) is discussed in Sec. 4.B.

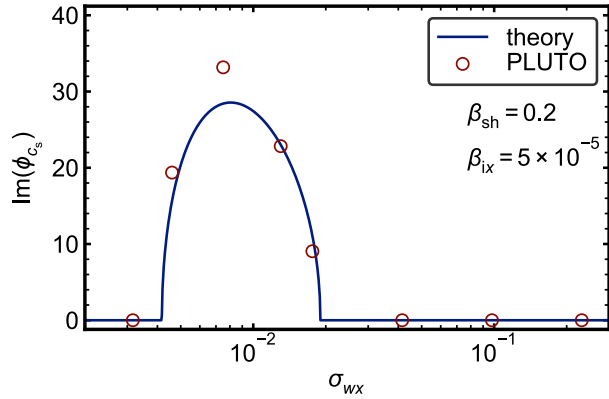


Figure 4.11: σ_{wx} dependence of growth rate, for the jet problem; comparison between simulations and numerically computed solutions to the dispersion relation. For the simulations shown here, $\beta_{ix} = 5 \times 10^{-5}$, $\beta_{sh} = 0.2$, $b_j = 0$, $b_w = 0$, $\rho_{0w}/\rho_{0j} = 1$, and $f = 0$.

In the next test, shown in Fig. 4.11, we explore (for the jet setup) the σ_w dependence of the growth rate $\text{Im}(\phi_{c_s})$ for fixed $\beta_{ix} = 5 \times 10^{-5}$ and $\beta_{sh} = 0.2$. This is a simple case similar to the previous, with $b_j = 0$, $b_w = 0$, $f = 0$, and $\rho_{0w}/\rho_{0j} = 1$. This case, unlike the previous, has both small β_{ix} and small σ_{wx} , so that temperature and magnetization are nonrelativistic. The curve shown in Fig. 4.11 corresponds to a vertical cut along σ_{wx} in panel B of Fig. 4.4 (the plots in Fig. 4.4 only extend down to $\beta_{ix} = 10^{-3}$, but give an impression of the part of parameter space that is probed in Fig. 4.11). The measured growth rate at $\sigma_{wx} \approx 8 \times 10^{-3}$ is larger than the prediction by a modest amount, and the other measurements within the unstable region show good agreement with the prediction. The predicted stable region shows robust agreement with the simulations.

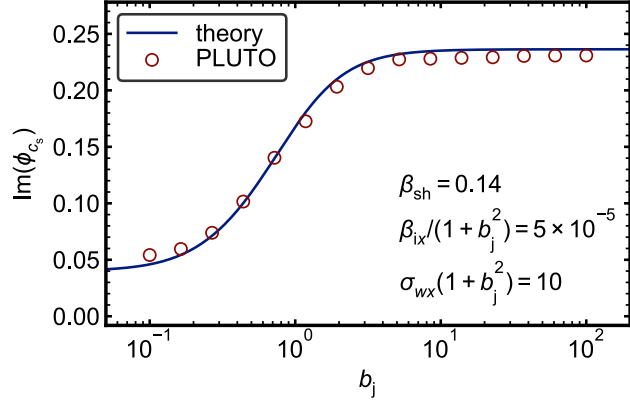


Figure 4.12: b_j dependence of growth rate, for the jet problem; comparison between simulations and numerically computed solutions to the dispersion relation. For the simulations shown here, $\beta_{sh} = 0.14$, $\beta_{ix}/(1 + b_j^2) = 5 \times 10^{-5}$, $\sigma_{wx} = 0.01(1 + b_j^2) = 5 \times 10^5$, $b_w = 0$, $\rho_{0w}/\rho_{0j} = 1$, and $f = 0$; β_{ix} and σ_{wx} are set so that the magnitude of the magnetic field is constant as b_j varies.

Next in the sequence, Fig. 4.12 shows the b_j dependence of the growth rate. For this test, the total ion plasma-beta $\beta_{i,tot} \equiv 2p_i/\mathbf{B}_0^2 = 5 \times 10^{-5}$ and total magnetization $\sigma_{w,tot} \equiv \mathbf{B}_0^2/w_0 = 10$ are fixed (still, $b_w = 0$, $f = 0$, and $\rho_{0w}/\rho_{0j} = 1$). At low b_j , the magnetic field is aligned approximately along x , and as b_j increases, the field is rotated to the out-of-plane direction (that is, z), and during this rotation, the magnitude of the magnetic field is held fixed. Fig. 4.12 reiterates physics that is familiar from discussions in Sec. 4.2.4: when the perturbation propagates along the direction of the magnetic field (as is the case for low b_j), it is subject to the stabilizing effect of magnetic tension; as b_j increases in Fig. 4.12, the field simply rotates from the in-plane direction to the out-of-plane direction (the magnitude of the magnetic field is fixed because $\beta_{i,tot}$ and $\sigma_{w,tot}$ are held constant), and the growth rate increases. Indeed, more variation in the growth rate $\text{Im}(\phi_{cs})$ happens around $b_j \sim 1$ than around, e.g., $b_j \sim 10$ because more rotation of the magnetic field is happening around $b_j \sim 1$ than $b_j \sim 10$.

The simulations agree well with the predicted growth rates.

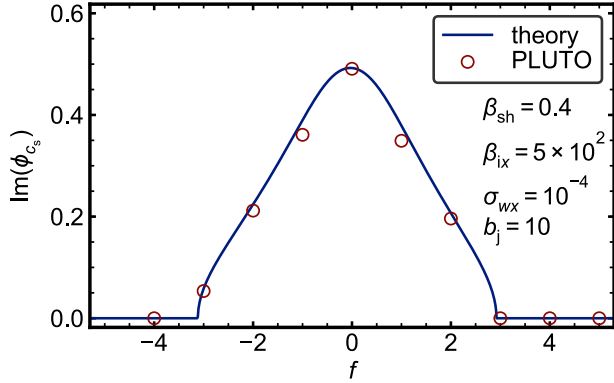


Figure 4.13: f dependence of growth rate, for the jet problem; comparison between 3D simulations and numerically computed solutions to the dispersion relation. For the simulations shown here, $\beta_{\text{sh}} = 0.4$, $\beta_{\text{ix}} = 5 \times 10^2$, $\sigma_{wx} = 10^{-4}$, $b_j = 10$, $b_w = 0$, and $\rho_{0w}/\rho_{0j} = 1$.

In Fig. 4.13, we use three-dimensional simulations to test the f dependence of the dispersion relation, for $\beta_{\text{sh}} = 0.4$, $\beta_{\text{ix}} = 5 \times 10^2$, $\sigma_w = 10^{-4}$, and $b_j = 10$. Because β_{ix} is large and σ_{wx} is small, this case approaches the hydrodynamic limit. The growth rate is symmetric with respect to f , which we expect in the HD limit; if in the present case, the magnetic field were strong instead of weak, varying f would in turn change the alignment of the propagating wave relative to the magnetic field; in this scenario, we expect the maximum of the growth rate to be centered around a value of f corresponding to propagation perpendicular to the magnetic field (i.e., the maximum of the growth rate should be achieved when $\mathbf{k} \cdot \mathbf{B}_{0-} \approx 0$).¹⁰ Fig. 4.13 also suggests that, in the absence of a strong magnetic field, the growth rate strictly decreases as $f \rightarrow \pm\infty$, or as the wave comes to propagate, in the plane of the interface, perpendicular to the direction of the shear flow. This is physically intuitive, based on symmetry.

Simulation results agree with the linear theory.

¹⁰Indeed, this expectation is confirmed in Fig. 5.7, where we show the f dependence of the growth rate for a case with $\sigma_{wx}=1$ and $b_j = 3$.

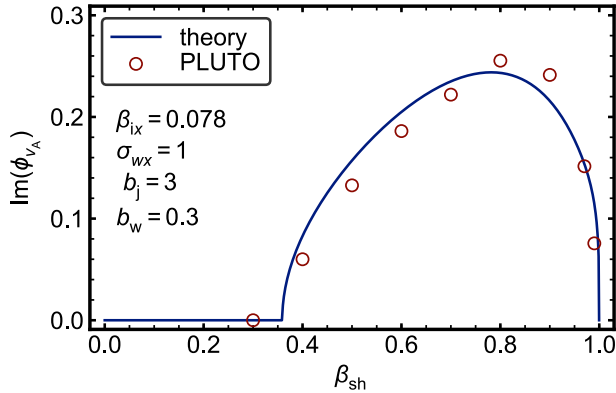


Figure 4.14: β_{sh} dependence of growth rate, for the jet problem; comparison between simulations and numerically computed solutions to the dispersion relation. For the simulations shown here, $\beta_{ix} = 0.078$, $\sigma_{wx} = 1$, $b_j = 3$, $b_w = 0.3$, $\rho_{0w}/\rho_{0j} = 4$, and $f = 0$.

Lastly, we explore a jet case that is more physically motivated than the previous several. Fig. 4.14 shows the β_{sh} dependence of the growth rate $\text{Im}(\phi_{v_A})$, for $\beta_{ix} = 0.078$, $\sigma_{wx} = 1$, $b_j = 3$, and also a guide-field component in the wind, $b_w = 0.3$. As β_i increases from zero to one, the system becomes unstable to perturbations around $\beta_{\text{sh}} = 0.35$. As we argued in 4.2.4, this stability bound is related to the stabilizing effect of magnetic tension; there is a certain threshold in β_{sh} that is required to activate the instability. Indeed, in the absence of an in-plane magnetic field, we might expect this case to be unstable all the way down to $\beta_{\text{sh}} = 0$. Fig. 4.14 also demonstrates that the growth rate is rapidly suppressed in the relativistic limit, i.e. $\beta_{\text{sh}} \rightarrow 1$.

The predicted curve agrees with the simulations.

4.3.3 Simulation results: symmetric shear flow

In this section, we present a few comparisons between growth rates computed via the symmetric KH dispersion relation, Eqs. 4.34 and 4.41, and growth rates obtained via numerical simulation.

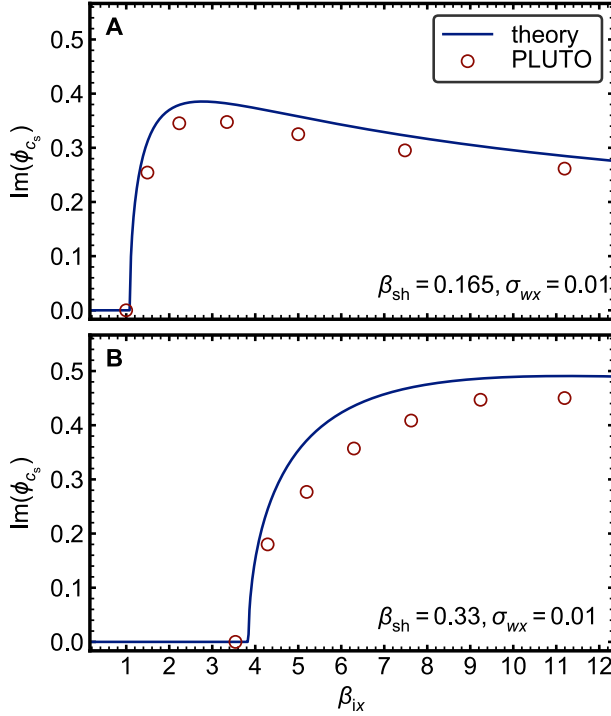


Figure 4.15: β_{ix} dependence of growth rate, for the symmetric shear problem; comparison between simulations and numerically computed solutions to the dispersion relation. For the simulations shown here, $\beta_{sh} = 0.165$, $\sigma_{wx} = 0.01$, and $f = 0$.

Fig. 4.15 shows the dependence of the growth rate on β_{ix} , for $\sigma_{wx} = 0.01$, and two values of shear speed, $\beta_{sh} = 0.165$ (panel A) and $\beta_{sh} = 0.33$ (panel B). We consider in-plane perturbations ($f = 0$). In panels A and B, we see that for both cases ($\beta_{sh} = 0.165$ and $\beta_{sh} = 0.33$), the system is stable for sufficiently low β_{ix} ; for $\beta_{sh} = 0.165$, $\beta_{ix} \lesssim 1$ corresponds to stability, and for $\beta_{sh} = 0.33$, $\beta_{ix} \lesssim 4$ corresponds to stability. We note that for the cases presented in panels A and B, $\sigma_w = 0.01$, and $\beta_i \gtrsim 1$, so this regime is similar to the classical HD limit. Furthermore, increasing β_{ix} in these cases serves as a temperature control (because σ_{wx} is fixed), and this corresponds to raising the sound speed in the fluid. In the pure HD limit, we recall the criterion for instability, $\beta_{sh} < c_s$ (ignoring factors of order unity). Taken together, panels A and B show qualitative agreement with this

criterion; $\beta_{\text{sh}} = 0.33$ is greater than $\beta_{\text{sh}} = 0.165$, so the former case demands a higher sound speed (equivalently, higher temperature, which is controlled by β_{ix}), so we expect that for $\beta_{\text{sh}} = 0.33$, the value of β_{ix} required for the system to be unstable is larger than the value of β_{ix} required for instability when $\beta_{\text{sh}} = 0.165$.

In Fig. 4.16, we present a three-dimensional test of the symmetric shear setup, and compare with the predictions of the dispersion relation. Fig. 4.16 shows the f dependence of the instability growth rate for $\beta_{\text{sh}} = 0.165$, $\beta_{\text{ix}} = 5$, and $\sigma_{wx} = 0.01$. The series of simulations shown in Fig. 4.16 parallels the two-dimensional simulation indicated by the point at $\beta_{\text{ix}} = 5$ in panel A of Fig. 4.15. The two-dimensional and three-dimensional simulations are reasonably converged: for the point at $f = 0$ in 4.16, $\text{Im}(\phi_{c_s}) \approx 0.31$, and for the point at $\beta_{\text{ix}} = 5$ in Fig. 4.15, $\text{Im}(\phi_{c_s}) \approx 0.32$. The parameters for these simulations again correspond approximately to HD, and so several of the features noted during the discussion of Fig. 4.13 reappear in Fig. 4.16; in particular, the curve appears to have a maximum at $f = 0$, as expected in pure HD.

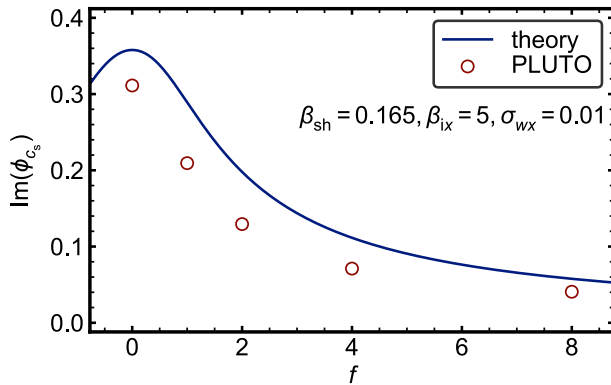


Figure 4.16: f dependence of growth rate, for the symmetric shear problem; comparison between 3D simulations and numerically computed solutions to the dispersion relation. For the simulations shown here, $\beta_{\text{sh}} = 0.165$, $\sigma_{wx} = 0.01$, and $\beta_{\text{ix}} = 5$

4.4 Summary

In this chapter, we have explored by means of linear analysis and relativistic MHD simulations the Kelvin-Helmholtz instability in a symmetric shearing flow setup, along with an astrophysically motivated problem corresponding to shear flow at the jet-wind interface. We derived a dispersion relation governing the propagation of waves at the interface of the jet and wind, and computed the growth-rate dependence on parameters of the jet-wind system. We confirmed that the jet dispersion relation Eqs. 4.84 and 4.85 respects the classical bound of stability for the hydrodynamic Kelvin-Helmholtz problem, $\beta_{\text{sh}}/c_s > \sqrt{2}$.

We have performed two-dimensional and three-dimensional relativistic MHD simulations to test the jet dispersion relation, and also the more well-studied dispersion relation for symmetric shear. In most cases, we find adequate agreement between linear theory and the dispersion relation, thus confirming the validity of the analytical calculations.

In the coming chapter, we extend this exploration of the KH instability with fully-kinetic particle-in-cell simulations, which are capable of capturing from first principles the interplay between magnetic fields and charged particles, and in effect the dissipation of magnetic energy in collisionless plasma. The question of magnetic dissipation via the KH instability in astrophysical jets remains largely underexplored, especially with respect to particle-in-cell simulations; such an investigation is thus important in clarifying the connection between the KH instability and magnetic dissipation in collisionless plasma (via, e.g., magnetic reconnection).

4.A Astrophysical jet: dispersion relation equations

Here, we state explicitly the form of the functions F_1 and F_2 in Eqs. 4.54 and 4.70, respectively, and elaborate on several practical details related to the calculation of solutions to the jet dispersion relation. While in Eqs. 4.54 and 4.70 we suppress the dependence on m_i/m_e (i.e., we assume $m_i/m_e = 1$), we have assumed in the derivation of Eqs. 4.84 and 4.85 that the plasma may consist

of ions and electrons with different masses. Note that, according to the arguments of F_1 and F_2 , each depends on both ρ_{0j} and ρ_{0w} ; this dependence is hidden in the placeholder function r_w (whose arguments are suppressed in Eqs. 4.84 and 4.85), which is provided further below (see Eq. 4.87).

In explicit form, Eq. 4.54 may be expressed as

$$\begin{aligned}
F_1(\phi_{v_A}, k, \beta_{ix}, \sigma_{wx}, \rho_{0j}, \rho_{0w}, \beta_{sh}, b_j, b_w, f, m_i/m_e) = & \\
& - (((1 + f^2)k^2(1 - \beta_{sh}^2)\sigma_{wx}(-(k + b_j f k)^2\beta_{ix}\Gamma_{ad,j}(1 + \sigma_{wx} + b_j^2\sigma_{wx}) \\
& + (1 + b_j^2)k^2(1 + \beta_{ix}\Gamma_{ad,j} + f^2(1 + \beta_{ix}\Gamma_{ad,j}) + \beta_{ix}\Gamma_{ad,j}\sigma_{wx} + 2b_j f \beta_{ix}\Gamma_{ad,j}\sigma_{wx} \\
& + b_j^2(1 + f^2(1 + \beta_{ix}\Gamma_{ad,j}\sigma_{wx})))\phi_{v_A}^2 - (1 + b_j^2)^2(1 + f^2)k^2\phi_{v_A}^4) \\
& \cdot (b_w^2 f^2 r_{cs}^2 r_w k^2 \beta_{ix} (1 - \beta_{sh}^2)^2 \Gamma_{ad,j} \sigma_{wx}^2 (1 + \sigma_{wx} + b_j^2 \sigma_{wx}) - (b_w^2 r_w (1 - \beta_{sh}^2) \sigma_{wx} \\
& + r_{cs}^2 \beta_{ix} \Gamma_{ad,j} \sigma_{wx})(k \beta_{sh} \sqrt{1 + \sigma_{wx} + b_j^2 \sigma_{wx}} - \sqrt{(1 + f^2)k^2} \\
& \cdot \sqrt{(1 + b_j^2) \sigma_{wx} \phi_{v_A}})^2)) / ((1 + \sigma_{wx} + b_j^2 \sigma_{wx})^2 (1 + b_w^2 r_w (1 - \beta_{sh}^2) \sigma_{wx}) \\
& \cdot ((k + b_j f k)^2 \beta_{ix} \Gamma_{ad,j} \sigma_{wx} - ((1 + b_j^2)(1 + f^2)k^2(1 + b_j^2 + \beta_{ix}\Gamma_{ad,j})\sigma_{wx}\phi_{v_A}^2) \\
& / (1 + \sigma_{wx} + b_j^2 \sigma_{wx}))((k \beta_{sh} - \sqrt{(1 + f^2)k^2} \sqrt{((1 + b_j^2) \sigma_{wx}) / (1 + \sigma_{wx} + b_j^2 \sigma_{wx})} \phi_{v_A})^4 \\
& + (b_w^2 f^2 r_{cs}^2 r_w k^2 \beta_{ix} (1 - \beta_{sh}^2)^2 \Gamma_{ad,j} \sigma_{wx}^2 (f^2 k^2 (1 - \beta_{sh}^2) + (k - \sqrt{(1 + f^2)k^2} \beta_{sh} \\
& \cdot \sqrt{((1 + b_j^2) \sigma_{wx}) / (1 + \sigma_{wx} + b_j^2 \sigma_{wx})} \phi_{v_A})^2)) / (1 + b_w^2 r_w (1 - \beta_{sh}^2) \sigma_{wx}) \\
& - (k \beta_{sh} - \sqrt{(1 + f^2)k^2} \sqrt{((1 + b_j^2) \sigma_{wx}) / (1 + \sigma_{wx} + b_j^2 \sigma_{wx})} \phi_{v_A})^2 \\
& \cdot (r_{cs}^2 \beta_{ix} \Gamma_{ad,j} \sigma_{wx} (f^2 k^2 (1 - \beta_{sh}^2) + (k - \sqrt{(1 + f^2)k^2} \beta_{sh} \\
& \cdot \sqrt{((1 + b_j^2) \sigma_{wx}) / (1 + \sigma_{wx} + b_j^2 \sigma_{wx})} \phi_{v_A})^2) + (b_w^2 r_w (1 - \beta_{sh}^2) \sigma_{wx} (f^2 k^2 (1 - \beta_{sh}^2) \\
& + (1 - r_{cs}^2 \beta_{ix} \Gamma_{ad,j} \sigma_{wx})(k - \sqrt{(1 + f^2)k^2} \beta_{sh} \sqrt{((1 + b_j^2) \sigma_{wx}) / (1 + \sigma_{wx} + b_j^2 \sigma_{wx})} \phi_{v_A})^2)) \\
& / (1 + b_w^2 r_w (1 - \beta_{sh}^2) \sigma_{wx}))), \\
\end{aligned} \tag{4.84}$$

and Eq. 4.70 may be written as

$$\begin{aligned}
F_2(\phi_{v_A}, k, \beta_{ix}, \sigma_{wx}, \rho_{0j}, \rho_{0w}, \beta_{sh}, b_j, b_w, f, m_i/m_e) = & \\
& ((1 + b_j^2)r_w(1 - \beta_{sh}^2)\sigma_{wx}((k + b_jfk)^2 - (1 + b_j^2)(1 + f^2)k^2\phi_{v_A}^2)) \\
& / (k(-((2\sqrt{(1 + f^2)k^2}\beta_{sh}((1 + b_j^2)\sigma_{wx})^{3/2}(-1 - b_w^2r_w(1 - \beta_{sh}^2)\sigma_{wx})\phi_{v_A})) \\
& / (\sigma_{wx}\sqrt{1 + \sigma_{wx} + b_j^2\sigma_{wx}}) + (1/(1 + \sigma_{wx} + b_j^2\sigma_{wx}))(1 + b_j^2)k((1 + \sigma_{wx} + b_j^2\sigma_{wx}) \\
& \cdot (b_w^2r_w\sigma_{wx}(1 - \beta_{sh}^2)(f^2(1 - \beta_{sh}^2) - \beta_{sh}^2) - \beta_{sh}^2) \\
& - \sigma_{wx}(1 + b_j^2)(1 + f^2)(1 + b_w^2r_w(1 - \beta_{sh}^2)\sigma_{wx})\phi_{v_A}^2))).
\end{aligned} \tag{4.85}$$

The expressions r_{c_s} and r_w appearing in Eqs. 4.84 and 4.85 are placeholders for auxiliary functions representing the ratios of sound speeds c_{sj}/c_{sw} and enthalpies w_{0j}/w_{0w} , respectively:

$$r_{c_s} \equiv \sqrt{\frac{\Gamma_{ad}(\theta_{0w})\theta_{0w}h_{0j}(\theta_{0j})}{\Gamma_{ad}(\theta_{0j})\theta_{0j}h_{0w}(\theta_{0w})}}, \tag{4.86}$$

$$r_w \equiv \frac{n_{0j}h_{0j}(\theta_{0j})}{\widetilde{n_{0w}h_{0w}(\theta_{0w})}}, \tag{4.87}$$

where

$$h_{0j}(\theta_{0j}) = \frac{1}{2} \left(\left(1 + \theta_{0j} \frac{\Gamma_{ad}(\theta_{0j})}{\Gamma_{ad}(\theta_{0j}) - 1} \right) + \frac{m_e}{m_i} \left(1 + \theta_{0j} \frac{m_i}{m_e} \frac{\Gamma_{ad}(\theta_{0j})}{\Gamma_{ad}(\theta_{0j}) - 1} \right) \right), \tag{4.88}$$

$$h_{0w}(\theta_{0w}) = \frac{1}{2} \left(\left(1 + \theta_{0w} \frac{\Gamma_{ad}(\theta_{0w})}{\Gamma_{ad}(\theta_{0w}) - 1} \right) + \frac{m_e}{m_i} \left(1 + \theta_{0w} \frac{m_i}{m_e} \frac{\Gamma_{ad}(\theta_{0w})}{\Gamma_{ad}(\theta_{0w}) - 1} \right) \right), \tag{4.89}$$

and the adiabatic index is evaluated using a fitting formula (Syngle, 1957; Service, 1986):

$$\begin{aligned}
\Gamma_{ad}(\theta) = & \frac{1}{3}(5 - 1.21937(\theta/(0.24 + \theta)) + 0.18203(\theta/(0.24 + \theta))^2 - 0.96583(\theta/(0.24 + \theta))^3 \\
& + 2.32513(\theta/(0.24 + \theta))^4 - 2.39332(\theta/(0.24 + \theta))^5 + 1.07136(\theta/(0.24 + \theta))^6)).
\end{aligned} \tag{4.90}$$

While we suppress the arguments of θ_{0j} and θ_{0w} in Eqs. 4.88 and 4.89 for readability, it should be noted that these are in fact functions of our canonical parameters. In practice, the first of these must be evaluated by means of a root-finding algorithms. In particular, we seek numerically a solution to the equation

$$\theta_{0j}(\beta_{ix}, \sigma_{wx}, m_i/m_e) = \beta_{ix}\sigma_{wx}h_{0j}(\theta_{0j}(\beta_{ix}, \sigma_{wx}, m_i/m_e)), \quad (4.91)$$

which may not exist. Indeed, it may be shown that solutions exist only for $\beta_{ix} < \beta_{ix,\max} \equiv 1/(4\sigma_{wx})$, which dictates the maximum possible β_{ix} , given σ_{wx} . To compute the wind-side dimensionless temperature, we use the equation

$$\begin{aligned} \theta_{0w}(\beta_{ix}, \sigma_{wx}, \rho_{0j}, \rho_{0w}, \beta_{sh}, b_j, b_w, f, m_i/m_e) = & \left(4(m_i/m_e)\rho_{0j}\theta_{0j}(\beta_{ix}, \sigma_{wx}, m_i/m_e) + (1 + m_i/m_e)\rho_{0j} \right. \\ & \cdot \left. (1 + b_j^2 - b_w^2(1 - \beta_{sh}^2)) \frac{2h_{0j}(\theta_{0j}(\beta_{ix}, \sigma_{wx}, m_i/m_e))\sigma_{wx}}{(1 + m_e/m_i)} \right) / \left(4\rho_{0w}(m_i/m_e)\sqrt{1 - \beta_{sh}^2} \right); \end{aligned} \quad (4.92)$$

this is derived from total pressure balance (including both thermal and magnetic pressure) at the interface of the shear.

4.B Convergence of measured growth rate with respect to α

In our simulations, we have explored the effect of varying the ratio of the length of the transition width to domain size in x , with regard to the measured growth rates we extract. In particular, we studied the effect of varying the parameter α (see Sec. 4.3.1), while fixing the number of cells with which the transition is resolved. We define the transition width as $\Delta_t = 2L_x\alpha$, where L_x is the length of the box in cells. We find that ~ 13 cells are required to adequately resolve the transition width Δ_t ; below this threshold value, we find that the onset of nonlinear effects is hastened, and obfuscates the linear growth phase that is the focus of our simulations.

In Fig. 4.17, we show four series of simulations (indicated by square, triangle, circle, and cross markers) with successively smaller values of α , yet in each of the four series, the transition width is resolved with ~ 13 cells; this is achieved by increasing the dimensions of the box as α decreases. In the limit that $\alpha \rightarrow 0$, the transition profile approaches a step function, which is the profile assumed in the derivations of the dispersion relations Eqs. 4.34, 4.41 and Eqs. 4.84, 4.85; for this reason, we suspect that as α decreases and Δ_t is held fixed, the growth rates measured in the simulations will approach the prediction of linear theory; the trend in Fig. 4.17 is suggestive of this convergence.

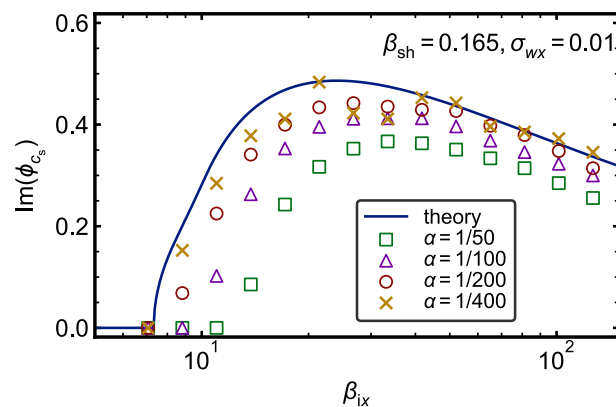


Figure 4.17: Four series (each indicated by a different shape) of simulations with progressively smaller ratios of transition width to box length in x ; for each series, the transition width in cells is fixed, $\Delta_t \sim 13$.

5. Kelvin-Helmholtz II

5.1 Introduction

In Ch. 4, we used relativistic MHD simulations to test an analytically derived dispersion relation (Eqs. 4.84 and 4.85), and found agreement between the simulations and theory, thereby confirming the validity of the jet dispersion relation. In this chapter, a companion to Ch. 4, we now assume that the jet dispersion relation is valid, and use it to study the jet setup in fully-kinetic particle-in-cell (PIC) simulations.

The outline of this chapter is as follows: In Sec. 5.2, we describe the setup and numerical choices in our PIC simulations. Next, in Sec. 5.3, we study the growth rate of the KH instability using the setup described in Sec. 5.2; we discuss also, for a sample case, magnetic dissipation induced by KH mixing. We conclude with a brief summary in Sec. 5.4.

5.2 Simulation setup

Here, we describe the simulation setup we use to study the KH instability, and specify the fiducial parameters and numerical choices we use in our simulations.

5.2.1 Description of setup

Since it is difficult to find a Vlasov equilibrium for the shearing flow problem (Henri et al., 2013), our setup is built on the notion of fluid equilibrium.¹ In the setup description below, naturalized Gaussian units are assumed, with $4\pi = c = k_B = 1$. The fields (electromagnetic, velocity, temperature, etc.), which implicitly depend on x , are uniform in the x direction, and so we suppress in our notation the explicit reference to the x dependence of the fields.

¹Especially when gradients in the magnetic field are large, kinetic effects (such as the grad-B, diamagnetic, or other particle drifts) may render the fluid equilibrium an unsuitable initial condition in a fully-kinetic simulation; in practice, we have addressed the appropriateness of using fluid equilibrium as an initial condition on a case-by-case basis.

The magnetic field $\mathbf{B}(y) = (B_x(y), B_y(y), B_z(y))$ is chosen to follow a smoothly varying profile:

$$B_x(y) = B_0 \left[1 - \frac{1}{2} \left(1 + \tanh \left(\frac{\ell_y}{\Delta_t} \sin \left(2\pi \frac{y - \ell_y/4}{\ell_y} \right) \right) \right) \right], \quad (5.1)$$

$$B_y(y) = 0, \quad (5.2)$$

$$B_z(y) = B_0 \left[b_w + \frac{1}{2} (b_j - b_w) \left(1 - \tanh \left(\frac{\ell_y}{\Delta_t} \sin \left(2\pi \frac{y - \ell_y/4}{\ell_y} \right) \right) \right) \right]. \quad (5.3)$$

Here, B_0 is the magnitude of the in-plane magnetic field (in the x direction), and $B_0 b_w$ and $B_0 b_j$ are the guide field strengths (in the z direction) in the wind and jet, respectively. Δ_t is the width of the jet-wind transition. The profiles here are similar to those used in Sec. 4.3.1 (see Eq. 4.81) for the setup of the jet problem in **PLUTO**, but note here that the argument of the hyperbolic tangent varies sinusoidally; this difference accounts for the periodic boundary conditions we use in our PIC setup (note that for the MHD setup of the jet problem, our boundary conditions are periodic along x , and outflowing along y , whereas for the present PIC setup, boundary conditions are periodic along both x and y). With the periodic boundary condition implied by Eq. 5.1, the part of the domain $(1/4)\ell_y \leq y \leq (3/4)\ell_y$ corresponds to the jet, and $y \leq (1/4)\ell_y$ or $y \geq (3/4)\ell_y$ corresponds to the wind.

We choose the profile of bulk velocity $\mathbf{v}(y) = (v_x(y), v_y(y), v_z(y))$ also to follow a smoothly varying profile:

$$v_x(y) = \frac{\beta_{sh}}{2} \left(1 + \tanh \left(\frac{\ell_y}{\Delta_t} \sin \left(2\pi \frac{y - \ell_y/4}{\ell_y} \right) \right) \right), \quad (5.4)$$

$$v_y(y) = 0, \quad (5.5)$$

$$v_z(y) = 0. \quad (5.6)$$

The magnetic field and bulk velocity profiles, along with the force free condition $\mathbf{E} = -\mathbf{v} \times \mathbf{B}$,

determine the electric field:

$$\begin{aligned}
E_x(y) &= 0, \\
E_y(y) &= -\frac{\beta_{\text{sh}}}{2} \left(1 + \tanh \left(\frac{\ell_y}{\Delta_t} \sin \left(2\pi \frac{y - \ell_y/4}{\ell_y} \right) \right) \right) \\
&\quad \cdot B_0 \left[b_w + \frac{1}{2} (b_j - b_w) \left(1 - \tanh \left(\frac{\ell_y}{\Delta_t} \sin \left(2\pi \frac{y - \ell_y/4}{\ell_y} \right) \right) \right) \right], \\
E_z(y) &= 0.
\end{aligned} \tag{5.7}$$

This electric field is not divergence free, and therefore requires nonzero charge density $\rho_q(y) = q_i(n_i(y) - n_e(y))$ to sustain the electric field (q_i here is the fundamental charge, with positive sign):

$$\begin{aligned}
\rho_q(y) &= \nabla \cdot \mathbf{E}(y), \\
&= -\frac{B_0 \pi \beta_{\text{sh}}}{\Delta_t} \cos \left(2\pi \frac{y - \ell_y/4}{\ell_y} \right) \operatorname{sech} \left(\frac{\ell_y}{\Delta_t} \sin \left(2\pi \frac{y - \ell_y/4}{\ell_y} \right) \right)^2 \\
&\quad \cdot \left[b_w - (b_j - b_w) \tanh \left(\frac{\ell_y}{\Delta_t} \sin \left(2\pi \frac{y - \ell_y/4}{\ell_y} \right) \right) \right].
\end{aligned} \tag{5.9}$$

Curl of the magnetic field generates (dimensionless) current $\mathbf{j}(y) = (j_x(y), j_y(y), j_z(y))$, via Ampère's law:

$$j_x(y) = \frac{B_0 \pi}{q_i \Delta_t} (b_w - b_j) \cos \left(2\pi \frac{y - \ell_y/4}{\ell_y} \right) \operatorname{sech} \left(\frac{\ell_y}{\Delta_t} \sin \left(2\pi \frac{y - \ell_y/4}{\ell_y} \right) \right)^2, \tag{5.10}$$

$$j_y(y) = 0, \tag{5.11}$$

$$j_z(y) = -\frac{B_0 \pi}{q_i \Delta_t} \cos \left(2\pi \frac{y - \ell_y/4}{\ell_y} \right) \operatorname{sech} \left(\frac{\ell_y}{\Delta_t} \sin \left(2\pi \frac{y - \ell_y/4}{\ell_y} \right) \right)^2. \tag{5.12}$$

Lastly, we choose an ‘unperturbed’ profile $\tilde{n}(y)$ for total number density, in the frame comoving

with the bulk flow along x (indicated by the overtilde):

$$\tilde{n}(y) = \tilde{n}_{0j} + \frac{1}{2}(\tilde{n}_{0w} - \tilde{n}_{0j}) \left(1 - \tanh \left(\frac{\ell_y}{\Delta_t} \sin \left(2\pi \frac{y - \ell_y/4}{\ell_y} \right) \right) \right). \quad (5.13)$$

In the limit of no currents and no shear velocity, the electron and proton number densities $n_e(y)$ and $n_i(y)$ (in the lab frame) add to the unperturbed profile, $n_e(y) + n_i(y) = n(y)$, but in general the total number density $n_e(y) + n_i(y)$ can be different from $\tilde{n}(y)$, depending on the local bulk velocity and requirements of Gauss's law. As we will see in Eqs. 5.25–5.27, the lab frame profiles $n_e(y)$ and $n_i(y)$ are in fact chosen so that 1) when their corresponding rest frame profiles $\tilde{n}_e(y)$ and $\tilde{n}_i(y)$ are multiplied by chosen² modulation factors $(1 + \Delta_{\tilde{n}}(y))^{-1}$ and $(1 - \Delta_{\tilde{n}}(y))^{-1}$, respectively, the sum $\tilde{n}_e(y)(1 + \Delta_{\tilde{n}}(y))^{-1} + \tilde{n}_i(y)(1 - \Delta_{\tilde{n}}(y))^{-1}$ is equal to the desired rest frame density profile, $\tilde{n}(y)$, and 2) the lab frame profiles satisfy Gauss's law, $\nabla \cdot \mathbf{E}(y) = q_i(n_i(y) - n_e(y))$.

Note that Eq. (5.13) prescribes a density profile $\tilde{n}(y)$ in the comoving frame; according to this density profile, some number of particles, each with four-momentum of the form $(\tilde{\gamma}, \tilde{\mathbf{u}})$, is initialized in the comoving frame, then a Lorentz transform is applied to convert the particle's momentum to the lab frame. Care must be taken in translating from the comoving frame to the lab frame, as the volume of a grid cell is held constant when applying the boost (Melzani et al., 2014; Zenitani, 2015). Following the insight of Zenitani (2015), consider the distribution initialized in the comoving frame, $\tilde{f}(\tilde{\mathbf{x}}, \tilde{\mathbf{u}})$; further consider that, to convert to the lab frame, this distribution is boosted along x by

²Both modulation factors are determined by the choice of $\Delta_{\tilde{n}}(y)$, which is treated as a free variable in Eqs. 5.21–5.27.

$(\Gamma, -\Gamma\beta_{\text{sh}}, 0, 0)$. Then the particle's four-momentum transforms as

$$\gamma = \Gamma(\tilde{\gamma} + \tilde{u}_x \beta_{\text{sh}}), \quad (5.14)$$

$$u_x = \Gamma(\beta_{\text{sh}}\tilde{\gamma} + \tilde{u}_x), \quad (5.15)$$

$$u_y = \tilde{u}_y, \quad (5.16)$$

$$u_z = \tilde{u}_z, \quad (5.17)$$

and the distribution as seen in the lab frame is $f(\mathbf{x}, \mathbf{u})$. Particle number is invariant under a Lorentz transformation,

$$f(\mathbf{x}, \mathbf{u}) d^3x d^3u = \tilde{f}(\tilde{\mathbf{x}}, \tilde{\mathbf{u}}) d^3\tilde{x} d^3\tilde{u}, \quad (5.18)$$

therefore the number density, expressed in terms of lab frame quantities, is

$$\begin{aligned} f(\mathbf{x}, \mathbf{u}) d^3u &= \tilde{f}(\tilde{\mathbf{x}}, \tilde{\mathbf{u}}) \frac{d^3\tilde{x}}{d^3x} d^3\tilde{u}, \\ &= \tilde{f}(\tilde{\mathbf{x}}, \tilde{\mathbf{u}}) \frac{\gamma}{\tilde{\gamma}} d^3\tilde{u}, \end{aligned} \quad (5.19)$$

which follows from conservation of four-volume, $\tilde{\gamma} d^3\tilde{x} = \gamma d^3x$. Averaging over particles, the second term on the right is (Zenitani, 2015)

$$\left\langle \frac{\gamma}{\tilde{\gamma}} \right\rangle = \langle \Gamma(1 + \beta_{\text{sh}}\tilde{u}_x/\tilde{\gamma}) \rangle = \Gamma, \quad (5.20)$$

which follows from Eq. (5.14), and because the distribution initialized in the comoving frame (i.e., Maxwell-Jüttner) is symmetric, $f(\tilde{u}_x) = f(-\tilde{u}_x)$. According to Eqs. 5.19 and 5.20, the number density as viewed in the lab frame is larger, by a factor of Γ , than that initialized in the comoving frame. If one naively initializes particles in the comoving frame, and then boosts momenta to

convert to the lab frame, a factor of Γ (owing to the Lorentz contraction of space) is missed. As an alternative to contracting cells along the direction of the boost (the PIC code **TRISTAN-MP** which we use for our simulations is not designed with this functionality), one may account for this factor of Γ by initializing in the comoving frame a number of particles that is larger than the originally specified comoving density, $\tilde{n}(y)$, by a factor of Γ ; this largely accounts for a self-consistent boost of the distribution function from the comoving frame to the lab frame.³

In our simulations, we choose (in the lab frame) electron and ion number densities $n_e(y), n_i(y)$, bulk velocities in the x and z directions $v_{xe}(y), v_{xi}(y)$ and $v_{ze}(y), v_{zi}(y)$, and an additional profile $\Delta_{\tilde{n}}(y)$, which serves to modulate the electron and ion number densities,⁴ to satisfy the following

³There is an additional (very important) subtlety to this method of boosting the distribution function via individual Lorentz transformations of particle four-momenta, which is discussed by Zenitani (2015). In short, each particle comprising the distribution in the comoving frame may require a different Lorentz transform, due to their different relative momenta along x ; particles with x momentum aligned with the direction of the boost get a greater Lorentz contraction than those with x momentum anti-aligned to the boost, and should therefore receive a larger correction to particle number than Γ , prior to the boost (a correction of Γ would be exact only for particles with $\tilde{u}_x = 0$). Similarly, particles with x momentum anti-aligned to the boost should get a correction to comoving particle number that is smaller than Γ . Zenitani (2015) developed an algorithm called the *flipping method* to account for the different corrections required by particles in the comoving frame, which, during initialization of particles, we apply independently before each boost in the x and z directions.

⁴To clarify the meaning of the profile $\Delta_{\tilde{n}}(y)$, we note here a few of its properties: the electron and ion rest frame densities are related to the total rest frame density by $\tilde{n}_e(y) = \frac{1}{2}\tilde{n}(y)(1 + \Delta_{\tilde{n}}(y))$ and $\tilde{n}_i(y) = \frac{1}{2}\tilde{n}(y)(1 - \Delta_{\tilde{n}}(y))$, respectively; also, the difference between rest-frame electron and ion number densities is equal to the modulation profile, $\tilde{n}_e(y) - \tilde{n}_i(y) = \Delta_{\tilde{n}}(y)$.

constraints:

$$j_x(y) = n_i(y)v_{xi}(y) - n_e(y)v_{xe}(y), \quad (5.21)$$

$$j_z(y) = n_i(y)v_{zi}(y) - n_e(y)v_{ze}(y), \quad (5.22)$$

$$v_x(y) = \frac{n_e(y)v_{xe}(y) + n_i(y)v_{xi}(y)}{n_e(y) + n_i(y)}, \quad (5.23)$$

$$v_z(y) = \frac{n_e(y)v_{ze}(y) + n_i(y)v_{zi}(y)}{n_e(y) + n_i(y)}, \quad (5.24)$$

$$\nabla \cdot \mathbf{E}(y) = q_i(n_i(y) - n_e(y)), \quad (5.25)$$

$$\frac{1}{2}\tilde{n}(y)(1 + \Delta_{\tilde{n}}(y)) = n_e(y)\sqrt{1 - v_{xe}(y)^2 - v_{ze}(y)^2}, \quad (5.26)$$

$$\frac{1}{2}\tilde{n}(y)(1 - \Delta_{\tilde{n}}(y)) = n_i(y)\sqrt{1 - v_{xi}(y)^2 - v_{zi}(y)^2}. \quad (5.27)$$

Eqs. 5.21–5.27 are arranged so that given values (supposing y is fixed) are on the left, and chosen valued are on the right (apart from the last two equations, which contain factors of $1 \pm \Delta_{\tilde{n}}(y)$ on the left). The first two constraints Eqs. 5.21 and 5.22 ensure that current carried by electrons and ions is consistent with the curl of the magnetic field.⁵ Eqs. 5.23 and 5.24 ensure that the number densities and velocities of electron and protons match the chosen bulk velocity profiles in x and z (there is no current in y , so there is no need to consider the motion of particles along y). The constraint Eq. 5.25 ensures that the electron and proton number densities are consistent with Gauss's law. The last two constraints Eqs. 5.26 and 5.27 enforce that the lab frame electron and ion number densities are consistent with the density profile in the comoving frame. Eqs. 5.21–5.27 may be solved to obtain explicit expressions for the seven unknown profiles $n_e(y)$, $n_i(y)$, $v_{xe}(y)$, $v_{xi}(y)$, $v_{ze}(y)$, $v_{zi}(y)$, and $\Delta_{\tilde{n}}(y)$, which we use as an initial condition in our simulations.

With the electron and proton number densities $n_e(y)$ and $n_i(y)$ ⁶ specified according to the solu-

⁵In **TRISTAN-MP**, there is a convention that currents are defined as the negative of physical currents defined here, which we account for in our implementation.

⁶Equivalently: the comoving densities $\tilde{n}_{ej}(y) \equiv n_e(y)/\Gamma_e(y)$ and $\tilde{n}_{ij}(y) \equiv n_i(y)/\Gamma_i(y)$, where $\Gamma_s(y) =$

tion of Eqs. 5.21–5.27, we compute the temperature profile in the comoving frame. The temperature profile must satisfy pressure balance in the lab frame, i.e. $T_{\text{tot}}^{yy} = \text{const.}$; here, T_{tot}^{yy} is the yy component of the total stress-energy tensor (including both particle and electromagnetic stress-energy), $T_{\text{tot}}^{\mu\nu} = T_{\text{prtl}}^{\mu\nu} + T_{\text{em}}^{\mu\nu}$, and

$$T_{\text{prtl}}^{\mu\nu} = \int m f(\mathbf{x}, \mathbf{u}) u^\mu u^\nu \frac{d^3 u}{\gamma}, \quad (5.28)$$

$$T_{\text{em}}^{\mu\nu} = F^{\mu\alpha} F_\alpha^\nu - \frac{1}{4} g^{\mu\nu} F_{\alpha\beta} F^{\alpha\beta}. \quad (5.29)$$

Here, u^μ is the particle four-momentum, $g^{\mu\nu} = \text{diag}(-1, 1, 1, 1)$ is the metric tensor, and $F^{\mu\nu}$ is the electromagnetic tensor; for practical calculations, it is useful to write Eqs. 5.28 and 5.29 in explicit matrix form,

$$\mathbf{T}_{\text{prtl}} = \sum_{\text{prtl}} \begin{pmatrix} mn\gamma & mn\beta_x\gamma & mn\beta_y\gamma & mn\beta_z\gamma \\ mn\beta_x\gamma & mn\beta_x^2\gamma & mn\beta_x\beta_y\gamma & mn\beta_x\beta_z\gamma \\ mn\beta_y\gamma & mn\beta_x\beta_y\gamma & mn\beta_y^2\gamma & mn\beta_y\beta_z\gamma \\ mn\beta_z\gamma & mn\beta_x\beta_z\gamma & mn\beta_y\beta_z\gamma & mn\beta_z^2\gamma \end{pmatrix} = \begin{pmatrix} e & p_x & p_y & p_z \\ p_x & p_{xx} & p_{xy} & p_{xz} \\ p_y & p_{xy} & p_{yy} & p_{yz} \\ p_z & p_{xz} & p_{yz} & p_{zz} \end{pmatrix}, \quad (5.30)$$

$$\mathbf{T}_{\text{em}} = \begin{pmatrix} \frac{1}{2}(B^2 + E^2) & B_z E_y - B_y E_z & -B_z E_x + B_x E_z & B_y E_x - B_x E_y \\ B_z E_y - B_y E_z & \frac{1}{2}(B^2 + E^2) - B_x^2 - E_x^2 & -B_x B_y - E_x E_y & -B_x B_z - E_x E_z \\ -B_z E_x + B_x E_z & -B_x B_y - E_x E_y & \frac{1}{2}(B^2 + E^2) - B_y^2 - E_y^2 & -B_y B_z - E_y E_z \\ B_y E_x - B_x E_y & -B_x B_z - E_x E_z & -B_y B_z - E_y E_z & \frac{1}{2}(B^2 + E^2) - B_z^2 - E_z^2 \end{pmatrix}. \quad (5.31)$$

In Eq. 5.30, the sum is taken over all particles in the volume under consideration; e is the total energy density, p_i are momentum densities, and p_{ij} are pressures and shears. For the jet problem

$1/\sqrt{1 - v_{xs}(y)^2 - v_{zs}(y)^2}$, $s \in \{\text{e, i}\}$, is the local bulk Lorentz factor.

we consider, electrons and protons can have initial bulk velocities in only the x and z directions, as currents only need to be initialized in the x and z directions (see Eqs. 5.10 and 5.12), and the component of velocity in the y direction is zero (see Eq. 5.5).

Particles are initialized in the comoving frame, and the yy component of particle stress-energy $\tilde{T}_{\text{prtl}}^{yy}$ is invariant under a boost in x , $(\Gamma, -\Gamma\beta_x, 0, -\Gamma\beta_z)$; to ensure pressure balance, it is enough that the sum $\tilde{T}_{\text{prtl}}^{yy} + T_{\text{em}}^{yy}$ is constant along y :

$$\tilde{p}_{yy}(y) + \frac{1}{2}(B(y)^2 + E(y)^2) - B_y(y)^2 - E_y(y)^2 = \text{const.} \quad (5.32)$$

We initialize an isotropic distribution in the comoving frame, therefore $\tilde{p}_{yy}/m = \tilde{n}\theta$, where $\theta = T/m$ is the dimensionless temperature in the comoving frame (T is temperature). The temperature profile for both particle species together must satisfy

$$\tilde{n}_{ej}(y)m_e\theta_e(y) + \tilde{n}_{ij}(y)m_i\theta_i(y) = \left(\text{const.} - \frac{1}{2}(B(y)^2 + E(y)^2) + B_y(y)^2 + E_y(y)^2 \right), \quad (5.33)$$

which follows from Eqs. 5.30 and 5.31, and the constant is solved for by considering pressure balance in the jet region, where electrons and protons are prescribed temperatures θ_{e0j} and θ_{i0j} , respectively.

Noting also that there are no currents or bulk velocities in the jet frame (so $\tilde{n}_{e0j} = \tilde{n}_{i0j} = \frac{1}{2}\tilde{n}_{0j}$), we solve for the constant:

$$\text{const.} = \frac{1}{2}\tilde{n}_{0j}(m_e\theta_{e0j} + m_i\theta_{i0j}) + \frac{1}{2}B_0^2(1 + b_j^2). \quad (5.34)$$

Combining Eqs. 5.33 and 5.34, the temperature profile (of either species) in the comoving frame is

$$\theta_e(y) = \frac{1}{2\tilde{n}_{ej}(y)m_e} \left(\frac{1}{2}\tilde{n}_{0j}(m_e\theta_{e0j} + m_i\theta_{i0j}) + \frac{1}{2}B_0^2(1 + b_j^2) - \frac{1}{2}(B(y)^2 + E(y)^2 + B_y(y)^2 + E_y(y)^2) \right), \quad (5.35)$$

$$\theta_i(y) = \frac{1}{2\tilde{n}_{ij}(y)m_i} \left(\frac{1}{2}\tilde{n}_{0j}(m_e\theta_{e0j} + m_i\theta_{i0j}) + \frac{1}{2}B_0^2(1 + b_j^2) - \frac{1}{2}(B(y)^2 + E(y)^2 + B_y(y)^2 + E_y(y)^2) \right). \quad (5.36)$$

5.2.2 Fiducial parameters and numerical choices

The physical parameters we use to specify the initial state of our PIC simulations are the same as those described in Sec. 4.2.1.2 (see also Tab. 4.1). Here, we restate them briefly.

The parameter β_{sh} is the speed of the wind relative to the jet. The strength of the in-plane magnetic field on the jet side is set by $\sigma_{wx} \equiv B_{x0}^2/w_0$, where B_{x0} is the magnitude of the in-plane magnetic field on the jet side, and w_0 is the initial enthalpy density in the jet (see Eq. 4.46). The initial temperature on the jet side is controlled by the ion plasma beta $\beta_{ix} \equiv p_{i0}/(B_{x0}^2/2)$, which is the ratio of (twice) the ion pressure to the magnetic pressure, computed with the in-plane component of magnetic field (see Eq. 4.45). For all of the simulations presented here, we consider an ion to electron mass ratio of unity, $m_i/m_e = 1$, and equal initial electron and ion temperatures, $T_{e0} = T_{i0}$; therefore also the dimensionless temperatures of electrons and ions are equal, $\theta_{e0} = \theta_{i0}$ (this is true on both the jet and wind sides individually: $\theta_{e0j} = \theta_{i0j}$ and $\theta_{e0w} = \theta_{i0w}$). The out-of-plane component of magnetic field is controlled by $b_j \equiv B_{z0j}/B_{x0j}$ (Eq. 4.4), and likewise the strength of the magnetic field in the wind is controlled by $b_w \equiv B_{z0w}/B_{x0j}$ (Eq. 4.4). The ratio of wind-side to jet-side density (in the lab frame) is set by $\rho_{0w}/\rho_{0j} = n_{0w}/n_{0j}$ (in the present investigation, we limit our focus to the case of equal electron and ion masses, $m_i/m_e = 1$). Lastly,

for 3D simulations, the parameter $f \equiv m/k$ controls the angle of propagation of perturbations. For the simulations we describe in Sec. 5.3, we typically fix $b_w/b_j = 0.1$ and $\widetilde{\rho_{0w}}/\rho_{0j} = 4$ ($\widetilde{\rho_{0w}}$ is the initial wind-side density in the rest frame).

In addition to the physical parameters described above, there are several numerical parameters we choose. We briefly specify the most important of these (see Sec. 3.3 for a comprehensive discussion). The electron skin depth on the jet side is c/ω_{pe} ; here $\omega_{pe} \equiv \sqrt{\tilde{n}_{0j}q_i^2/(\gamma_{e0j}m_e)}$ is the plasma frequency, with $\gamma_{e0j} = 1 + u_{e0j}/(\tilde{n}_{0j}m_ec^2)$, where u_{e0j} is the initial electron internal energy on the jet side. The skin depth, which controls the temporal resolution of the simulation, is resolved with 16 cells on the jet side (this corresponds to a timestep $\Delta_{ts} = 0.028125 \omega_{pe}^{-1}$). On the wind side, where we typically fix the rest-frame density to be a factor of four larger than on the jet side, the skin depth is $16/\sqrt{4} = 8$, corresponding to a temporal resolution of $0.05625 \omega_{pe}^{-1}$. For numerical stability and to satisfy the Courant condition, we set the speed of light in our simulation to $c = 0.45$.

We perform our simulations on a box of size $L_x \times L_y \approx 1000 c/\omega_{pe} \times 3000 c/\omega_{pe}$, which we find is sufficiently large to yield converged measurements of the growth rates we discuss in Sec. 5.3.2 (see Sec. 5.A for further discussion). The transition width is resolved with $\Delta_t = 45 c/\omega_{pe}$, which, for the cases we present in Sec. 5.3.2, has a gradient in the magnetic field gradual enough that kinetic effects do not cause our initialized fluid equilibrium to be unstable. Lastly, for all cases discussed here, we consider electron-positron plasma, i.e. the mass ratio $m_i/m_e = 1$.

We remark on an important difference between the setup of our PIC simulations, and that of the relativistic MHD simulations discussed in Sec. 4.3.1. Whereas a box-sized perturbation was initialized in the relativistic MHD simulations, in the PIC simulations we allow perturbations to grow from thermal noise, and do not initialize a perturbation.⁷

⁷We have tested a PIC setup where we do initialize a perturbation, but the wave is quickly saturated by thermal noise, and the simulation behaves as if no perturbation had been initialized.

5.3 Results

In this section, we present the results of our PIC simulations of the KH instability in astrophysical jets. We discuss the time evolution of the instability in Sec. 5.3.1. Next, in Sec. 5.3.2, we present measurements of the growth rate, and compare with the theoretical predictions (as in Ch. 4, these are computed according to Eqs. 4.84 and 4.85). Lastly, in Sec. 5.3.3, we use a test case to investigate the possibility of KH-induced magnetic reconnection.

5.3.1 Time evolution

In Fig. 5.1, we show the time evolution of the KH instability in a simulation with $\beta_{\text{sh}} = 0.8$, $\sigma_{wx} = 1$, $\beta_{ix} = 0.078$, $b_j = 3$, $b_w = 0.3$, and ratio of wind-side to jet-side initial density $\rho_{0w}/\rho_{0j} = 6.7$ (this corresponds to a ratio $\widetilde{\rho_{0w}}/\rho_{0j} = 4$, where $\widetilde{\rho_{0w}}$ is the initial density in the rest frame of the wind). Panels A–D show the number density in units of initial number density (n/n_0) for t in the range $27(v_A k_{x0})^{-1}$ – $87(v_A k_{x0})^{-1}$. Blue corresponds to the (low density and magnetized) jet, whereas red shows the (high density and weakly magnetized) wind. In panel A, the KH instability is nearing the end of the linear growth phase. In panels B–D, we see the nonlinear evolution of the jet-wind system after the KH instability has saturated. In panel D, an inset plot in the upper right shows a structure in the mixing layer between the jet and wind. Mixing during the nonlinear phase, which is highlighted here, is suggestive of the possibility for KH-induced reconnection, due to stretching of magnetic fields within the KH structures at the mixing interface (Liu et al., 1988; Steinberg et al., 2007; Faganello et al., 2012); we further explore the question of KH-induced magnetic dissipation in Sec. 5.3.3.

5.3.2 Instability growth rates

A main focus of this chapter is to compare the theoretically predicted growth rate of the KH instability, specialized to the case of an astrophysical jet (see Eqs. 4.84 and 4.85), with those obtained in PIC simulations. Several PIC studies of the KH instability exist in the literature

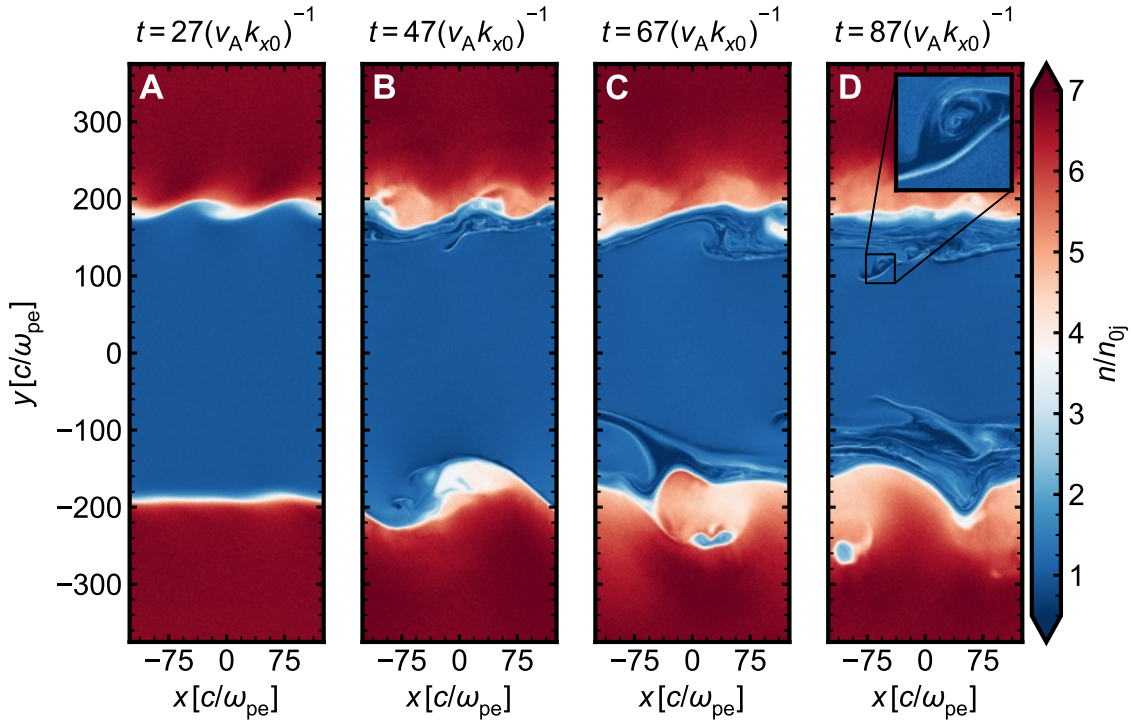


Figure 5.1: Time evolution of number density (in units of initial number density on the jet side) for the jet setup; red shows the wind side and blue shows the jet side.

(Henri et al., 2013; Lee et al., 2015; Shukla et al., 2016), including several which address the KH instability in astrophysical jets (Alves et al., 2012; Nishikawa et al., 2012; Grismayer et al., 2013; Alves et al., 2014). From first-principles it is not immediately clear that collisionless PIC simulations should capture the physics of a fluid instability such as KH. However, one expects that strongly magnetized plasma may operate as an MHD fluid. Indeed, Henri et al. (2013) demonstrated that, with regard to measured growth rates of the KH instability, fully-kinetic PIC simulations and MHD simulations agree in the strongly magnetized limit; they considered guide fields $b_g \sim 20$ in a conventional KH setup, where $b_g \equiv B_{z0}/B_{x0}$. However, the validity of PIC in modeling the KH instability in moderately, or even weakly, magnetized plasma remains unexplored, and is an impetus for the present investigation.

The method we use to measure growth rates in PIC simulations is similar to that described in Sec.

4.3.3. Briefly, we use the growth of Fourier power $|\tilde{v}_y(k_{x0})|^2$ as a proxy for growth of the instability, where $|\tilde{v}_y(k_{x0})|^2$ is the Fourier power in the velocity field v_y evaluated at $\mathbf{k} = (k_{x0}, k_{y0})$; k_{x0} and k_{y0} here are the wavevectors of the longest wavelength perturbation in x and y , respectively. Note that in the PIC case (unlike the RMHD simulations described in Sec. 4.3.1), we do not initialize a perturbation (see Sec. 5.2), so k_{x0} refers simply to the largest-wavelength perturbation in x , rather than to an initialized perturbation. Before computing the Fourier power $|\tilde{v}_y(k_{x0})|^2$, we apply a Gaussian filter to the field v_y , which helps reduce noise in $|\tilde{v}_y(k_{x0})|^2$; the width of the filter is 20% of the domain size in y , however, we have tested that the measured growth rate of $|\tilde{v}_y(k_{x0})|^2$ is insensitive to the choice of filter width.

In Fig. 5.2, we show the growth of $|\tilde{v}_y(k_{x0})|^2$ for a simulation with $\beta_{\text{sh}} = 0.8, \sigma_{wx} = 1, \beta_{ix} = 0.078, b_j = 3, b_w = 0.3$, and $\widetilde{\rho_{0w}}/\rho_{0j} = 4$ (this corresponds to the simulation shown in Fig. 5.1). The red curve shows the growth measured in PIC, and the blue dashed line indicates the predicted rate of growth (from Eqs. 4.84 and 4.85). The PIC growth rate is slightly below the prediction, but shows adequate agreement. The growth of the instability saturates around $t \approx 45(v_A k_{x0})^{-1}$. The four vertical dotted lines correspond to the times at which the spatial profiles of number density in panels A–D of Fig. 5.1 are shown.

Next, in Fig. 5.3 we show a comparison between the predicted growth rate and PIC simulation as a function of the shear velocity β_{sh} . For the simulations here, $\sigma_{wx} = 1, \beta_{ix} = 0.078, b_j = 3, b_w = 0.3$, and $\widetilde{\rho_{0w}}/\rho_{0j} = 4$. The blue curve shows the predicted growth rate $\text{Im}(\phi_{v_A})$, and the red points show the growth rates measured in simulations. The error bars indicate uncertainty on the PIC measurements of the growth rate (see Sec. 5.B for further discussion). The instability has a stable region for $\beta_{\text{sh}} \lesssim 0.35$, which is related to in-plane magnetic tension (Chandrasekhar, 1961; Miura & Pritchett, 1982), and approaches zero also in the relativistic limit (Bodo et al., 2004; Osmanov et al., 2008). The prediction and the growth rates measured in PIC simulations show agreement.

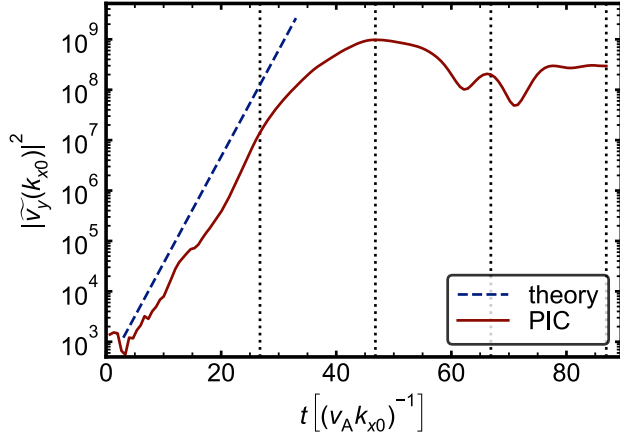


Figure 5.2: Time evolution of Fourier power $|\tilde{v}_y(k_{x0})|^2$, for the simulation shown in Fig. 5.1; the four vertical dotted lines from left to right correspond to panels A–D in Fig. 5.1 respectively, indicating the time at which each density profile is shown. The red curve is smoothed slightly (using a Savitzky & Golay (1964) filter) for presentation.

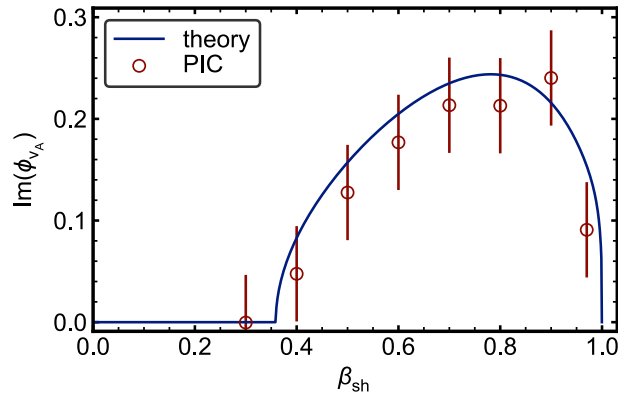


Figure 5.3: Comparison of analytically predicted growth rate (blue line) and PIC simulations (red circles). Here, $\sigma_{wx} = 1$, $\beta_{ix} = 0.078$, $b_i = 3$, and $b_w = 0.3$. β_{sh} dependence of the growth rate is shown.

Fig. 5.4 is similar to Fig. 5.3, but here we fix $\beta_{sh} = 0.8$ and study the σ_{wx} dependence of the instability (the other parameters are the same as before: $\beta_{ix} = 0.001$, $b_i = 3$, $b_w = 0.3$, and $\widetilde{\rho_{0w}}/\rho_{0j} = 4$). There is a region of stability for $\sigma_w \lesssim 5 \times 10^{-2}$, which as we discussed in Sec. 4.2.4 is related to the classical criterion for stability, $\beta_{sh} \lesssim c_s$. Allowing for uncertainties, as indicated by the errorbars, the PIC simulation in this regime is consistent with stability. Also, above $\sigma_w \sim 0.1$, we find acceptable agreement between the predicted and measured growth rates.

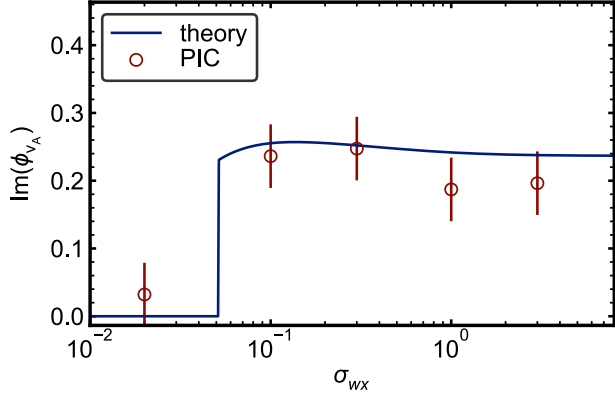


Figure 5.4: The layout here is similar to that of Fig. 5.3; comparison of analytically predicted growth rate (blue line) and PIC simulations (red circles). Here, $\beta_{\text{sh}} = 0.8$, $\beta_{\text{ix}} = 0.001$, $b_j = 3$, and $b_w = 0.3$. σ_{wx} dependence of the growth rate is shown.

Next, in Fig. 5.5 we show the b_j dependence of the growth rate, as measured in PIC, and compare with theory. The fixed parameters are similar to before: $\beta_{\text{sh}} = 0.8$, $\sigma_{wx} = 1$, $\beta_{\text{ix}} = 0.078$, and $\widetilde{\rho_{0w}}/\rho_{0j} = 4$; in each case, we set $b_w = b_j/10$. For $b_j = 0$, the magnetic field on the jet side is entirely in-plane, whereas for $b_j \rightarrow \infty$, the magnetic field on the jet side points completely out-of-plane. Since the simulations here are 2D (and thus the perturbations propagate in-plane), the growing instability is subject to the stabilizing effect of magnetic tension as b_j approaches zero, and this stabilizing effect is removed as b_j increases. The growth rate saturates beyond $b_j \approx 10$, because increasing the guide field further has a negligibly small effect on the in-plane magnetic tension. The measured and predicted growth rates show adequate agreement.

In Fig. 5.6, we show the β_{ix} dependence of the growth rate and compare with theory. Similar to before, the fixed parameters are $\beta_{\text{sh}} = 0.8$, $\sigma_{wx} = 1$, $b_j = 3$, $b_w = 0.3$, and $\widetilde{\rho_{0w}}/\rho_{0j} = 4$. The shaded gray region beginning at $\beta_{\text{ix}} = \beta_{\text{ix},\text{max}} \equiv 1/(4\sigma_{wx}) = 0.25$ lies beyond the maximum possible value of β_{ix} given that $\sigma_{wx} = 1$, and thus corresponds to a physically inaccessible part of the parameter space.⁸ The growth rate is about constant as β_{ix} decreases from $\beta_{\text{ix}} = 0.25$ down towards $\beta_{\text{ix}} = 10^{-3}$.

⁸Note, however, that this does not indicate a maximum possible temperature: as $\beta_{\text{ix}} \rightarrow \beta_{\text{ix},\text{max}}$, the corresponding temperature $\theta \rightarrow \infty$; see Sec. 4.A for further details.

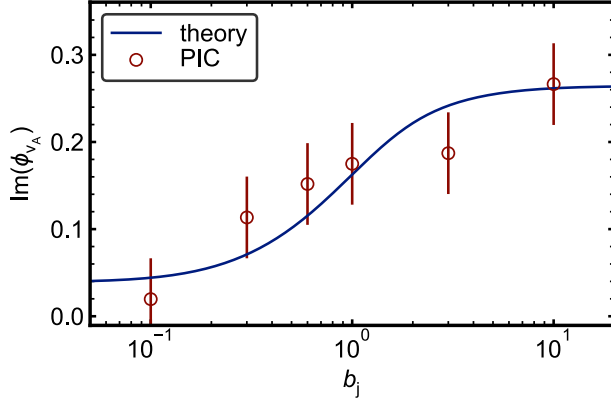


Figure 5.5: The layout is again similar to that of Fig. 5.3; comparison of analytically predicted growth rate (blue line) and PIC simulations (red circles). Here, $\beta_{sh} = 0.8$, $\sigma_{wx} = 1$, and $\beta_{ix} = 0.001$. The guide field on the wind side is set by $b_w/b_j = 0.1$ in all cases. b_j dependence of the growth rate is shown.

The PIC simulations and prediction show adequate agreement.

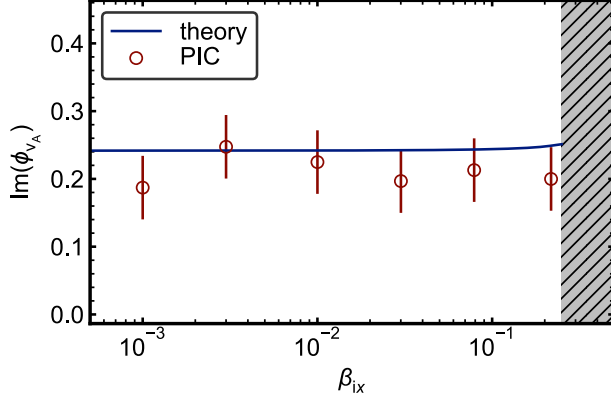


Figure 5.6: Similar to Fig. 5.3; comparison of analytically predicted growth rate (blue line) and PIC simulations (red circles). Here, $\beta_{sh} = 0.8$, $\sigma_{wx} = 1$, $b_j = 3$, and $b_w = 0.3$. The gray shaded region on the far right indicates a physically inaccessible range of β_{ix} when $\sigma_{wx} = 1$. β_{ix} dependence of the growth rate is shown.

For a three-dimensional case, we have tested the dependence of the growth rate on the ratio $f = m/k$, which controls the angle of propagation of unstable modes, $\arctan(f)$. The comparison between measurements and predicted growth rates is shown in Fig. 5.7. This case mirrors the 2D simulation shown in Fig. 5.1 (the physical parameters are the same: $\beta_{sh} = 0.8$, $\sigma_{wx} = 1$, $\beta_{ix} = 0.078$, $b_j = 3$, $b_w = 0.3$, and $\widetilde{\rho_0 w}/\rho_0 j = 4$), but the simulation was performed on a box that is four

times as small in the x and y dimensions (the length in z is equal to the length in x).

We measured the growth rates of modes with $f \neq 0$ analogously to the way we measure the growth rate of the mode with $k = k_{x0}$ in 2D simulations, as described in Sec. 4.3.3. To better resolve the predicted unstable region in Fig. 5.7 from $\arctan(f) \approx -49^\circ$ to $\arctan(f) \approx 26^\circ$, we considered modes with $k = 5k_{x0}$. It is interesting to note that the maximum of the growth rate in Fig. 5.7 is around $\arctan(f) \approx -15^\circ$, which corresponds closely to a wavevector satisfying $\mathbf{k} \cdot \mathbf{B} = 0$ (Chandrasekhar, 1961; Miura & Pritchett, 1982). Below $\arctan(f) \approx -49^\circ$ and above $\arctan(f) \approx 26^\circ$, the magnetic tension of the guide field is evidently strong enough to suppress the instability entirely. The predicted growth rate agrees with the measurement.

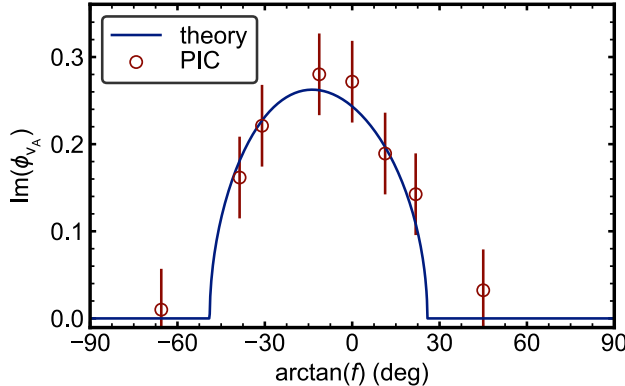


Figure 5.7: Comparison of analytical growth rate and measured growth rates in PIC, for a 3D simulation. The simulation parameters here are $\beta_{\text{sh}} = 0.8$, $\sigma_{wx} = 1$, $\beta_{ix} = 0.001$, $b_j = 3$, and $b_w = 0.3$. Angle-of-propagation $\arctan(f)$ dependence of the growth rate is shown.

In Fig. 5.8, we show the volumetric profile of density (in units of n_{0j} , the initial number density on the jet side) of the 3D simulation under discussion. The density profile is shown at times $t = 32(v_A k_{x0})^{-1}$ (panel A), and $t = 41(v_A k_{x0})^{-1}$ (panel B); the former is at the tail end of the linear growth phase, and the latter is during the nonlinear evolution of the instability. Only a fraction of the box from $y = 0 c/\omega_{pe}$ to $y = 100 c/\omega_{pe}$ is shown (the full box extends to $y = 750 c/\omega_{pe}$). Blue corresponds to the jet, red to the wind, and white shows the mixing layer between the two. As the

volumetric profile in panel A shows, we see a large-wavelength mode that appears to be propagating in the xz plane, slightly obliquely to the x direction (note that according to the prediction shown in Fig. 5.7, the maximum growth rate of the instability is at $\arctan(f) \approx -15^\circ$). Panel B shows the density profile during the nonlinear phase, and shows nonuniformity in the z direction, confirming that the unstable modes have nonzero k_z ; this suggests that 2D and 3D simulations could give different results with regard to quantities measured during the nonlinear phase, a well known fact from studies comparing, e.g., magnetic reconnection in 2D and 3D simulations (Dahlin et al., 2015; Munoz & Büchner, 2018).

We show in Fig. 5.9 a comparison between the growth of $|\tilde{v}_y(k_{x0})|^2$ as measured in 2D and 3D (for $f = 0$) simulations. Red shows the 2D result (this is the same as in Fig. 5.2), green the 3D result, and the dashed blue line corresponds to the predicted linear growth (an offset has been added to the green curve to allow for easier comparison of the slopes of the red, dashed blue, and green curves). The growth rates extracted from the 2D and 3D simulations both show reasonable agreement with the prediction. We note that the green curve oversaturates the prediction, even though this simulation has smaller x and y dimensions than the corresponding 2D simulation (this is contrary to the box-size convergence for 2D simulations that we discuss in Sec. 5.A). It is possible that this is just a random fluctuation (see Sec. 5.B). A full set of convergence tests in 3D is needed for a full understanding, which is beyond the scope of this chapter.

5.3.3 Magnetic dissipation

The role of magnetic dissipation in the KH instability is underexplored in the context of astrophysical jets. Faganello et al. (2008) used hybrid numerical simulations to study KH-induced reconnection in Earth's magnetosphere; Fermo et al. (2012) used fully-kinetic PIC to demonstrate that plasmoids can be generated by the KH instability; many PIC studies have focused on the KH instability in jets (Alves et al., 2012; Nishikawa et al., 2012; Grismayer et al., 2013; Alves

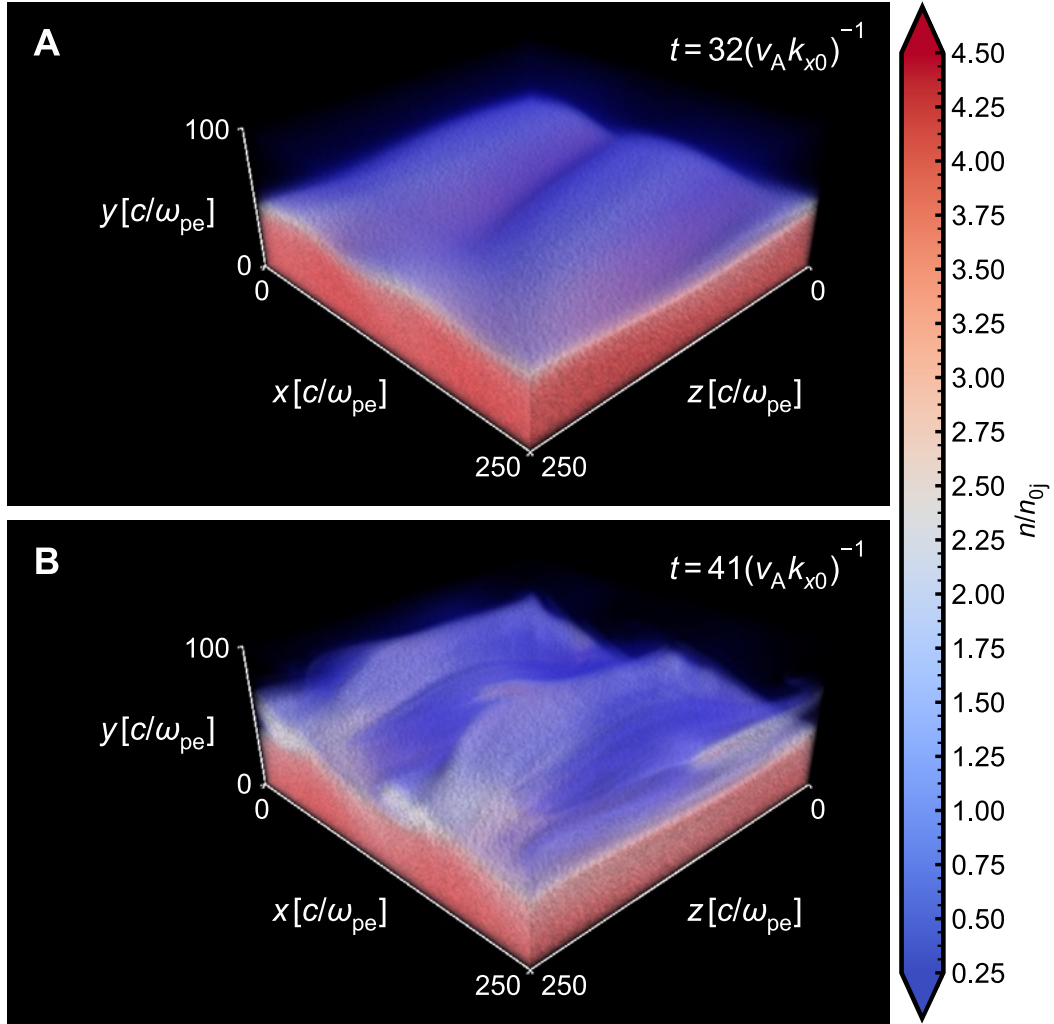


Figure 5.8: Volumetric profiles of number density, in units of the initial jet-side density, from 3D simulation with $\beta_{\text{sh}} = 0.8$, $\sigma_{wx} = 1$, $\beta_{ix} = 0.001$, $b_j = 3$, and $b_w = 0.3$. The simulation shown here is the same as the one presented in Fig. 5.7.

et al., 2014); but the number of studies which have focused on the link between the KH instability and dissipation of magnetic energy in jets is limited. In this section, we use as a case study a simulation which shows pronounced jet-wind mixing during the nonlinear phase (the parameters are $\beta_{\text{sh}} = 0.8$, $\sigma_{wx} = 1$, $b_j = 3$, $b_w = 0.3$, $\beta_{ix} = 0.078$, and $\widetilde{\rho_0 w}/\rho_0 j = 4$) to explore the possibility of KH-induced magnetic energy dissipation at the jet-wind interface. The results here are preliminary.

In Fig. 5.10, panel A, we compare the (volume-integrated) time evolution of the energy dissipation measures $\mathbf{j}_{||} \cdot \mathbf{E}_{||}$ (red curve) and $\mathbf{j} \cdot \mathbf{E}$, (blue curve), both normalized to the initial in-plane

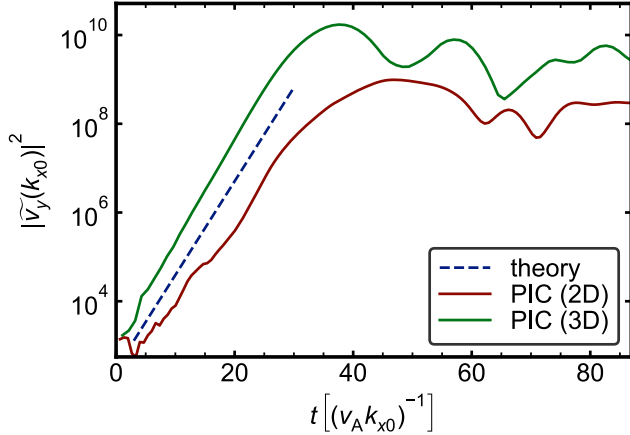


Figure 5.9: 2D vs. 3D comparison of the growth of Fourier power $|\tilde{v}_y(k_{x0})|^2$. For both simulations, the parameters are $\beta_{sh} = 0.8$, $\sigma_{wx} = 1$, $\beta_{ix} = 0.001$, $b_j = 3$, and $b_w = 0.3$. The 2D simulation corresponds to the one at $\beta_{ix} = 10^{-3}$ in Fig. 5.6, and the 3D simulation corresponds to the one presented in Figs. 5.8 and 5.7.

magnetic energy in the box, ε_{B_x0} . The presence of a parallel electric field \mathbf{E}_{\parallel} is typically understood as an indicator of magnetic reconnection (Schindler & Hesse, 1988; Mozer & Pritchett, 2010; Makwana et al., 2017), so $\mathbf{j}_{\parallel} \cdot \mathbf{E}_{\parallel}$ can be taken as a proxy for magnetic dissipation associated with magnetic reconnection. The heating associated with E_{\parallel} is negligible until around $t = 50(v_A k_{x0})^{-1}$; over this same range of time (from $t = 0(v_A k_{x0})^{-1}$ to $t = 50(v_A k_{x0})^{-1}$), the total volume-integrated $\mathbf{j} \cdot \mathbf{E}/\varepsilon_{B_x0}$ is for the most part negative, which simply means that kinetic motion of the plasma creates electromagnetic fields. However, at late times ($t \gtrsim 75(v_A k_{x0})^{-1}$), the dissipation due to E_{\parallel} and the total dissipation are roughly equal (see the rough overlap between red and blue lines for $t \gtrsim 75(v_A k_{x0})^{-1}$), which indicates that the total dissipation $\mathbf{j} \cdot \mathbf{E} = \mathbf{j}_{\parallel} \cdot \mathbf{E}_{\parallel} + \mathbf{j}_{\perp} \cdot \mathbf{E}_{\perp}$ is due primarily to heating associated with the parallel electric field. This is suggestive that reconnection is the dominant mechanism controlling magnetic dissipation and heating at late times, for this particular simulation.

Panel B of Fig. 5.10 shows the evolution of transverse magnetic energy $\Delta\varepsilon_{B_T} \equiv \varepsilon_{B_T}(t) - \varepsilon_{B_T}(0)$, in units of the initial in-plane magnetic energy in the box, ε_{B_x0} . Comparing with panel A shows that

indeed, the growth of $\Delta\epsilon_{B_T}$ occurs during the time when $\mathbf{j} \cdot \mathbf{E}$ is negative, and that the agreement between $\mathbf{j} \cdot \mathbf{E}$ and $\mathbf{j}_{||} \cdot \mathbf{E}_{||}$ at late times occurs after the linear growth of the instability has saturated. The magnetic energy shows a decrease from $t \approx 65(v_A k_{x0})^{-1}$ to $t \approx 87(v_A k_{x0})^{-1}$.

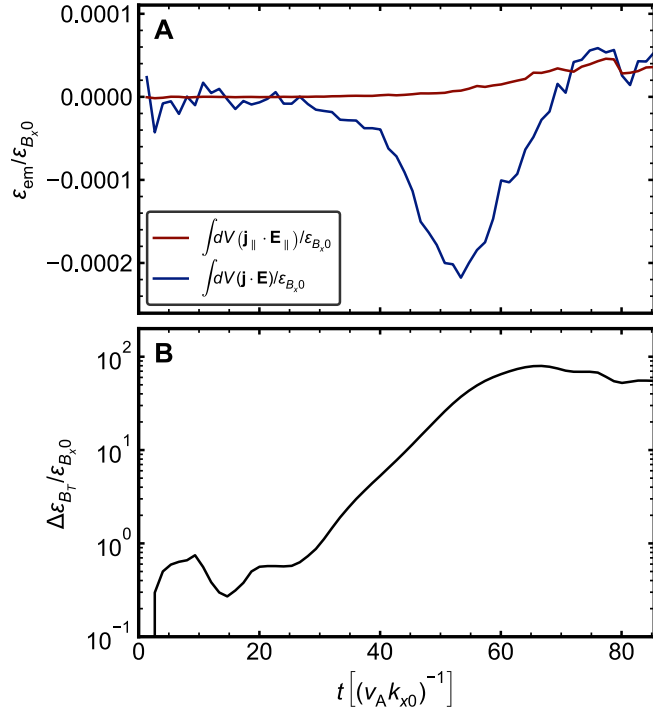


Figure 5.10: Time evolution of (A) volume-integrated $E_{||}$ dissipation, in units of initial in-plane magnetic energy (red line), and volume-integrated total dissipation, also in units of initial in-plane magnetic energy (blue line); (B) Time evolution of transverse (i.e., in the xy plane; *transverse* to the out-of-plane guide field) magnetic energy $\Delta\epsilon_{B_T} \equiv \epsilon_{B_T}(t) - \epsilon_{B_T}(0)$, in units of initial in-plane magnetic energy.

We show in Fig. 5.11, for the same simulation corresponding to Fig. 5.10, the 2D spatial profiles at time $t = 75(v_A k_{x0})^{-1}$ of $[\mathbf{B} \times (\nabla \times \mathbf{E}_{||})]_z$ (in panel A), $E_{||}$ (panel B), $j_{||}$ (panel C), and $\mathbf{j}_{||} \cdot \mathbf{E}_{||}$ (panel D). Nonzero $[\mathbf{B} \times (\nabla \times \mathbf{E}_{||})]_z$ corresponds to regions where plasma does not move with the (in-plane) $\mathbf{E} \times \mathbf{B} / B^2$ velocity, thereby violating the flux-freezing condition, and is thus a prerequisite for energy dissipation via magnetic reconnection. The quantities $j_{||}$, $E_{||}$, and $\mathbf{j}_{||} \cdot \mathbf{E}_{||}$ together indicate the relative importance of $j_{||}$ and $E_{||}$ with regard to $E_{||}$ -associated dissipation, $\mathbf{j}_{||} \cdot \mathbf{E}_{||}$.

Focusing on panel A, we see that the quantity $[\mathbf{B} \times (\nabla \times \mathbf{E}_{||})]_z$, though noisy, is noticeably nonzero

(as indicated by white, pink, and blue regions) in certain regions along the mixing interface between the jet and wind ($y \approx \pm 70 c/\omega_{pe}$); one such region is displayed in an inset plot on the far right of panel A (and correspondingly, the same region is shown in an inset plot in panels B–D). In panel B, we see that there are indeed regions of markedly nonzero E_{\parallel} (shown by green and yellow), which is a signature of magnetic reconnection. Comparing panel B, C and D altogether, we can see that the regions of nonzero $\mathbf{j}_{\parallel} \cdot \mathbf{E}_{\parallel}$ (pink and white regions) are indeed correlated also with nonzero E_{\parallel} ; there appear to be many more regions with nonzero j_{\parallel} than regions with nonzero E_{\parallel} , so E_{\parallel} , as opposed to j_{\parallel} , in a sense limits the dissipation $\mathbf{j}_{\parallel} \cdot \mathbf{E}_{\parallel}$.

In Fig. 5.12, we show (for the same simulation corresponding to Figs. 5.10 and 5.11) the time evolution of the electron energy spectrum, for electrons initially in the jet; γ_j here indicates the Lorentz factor of these electrons. As the color of the line changes from blue to red, the time increases from $t = 0(v_A k_{x0})^{-1}$ to $t = 87(v_A k_{x0})^{-1}$. The time evolution of the energy spectrum seems to indicate an overall heating of particles: the peak of the distribution shifts from around $(\gamma_j - 1) \approx 10^{-3}$ to $(\gamma_j - 1) \approx 2 \times 10^{-3}$. At late times ($t \gtrsim 70(v_A k_{x0})^{-1}$), electrons populate the distribution up to $(\gamma_j - 1) \approx 10$. There is a local maximum in the energy spectrum at $(\gamma_j - 1) \approx 2 \times 10^{-1}$ and $t \approx 75(v_A k_{x0})^{-1}$ (indicated by bright red; this time corresponds to the time at which spatial profiles in Fig. 5.11 are shown).

For the simulation corresponding to the energy spectrum shown in Fig. 5.12, the initial dimensionless electron temperature of the wind is $\theta_{e0w} \approx 0.1$; though the energy spectrum tracks only electrons initially in the jet region, still the electrons are heated to a temperature that is close to that of the initial temperature of the wind, which makes it unclear whether there are numerical collisions between the jet and wind particles which contribute to the energization of jet electrons. To argue against this explanation, we show in Fig. 5.13 the time evolution of the total (i.e., including particles from the jet, wind, and transition regions) electron energy spectrum, for a simulation in

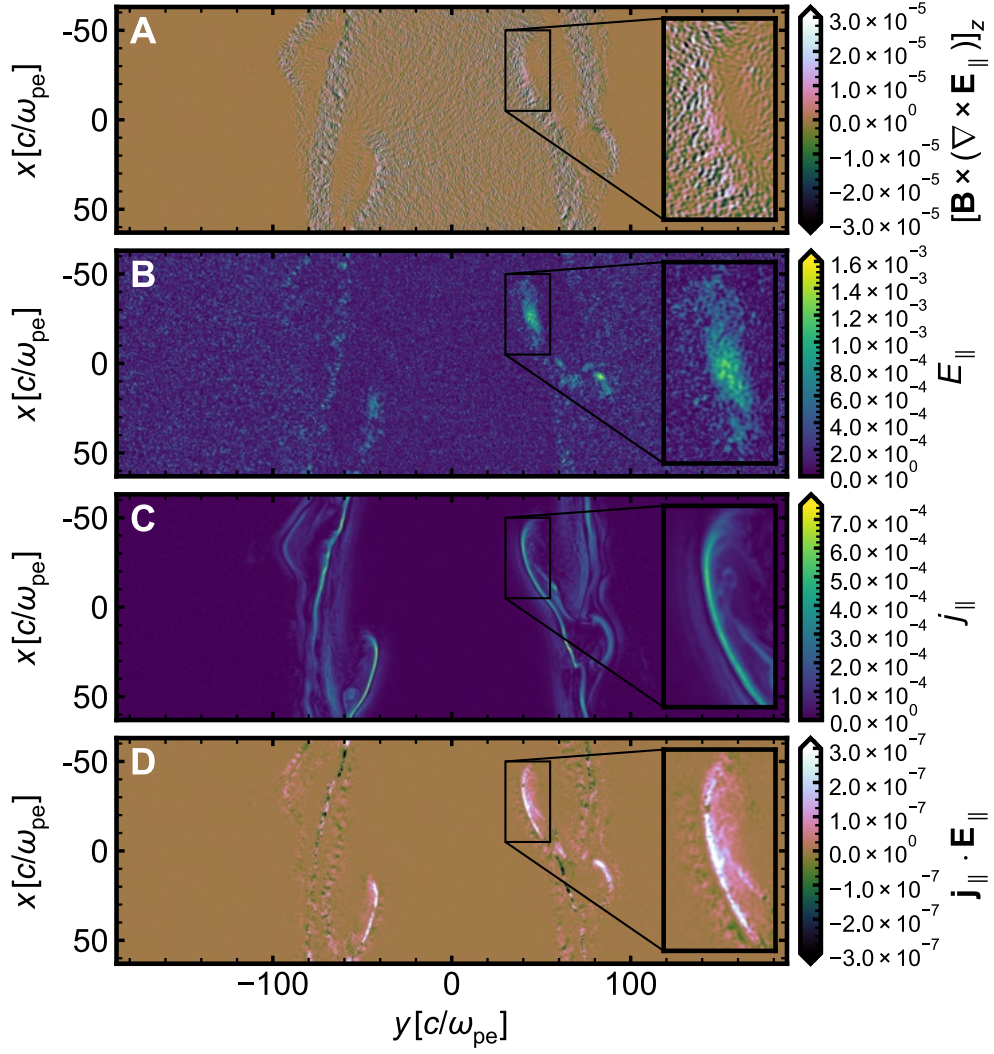


Figure 5.11: For a simulation (the same as that presented in Fig. 5.10) with $\beta_{sh} = 0.8, \sigma_{wx} = 1, b_j = 3, b_w = 0.3, \beta_{ix} = 0.078$, the 2D spatial profiles at $t = 75(v_A k_x0)^{-1}$ of: (A) $[\mathbf{B} \times (\nabla \times \mathbf{E}_{\parallel})]_z$, which indicates violation of the frozen-in condition; (B) Magnitude of the parallel electric field E_{\parallel} , which is an indicator of magnetic reconnection; (C) Magnitude of the parallel current density j_{\parallel} ; and (D) E_{\parallel} -associated dissipation, $\mathbf{j}_{\parallel} \cdot \mathbf{E}_{\parallel}$, which indicates heating and dissipation associated with a parallel electric field.

which electrons and ions⁹ start initially with the same temperature. The peak of the distribution

starts initially at $\gamma - 1 \approx 0.1$, and by $t \gtrsim 100(v_A k_x0)^{-1}$, a high-energy tail of electrons develops,

⁹For this simulation, we consider an electron-positron jet and electron-proton wind, which is a more realistic model of the jet-wind interface than electron-positron composition throughout; we employ a reduced mass ratio of $m_i/m_e = 5$.

with electron $\gamma - 1$ reaching up to $\gamma - 1 \approx 20$, which is larger than the initial dimensionless temperature of either the wind or jet (and for any of the species: electrons, positrons, or protons). This suggests that the electron energization is indeed physical, and not a result of numerical collisions.

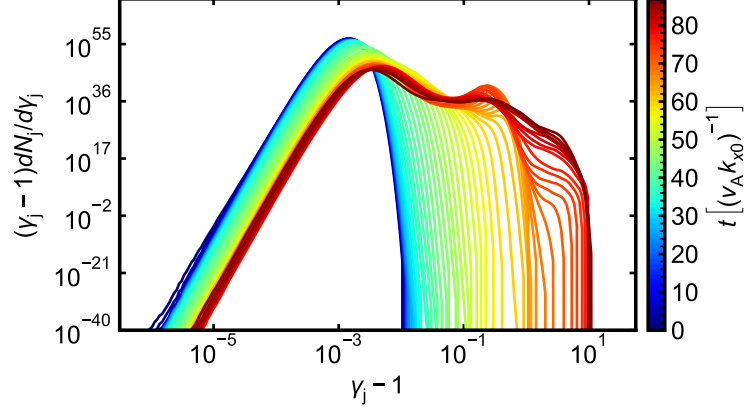


Figure 5.12: Time evolution of energy spectrum of electrons initially on the jet side. As the curves progress from blue to red, the time increases from $t = 0(v_A k_{x0})^{-1}$ to $t = 87(v_A k_{x0})^{-1}$. The simulation corresponding to this energy spectrum is the same one presented in Figs. 5.10 and 5.11.

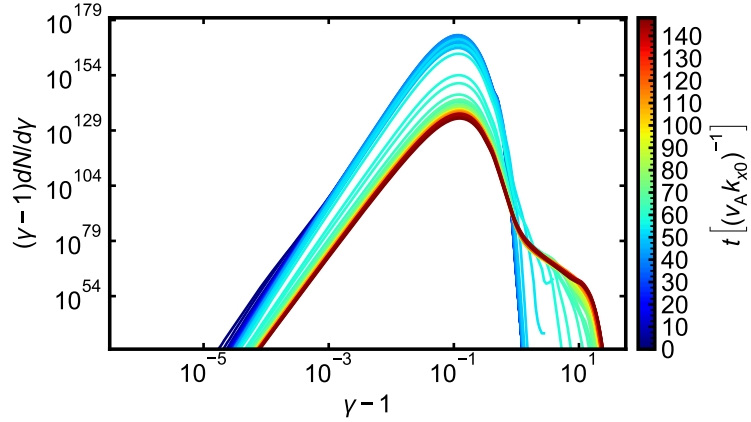


Figure 5.13: The layout here is similar to that of Fig. 5.12; time evolution of total electron energy spectrum (including electrons from the jet, wind, and transition regions). As the curves progress from blue to red, the time increases from $t = 0(v_A k_{x0})^{-1}$ to $t = 145(v_A k_{x0})^{-1}$. For the simulation corresponding to this energy spectrum, we assume an electron-positron jet and electron-proton wind (we use a reduced mass ratio of $m_i/m_e = 5$), which is more realistic than assuming that both the jet and wind are composed of electron-positron plasma.

5.4 Summary

In this chapter, we used fully-kinetic PIC simulations to study the KH instability in jets. We described a PIC implementation of the jet setup, giving explicit equations that can be used to ensure fluid equilibrium. We demonstrated that growth rates of the KH instability extracted from PIC simulations, even for plasma that is only moderately magnetized, show agreement with the growth rates predicted by MHD theory, thereby justifying study of the KH instability in the context of collisionless plasmas in astrophysical jets. An important goal of PIC simulation is to study particle heating and acceleration. In this connection, we presented preliminary results aimed at probing the connection between the KH instability and magnetic dissipation in jets; our investigation is based on only one simulation, but the analysis is suggestive that the KH instability can induce magnetic dissipation in jets, and can cause both particle heating and acceleration into a power-law energy tail. Further work is necessary to rigorously quantify the role of the KH instability with regard to magnetic reconnection in jets.

In Ch. 4, we used relativistic MHD simulations to test and validate the analytical dispersion relation for KH modes in the jet setup; building on the KH investigation of Ch. 4, we extended the investigation in this chapter to include fully-kinetic particle-in-cell simulations, which allows one to study the question of magnetic dissipation in collisionless plasma, and to therefore probe the connection between the KH instability and the fundamental plasma physics process of magnetic reconnection. While this question has been studied previously by means of hybrid-kinetic simulations, the use of fully-kinetic simulations to study KH-induced reconnection is underexplored. The present work provides important justification for the use of PIC simulations to study KH-induced magnetic reconnection, and suggests that the KH instability in jets can energize particles through dissipated magnetic energy.

5.A Convergence of measured growth rate with respect to box size

We explored the convergence of our measured growth rates in PIC (see Sec. 5.3.2) with respect to the simulation box size (keeping fixed the plasma skin depth c/ω_{pe}). Increasing the box size leads to improved spatial resolution of the box-sized perturbation in v_y that we use to measure the dimensionless growth rate $\text{Im}(\phi_{v_A})$, so one expects that below a certain threshold in ℓ_x (the domain size in cells), simulations will undersaturate the predicted growth, and above the threshold, the growth rate extracted from simulations should demonstrate convergence. For the box-size convergence test we discuss here, all dimensions are scaled according to the box width ℓ_x (including the box length ℓ_y and the transition width).

Fig. 5.14 shows the time evolution of $|\tilde{v}_y(k_{x0})|^2$ for simulations with domain sizes ℓ_x in the range 1008–4036 (we fix the parameters $\beta_{sh} = 0.8$, $\sigma_{wx} = 1.0$, $\beta_i = 10^{-3}$, $b_j = 3$, $b_w = 0.3$, and $\widetilde{\rho_{0w}}/\rho_{0j} = 4$). The predicted growth is indicated by the dashed black line (in both the main plot and the inset). The inset plot in the lower right shows the extracted growth rates as a function of box width ℓ_x . We find that the measured growth rate converges to $\text{Im}(\phi_{v_A}) \approx 0.2$ beyond $\ell_x = 2 \times 10^3$. Our choice of fiducial box size, $\ell_x \approx 4 \times 10^3$ in the simulations discussed in this chapter, is thus safe and conservative. We note that the growth rates measured in simulations converge to a value that is smaller than the predicted growth rate, which we expect is controlled partly by the finite transition width in our simulations (see also Sec. 4.B for discussion of a convergence test, performed with relativistic MHD simulations, which probes the role of the ratio of transition width to box width in controlling the measured growth rates).

5.B Estimate of uncertainty using different random initial conditions

For the measured growth rates we present in Sec. 5.3.2, we include error bars on the measurements which are meant as a notion of the random variation in our measured growth rates, resulting from different random initial conditions. In Fig. 5.15, we show the time evolution of $|\tilde{v}_y(k_{x0})|^2$ for

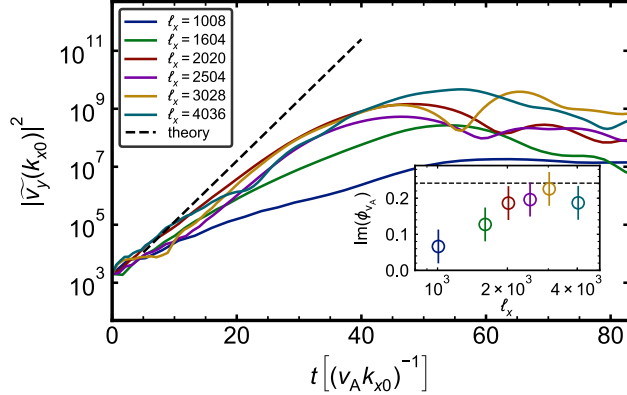


Figure 5.14: Test of convergence of measured growth rates in PIC with respect to simulation box-size. For the simulations here, $\beta_{\text{sh}} = 0.8$, $\sigma_{wx} = 1.0$, $\beta_i = 10^{-3}$, $b_j = 3$, and $b_w = 0.3$.

four simulations (indicated by colored lines) which are identical, except that each was initialized with a different random seed ‘dseed’ which is used to set initial locations of particles; there is a fifth simulation (labeled ‘dseed = 123457’, corresponding to the blue line) which uses the same random seed as the simulation corresponding to the green line (labeled ‘dseed = 123457.pu’), but is performed with an old and differently structured version of the code, which we treat as a fifth random seed. The error bars shown with our measurements in Sec. 5.3.2 are computed as the standard deviation of the slopes measured in these five simulations (we use human judgment to select the part of the line from which to fit a line and extract the growth rate). The estimated value of the standard deviation is $\sigma \approx 0.047$.

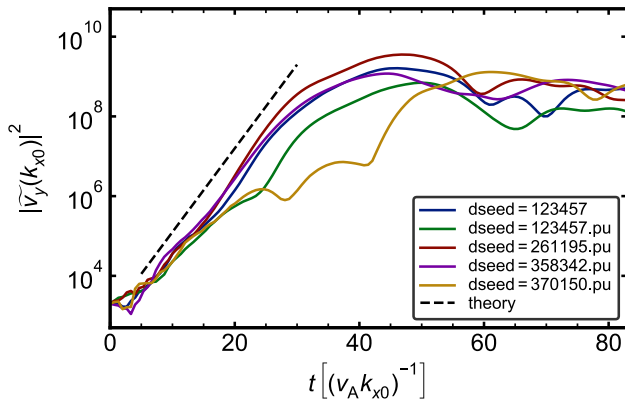


Figure 5.15: Comparison of growth of $|\tilde{v}_y(k_{x0})|^2$ for four simulations with different random initial conditions (these are indicated in the legend as ‘dseed=123457.pu’, ‘dseed=261195.pu’, ‘dseed=358342.pu’, and ‘dseed=370150.pu’), along with a fifth simulation, indicated by ‘dseed=123457’ in the legend, which was run with a differently structured version of the code; we treat this last one as having a unique random seed, like the other four. Together, we use these five simulations to estimate uncertainty on the growth rates we present in Sec. 5.3.

6. Esirkepov current deposition scheme

6.1 Introduction

Numerical noise in particle in cell (PIC) simulations can limit their effectiveness in modeling plasma phenomena. A number of strategies have been proposed to improve control of numerical heating in PIC, for example filtering the charge and current densities (Buneman et al., 1993; Spitkovsky, 2005). Recently, the use of higher-order particle form-factors has been proposed as a different method to improve energy conservation in PIC simulations, and its effectiveness has been demonstrated with the 1D electrostatic code **SHARP** (Shalaby et al., 2017). The utility of higher-order shape functions in 2D and 3D electromagnetic codes remains under-explored.

In this document, we investigate the use of higher-order shape functions in improving energy conservation, via the **Esirkepov** (2001) density decomposition algorithm for current deposition. The outline is as follows: In Section 6.2, we review the Esirkepov scheme. In Section 6.3, we present several tests of our code, and check that it is a correct implementation of the Esirkepov algorithm. In Section 6.4, we compare the performance of the Esirkepov density decomposition with the zigzag scheme, for the current deposition and particle pusher. We conclude in Section 6.5.

6.2 Esirkepov scheme

In this section, we review briefly the Esirkepov density decomposition scheme for current deposition (Esirkepov, 2001).

Consider the motion of a quasi-particle on a Cartesian grid from initial position (x, y, z) to $(x + \Delta x, y + \Delta y, z + \Delta z)$. The particle motion produces current that is deposited on the grid, as determined by the continuity equation,

$$\frac{d\rho}{dt} + \nabla \cdot \mathbf{j} = 0, \quad (6.1)$$

or written as a finite difference equation,

$$\frac{\rho_{n+1}^{i,j,k} - \rho_n^{i,j,k}}{\Delta_t} + \frac{j_x^{i+1,j,k} - j_x^{i,j,k}}{\Delta_x} + \frac{j_y^{i,j+1,k} - j_y^{i,j,k}}{\Delta_y} + \frac{j_z^{i,j,k+1} - j_z^{i,j,k}}{\Delta_z} = 0, \quad (6.2)$$

where the subscript n denotes the timestep, superscripts i, j, k refer to grid coordinates in the directions x, y , and z ; Δ_x, Δ_y , and Δ_z are grid spacings in the directions x, y , and z , and Δ_t is the timestep. Since the particle motion is independent in the x, y , and z directions, Eq. 6.2 may be recast as three separate equations governing current deposition along each direction:

$$j_x^{i+1,j,k} = j_x^{i,j,k} - q \frac{\Delta_x}{\Delta_t} W_x^{i,j,k}, \quad (6.3)$$

$$j_y^{i,j+1,k} = j_y^{i,j,k} - q \frac{\Delta_y}{\Delta_t} W_y^{i,j,k}, \quad (6.4)$$

$$j_z^{i,j,k+1} = j_z^{i,j,k} - q \frac{\Delta_z}{\Delta_t} W_z^{i,j,k}, \quad (6.5)$$

where q is the charge of the quasi-particle. Eqs. 6.3, 6.4, and 6.5 define a vector of weights $\mathbf{W}^{i,j,k} = [W_x^{i,j,k}, W_y^{i,j,k}, W_z^{i,j,k}]$, which are the densities $(\rho_{x,n+1}^{i,j,k} - \rho_{x,n}^{i,j,k})/q$, $(\rho_{y,n+1}^{i,j,k} - \rho_{y,n}^{i,j,k})/q$, and $(\rho_{z,n+1}^{i,j,k} - \rho_{z,n}^{i,j,k})/q$ associated to current deposition along each direction. If the total charge density $\rho^{i,j,k}$ is expressed in terms of an arbitrary particle form-factor (or density) $S^{i,j,k}$,

$$\rho^{i,j,k}(x, y, z) = q S^{i,j,k}(x, y, z), \quad (6.6)$$

then by the continuity equation 6.2, the densities $W_x^{i,j,k}, W_y^{i,j,k}, W_z^{i,j,k}$ satisfy

$$W_x^{i,j,k} + W_y^{i,j,k} + W_z^{i,j,k} = S^{i,j,k}(x + \Delta x, y + \Delta y, z + \Delta z) - S^{i,j,k}(x, y, z). \quad (6.7)$$

To employ the independence of Eqs. 6.3, 6.4, and 6.5, the individual components of $\mathbf{W}^{i,j,k}$

(rather than the sum, as in Eq. 6.7) must be expressed as differences of form-factors $S^{i,j,k}$. The motion of the quasi-particle can generate 8 possible form-factors,

$$\begin{aligned}
& S(x + \Delta x, y + \Delta y, z + \Delta z), \\
& S(x, y + \Delta y, z + \Delta z), S(x + \Delta x, y, z + \Delta z), S(x + \Delta x, y + \Delta y, z), \\
& S(x, y, z + \Delta z), S(x, y + \Delta y, z), S(x + \Delta x, y, z), \\
& S(x, y, z),
\end{aligned} \tag{6.8}$$

so in general, the components of \mathbf{W} may be written as linear sums of these factors. \mathbf{W} may in fact be expressed as a unique linear combination of the functions above, if the following properties of \mathbf{W} are enforced ([Esirkepov, 2001](#)):

1. The sum of weights W_x, W_y, W_z is equal to the difference of form-factors (Eq. 6.7).
2. If the shift in any direction is zero, the corresponding weight is zero, i.e.

$$\Delta x = 0 \iff W_x = 0, \tag{6.9}$$

$$\Delta y = 0 \iff W_y = 0, \tag{6.10}$$

$$\Delta z = 0 \iff W_z = 0. \tag{6.11}$$

3. Symmetry with respect to permutation of coordinates:

$$S(x, y, z) = S(y, x, z) \text{ and } \Delta x = \Delta y \iff W_x = W_y, \tag{6.12}$$

$$S(x, y, z) = S(x, z, y) \text{ and } \Delta y = \Delta z \iff W_y = W_z, \tag{6.13}$$

$$S(x, y, z) = S(z, y, x) \text{ and } \Delta x = \Delta z \iff W_x = W_z. \tag{6.14}$$

Esirkepov was able to formulate and solve this problem. The unique solution for W_x, W_y, W_z

subject to the above constraints is ([Esirkepov, 2001](#)):

$$\begin{aligned}
W_x &= \frac{1}{3}S(x + \Delta x, y + \Delta y, z + \Delta z) - \frac{1}{3}S(x, y + \Delta y, z + \Delta z) \\
&\quad + \frac{1}{6}S(x + \Delta x, y, z + \Delta z) - \frac{1}{6}S(x, y, z + \Delta z) \\
&\quad + \frac{1}{6}S(x + \Delta x, y + \Delta y, z) - \frac{1}{6}S(x, y + \Delta y, z) \\
&\quad + \frac{1}{3}S(x + \Delta x, y, z) - \frac{1}{3}S(x, y, z),
\end{aligned} \tag{6.15}$$

$$\begin{aligned}
W_y &= \frac{1}{3}S(x + \Delta x, y + \Delta y, z + \Delta z) - \frac{1}{3}S(x + \Delta x, y, z + \Delta z) \\
&\quad + \frac{1}{6}S(x, y + \Delta y, z + \Delta z) - \frac{1}{6}S(x, y, z + \Delta z) \\
&\quad + \frac{1}{6}S(x + \Delta x, y + \Delta y, z) - \frac{1}{6}S(x + \Delta x, y, z) \\
&\quad + \frac{1}{3}S(x + \Delta x, y, z) - \frac{1}{3}S(x, y, z),
\end{aligned} \tag{6.16}$$

$$\begin{aligned}
W_z &= \frac{1}{3}S(x + \Delta x, y + \Delta y, z + \Delta z) - \frac{1}{3}S(x + \Delta x, y + \Delta y, z) \\
&\quad + \frac{1}{6}S(x, y + \Delta y, z + \Delta z) - \frac{1}{6}S(x, y + \Delta y, z) \\
&\quad + \frac{1}{6}S(x + \Delta x, y, z + \Delta z) - \frac{1}{6}S(x + \Delta x, y, z) \\
&\quad + \frac{1}{3}S(x, y, z + \Delta z) - \frac{1}{3}S(x, y, z).
\end{aligned} \tag{6.17}$$

In a two dimensional problem, Eqs. 6.15, 6.16, and 6.17 admit a simplified form ([Esirkepov, 2001](#)),

$$\begin{aligned}
W_x^{2D} &= \frac{1}{2}S^{2D}(x + \Delta x, y + \Delta y) - \frac{1}{2}S^{2D}(x, y + \Delta y) \\
&\quad + \frac{1}{2}S^{2D}(x + \Delta x, y) - \frac{1}{2}S^{2D}(x, y),
\end{aligned} \tag{6.18}$$

$$\begin{aligned}
W_y^{2D} &= \frac{1}{2}S^{2D}(x + \Delta x, y + \Delta y) - \frac{1}{2}S^{2D}(x + \Delta x, y, z + \Delta z) \\
&\quad + \frac{1}{2}S^{2D}(x, y + \Delta y) - \frac{1}{2}S^{2D}(x, y),
\end{aligned} \tag{6.19}$$

$$\begin{aligned}
W_z^{2D} &= \frac{1}{3}S^{2D}(x + \Delta x, y + \Delta y) + \frac{1}{6}S^{2D}(x, y + \Delta y) \\
&\quad + \frac{1}{6}S^{2D}(x + \Delta x, y) + \frac{1}{3}S^{2D}(x, y).
\end{aligned} \tag{6.20}$$

Note that in the 2D case, translational invariance in the z direction is assumed, so that $j_z^{i,j,k+1} - j_z^{i,j,k}$ vanishes. In this case, Eqs. 6.3, 6.4, and 6.5 reduce to

$$j_x^{i+1,j} = j_x^{i,j} - q \frac{\Delta_x}{\Delta_t} W_x^{(2D)i,j}, \quad (6.21)$$

$$j_y^{i,j+1} = j_y^{i,j} - q \frac{\Delta_y}{\Delta_t} W_y^{(2D)i,j}, \quad (6.22)$$

$$j_z^{i,j} = q v_z W_z^{(2D)i,j}, \quad (6.23)$$

where v_z is the velocity of the quasi-particle in the z direction. In the 2D case, current deposited in the z direction is computed as a weighted average of the charge flux, over the initial position (x, y) , two intermediate positions $(x + \Delta x, y)$ and $(x, y + \Delta y)$, and the final position $(x + \Delta x, y + \Delta y)$; see Eq. 6.20. Additional details of the derivation are provided in Appendix 6.A.

One advantage of the Esirkepov scheme is that it allows for the straightforward implementation of different particle form-factors, which enter through the definition of weights, Eqs. 6.15, 6.16, and 6.17 (or in 2D, Eqs. 6.18, 6.19, and 6.20). In particular, higher-order shape functions may be implemented with ease, which is suggested as a method of controlling numerical heating in PIC simulations ([Shalaby et al., 2017](#)).

In the remaining sections, we investigate the effect of higher-order shape functions in a few test problems, and compare to another commonly used charge-conserving method of current deposition, the zigzag scheme ([Umeda et al., 2003](#)). To study the higher-order form-factors and compare with the zigzag algorithm, we use an implementation of the Esirkepov density decomposition in the electromagnetic PIC code **TRISTAN-MP** ([Buneman et al., 1993; Spitkovsky, 2005](#)). Details of the implementation are included in App. C.

We focus on shape functions of order 1, 2, and 3, which are defined as follows.¹ Starting with

¹These definitions are for 1D shape functions. Note that the form-factors in Eqs. 6.18, 6.19, 6.20, 6.15, 6.16, and 6.17 are 2D and 3D shape functions. The relation between 1D and 2D is: $S^{2D}(x, y) = S^{1D}(x)S^{1D}(y)$,

the zeroth-order shape function,

$$S^0(x) = \begin{cases} 1 & \text{if } |x| < \frac{1}{2}, \\ 0 & \text{otherwise,} \end{cases} \quad (6.24)$$

shape functions of higher order are defined via recursion:

$$S^{n+1}(x) = \int S^0(x - y) S^n(y) dy. \quad (6.25)$$

The first few shape functions have the explicit forms

$$S^1(x) = \begin{cases} x + 1 & \text{if } -1 < x \leq 0, \\ 1 - x & \text{if } 0 < x < 1, \\ 0 & \text{otherwise,} \end{cases} \quad (6.26)$$

$$S^2(x) = \begin{cases} \frac{1}{8}(2x + 3)^2 & \text{if } -\frac{3}{2} < x \leq -\frac{1}{2}, \\ \frac{3}{4} - x^2 & \text{if } -\frac{1}{2} < x \leq \frac{1}{2}, \\ \frac{1}{8}(3 - 2x)^2 & \text{if } \frac{1}{2} < x < \frac{3}{2}, \\ 0 & \text{otherwise.} \end{cases} \quad (6.27)$$

for example (and similarly for 3D).

$$S^3(x) = \begin{cases} \frac{1}{6}(x+2)^3 & \text{if } -2 < x \leq -1, \\ \frac{1}{6}(4 - 3x^2(x+2)) & \text{if } -1 < x \leq 0, \\ \frac{1}{6}(3(x-2)x^2 + 4) & \text{if } 0 < x < 1, \\ -\frac{1}{6}(x-2)^3 & \text{if } 1 \leq x < 2, \\ 0 & \text{otherwise.} \end{cases} \quad (6.28)$$

The shape functions Eqs. 6.24, 6.26, 6.27, and 6.28 are plotted in Fig. 6.1.

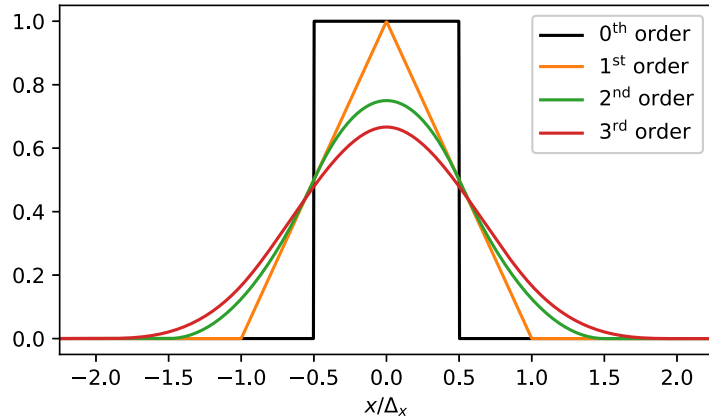


Figure 6.1: Particle form-factors of order 0, 1, 2, and 3.

6.3 Tests

In this section, we present a few test cases (heating and energy non-conservation in a single-temperature plasma; filamentation instability; numerical Cherenkov instability) to demonstrate the effect of higher-order shape functions in an electromagnetic PIC code. In each test problem, we compare the zigzag current deposit scheme, as well as the Esirkepov density decomposition scheme for 1st, 2nd, and 3rd order shape functions. We note that the zigzag scheme of Umeda et. al, which assumes a 1st order particle shape function, still differs from the 1st order Esirkepov density decomposition scheme in the assumed motion of the particle (Umeda et al., 2003). In the zigzag method,

particles may travel along trajectories that resemble a zigzag pattern, whereas in the Esirkepov density decomposition, particle trajectories are treated as straight lines.

For all of the test problems presented here, the initial magnetic field is zero.

6.3.1 Numerical heating in a uniform plasma

Here, we investigate the effect of different current deposit schemes on numerical heating in a uniform plasma initialized at rest. The ion and electron masses are equal, $m = m_i = m_e$, and the plasma is single-temperature, $T_i = T_e = T$. Each simulation is initialized with a different choice of dimensionless temperature,

$$\theta = \frac{k_B T}{mc^2}. \quad (6.29)$$

To avoid severe heating associated with the Finite Grid instability, we study plasmas with temperature less than the numerical Debye temperature, $\theta < \theta_D$ ([Birdsall & Maron, 1980](#); [Birdsall & Langdon, 1991](#)); this is the temperature at which the Debye length

$$\lambda_D = \sqrt{\frac{k_B T}{4\pi n_0 e^2}} \quad (6.30)$$

is equal to the grid spacing, $\Delta_x = \Delta_y = \Delta_z = \Delta$; here, n_0 is number density and e is electric charge. With $\lambda_D = \Delta$, the dimensionless Debye temperature can be written

$$\theta_D = \left(\frac{\Delta}{c/\omega_p} \right)^2, \quad (6.31)$$

where c/ω_p is the plasma skin depth, and the plasma frequency is

$$\omega_p = \sqrt{\frac{4\pi n_0 e^2}{m}}. \quad (6.32)$$

The violent numerical heating associated with the Finite Grid Instability is strongest at $\theta = \theta_D$, and its effect is mitigated at temperatures above or below θ_D (Birdsall & Maron, 1980). In the simulations presented here, we use 10 cells per electron skin depth, so that the numerical Debye temperature is $\theta_D = 10^{-2}$. We study numerical heating in plasmas with initial dimensionless temperatures $\theta_0 = 10^{-5}, 10^{-4}$, and 10^{-3} . Plasma with temperature θ is initialized according to a Maxwell-Jüttner distribution,

$$f_{\text{MJ}}(\gamma, \theta) \propto \gamma(\gamma^2 - 1)^{\frac{d}{2}-1} \exp(-\gamma/\theta), \quad (6.33)$$

where γ is the particle Lorentz factor and d is the number of dimensions; for the simulations in this section, $d = 3$. The plasma is initialized in a box of dimension $L_x = 15 c/\omega_p, L_y = 30 c/\omega_p, L_z = 15 c/\omega_p$. The simulation domain is periodic in x, y , and z . The number of particles per cell is $N_{\text{ppc}} = 64$.

In Fig. 6.2, we demonstrate the effect of different current deposit schemes on numerical heating in a uniform plasma. Columns 1, 2, 3, and 4 correspond to zigzag, 1st order, 2nd order, and 3rd order density decomposition, respectively. Panels (a) – (d) show the evolution of dimensionless temperature θ as a function of dimensionless time, $t\omega_p$. Panels (e) – (h) show the fractional error in mean particle Lorentz factor relative to the initial mean value $\langle \gamma_0 \rangle - 1$, i.e. $(\langle \gamma \rangle - \langle \gamma_0 \rangle)/(\langle \gamma_0 \rangle - 1)$; here, $\gamma_0 \equiv 1 + \theta_0/(\Gamma_{\text{ad}}(\theta_0) - 1)$, where the adiabatic index Γ_{ad} is a function of dimensionless temperature θ .

In an ideal simulation, the fractional error should remain zero, but due to numerical heating, the fractional error increases. The zigzag scheme and 1st order density decomposition have similar values for the fractional error over the runtime of the simulations (which is roughly $t\omega_p = 8 \times 10^3$). By using a higher-order particle shape, as in panels (g) and (h), the fractional error induced by

numerical heating is decreased; for example, with a 3rd order shape function, the fractional error is reduced by about 1.5 orders of magnitude, relative to zigzag or 1st order density decomposition.

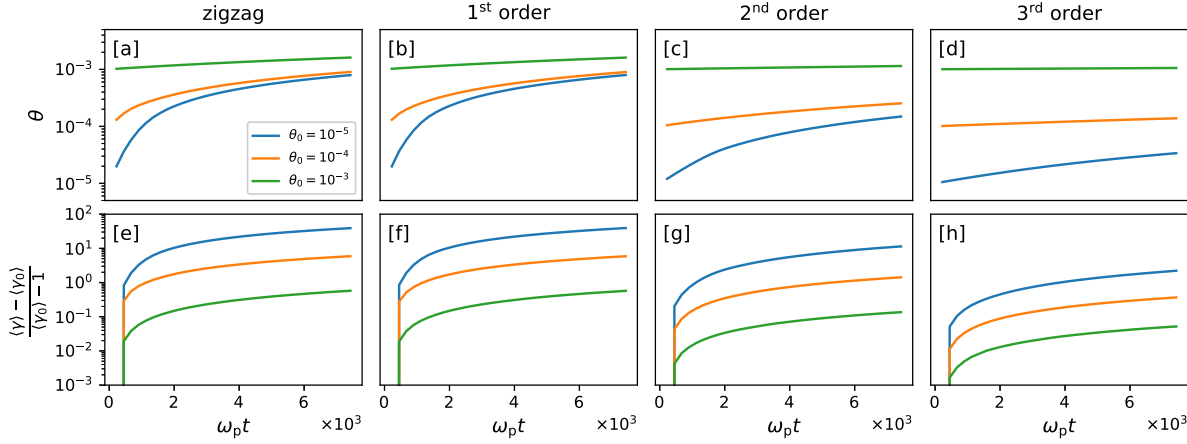


Figure 6.2: ((a) – (d)) Evolution of dimensionless temperature and ((e) – (h)) fractional error in a uniform plasma with initial dimensionless temperatures $\theta_0 = 10^{-5}, 10^{-4}$, and 10^{-3} , for zigzag, 1st, 2nd, and 3rd order Esirkepov (columns 1 – 4, respectively). The simulations presented here are in full 3D.

Numerical heating in the 2D case is similar to that of the 3D case discussed here; see Appendix 6.B.

An alternate method that allows for improved control of numerical heating is the application of a filter to smooth the charge and current densities (Buneman et al., 1993; Spitkovsky, 2005). One such implementation is to, at each timestep and in each direction, redistribute the value of the current density at a grid point into neighboring cells, according to prescribed weights; a commonly used choice of weights is 1-2-1. By repeated application of such a filter, the current density is smoothed, which improves energy conservation in the PIC simulation.

How does the effect of such a filter on numerical heating compare with that of a higher-order shape function? We can get a rough idea by repeated convolution of a 1-2-1 filter on a square-shaped quasi-particle of width Δ , equal to the grid spacing; we consider applying the filter a total number of times n_{times} . After each application of the filter, the width of the particle at half maximum can be measured, yielding a correspondence between n_{times} and the particle full width at

half maximum (fwhm). Alternatively, based on the definition of particle shape function Eqs. 6.24, 6.25, the fwhm can be computed as a function of the order of the particle shape. To demonstrate the rough correspondence between n_{times} and order of shape function, with respect to the effective fwhm of the quasi-particle, we show in Fig. 6.3 (b) a plot of n_{times} vs. fwhm and order vs. fwhm. The fwhm scales roughly as the square root of n_{times} , $\text{fwhm}/\Delta \propto n_{\text{times}}^{0.49}$, and the scaling with order of the particle shape is slightly weaker, $\text{fwhm}/\Delta \propto \text{order}^{0.47}$. This comparison shows that repeated convolution of a 1-2-1 filter and higher-order shape functions both increase the effective fwhm of the quasi-particle, so both methods should result in improved control of numerical heating.

While intuitive, this comparison is a simplified picture of the two methods, and cannot capture the full details of a PIC simulation. To demonstrate a more robust comparison of the filter smoothing and higher-order shape function, we show in Fig. 6.3 (a) the time evolution of fractional error in a plasma with initial temperature $\theta_0 = 10^{-4}$, for simulations with 1st order shape function and $n_{\text{times}} = 1, 3, 5$, and a simulation with a 3rd order shape function, but $n_{\text{times}} = 0$. In this case, we find a close equivalence, in terms of evolution of fractional error, for the simulation with a 1st order shape function, $n_{\text{times}} = 5$, and 3rd order shape function, $n_{\text{times}} = 0$. With respect to fractional error, the scalings shown in Fig. 6.3 (b) predict an equivalence between a 3rd order shape function, and $n_{\text{times}} \approx 2$, which differs from the empirically measured equivalence between 3rd order shape, and $n_{\text{times}} \approx 5$, shown in panel (a); the simplified picture which leads to the scalings $\text{fwhm}/\Delta \propto n_{\text{times}}^{0.49}$ and $\text{fwhm}/\Delta \propto \text{order}^{0.47}$ is probably insufficient to capture the full details of the PIC implementation.

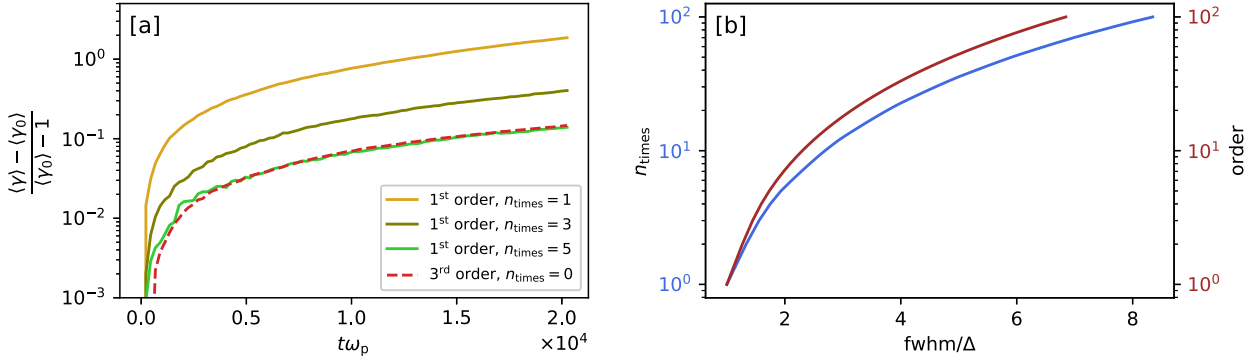


Figure 6.3: (a) For 2D simulations with $\theta_0 = 10^{-4}$, comparison of fractional error for 1st order form-factor and $n_{\text{times}} = 1, 3, 5$ (solid lines) vs. 3rd order shape and $n_{\text{times}} = 0$ (dashed); (b) n_{times} vs. effective fwhm (blue) and order of particle shape vs. effective fwhm (dark red).

6.3.2 Filamentation instability

For the next test, we consider a counterstreaming beam. The beam is aligned with the x direction. We choose equal densities for the beam and background plasma, and consider two cases, one where the beam Lorentz factor γ_b is nonrelativistic ($v_b/c = 0.5 \rightarrow \gamma_b \approx 1.15$), and a second with a relativistic beam ($v_b/c = 0.95 \rightarrow \gamma_b \approx 3.20$). Given the initial anisotropy of this setup, plasma instabilities will grow to drive the particle distribution function towards isotropy. Here, we consider the growth of the perpendicular mode, known as the filamentation instability, which is the fastest growing mode for symmetric beams. It has a maximum growth rate (Bret, 2012)

$$\delta_{\max, \text{th}} = \frac{v_b}{c} \omega_p, \quad (6.34)$$

where ω_p is the plasma frequency, with mass rescaled by γ_b , $\omega_p = \sqrt{4\pi n_0 e^2 / (\gamma_b m)}$, and n_0 is the total number density of positrons and electrons.

For the 3D simulations presented here, we use a periodic box whose dimensions are $L_x = L_y = L_z = 12.6 c/\omega_p$, with $c/\omega_p = 10$ cells. In the nonrelativistic case, the box length is about equal to the wavelength of the unstable mode; however, we have checked that our results agree with those

obtained with a box that is three times as large in the perpendicular (z) direction. The initial dimensionless temperature of the plasma is $\theta_0 = 2 \times 10^{-5}$, and we use $N_{\text{ppc}} = 64$ particles per cell. For 2D simulations, we use the same choice of numerical parameters, except for the box size which is $L_x = L_y = 12.8 c/\omega_p$.

In Fig. 6.4, we show evolution of (2 \times)perpendicular magnetic energy $\langle |B_z|^2 \rangle / (4\pi nmc^2)$, where angle brackets denote a spatial average over the simulation domain, which is 3D. Panels (a) and (b) show the growth rates for the nonrelativistic and relativistic cases, respectively. The measured growth rate is presented for zigzag, as well as Esirkepov's scheme with 1st, 2nd, and 3rd order shape functions. The measured growth rates are compared with the analytical growth rate, Eq. 6.34. In the relativistic case, the different current deposit schemes show acceptable agreement with the predicted maximum growth rate of the unstable mode. In the nonrelativistic case, the density decomposition with 2nd and 3rd order shape functions show reasonable agreement with the analytical prediction, however, the zigzag and density decomposition with 1st order shape function do not show a close agreement to the prediction. In these cases, however, the agreement improves with increased number of particles per cell N_{ppc} , which is another way to control numerical heating, apart from the filtering and higher-order shape functions discussed in Section 6.3.1. For the zigzag scheme, we find improved agreement with the analytical prediction when the number of particles per cell is increased; we have tested with $N_{\text{ppc}} = 512$. The disagreement between the analytical prediction, as compared to zigzag and 1st order density decomposition, is likely linked to numerical heating at early times which distorts the measured growth rate, rather than an intrinsic limitation of 1st order shape functions in capturing the physics of the filamentation instability. The agreement between the analytically predicted maximum growth rate (Eq. 6.34) and the measured growth rates in Fig. 6.4 supports that our implementation of the Esirkepov scheme is valid, as it correctly captures the physics necessary to model the filamentation instability.

In Figs. 6.5 and 6.6, we show spatial profiles of $(2\times)$ magnetic energy, B_z , and density normalized to initial density n_0 , for 2D simulations with nonrelativistic and relativistic beams, respectively. The first, second, third, and fourth columns correspond to different schemes for current deposition: zigzag, 1st, 2nd, and 3rd order density decomposition. In each figure, the spatial profiles are shown close to the saturation of the instability; for the nonrelativistic case, this is around $t\omega_p \approx 22.73$, and for the relativistic case, $t\omega_p \approx 16.88$. In each case, nonrelativistic and relativistic, the four simulations start with the same initial conditions, so any slight differences in the spatial profiles are caused by the different current deposition algorithms employed in each of the four cases.

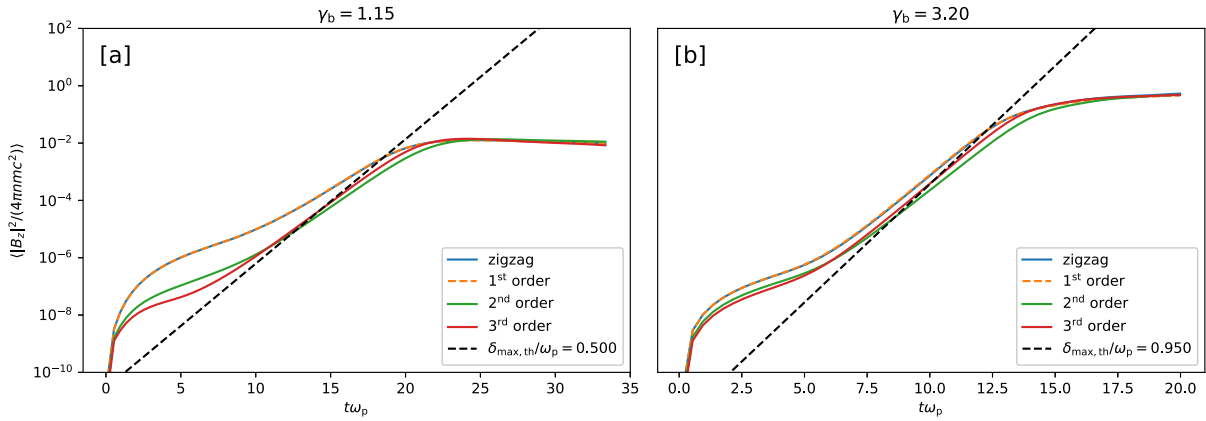


Figure 6.4: Time evolution of perpendicular magnetic energy for (a) nonrelativistic and (b) relativistic counterstreaming beam, for zigzag, 1st, 2nd, and 3rd order Esirkepov. Solid lines show the measured growth rates, and dashed lines show the analytical prediction (see Eq. 6.34). The simulations here are 3D.

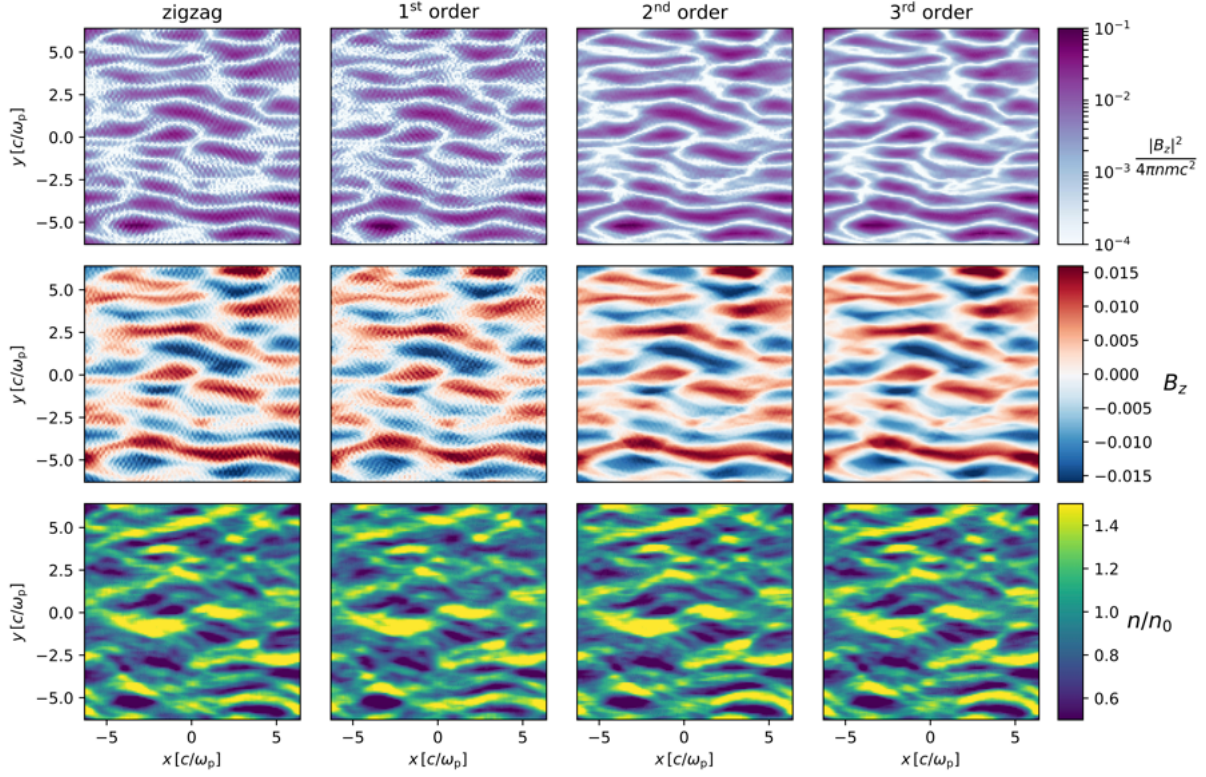


Figure 6.5: For the nonrelativistic counterstreaming setup ($\gamma_b \approx 1.15$): 2D spatial profiles of magnetic energy (first row), z component of magnetic field (second row), and density in units of initial density (third row), for 1st, 2nd, and 3rd order Esirkepov (columns 1 – 4). The spatial profiles are from 2D simulations at $t\omega_p \approx 22.73$, which is near saturation of the growth of the unstable mode. The spatial profiles shown here are from 2D simulations.

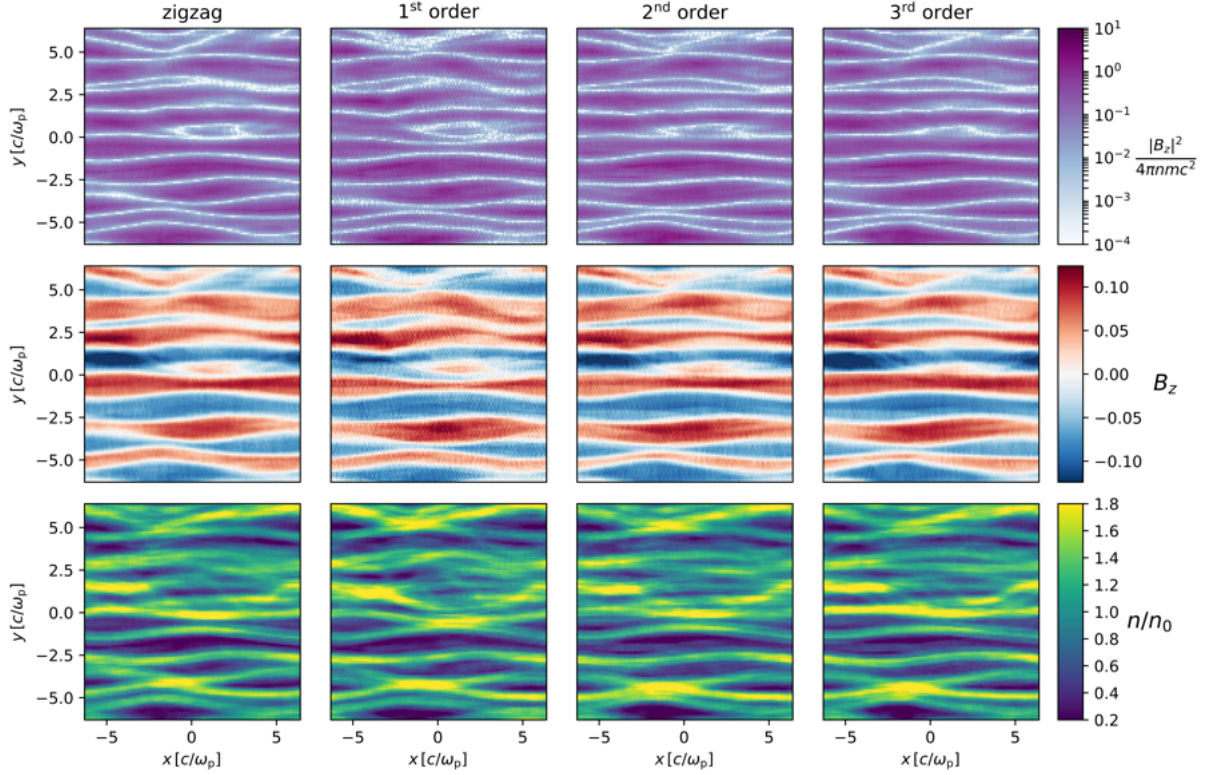


Figure 6.6: Similar to Fig. 6.5, but for the relativistic counterstreaming setup ($\gamma_b \approx 3.20$): 2D spatial profiles of magnetic energy (first row), z component of magnetic field (second row), and density in units of initial density (third row), for 1st, 2nd, and 3rd order Esirkepov (columns 1 – 4). The spatial profiles are from 2D simulations at $t\omega_p \approx 16.88$, which is near saturation of the growth of the unstable mode. The spatial profiles shown here are again from 2D simulations.

6.3.3 Numerical Cherenkov instability

Numerical dispersion in relativistic plasma flows generates a nonphysical numerical instability, known as the numerical Cherenkov instability (Godfrey, 1974). Here, we investigate the effect of different current deposition schemes on the growth of the numerical Cherenkov instability. The simulations presented here are similar to the 2D simulations described in Section 6.3.2, however we use a single beam streaming in the $+x$ direction, with Lorentz factor $\gamma_b \approx 22.37$, and $N_{ppc} = 16$. Again, the plasma is electron-positron with initial dimensionless temperature $\theta_0 = 2 \times 10^{-5}$.

In Fig. 6.7, we show the growth of $(2\times)$ perpendicular magnetic energy $\langle |B_z|^2 \rangle / (4\pi nmc^2)$, for the current deposit schemes zigzag, 1st, 2nd, and 3rd order Esirkepov. The growth of the instability

is shown with respect to dimensionless time $t\omega_p$, with the plasma frequency defined as in Section 6.3.2. The solid lines show the measured growth of the instability, whereas dashed lines show fits proportional to $\exp(\delta_{\max}t)$, used to extract the maximum growth rate in each case. The growth rate of the instability is reduced by use of higher-order shape functions; the maximum growth rate for the simulation which uses a 3rd order form-factor is a factor of two smaller than in the 1st order Esirkepov simulation. Compared to the simulation with zigzag current deposit, the simulation which uses a 3rd order form-factor has a maximum growth rate that is a factor of four smaller.

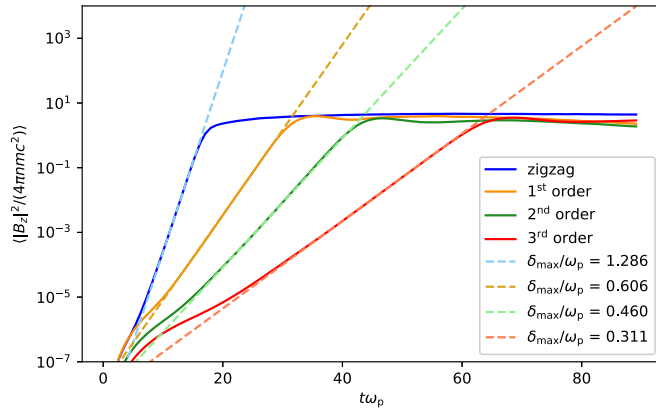


Figure 6.7: Time evolution of perpendicular magnetic energy for zigzag, 1st, 2nd, and 3rd order Esirkepov (solid lines), and measured maximum growth rates (dashed). These simulations are 2D.

In Fig. 6.8, we show the \mathbf{k} -space profiles of the Fourier power spectrum $|\tilde{B}_z(k_x c/\omega_p, k_y c/\omega_p)|^2$, in the first row, and the spatial profile of density, in units of initial density, in the second row. Columns 1–4 correspond to zigzag, 1st, 2nd, and 3rd order Esirkepov schemes. For each current deposit scheme, the spatial profiles are shown at a snapshot in time near the end of the exponential growth phase of the numerical Cherenkov instability ($t\omega_p \approx 20, 40, 50$, and 70 for zigzag, 1st, 2nd, and 3rd order Esirkepov, respectively; see Fig. 6.7). The density plots show a streak pattern that is characteristic of the numerical Cherenkov instability. Profiles of the Fourier power spectrum also show a signature of the excited Cherenkov modes. The unstable wave numbers are regulated by

the equation (Ikeya & Matsumoto, 2015)

$$k_y \Delta_y = 2 \arcsin \left[\pm \frac{\Delta_y}{c \Delta_t} \sqrt{\tan^2 \left(\frac{\beta_b k_x c \Delta_t}{2} \right)} - \left(c \frac{\Delta_t}{\Delta_x} \sin \left(\frac{k_y \Delta_y}{2} \right) \right)^2 \right], \quad (6.35)$$

where Δ_t is the simulation timestep and $\beta_b = v_b/c$, the dimensionless velocity of the beam. In our simulations, $\Delta_x = \Delta_y$. The locus of wavenumbers k_x, k_y satisfying the condition Eq. 6.35 is shown by dashed red curves in the first row of Fig. 6.8. The agreement between wavenumbers predicted to be unstable due to the numerical Cherenkov instability (Eq. 6.35) and the distribution of Fourier power in \mathbf{k} -space, shown in the first row of Fig. 6.8, demonstrates that the density waves present in the second row of Fig. 6.8 indeed correspond to numerical Cherenkov modes.

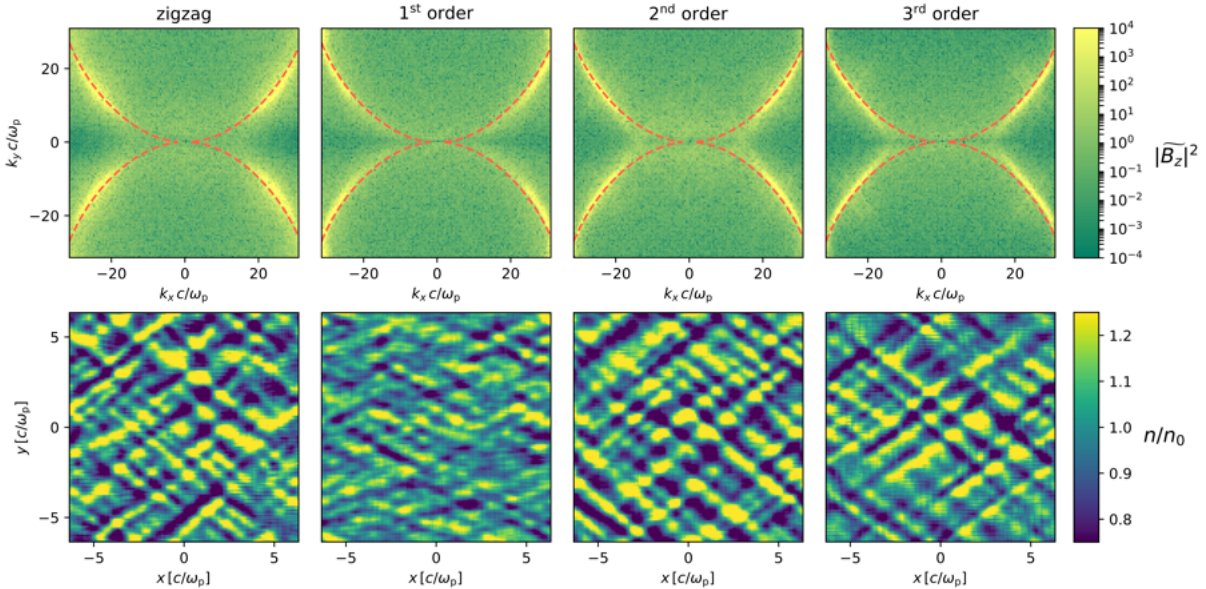


Figure 6.8: For a 2D, relativistic single beam simulation ($\gamma_b \approx 22.7$): \mathbf{k} -space profiles of the Fourier power spectrum $|\tilde{B}_z(k_x c/\omega_p, k_y c/\omega_p)|^2$ (first row), and spatial profiles of density in units of initial density (second row), for zigzag, 1st, 2nd, and 3rd order Esirkepov (columns 1 – 4). Dashed red lines in the first row show k_x, k_y satisfying Eq. 6.35. For each case, the \mathbf{k} -space and spatial profiles are shown near saturation of the Numerical Cherenkov instability; the simulations here are the same as those shown in Fig. 6.7.

6.4 Performance

In this section, we compare the performance of our implementation of zigzag, 1st, 2nd, and 3rd order density decomposition for the current deposit step of the PIC loop.

In Fig. 6.9, we show the average CPU time per step for the current deposit as a function of N_{ppc} , for 2D and 3D (panels (a) and (b), respectively). The zigzag and 1st order Esirkepov schemes show similar performance in 2D, but the zigzag implementation is fastest in 3D, by roughly a factor of 6.5 for the current deposit, and 3.2 for the particle push. For 3D, the average time of the current deposit step, when using a 3rd order shape function, is nearly an order of magnitude larger than the time required by zigzag. The number of operations needed during the current deposit step, when using the Esirkepov method, scales with both the number of particles and the number of array elements over which the 1D particle shape has support (we can call the latter $N_{\text{shape}}^{\text{1D}}$). The average CPU time should scale roughly as $(N_{\text{ppc}} \times N_{\text{shape}}^{\text{1D}})^2$ in 2D, and $(N_{\text{ppc}} \times N_{\text{shape}}^{\text{1D}})^3$ in 3D. The dependence on the dimension of the simulation at least partly explains why, for fixed N_{ppc} , the difference in CPU time between the 3rd and 1st order schemes is greater in 3D than in 2D (see by comparing panels (a) and (b)).

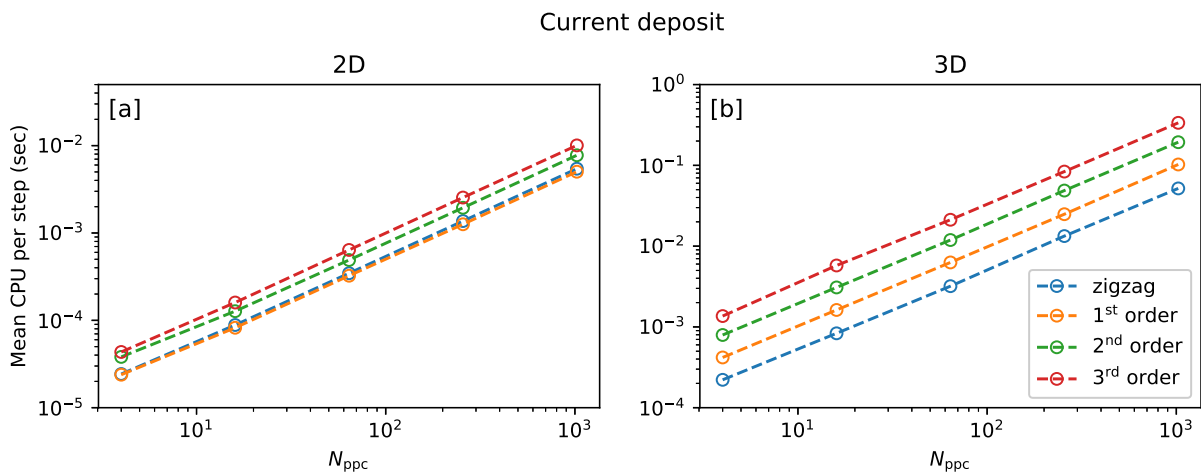


Figure 6.9: For current deposit, the mean CPU time per step, as a function of particles per cell for (a) 2D and (b) 3D.

Fig. 6.10 is similar to Fig. 6.9, but here we compare the performance of the particle pusher for the different implementations. The performance of each scheme can differ, depending on how the electromagnetic fields are interpolated to the location of a particle. For zigzag, we compute field values via a linear interpolation from Yee (1966) lattice points (see Fig. 6.11) to gridpoints, then gridpoints to particle location; the procedure is described in detail in Cai et al. (2003).

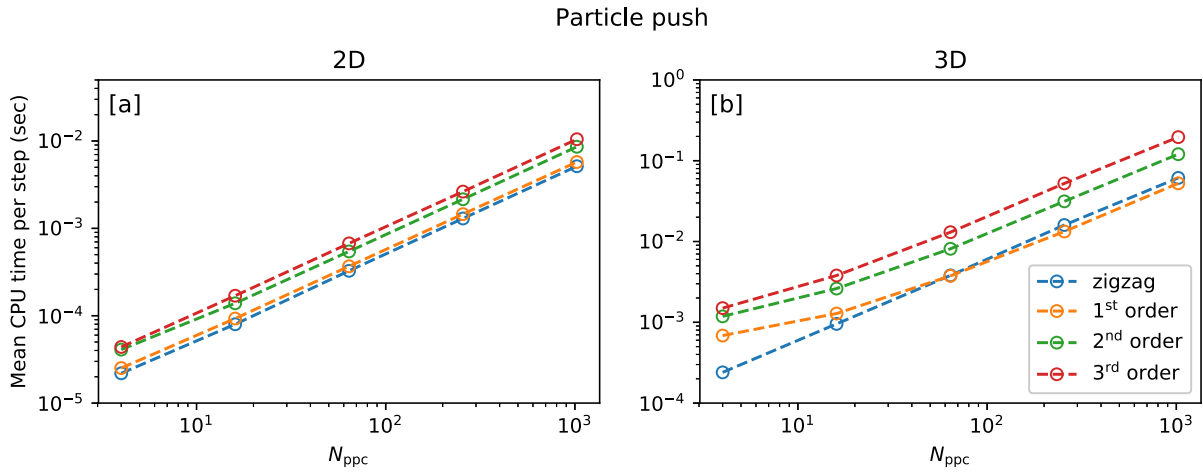


Figure 6.10: For particle push, the mean CPU time per step, as a function of particles per cell for (a) 2D and (b) 3D. This is similar to Fig. 6.9.

For the 1st, 2nd, and 3rd order schemes, the field value at a particle location $F(x, y, z)$ is computed as a sum over the product of the particle shape and field, over cells where the form-factor is nonzero:²

$$F(x, y, z) = \sum_{n|S^{3D}(i_n, j_n, k_n) \neq 0} F(i_n, j_n, k_n) S_x^{1D}(i_n) S_y^{1D}(j_n) S_z^{1D}(k_n). \quad (6.36)$$

Here, i_n , j_n , and k_n denote the cell location. The fields at location $F(i_n, j_n, k_n)$ can be computed via linear interpolation of the fields defined on the Yee (1966) lattice. As an example, consider the case $F = E_x$; on the Yee lattice, the x component of the electric field is defined at points staggered (with respect to the primal grid) by half a cell, $(i_n + \Delta/2, j_n, k_n)$. To interpolate from

²The field interpolation in 2D is analogous; homogeneity is assumed in the z direction, so $F(x, y, z) = F(x, y) = \sum_{n|S^{2D}(i_n, j_n) \neq 0} F(i_n, j_n) S_x^{1D}(i_n) S_y^{1D}(j_n)$.

Yee lattice gridpoints to midpoints (thereby obtaining the first term on the righthand side of Eq. 6.36), $E_x(i_n, j_n, k_n)$ is computed from two surrounding points as

$$E_x(i_n, j_n, k_n) = \frac{1}{2} [E_x(i_n + \Delta/2, j_n, k_n) + E_x(i_n - \Delta/2, j_n, k_n)], \quad (6.37)$$

and the other EM field components are computed similarly. With the EM fields computed at the same grid points over which the particle shape function is defined, Eq. 6.36 yields the field components at the particle location, and allows for calculation of the force on a particle.

From Eq. 6.36, the particle push step depends on $(N^{1D})^3$ in 3D, and is also proportional to $(N_{ppc})^3$, so the required time should scale as $(N_{ppc} \times N_{shape}^{1D})^3$ (or in 2D, $(N_{ppc} \times N_{shape}^{1D})^2$), as in the current deposit step. Comparing panels (a) in Figs. 6.9 and 6.10, and also panels (b), the current deposit and particle push steps show similar scalings with N_{ppc} , for each scheme. The current deposit and particle push steps in 3D show some differences for zigzag and 1st order density decomposition.

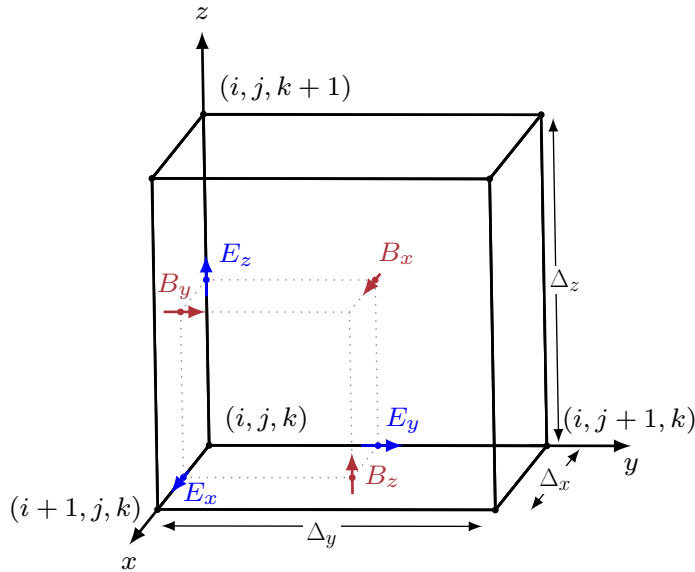


Figure 6.11: Diagram of Yee lattice. E_x, E_y , and E_z are defined at edge midpoints; B_x, B_y , and B_z are defined at face centers.

6.5 Summary

In this chapter, we investigated the use of higher-order shape functions in PIC simulations, by use of the Esirkepov density decomposition scheme for current deposition, and compared with the zigzag scheme. We show that higher-order shape functions offer increased control with respect to numerical heating, and that a smoothing filter can offer similar improvements. We demonstrate the correctness of our implementation by comparing the analytical growth rate of the filamentation instability to the measured growth rate in simulations. For a relativistic plasma, we demonstrate that the use of higher-order shape functions offers some reduction in the growth rate of the numerical Cherenkov instability. Last, we assess the performance of our implementation of the Esirkepov density decomposition scheme, and compare with zigzag, for the current deposit and particle push steps of the PIC loop, in both 2D and 3D; the 1st order density decomposition shows similar performance to zigzag for the current deposit and particle push steps in 2D; in 3D, zigzag current deposit is fastest, and at low N_{ppc} , its associated particle push implementation is faster than that of the 1st order Esirkepov scheme.

6.A Esirkepov coefficients

Here, we elaborate on the derivation of numerical coefficients which relate densities W_x , W_y , and W_z to form-factors (i.e., the coefficients in Eqs. 6.15, 6.16, and 6.17). To shorten notation, define a vector of the possible form-factors generated by particle motion in 3D on a Cartesian grid, Eq. 6.8,

$$\begin{aligned} \mathbf{v} = & [S(x + \Delta x, y + \Delta y, z + \Delta z), \\ & S(x, y + \Delta y, z + \Delta z), S(x + \Delta x, y, z + \Delta z), S(x + \Delta x, y + \Delta y, z), \\ & S(x, y, z + \Delta z), S(x, y + \Delta y, z)S(x + \Delta x, y, z), \\ & S(x, y, z)]. \end{aligned} \tag{6.38}$$

We assume that the densities W_x , W_y , and W_z are linear combinations of the functions Eq. 6.8,

$$W_x(x, y, z, \Delta x, \Delta y, \Delta z) = \sum_{i=1}^8 a^i v^i, \quad (6.39)$$

$$W_y(x, y, z, \Delta x, \Delta y, \Delta z) = \sum_{i=1}^8 b^i v^i, \quad (6.40)$$

$$W_z(x, y, z, \Delta x, \Delta y, \Delta z) = \sum_{i=1}^8 c^i v^i. \quad (6.41)$$

Here, we consider the weights to have six arguments, corresponding to the particle position (x, y, z) for the first three, and the shift $(\Delta x, \Delta y, \Delta z)$ for the last three; with this notation,

$$W_x(x + \Delta x, y, z) \equiv W_x(x, y, z, \Delta x, 0, 0), \quad (6.42)$$

for example. Our task is to determine the coefficients a^i, b^i, c^i , subject to the constraints (1, 2, and 3) on \mathbf{W} listed in Section 6.2. We translate the three constraints into a system of equations which uniquely determines the 24 coefficients a^i, b^i , and c^i .

The first constraint we consider, item 1, can be understood as enforcing that the weights W_x , W_y , and W_z satisfy the continuity equation (Eq. 6.2). Inserting the definitions 6.39, 6.40, and 6.41 into Eq. 6.7, we obtain

$$\sum_{i=1}^8 (a^i + b^i + c^i) v^i = S(x + \Delta x, y + \Delta y, z + \Delta z) - S(x, y, z). \quad (6.43)$$

The next property of \mathbf{W} , item 2, ensures that if the particle shift in a direction is zero, then no current is deposited along that direction. This allows us to set Δx , Δy , and Δz each to zero in Eq.

6.43 to get three sets of constraints,

$$W_x(x, y, z, \Delta x, \Delta y, 0) + W_y(x, y, z, \Delta x, \Delta y, 0) = S(x + \Delta x, y + \Delta y, z) - S(x, y, z), \quad (6.44)$$

$$W_x(x, y, z, \Delta x, 0, \Delta z) + W_z(x, y, z, \Delta x, 0, \Delta z) = S(x + \Delta x, y, z + \Delta z) - S(x, y, z), \quad (6.45)$$

$$W_y(x, y, z, 0, \Delta y, \Delta z) + W_z(x, y, z, 0, \Delta x, \Delta z) = S(x, y + \Delta y, z + \Delta z) - S(x, y, z), \quad (6.46)$$

or

$$\sum_{i=1}^8 a^i v^i|_{\Delta z=0} + \sum_{i=1}^8 b^i v^i|_{\Delta z=0} = S(x + \Delta x, y + \Delta y, z) - S(x, y, z), \quad (6.47)$$

$$\sum_{i=1}^8 a^i v^i|_{\Delta y=0} + \sum_{i=1}^8 c^i v^i|_{\Delta y=0} = S(x + \Delta x, y, z + \Delta z) - S(x, y, z), \quad (6.48)$$

$$\sum_{i=1}^8 b^i v^i|_{\Delta x=0} + \sum_{i=1}^8 c^i v^i|_{\Delta x=0} = S(x, y + \Delta y, z + \Delta z) - S(x, y, z). \quad (6.49)$$

Additionally, we have

$$W_x(x, y, z, \Delta x, \Delta y, 0) = 0, \quad (6.50)$$

$$W_x(x, y, z, \Delta x, 0, \Delta z) = 0, \quad (6.51)$$

$$W_y(x, y, z, 0, \Delta y, \Delta z) = 0, \quad (6.52)$$

which yields 12 constraints,

$$a^1 = -a^2, a^3 = -a^4, a^5 = -a^6, a^7 = -a^8, \quad (6.53)$$

$$b^1 = -b^2, b^3 = -b^4, b^5 = -b^6, b^7 = -b^8, \quad (6.54)$$

$$c^1 = -c^2, c^3 = -c^4, c^5 = -c^6, c^7 = -c^8. \quad (6.55)$$

Lastly, we consider the symmetry constraint, item 3. Suppose that the form-factors are invariant with respect to permutation of coordinates, and shifts are identical: $\Delta x = \Delta y = \Delta z = \Delta$. Then, for example, $S(x, y + \Delta, z) = S(y + \Delta, x, z)$. Moreover, invariance with respect to permutations of (x, y) , (y, z) , and (x, z) yield, respectively, the equations

$$W_x(x, y, z, \Delta, \Delta, \Delta) - W_y(x, y, z, \Delta, \Delta, \Delta) = 0, \quad (6.56)$$

$$W_y(x, y, z, \Delta, \Delta, \Delta) - W_z(x, y, z, \Delta, \Delta, \Delta) = 0, \quad (6.57)$$

$$W_x(x, y, z, \Delta, \Delta, \Delta) - W_z(x, y, z, \Delta, \Delta, \Delta) = 0, \quad (6.58)$$

or, inserting Eqs. 6.39, 6.40, and 6.41,

$$\begin{aligned} & (a^1 - b^1)S(x + \Delta, y + \Delta, z + \Delta) + (a^2 - b^3)S(x, y + \Delta, z + \Delta) \\ & + (a^3 - b^2)S(x + \Delta, y, z + \Delta) + (a^4 - b^4)S(x, y, z + \Delta) \\ & + (a^5 - b^5)S(x + \Delta, y + \Delta, z) + (a^6 - b^7)S(x, y + \Delta, z) \\ & + (a^7 - b^6)S(x + \Delta, y, z) + (a^8 - b^8)S(x, y, z) = 0, \end{aligned} \quad (6.59)$$

$$\begin{aligned} & (b^1 - c^1)S(x + \Delta, y + \Delta, z + \Delta) + (b^2 - c^5)S(x + \Delta, y, z + \Delta) \\ & + (b^3 - c^3)S(x, y + \Delta, z + \Delta) + (b^4 - c^7)S(x, y, z + \Delta) \\ & + (b^5 - c^2)S(x + \Delta, y + \Delta, z) + (b^6 - c^6)S(x + \Delta, y, z) \\ & + (b^7 - c^4)S(x, y + \Delta, z) + (b^8 - c^8)S(x, y, z) = 0, \end{aligned} \quad (6.60)$$

$$\begin{aligned}
& (a^1 - c^1)S(x + \Delta, y + \Delta, z + \Delta) + (a^2 - c^3)S(x, y + \Delta, z + \Delta) \\
& + (a^3 - c^5)S(x + \Delta, y, z + \Delta) + (a^4 - c^7)S(x, y, z + \Delta) \\
& + (a^5 - c^2)S(x + \Delta, y + \Delta, z) + (a^6 - c^4)S(x, y + \Delta, z) \\
& + (a^7 - c^6)S(x + \Delta, y, z) + (a^8 - c^8)S(x, y, z) = 0.
\end{aligned} \tag{6.61}$$

Enforcing the symmetry property in each of Eqs. 6.59, 6.60, and 6.61, we can group together equivalent form-factors. The linearly independent terms in each equation must still vanish, individually, and we obtain the constraints

$$a^8 = b^8, a^4 = b^4, a^5 = b^5, a^1 = b^1, a^7 - b^6 = b^7 - a^6, a^3 - b^2 = b^3 - a^2, \tag{6.62}$$

$$b^8 = c^8, b^3 = c^3, b^6 = c^6, b^1 = c^1, b^4 - c^7 = c^4 - b^7, b^2 - c^5 = c^2 - b^5, \tag{6.63}$$

$$a^8 = c^8, a^1 = c^1, a^6 = c^4, a^3 = c^5, a^4 - c^7 = c^6 - a^7, a^2 - a^3 = c^2 - a^5. \tag{6.64}$$

Solving the (overconstrained, but still consistent) set of Eqs. 6.43, 6.47, 6.48, 6.49, 6.53, 6.54, 6.55, 6.62, 6.63, and 6.64, we obtain the coefficients,

$$\begin{aligned}
a^1 &= \frac{1}{3}, a^2 = -\frac{1}{3}, a^3 = \frac{1}{6}, a^4 = -\frac{1}{6}, a^5 = \frac{1}{6}, a^6 = -\frac{1}{6}, a^7 = \frac{1}{3}, a^8 = -\frac{1}{3}, \\
b^1 &= \frac{1}{3}, b^2 = -\frac{1}{3}, b^3 = \frac{1}{6}, b^4 = -\frac{1}{6}, b^5 = \frac{1}{6}, b^6 = -\frac{1}{6}, b^7 = \frac{1}{3}, b^8 = -\frac{1}{3}, \\
c^1 &= \frac{1}{3}, c^2 = -\frac{1}{3}, c^3 = \frac{1}{6}, c^4 = -\frac{1}{6}, c^5 = \frac{1}{6}, c^6 = -\frac{1}{6}, c^7 = \frac{1}{3}, c^8 = -\frac{1}{3}.
\end{aligned} \tag{6.65}$$

6.B Numerical heating in 2D

Fig. 6.12 shows the evolution of dimensionless temperature and fractional error for a set of simulations with initial dimensionless temperatures $\theta_0 = 10^{-5}, 10^{-4}$, and 10^{-3} , in 2D. Apart from box dimensions and the distribution used for initialization of the plasma (see Eq. 6.33), the numerical

parameters of these simulations are the same as in the 3D cases presented in Section 6.3.1.

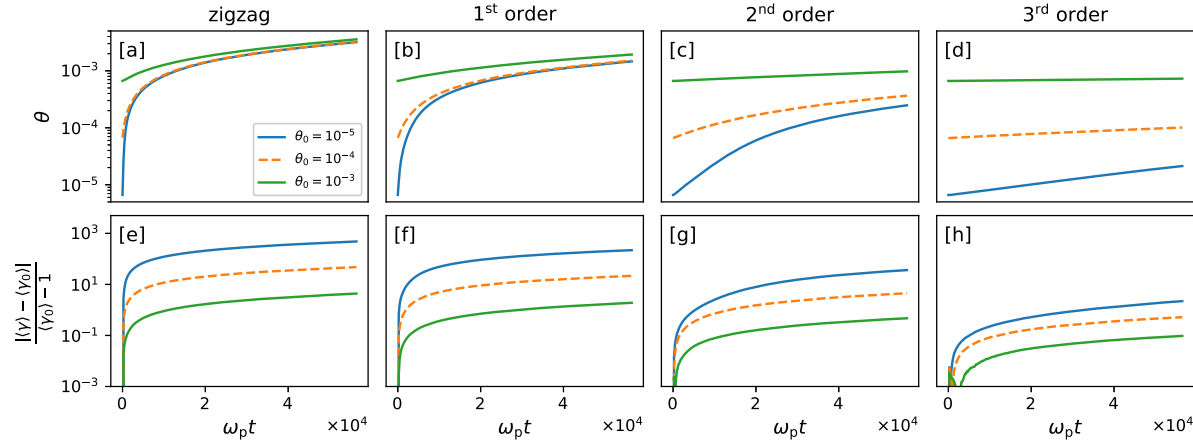


Figure 6.12: Similar to Fig. 6.2, but for 2D rather than 3D simulations; ((a) – (d)) Evolution of dimensionless temperature and ((e) – (h)) fractional error in a uniform plasma with initial dimensionless temperatures $\theta_0 = 10^{-5}, 10^{-4}$, and 10^{-3} , for zigzag, 1st, 2nd, and 3rd order Esirkepov (columns 1 – 4, respectively).

A. Performance and parallel scaling of **TRISTAN-MP**

Here, we present code performance measurements and parallel scalability data for the PIC code **TRISTAN-MP**. In Sec. A.1, we present measurements of the computing time needed to update one computational cell (t_{cell}) and one computational particle (t_{prt}); the numbers reported here correspond to update times needed in 3D simulations. In Sec. A.2, we present the performance of **TRISTAN-MP** when scaling to a large number of nodes. The tests were performed on Stampede2 at the Texas Advanced Computing Center (TACC).

A.1 Code performance

Table A.1 shows the reference values for the computational time needed to update one cell (t_{cell}) and one particle (t_{prt}), for 3D simulations using **TRISTAN-MP**. Measurements were obtained from simulations of counterstreaming plasma beams with periodic boundary conditions, with a constant number of particles and cells, and results were averaged over 250 time iterations. Each computational cell was initialized with two particles. All diagnostics in the code were off, i.e. the writing of HDF5 output to disk was disabled.

The tests on Stampede2 were performed using both Knights Landing (KNL) and Skylake (SKX) nodes. For KNL nodes, the tests were performed with a computational domain of $L_x \times L_y \times L_z = 544 \times 10000 \times 16$ cells assigned to each node, and 68 tasks per node (within the recommended range 64–68). For SKX nodes, the tests were performed with a computational domain of $L_x \times L_y \times L_z = 384 \times 10000 \times 16$ cells assigned to each node, and 48 tasks per node. In both sets of tests, the domain was decomposed along the x direction, fixing the computational load per core in each case to be the same, i.e. a domain of $L_x \times L_y \times L_z = 8 \times 10000 \times 16$ cells was assigned to each core. The measurements presented in Table A.1 may be interpreted as the time required by a *typical* core (when averaging over all cores in one node) to update one particle and one cell. As we show in Sec.

<i>System</i>	<i>time/cell</i> ‘ t_{cell} ’ [μs]	<i>time/particle</i> ‘ t_{prt} ’ [μs]
Stampede2 (KNL)	0.099	0.68
Stampede2 (SKX)	0.088	0.26

Table A.1: Performance of **TRISTAN-MP** on Stampede2, for Knight’s Landing (KNL) and Skylake (SKX) nodes.

A.2, the efficiency of **TRISTAN-MP** does not decrease significantly when scaling to more than one node, so the results presented in Table A.1 can be used as indicative figures for larger simulations.

A.2 Parallel scaling

We performed a weak scaling test on Stampede2, from 1 up to 64 nodes (68 up to 4352 cores) on KNL nodes, and 1 up to 16 nodes (48 up to 768 cores) on SKX nodes. The parallel scaling measurements are shown in Fig. A.1.

For the weak scaling test, the problem size was increased linearly with the number of nodes used, fixing the computational load per node. Again, we used a periodic simulation box with two particles per cell, and computational load *per processor* of $L_x \times L_y \times L_z = 10000 \times 8 \times 16$ cells. The measured parallel efficiency, defined as the ratio of actual computing time per iteration to the ideal time per iteration (benchmarked to 1 node in Fig. A.1), remains remarkably constant when scaling to more than one node. This justifies the choice of ‘averaging’ over one node when measuring the reference values for the time needed to update one particle and one cell (see Table A.1 in Sec. A.1).

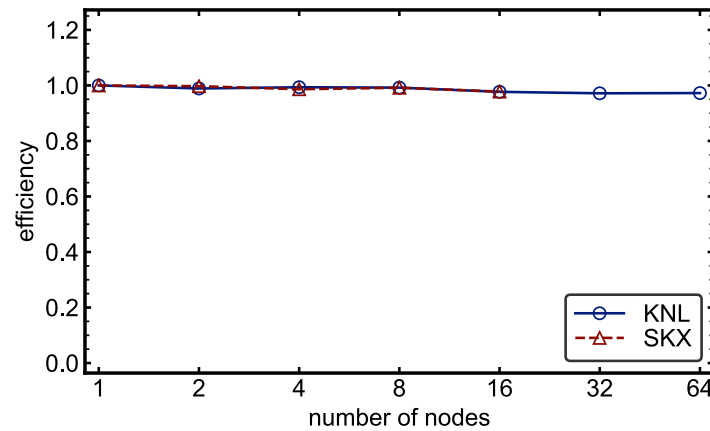


Figure A.1: Parallel efficiency for the weak scaling test on Stampede2, for both KNL and SKX nodes; from 1 up to 64 nodes (KNL; 68 up to 4352 cores), and from 1 up to 16 nodes (SKX; 48 up to 768 cores).

B. **WidPy**: Tool for visualization and analysis of **TRISTAN-MP** data

To allow for on-the-fly visualization and analysis of **TRISTAN-MP** data, we developed the interactive tool ‘**WidPy**,’ which is built for **Python 3.6** using the **PyQt5** and **PyQtgraph** (author: Luke Campagnola; see <http://www.pyqtgraph.org/>) libraries. The tool **WidPy** is designed in the same spirit as the **IDL** widget **wid.pro** (authors: Anatoly Spitkovsky, Lorenzo Sironi, and Uri Keshet) and **Python** package **Iseult** (author: Patrick Crumley; see <https://github.com/pcrumley/Iseult>).

Fig. B.1 shows a screenshot of the **WidPy** interface.

WidPy is intended for general-purpose visualization of **TRISTAN-MP** data, but also includes features that are specific to simulations of magnetic reconnection:

- Option to display a contour delineating the reconnection region, according to user selected threshold value;
- Slider controlling the reconnection threshold value, **dthresh**; the reconnection region is selected based on a mixing criterion between right-tagged and left-tagged particles (see Eq. 2.7);
- ‘Drag-and-drop’ box which allows for selection of particles in a given region and displays the corresponding energy spectrum.

A short demonstration and tutorial on **WidPy** can be found at <https://github.com/mrowan137/widpy>.

The **WidPy** project is licensed under the GPLv3 License.

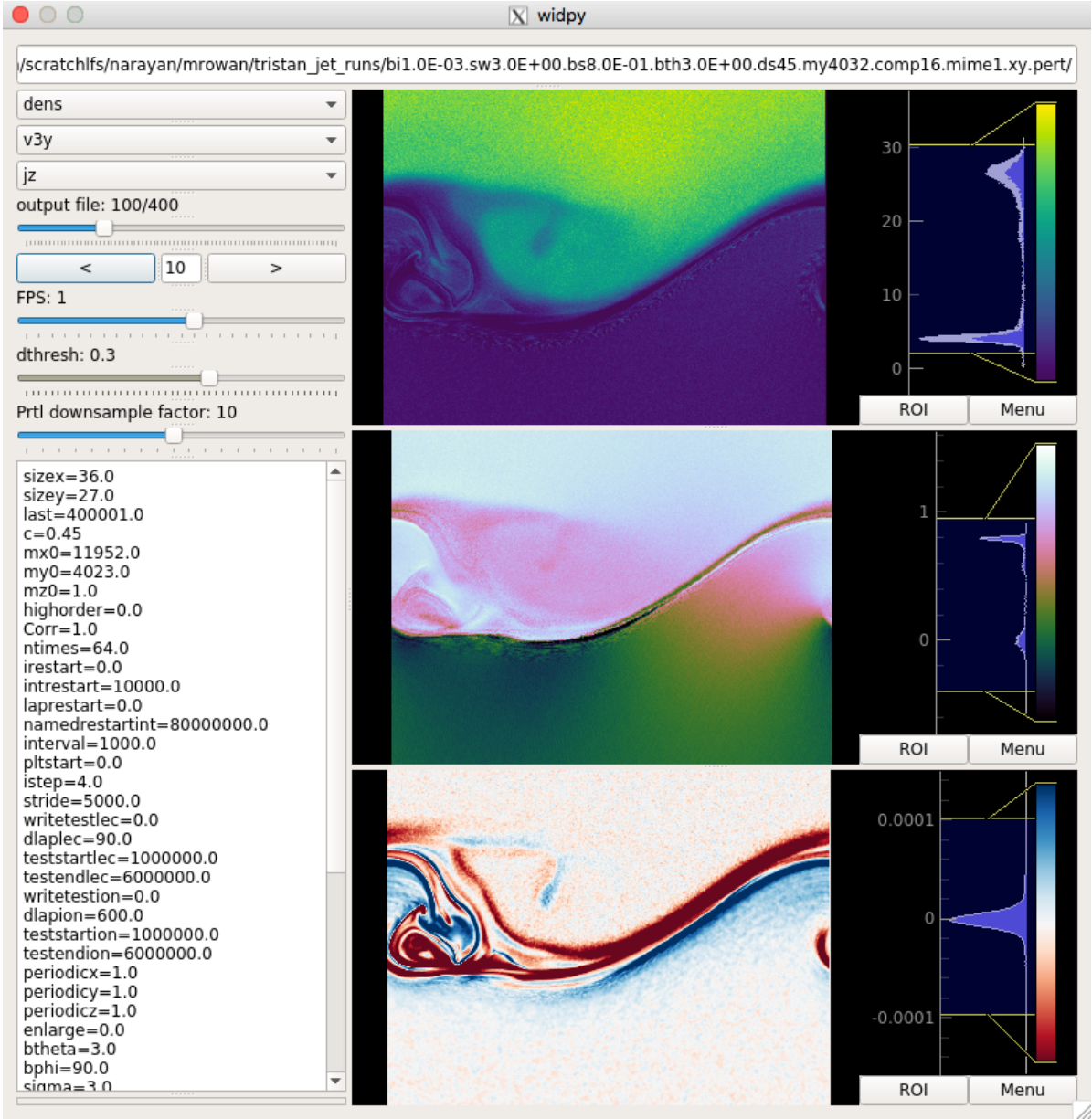


Figure B.1: Screenshot of the WidPy interface. Dropdown menus on the left allow for display of different fields of TRISTAN-MP output (the three vertical panels in the middle display the selected fields); a slider and arrow buttons on the left allow for selection of the timestep at which to display fields. For small data files, the FPS slider on the left may be used to control the framerate for the movie setting, which (when enabled) steps through the output files sequentially, displaying a movie in real time. Other controls and information about the simulation are also contained on the left.

C. Implementation of Esirkepov density decomposition

In Ch. 6, we present tests of the [Esirkepov \(2001\)](#) density decomposition algorithm, which we have implemented in the electromagnetic particle-in-cell code [TRISTAN-MP](#) ([Spitkovsky, 2005](#)), a massively-parallel version of [TRISTAN](#) ([Buneman, 1993](#)). Here, we show as an example our implementation (in unoptimized form) of the 3rd-order Esirkepov scheme. In the example below, the algorithm is written for readability rather than speed.

We consider a particle that moves from position $p_1 = (x_1, y_1, z_1)$ to $p_2 = (x_2, y_2, z_2)$. First, we compute the 3rd order shape functions when the particle is at p_1 : `Sx1`, `Sy1`, and `Sz1`. These arrays are computed according to Eq. 6.28. `Sx1`, `Sy1`, and `Sz1` are length-six arrays; `dx1`, `dy1`, and `dz1` are distances from p_1 to the primal grid point ($\lfloor x_1 \rfloor, \lfloor y_1 \rfloor, \lfloor z_1 \rfloor$):

```

if (dx1.le.0.5) then
    Sx1(2) = (-1/6.)*(dx1 - 1.)*(dx1 - 1.)*(dx1 - 1.)
    Sx1(3) = (2/3.) + 0.5*(dx1 - 2.)*dx1*dx1
    Sx1(5) = (1/6.)*dx1*dx1*dx1
    !Sx1(4)=(1/6.)*(1.+3.*dx1*(1.+dx1-dx1*dx1))
    Sx1(4) = 1. - Sx1(5) - Sx1(3) - Sx1(2)
    iterx1min = 2
    iterx1max = 5
elseif (dx1.gt.0.5) then
    Sx1(5) = (1/6.)*dx1*dx1*dx1
    Sx1(4) = (2/3.) + 0.5*(-1. - dx1)*(1. - dx1)*(1. - dx1)
    Sx1(2) = (1/6.)*(1. - dx1)*(1. - dx1)*(1. - dx1)
    !Sx1(3)=(1/6.)*(1.+3.*(1.-dx1)*(2.-(1.-dx1)*(1.-dx1)-dx1))
    Sx1(3) = 1. - Sx1(5) - Sx1(4) - Sx1(2)
    iterx1min = 2
    iterx1max = 5
endif
```

```

if (dy1.le.0.5) then
    Sy1(2) = (-1/6.)*(dy1 - 1.)*(dy1 - 1.)*(dy1 - 1.)
    Sy1(3) = (2/3.) + 0.5*(dy1 - 2.)*dy1*dy1
    Sy1(5) = (1/6.) *dy1*dy1*dy1
    !Sy1(4) = (1/6.)*(1.+3.*dy1*(1.+dy1-dy1*dy1))
    Sy1(4) = 1. - Sy1(5) - Sy1(3) - Sy1(2)
    itery1min = 2
    itery1max = 5
elseif (dy1.gt.0.5) then
    Sy1(5) = (1/6.)*dy1*dy1*dy1
    Sy1(4) = (2/3.) + 0.5*(-1. - dy1)*(1. - dy1)*(1. - dy1)
    Sy1(2) = (1/6.)*(1. - dy1)*(1. - dy1)*(1. - dy1)
    !Sy1(3)=(1/6.)*(1.+3.*(1.-dy1)*(2.-(1.-dy1)*(1.-dy1)-dy1))
    Sy1(3) = 1. - Sy1(5) - Sy1(4) - Sy1(2)
    itery1min = 2
    itery1max = 5
endif

#ifndef twoD
if (dz1.le.0.5) then
    Sz1(2) = (-1/6.)*(dz1 - 1.)*(dz1 - 1.)*(dz1 - 1.)
    Sz1(3) = (2/3.) + 0.5*(dz1 - 2.)*dz1*dz1
    Sz1(5) = (1/6.)*dz1*dz1*dz1
    !Sz1(4)=(1/6.)*(1.+3.*dz1*(1.+dz1-dz1*dz1))
    Sz1(4) = 1. - Sz1(5) - Sz1(3) - Sz1(2)
    iterz1min = 2
    iterz1max = 5
elseif (dz1.gt.0.5) then
    Sz1(5) = (1/6.)*dz1*dz1*dz1
    Sz1(4) = (2/3.) + 0.5*(-1. - dz1)*(1. - dz1)*(1. - dz1)
    Sz1(2) = (1/6.)*(1. - dz1)*(1. - dz1)*(1. - dz1)
    !Sz1(3) = (1/6.)*(1.+3.*(1.-dz1)*(2.-(1.-dz1)*(1.-dz1)-dz1))
    Sz1(3) = 1. - Sz1(5) - Sz1(4) - Sz1(2)
    iterz1min = 2
    iterz1max = 5
endif
#endif

```

We compute also the 3rd order shape functions when the particle is at p_2 : S_{x2} , S_{y2} , and S_{z2} ;

here, $dx2$, $dy2$, and $dz2$ are distances from p_2 to the primal grid point ($\lfloor x_2 \rfloor$, $\lfloor y_2 \rfloor$, $\lfloor z_2 \rfloor$):

```
if (dx2.le.0.5) then
    Sx2(2+shifti) = (-1/6.)*(dx2 - 1.)*(dx2 - 1.)*(dx2 - 1.)
    Sx2(3+shifti) = (2/3.) + 0.5*(dx2 - 2.)*dx2*dx2
    Sx2(5+shifti) = (1/6.)*dx2*dx2*dx2
    !Sx2(4)=(1/6.)*(1.+3.*dx2*(1.+dx2-dx2*dx2))
    Sx2(4+shifti) = 1. - Sx2(5+shifti) - Sx2(3+shifti) &
        - Sx2(2 + shifti)
    iterx2min = 2 + shifti
    iterx2max = 5 + shifti
elseif (dx2.gt.0.5) then
    Sx2(5+shifti) = (1/6.)*dx2*dx2*dx2
    Sx2(4+shifti) = (2/3.) + 0.5*(-1. - dx2)*(1. - dx2)*(1. - dx2)
    Sx2(2+shifti) = (1/6.)*(1. - dx2)*(1. - dx2)*(1. - dx2)
    Sx2(3+shifti) = 1. - Sx2(5+shifti) - Sx2(4+shifti) &
        - Sx2(2 + shifti)
    iterx2min = 2 + shifti
    iterx2max = 5 + shifti
endif

if (dy2.le.0.5) then
    Sy2(2+shiftj) = (-1/6.)*(dy2 - 1.)*(dy2 - 1.)*(dy2 - 1.)
    Sy2(3+shiftj) = (2/3.) + 0.5*(dy2 - 2.)*dy2*dy2
    Sy2(5+shiftj) = (1/6.)*dy2*dy2*dy2
    Sy2(4+shiftj) = 1. - Sy2(5+shiftj) - Sy2(3+shiftj) - Sy2(2+shiftj)
    itery2min = 2 + shiftj
    itery2max = 5 + shiftj
elseif (dy2.gt.0.5) then
    Sy2(5+shiftj) = (1/6.)*dy2*dy2*dy2
    Sy2(4+shiftj) = (2/3.) + 0.5*(-1. - dy2)*(1. - dy2)*(1. - dy2)
    Sy2(2+shiftj) = (1/6.)*(1. - dy2)*(1. - dy2)*(1. - dy2)
    Sy2(3+shiftj) = 1. - Sy2(5+shiftj) - Sy2(4+shiftj) &
        - Sy2(2 + shiftj)
    itery2min = 2 + shiftj
    itery2max = 5 + shiftj
endif
```

```

iterxmin = min(iterx1min, iterx2min)
iterxmax = max(iterx1max, iterx2max)
iterymin = min(itery1min, itery2min)
iterymax = max(itery1max, itery2max)

#ifndef twoD
    if (dz2.le.0.5) then
        Sz2(2+shiftk) = (-1/6.)*(dz2 - 1.)*(dz2 - 1.)*(dz2 - 1.)
        Sz2(3+shiftk) = (2/3.) + 0.5*(dz2 - 2.)*dz2*dz2
        Sz2(5+shiftk) = (1/6.) *dz2*dz2*dz2
        Sz2(4+shiftk) = 1. - Sz2(5+shiftk)-Sz2(3+shiftk) &
            -Sz2(2 + shiftk)
        iterz2min = 2 + shiftk
        iterz2max = 5 + shiftk
    elseif (dz2.gt.0.5) then
        Sz2(5+shiftk) = (1/6.)*dz2*dz2*dz2
        Sz2(4+shiftk) = (2/3.) + 0.5*(-1. - dz2)*(1. - dz2) &
            *(1. - dz2)
        Sz2(2+shiftk) = (1/6.)*(1. - dz2)*(1. - dz2)*(1. - dz2)
        Sz2(3+shiftk) = 1. - Sz2(5+shiftk) - Sz2(4+shiftk) &
            - Sz2(2 + shiftk)
        iterz2min = 2 + shiftk
        iterz2max = 5 + shiftk
    endif
    iterzmin = min(iterz1min,iterz2min)
    iterzmax = max(iterz1max,iterz2max)
#endif

```

With the shape functions at p_1 and p_2 defined, we compute the charge weights w_x, w_y , and w_z (six-by-six arrays) according to Eqs. 6.15, 6.16, and 6.17:

```

do iter = 1,6
    DSx(iter) = Sx2(iter) - Sx1(iter)
    DSy(iter) = Sy2(iter) - Sy1(iter)
    DSz(iter) = Sz2(iter) - Sz1(iter)
enddo

do iter2 = 1,6
    do iter1 = 1,6
        do iter = 1,6
            Wx(iter, iter1, iter2) = &
                DSx(iter)*(Sy1(iter1)*Sz1(iter2)) &
                + 0.5*DSy(iter1)*Sz1(iter2) &
                + 0.5*Sy1(iter1)*DSz(iter2) &
                + (1/3.)*DSy(iter1)*DSz(iter2))
            Wy(iter, iter1, iter2) = &
                DSy(iter1)*(Sx1(iter)*Sz1(iter2)) &
                + 0.5*DSx(iter)*Sz1(iter2) &
                + 0.5*Sx1(iter)*DSz(iter2) &
                + (1/3.)*DSx(iter)*DSz(iter2))
            Wz(iter, iter1, iter2) = &
                DSz(iter2)*(Sx1(iter)*Sy1(iter1)) &
                + 0.5*DSx(iter)*Sy1(iter1) &
                + 0.5*Sx1(iter)*DSy(iter1) &
                + (1/3.)*DSx(iter)*DSy(iter1))
        enddo
    enddo
enddo

```

The weights W_x , W_y , and W_z determine the current to deposit on the grid. The deposited currents due to x , y , and z motion are computed and then stored temporarily in seven-by-seven arrays tmp_x , tmp_y , and tmp_z :

```

do iter = 1,6
  do iter1 = 1,6
    do iter2 = 1,6
      if(iter.eq.1) then
        tmpx(iter, iter1, iter2) = q*wx(iter, iter1, iter2)
      else
        tmpx(iter, iter1, iter2) = tmpx(iter-1, iter1, iter2) &
          + q*wx(iter, iter1, iter2)
      endif
    enddo
  enddo
enddo

do iter = 1,6
  do iter1 = 1,6
    do iter2 = 1,6
      if(iter1.eq.1) then
        tmpy(iter, iter1, iter2) = q*wy(iter, iter1, iter2)
      else
        tmpy(iter, iter1, iter2) = tmpy(iter, iter1-1, iter2) &
          + q*wy(iter, iter1, iter2)
      endif
    enddo
  enddo
enddo

do iter = 1,6
  do iter1 = 1,6
    do iter2 = 1,6
      if(iter2.eq.1) then
        tmpz(iter, iter1, iter2) = q*wz(iter, iter1, iter2)
      else
        tmpz(iter, iter1, iter2) = tmpz(iter, iter1, iter2-1) &
          + q*wz(iter, iter1, iter2)
      endif
    enddo
  enddo
enddo

```

The global current arrays `curx`, `cury`, and `curz` are updated according to the deposited currents

`tmpx`, `tmpy`, and `tmpz`:

```
do iter=1,6
  do iter1=1,6
    do iter2=1,6
      curx(i1-3+iter, j1-3+iter1, k1-3+iter2) = &
        curx(i1-3+iter, j1-3+iter1, k1-3+iter2) &
        + tmpx(iter, iter1, iter2)
      cury(i1-3+iter, j1-3+iter1, k1-3+iter2) = &
        cury(i1-3+iter, j1-3+iter1, k1-3+iter2) &
        + tmpy(iter, iter1, iter2)
      curz(i1-3+iter, j1-3+iter1, k1-3+iter2) = &
        curz(i1-3+iter, j1-3+iter1, k1-3+iter2) &
        + tmpz(iter, iter1, iter2)
    enddo
  enddo
enddo
```

During the particle-push step, the electric and magnetic fields are interpolated to the particle location in a way that is consistent with the choice of particle stencil (see Eq. 6.36). In the block of code below, `Sxp`, `Syp`, and `Szp` are the shape functions, and `ex_p`, `ey_p`, `ez_p`, `bx_p`, `by_p`, and `bz_p` are the electromagnetic fields interpolated to the primal gridpoints.

```

#ifndef twoD
    do iter3 = iter3min,iter3max
        do iter2 = iter2min,iter2max
            ex0=ex0 + sum(ex_p(ip-3+iter1min:ip-3+iter1max, &
                jp-3+iter2, kp-3+iter3)
                *Sxp(iter1min:iter1max))*Syp(iter2)*Szp(iter3)
            ey0=ey0 + sum(ey_p(ip-3+iter1min:ip-3+iter1max, &
                jp-3+iter2, kp-3+iter3)
                *Sxp(iter1min:iter1max))*Syp(iter2)*Szp(iter3)
            ez0=ez0 + sum(ez_p(ip-3+iter1min:ip-3+iter1max, &
                jp-3+iter2, kp-3+iter3)
                *Sxp(iter1min:iter1max))*Syp(iter2)*Szp(iter3)
            bx0=bx0+sum(bx_p(ip-3+iter1min:ip-3+iter1max, &
                jp-3+iter2, kp-3+iter3)
                *Sxp(iter1min:iter1max))*Syp(iter2)*Szp(iter3)
            by0=by0 + sum(by_p(ip-3+iter1min:ip-3+iter1max, &
                jp-3+iter2, kp-3+iter3)
                *Sxp(iter1min:iter1max))*Syp(iter2)*Szp(iter3)
            bz0=bz0+sum(bz_p(ip-3+iter1min:ip-3+iter1max, &
                jp-3+iter2, kp-3+iter3)
                *Sxp(iter1min:iter1max))*Syp(iter2)*Szp(iter3)
        enddo
    enddo
#else
    do iter2 = iter2min,iter2max
        do iter1 = iter1min,iter1max
            lpp = (ip-3+iter1) + iy*(jp-3+iter2-1)
            lpd = (ip-3+iter1) + iy*(jd-3+iter2-1)
            ldp = (id-3+iter1) + iy*(jp-3+iter2-1)
            ldd = (id-3+iter1) + iy*(jd-3+iter2-1)
            ex0 = ex0 + ex(ldp, 1, 1)*Sxd(iter1)*Syp(iter2)
            ey0 = ey0 + ey(lpd, 1, 1)*Sxp(iter1)*Syd(iter2)
            ez0 = ez0 + ez(lpp, 1, 1)*Sxp(iter1)*Syp(iter2)
            bx0 = bx0 + bx(lpd, 1, 1)*Sxp(iter1)*Syd(iter2)
            by0 = by0 + by(ldp, 1, 1)*Sxd(iter1)*Syp(iter2)
            bz0 = bz0 + bz(ldd, 1, 1)*Sxd(iter1)*Syd(iter2)
        enddo
    enddo
#endif

```

References

- Abramowicz, M. A., Chen, X., Kato, S., Lasota, J.-P., & Regev, O. 1995, ApJL, 438
- Alves, E. P., Grismayer, T., Fonseca, R. A., & Silve, L. O. 2014, New J. Phys., 16, 035007
- Alves, E. P., Grismayer, T., Martins, S. F., et al. 2012, ApJL, 746, 14
- Anile, A. M. 1990, Relativistic fluids and magneto-fluids, Vol. 21 (Cambridge University Press)
- Ball, D., Ozel, F., Psaltis, D., Chan, C.-k., & Sironi, L. 2017, arXiv:1705.06293v1
- Ball, D., Özel, F., Psaltis, D., & kwan Chan, C. 2016, The Astrophysical Journal, 826, 77
- Ball, D., Sironi, S., & Özel, F. 2018, ApJ, 826, 77
- Beckwith, K., Hawley, J. F., & Krolik, J. H. 2008, ApJ, 678, 1180
- Berlok, T., & Pfrommer, C. 2011, MNRAS, 485, 908
- Birdsall, C. K., & Langdon, A. B. 1991, Plasma Physics via Computer Simulation
- Birdsall, C. K., & Maron, N. 1980, Journal of Computational Physics, 36, 1
- Birn, J., Drake, J. F., Shay, M. A., et al. 1957, J. Geophys. Res., 106, 3715
- Blumen, W., Drazin, P. G., & Billings, D. F. 1975, J. Fluid Mech., 71, 305
- Bodo, G., Mignone, A., & Rosner, R. 2004, Phys. Rev. E, 70, 036304
- Boldyrev, S., & Loureiro, N. F. 2017, ApJ, 844, 125
- Boris, J. 1970, in Proceedings of the Fourth Conference on Numerical Simulation of Plasmas, Naval Research Laboratory, 3
- Borovsky, J. E., Hesse, M., Birn, J., & Kuznetsova, M. M. 2008, J. of Geophys. Res., 113, A072190
- Bret, A. 2012, arXiv:1205.6259
- Buneman, O. 1959, Phys. Rev., 115
- . 1993, in Computer Space Plasma Physics: Simulation Techniques and Software, ed. H. T. D. Guyenne & J. J. Hunt (ESA)
- Buneman, O., Nishikawa, K.-I., & Neubert, T. 1993, in Plasma Physics and Controlled Nuclear Fusion (ITC-4), ed. H. Matsumoto, Y. Omura, & E. Sindoni (Terra Scientific), 285
- Cai, D., Li, Y., Nishikawa, K.-I., & et al. 2003, in Lecture Notes in Physics, Berlin Springer Verlag, Vol. 615, Space Plasma Simulation, ed. J. Büchner, C. Dum, & M. Scholer, 25–53

- Cassak, P. A., Liu, Y. H., & Shay, M. A. 2017, *J. Plasma Phys.*, 83, 715830501
- Chael, A., Rowan, M., Narayan, R., Johnson, M., & Sironi, L. 2018, *MNRAS*, 478, 5209
- Chael, A. A., Narayan, R., & Sadowski, A. 2017, *Monthly Notices of the Royal Astronomical Society*, 470, 2367
- Chandrasekhar, S. 1961, 42, 362
- Chiou, H. 1973, *Phys. Fluids*, 16, 825
- Comisso, L., & Bhattacharjee, L. 2016, *J. Plasma Phys.*, 82, 595820601
- Comisso, L., & Sironi, L. 2018, *Phys. Rev. Lett.*, 121, 255101
- Dahlin, J. T., Drake, J. F., & Swisdak, M. 2014, *Phys. of Plasmas*, 21, 092304
- . 2015, *Phys. of Plasmas*, 22, 100704
- Dallilar, Y., et al. 2017, *Science*, 358, 1299
- Daughton, W., & Karimabadi, H. 2007, *Phys. of Plasmas*, 14, 072303
- Daughton, W., Nakamura, T. K. M., Karimabadi, H., Roytershteyn, V., & Loring, B. 2014, *Physics of Plasmas*, 21
- Dawson, J. M. 1962, *Phys. Fluids*, 5
- . 1983, *Reviews of Modern Physics*, 55
- Dixon, G. 1978, *Special Relativity, the Foundation of Macroscopic Physics* (Cambridge Univ. Press, Cambridge)
- Doeleman, S., et al. 2008, *Nature*, 455, 78
- . 2009, Astro2010: The Astronomy and Astrophysics Decadal Survey, Science White Papers, Tech. rep.
- Drake, J. F., M., S., Che, H., & Shay, M. A. 2006, *Nature*, 443, 553
- Drake, J. F., Opher, M., Swisdak, M., & Chamoun, J. N. 2010, *Astrophys. J.*, 709, 963
- Dungey, J. W. 1953, *Phil. Mag.*, 44, 725
- Duran, R. B., Tchekhovskoy, A., & Giannios, D. 2017, *MNRAS*, 469, 4957
- Dyson, F. 1960, *Phys. Fluids*, 3, 155
- Eastwood, J. P., Mistry, R., Phan, T. D., et al. 2018, *Geophysical Research Letters*, 45, 4569
- Eastwood, J. P., Phan, T. D., Drake, J. F., et al. 2013, *Phys. Rev. Lett.*, 110, 225001

- Esirkepov, T. Z. 2001, Computational Physics Communications, 135, 144
- Faganello, M., Califano, F., & Pegoraro, F. 2008, Phys. Rev. Lett., 100, 015001
- Faganello, M., Califano, F., Pegoraro, F., Andreussi, T., & Berkadda, S. 2012, Plasma Physics and Controlled Fusion, 100, 015001
- Fermo, R. L., Drake, J. F., & Swisdak, M. 2012, Phys. Rev. Lett., 108, 255005
- Ferrari, A., Trussoni, E., & Zaninetti, L. 1980, MNRAS, 193, 469
- Godfrey, B. 1974, Journal of Computational Physics, 15, 504
- Grismayer, T., Alves, E. P., Fonseca, R. A., & Silve, L. O. 2013, Phys. Rev. Lett., 111, 015005
- Guo, F., Li, X., Li, H., et al. 2016, The Astrophysical Journal, 818, L9
- Haggerty, C. C., Shay, M. A., Drake, J. F., Phan, T. D., & McHugh, C. T. 2015, Geophysical Research Letters, 42, 9657
- Hamlin, N., & Newman, W. 2013, Phys. Rev. E, 87, 043101
- Hardee, P. E. 2004, Ap&SS, 293, 117
- Hardee, P. E., Mizuno, Y., & Nishikawa, K.-I. 2007, Ap&SS, 311, 281
- Henri, P., Cerri, S. S., Califano, F., et al. 2013, Phys. of Plasmas, 20, 102118
- Hesse, M., & Zenitani, S. 2007, Phys. of Plasmas, 14, 112102
- Ho, L. C. 2008, Ann. Rev. Astron. Astrophys., 46, 1
- Hockney, R. W., & Eastwood, J. W. 1988 (CRC Press)
- Hoshino, M. 2018, ApJL, 868, 2
- Hoshino, M., Hiraide, K., & Mukai, T. 2001, Earth, Planets and Space, 53, 627
- Howes, G. G. 2010, MNRAS, 409, 1
- Huba, J. D. 2005, Phys. of Plasmas, 12, 012322
- Igumenshchev, I. V., Narayan, R., & Abramowicz, M. A. 2003, ApJ, 592, 1042
- Ikeya, N., & Matsumoto, Y. 2015, Publications of the Astronomical Society of Japan, 67, 64
- Jaroschek, C. H., Treumann, R. A., Lesch, H., & Scholer, M. 2004, Physics of Plasmas, 11, 1151
- Johnson, M. D., et al. 2015, Science, 350, 1242
- Kawazura, Y., Barnes, M., & Schekochihin, A. A. 2019, PNAS, 116, 771

- Komissarov, S. S. 1999, MNRAS, 303, 343
- Konigl, A. 1980, Phys. Fluids, 23, 1083
- Lapenta, G. 2015, Kinetic Plasma Simulation: Particle In Cell Method, doi:10.13140/RG.2.1.3319.2801
- Le, A., Egedal, J., & Daughton, W. 2016, Physics of Plasmas, 23, 1
- Le, A., Egedal, J., Daughton, W., Fox, W., & Katz, N. 2009, Phys. Rev. Lett., 102, 085001
- Lee, S. Y., Lee, E., Kim, K. H., et al. 2015, Phys. of Plasmas, 22, 12213
- Li, X., Guo, F., Li, H., & Birn, J. 2018, ApJ, 855, 80
- Li, X., Guo, F., Li, H., & Li, G. 2015, The Astrophysical Journal, 811, L24
- . 2017a, The Astrophysical Journal, 843, 21
- Li, Y.-P., Yuan, F., & Wang, Q. D. 2017b, MNRAS, 468, 2552
- Liu, Y.-H., Daughton, W., Karimabadi, H., Li, H., & Gary, S. P. 2014, Phys. of Plasmas, 21, 022113
- Liu, Y.-H., Hesse, M., Guo, F., et al. 2017, Phys. Rev. Lett., 118, 085101
- Liu, Z. X., et al. 1988, Geophys. Res. Lett., 15, 752
- Livingston, W., Harvey, J. W., Malanushenko, O. V., & Webster, L. 2006, Sol. Phys., 239, 41
- Lord Kelvin. 1871, Philos. Mag., 42, 362
- Loureiro, N. F., & Boldyrev, S. 2017, ApJ, 850, 182
- Loureiro, N. F., Schekochihin, A. A., & Zocco, A. 2013, Phys. Rev. Lett., 111, 025002
- Makwana, K., Li, H., Guo, F., & Li, X. 2017, J. Phys.: Conf. Ser., 837, 012004
- Mallet, A., Schekochihin, A. A., & Chandran, B. D. G. 2017, MNRAS, 468, 4862
- Melzani, M., Walder, R., Folini, D., Winisdoerffer, C., & Favre, J. M. 2014, Astronomy & Astrophysics, 570, A111
- Melzani, M., Winisdoerffer, C., Walder, R., et al. 2013, Astronomy & Astrophysics, 558, A133
- Mignone, A., Mattia, G., & Bodo, G. 2018, Phys. of Plasmas, 25, 092114
- Mignone, A., Zanni, C., Tzeferacos, P., et al. 2011, ApJS, 198
- Miura, A., & Pritchett, P. L. 1982, J. of Geophys. Res., 87, 7431

- Mizuno, Y., Hardee, P. E., & Nishikawa, K.-I. 2006, PoSMQW6, 86
- Mozer, F., & Pritchett, P. 2010, Physics Today, 63, 34
- Munoz, P. A., & Büchner, J. 2018, Phys. Rev. E, 98, 043205
- Narayan, R., & McClintock, J. E. 2008, New Astronomy Reviews, 51, 733
- Narayan, R., & Yi, I. 1994, The Astrophysical Journal, 428, 1316
- . 1995a, ApJ, 452, 710
- . 1995b, The Astrophysical Journal, 452, 710
- NASA. 2008, Halloween Storms of 2003 Still the Scariest, https://www.nasa.gov/topics/solarsystem/features/halloween_storms.html, accessed: 07-24-2019
- Nishikawa, I. K., Hardee, P. E., Dutan, I., et al. 2012, ApJ, 793, 60
- Northrop, T. G. 1961, Ann. of Phys., 15, 1
- . 1963a, Rev. Geophys., 1, 3
- . 1963b, Adiabatic Motion of Charged Particles, Vol. 21 (Interscience Publishers)
- Numata, R., & Loureiro, N. 2015, J. Plasma Phys., 81, 305810201
- Osmanov, Z., Mignone, A., Massaglia, S., Bodo, G., & Ferrari, A. 2008, Astronomy & Astrophysics, 490, 493
- Parker, E. N. 1957, J. Geophys. Res., 62, 509
- . 1963, Ap. J., 8, 177
- . 1973, Ap. J., 180, 247
- Phan, T. D., Shay, M. A., Gosling, J. T., et al. 2013, Geophysical Research Letters, 40, 4475
- Pritchett, P. L. 2003, in Lecture Notes in Physics, Berlin Springer Verlag, Vol. 615, Space Plasma Simulation, ed. J. Büchner, C. Dum, & M. Scholer, 1–24
- Quataert, E., Dorland, W., & Hammett, G. W. 2002, The Astrophysical Journal, 577, 524
- Quataert, E., & Gruzinov, A. 1999, ApJ, 520, 248
- Ressler, S. M., Tchekhovskoy, A., Quataert, E., Chandra, M., & Gammie, C. F. 2015, Monthly Notices of the Royal Astronomical Society, 454, 1848
- Ressler, S. M., Tchekhovskoy, A., Quataert, E., & Gammie, C. F. 2017a, MNRAS, 467, 3604
- . 2017b, Monthly Notices of the Royal Astronomical Society, 467, 3604

- Ricci, P., Lapenta, G., & Brackbill, J. U. 2003, Phys. of Plasmas, 10, 3554
- Riquelme, M. A., Quataert, E., Sharma, P., & Spitkovsky, A. 2012, The Astrophysical Journal, 50
- Riquelme, M. A., Quataert, E., & Verscharen, D. 2015, The Astrophysical Journal, 800, 27
- Rowan, M. E., Sironi, L., & Narayan, R. 2017, ApJ, 850, 29 (RSN17)
- Ryan, B. R., Ressler, S. M., Dolence, J. C., Gammie, C., & Quataert, E. 2018, ApJ, 864, 126
- Sadowski, A., Sironi, L., Abarca, D., et al. 2013, Monthly Notices of the Royal Astronomical Society, 432, 478
- Sadowski, A., Wielgus, M., Narayan, R., et al. 2017, Monthly Notices of the Royal Astronomical Society, 466, 705
- Savitzky, A., & Golay, M. J. E. 1964, Analytical Chemistry, 36, 1627
- Schindler, K., & Hesse, M. 1988, J. Geophys. Res., 93, 5547
- Schoeffler, K. M., Drake, J. F., & Swisdak, M. 2011, The Astrophysical Journal, 743, 70
- Schoeffler, K. M., Drake, J. F., Swisdak, M., & Knizhnik, K. 2013, The Astrophysical Journal, 764, 126
- Service, A. T. 1986, ApJ, 307
- Shalaby, M., Broderick, A. E., Chang, P., et al. 2017, The Astrophysical Journal, 841, 52
- Shay, M. A., Frake, J. F., & Swisdak, M. 2007, Phys. Rev. Lett., 99, 155002
- Shay, M. A., Haggerty, C. C., Matthaeus, W. H., et al. 2018, Phys. of Plasmas, 25, 012304
- Shay, M. A., Haggerty, C. C., Phan, T. D., et al. 2014, Phys. of Plasmas, 21, 122902
- Shukla, C., Das, A., & Patel, K. 2016, Phys. of Plasmas, 23, 082108
- SILSO World Data Center. 1818–2017, International Sunspot Number Monthly Bulletin and online catalogue
- Sironi, L. 2015, ApJ, 800, 89
- Sironi, L., Giannios, D., & Petropoulou, M. 2016, Monthly Notices of the Royal Astronomical Society, 462, 48
- Sironi, L., & Narayan, R. 2015, ApJ, 800, 88
- Sironi, L., Petropoulou, M., & Giannios, D. 2015, Monthly Notices of the Royal Astronomical Society, 450, 183

- Sironi, L., & Spitkovsky, A. 2011, *The Astrophysical Journal*, 726, 75
- . 2014, *ApJL*, 783, 1
- Spitkovsky, A. 2005, *AIP Conference Proceedings*, 801, 345
- Steinberg, G., et al. 2007, *Ann. Geophys.*, 25, 2439
- Stone, J. M., Pringle, J. E., & Begelman, M. C. 1999, *MNRAS*, 310, 1002
- Sweet, P. A. 1958, in IAU Symposium 6, *Electromagnetic Phenomena in Cosmical Physics*, ed. B. Lehnert, Vol. 123, 25–53
- Synge, J. L. 1957, *The relativistic Gas* (North-Holland Publishing Company)
- Tchekhovskoy, A., Narayan, R., & McKinney, J. C. 2011, *MNRAS Letters*, 418, L79
- TenBarge, J. M., Daughton, W., Karimabadi, H., Howes, G. G., & Dorland, W. 2013, *Phys. of Plasmas*, 21, 020708
- The EHT Collaboration, et al. 2019, *ApJL*, 875
- Umeda, T., Omura, Y., Tominaga, T., & Matsumoto, H. 2003, *Computational Physics Communications*, 156, 73
- Uzdensky, D. A. 2011, *Space Science Reviews*, 160, 45
- Uzdensky, D. A., Loureiro, N. F., & Schekochihin, A. A. 2010, *Phys. Rev. Lett.*, 105, 16
- Vay, J.-L. 2008, *Physics of Plasmas*, 15, 056701
- Von Helmholtz, H., & Monats, K. 1868, *Preuss. Akad. Wiss. Berlin*, 23, 215
- Wang, S., Chen, L.-J., Bessho, N., et al. 2016, *J. of Geophys. Res.*, 121, 3
- Werner, G. R., & Uzdensky, D. A. 2017, *ApJL*, 843, 2
- Werner, G. R., Uzdensky, D. A., Begelman, M. C., Cerutti, B., & Nalewajko, K. 2016, *MNRAS*, 473, 4840
- Yamada, M., Yoo, J., Jara-Almonte, J., et al. 2015, *Physics of Plasmas*, 22, 056501
- Yee, K. 1966, *IEEE Transactions on Antennas and Propagation*, 14, 302
- Yuan, F., Markoff, S., & Falcke, H. 2002, *Astronomy & Astrophysics*, 383, 854
- Yuan, F., & Narayan, R. 2014, *Annual Review of Astronomy and Astrophysics*, 52, 529
- Yuan, F., Quataert, E., & Narayan, R. 2003, *ApJ*, 598, 301
- Zenitani, S. 2015, *Phys. of Plasmas*, 22, 042116

Zenitani, S., & Hoshino, M. 2008, ApJ, 677, 1

Zhdankin, V., Uzdensky, D. A., Werner, G. R., & Begelman, M. C. 2019, Phys. Rev. Lett., 122, 055101